Moment redistribution and post-peak behaviour of steel fibre reinforced concrete flexural members

Author:
Mahmood, S M Faisal

Publication Date:
2020

DOI:
https://doi.org/10.26190/unsworks/22166

MOMENT REDISTRIBUTION AND POST-PEAK BEHAVIOUR OF STEEL FIBRE REINFORCED CONCRETE FLEXURAL MEMBERS

by

S M Faisal Mahmood

A thesis submitted in fulfilment of the requirements for the degree of

Doctor of Philosophy

School of Civil and Environmental Engineering

The University of New South Wales, Sydney, Australia

March 2020

Thesis/Dissertation Sheet

Surname/Family Name	:	**MAHMOOD**
Given Name/s	:	**S M FAISAL**
Abbreviation for degree as give in the University calendar	:	**PhD**
Faculty	:	**Engineering**
School	:	**Civil and Environmental Engineering**
Thesis Title	:	**MOMENT REDISTRIBUTION AND POST-PEAK BEHAVIOUR OF STEEL FIBRE REINFORCED CONCRETE FLEXURAL MEMBERS**

Abstract

This thesis presents a study of the moment redistribution capability and post-peak behaviour of conventionally reinforced steel fibre reinforced concrete (R-SFRC) continuous members designed for moment redistribution. Because of the lack of research in this area, limitations are placed in design standards on the application of steel fibres in RC continuous members designed for moment redistribution and no guidelines are available in the standards on the requirement for minimum reinforcement for which R-SFRC flexural members will show sufficient level of ductility. Consequently, two sets of experiments were designed to investigate the moment redistribution capability and post-peak behaviour of R-SFRC continuous members.

In the first set of experiments, six full-scale two-span continuous RC beams with and without fibres were designed for ±30% of moment redistribution with respect to the linear-elastic condition. Dramix 5D steel fibres with nominal dosages of 30 and 60 kg/m^3 were used and the tensile reinforcement ratios varied between 0.69% and 1.38%. The second set of experiments comprised of six full-scale two-span continuous one-way RC slabs with and without fibres, which were designed for 0 to 30% of positive moment redistribution with respect to the linear-elastic condition by varying the tensile reinforcement ratios between 0.21% and 0.42%. Dramix 3D steel fibres with a nominal dosage of 60 kg/m^3 were used.

The test results showed that in all R-SFRC beam and slab tests, two plastic hinges fully formed to develop the failure mechanism indicating the ability of R-SFRC continuous members to achieve the theoretical (elastic) design moment redistribution. The R-SFRC beams having tensile reinforcement ratios more than 0.5% maintained their capacity up to a displacement of 50 mm whereas the R-SFRC slabs having tensile reinforcement ratios less than 0.5% showed a shorter displacement length over which hardening occurred before the peak load was reached, followed by a period of gentle softening. A comparison of ductility based on displacement and work done indicates that all the specimens had a good level of ductility, however, the ductility decreased with increasing moment redistribution.

Finally, the post-peak behaviour of R-SFRC flexural members was investigated using finite element (FE) models, with the models validated using the test data collected in this study. Parametric studies were undertaken to investigate the influence of volume and degree of hardening of tensile reinforcement, and dosage and softening slope of SFRC on the post-peak behaviour of R-SFRC flexural members. From this study, a model was proposed for defining the conditions needed to achieve a defined level of ductility for R-SFRC flexural members and based on the model the relationships for minimum tensile reinforcement for which R-SFRC flexural members show sufficient ductility were developed and verified against the tests undertaken in this study.

ORIGINALITY STATEMENT

‘I hereby declare that this submission is my own work and to the best of my knowledge it contains no materials previously published or written by another person, or substantial proportions of material which have been accepted for the award of any other degree or diploma at UNSW or any other educational institution, except where due acknowledgement is made in the thesis. Any contribution made to the research by others, with whom I have worked at UNSW or elsewhere, is explicitly acknowledged in the thesis. I also declare that the intellectual content of this thesis is the product of my own work, except to the extent that assistance from others in the project's design and conception or in style, presentation and linguistic expression is acknowledged.’

Signed ……………………………………………..............

Date ……………………………………………..............

COPYRIGHT STATEMENT

'I hereby grant the University of New South Wales or its agents a non-exclusive licence to archive and to make available (including to members of the public) my thesis or dissertation in whole or part in the University libraries in all forms of media, now or here after known. I acknowledge that I retain all intellectual property rights which subsist in my thesis or dissertation, such as copyright and patent rights, subject to applicable law. I also retain the right to use all or part of my thesis or dissertation in future works (such as articles or books).'

'For any substantial portions of copyright material used in this thesis, written permission for use has been obtained, or the copyright material is removed from the final public version of the thesis.'

Signed ……………………………………………...........................

Date ……………………………………………...........................

AUTHENTICITY STATEMENT

'I certify that the Library deposit digital copy is a direct equivalent of the final officially approved version of my thesis.'

Signed ……………………………………………...........................

Date ……………………………………………...........................

INCLUSION OF PUBLICATIONS STATEMENT

UNSW is supportive of candidates publishing their research results during their candidature as detailed in the UNSW Thesis Examination Procedure.

Publications can be used in their thesis in lieu of a Chapter if:

- The candidate contributed greater than 50% of the content in the publication and is the "primary author", ie. the candidate was responsible primarily for the planning, execution and preparation of the work for publication
- The candidate has approval to include the publication in their thesis in lieu of a Chapter from their supervisor and Postgraduate Coordinator.
- The publication is not subject to any obligations or contractual agreements with a third party that would constrain its inclusion in the thesis

Please indicate whether this thesis contains published material or not:

☐ This thesis contains no publications, either published or submitted for publication

☒ Some of the work described in this thesis has been published and it has been documented in the relevant Chapters with acknowledgement

☐ This thesis has publications (either published or submitted for publication) incorporated into it in lieu of a chapter and the details are presented below

CANDIDATE'S DECLARATION

I declare that:

- I have complied with the UNSW Thesis Examination Procedure
- where I have used a publication in lieu of a Chapter, the listed publication(s) below meet(s) the requirements to be included in the thesis.

Candidate's Name	**Signature**	**Date (dd/mm/yy)**
S M Faisal Mahmood		

This thesis is dedicated to

Sumaiya and Shodyo

ACKNOWLEDGEMENTS

My most sincere gratitude is to my supervisor Prof. Stephen Foster whose continuous support, supervision, guidance and counsel made the work of this thesis possible. It is an honour to work under his supervision. I would like to express gratitude to my co-supervisor Assoc. Prof. Hamid Valipour who always greeted me with a smile and helped me when requested.

I would like to thank post-doctoral fellow Dr. Ahsan Parvez and Dr. Ankit Agarwal for their advice and guidance. I would also like to thank my research group mates Iman Al-Damad, Aziz Hasan Mahmood, Firas Matar, Mohsen Khalaj and Lakshminarayanan Mohana for helping me out during the casting and testing of the specimens.

The experimental works presented in this thesis were performed at the Randwick Heavy Structures Laboratory. The author would like to thank and acknowledge the support of the laboratory staffs - Dr. Zhen-Tian Chang, Ron Moncay, John Gilbert, Greg Worthing, Sanjeewa Herath and Ben Pauley.

The research in this thesis was funded by Australian Research Council Discovery Project DP150104107 and the steel fibres were provided by BOSFA Australia. The support of the ARC, Australia and BOSFA is acknowledged with thanks.

I cannot thank enough my lovely wife Sumaiya who accepted my non-existence at home and waited patiently for the last four years for the completion of my PhD, and my son Shodyo who could not get much of company. Finally, I am grateful to my parents for keeping me in their prayers.

ABSTRACT

This thesis presents a study of the moment redistribution capability and post-peak behaviour of conventionally reinforced steel fibre reinforced concrete (R-SFRC) continuous members designed for moment redistribution. Because of the lack of research in this area, limitations are placed in design standards on the application of steel fibres in RC continuous members designed for moment redistribution and no guidelines are available in the standards on the requirement for minimum reinforcement for which R-SFRC flexural members will show sufficient level of ductility. Consequently, two sets of experiments were designed to investigate the moment redistribution capability and post-peak behaviour of R-SFRC continuous members.

In the first set of experiments, six full-scale two-span continuous RC beams with and without fibres were designed for ±30% of moment redistribution with respect to the linear-elastic condition. Dramix 5D steel fibres with nominal dosages of 30 and 60 kg/m^3 were used and the tensile reinforcement ratios varied between 0.69% and 1.38%. The second set of experiments comprised of six full-scale two-span continuous one-way RC slabs with and without fibres, which were designed for 0 to 30% of positive moment redistribution with respect to the linear-elastic condition by varying the tensile reinforcement ratios between 0.21% and 0.42%. Dramix 3D steel fibres with a nominal dosage of 60 kg/m^3 were used.

The test results showed that in all R-SFRC beam and slab tests, two plastic hinges fully formed to develop the failure mechanism indicating the ability of R-SFRC continuous members to achieve the theoretical (elastic) design moment redistribution. The R-SFRC beams having tensile reinforcement ratios more than 0.5% maintained their capacity up

to a displacement of 50 mm whereas the R-SFRC slabs having tensile reinforcement ratios less than 0.5% showed a shorter displacement length over which hardening occurred before the peak load was reached, followed by a period of gentle softening. A comparison of ductility based on displacement and work done indicates that all the specimens had a good level of ductility, however, the ductility decreased with increasing moment redistribution.

Finally, the post-peak behaviour of R-SFRC flexural members was investigated using finite element (FE) models, with the models validated using the test data collected in this study. Parametric studies were undertaken to investigate the influence of volume and degree of hardening of tensile reinforcement, and dosage and softening slope of SFRC on the post-peak behaviour of R-SFRC flexural members. From this study, a model was proposed for defining the conditions needed to achieve a defined level of ductility for R-SFRC flexural members and based on the model the relationships for minimum tensile reinforcement for which R-SFRC flexural members show sufficient ductility were developed and verified against the tests undertaken in this study.

LIST OF PUBLICATIONS

Following publications have been written as a part of this thesis:

Mahmood, S. M. F., Agarwal, A., Foster, S. J., and Valipour, H., *Flexural performance of steel fibre reinforced concrete beams designed for moment redistribution*. Engineering Structures, 2018. 177: 695-706.

Mahmood, S. M. F., Foster, S. J., and Valipour, H., *Nonlinear FE analysis of steel fibre reinforced concrete continuous beams*, The International Federation for Structural Concrete 5th International fib Congress, 7 – 11 October 2018, Melbourne, Australia.

TABLE OF CONTENTS

NOMENCLATURE

A_{sc}	cross-sectional area of compressive reinforcement
A_{st}	cross-sectional area of tensile reinforcement
a	shear span
b	width of a rectangular cross-section or member
C_c	compressive force of concrete
C_s	compressive force of steel reinforcement
D	overall depth of a cross-section in the plane of bending
d	effective depth of a cross-section in the plane of bending
d_c	distance from the extreme compression fibre of a cross-section to the centroid of compressive reinforcement
d_f	diameter of fibre
d_n	distance from the extreme compression fibre to the neutral axis of a cross-section
d_t	distance from the extreme compression fibre of a cross-section to the centroid of tensile reinforcement
E_0	initial modulus of elasticity of concrete
E_c	modulus of elasticity of concrete at 28 days
E_{cp}	secant modulus of elasticity of concrete
E_s	modulus of elasticity of steel reinforcement
f_c	compressive stress of concrete
f_{ct}	tensile strength of concrete
f_{cp}	peak in-situ compressive stress of concrete
f_{su}	ultimate tensile strength of steel reinforcement
f_{sw}	tensile stress of steel reinforcement corresponding to a strain of ε_{sw}
f_{sy}	yield strength of steel reinforcement

f_{tf}	tensile strength provided by fibres
$f'_{0.5}$	characteristic residual tensile strength of concrete at a Crack Opening Depth (COD) of 0.5 mm
$f'_{1.0}$	characteristic residual tensile strength of concrete at a Crack Opening Depth (COD) of 1.0 mm
$f'_{1.5}$	characteristic residual tensile strength of concrete at a Crack Opening Depth (COD) of 1.5 mm
$f'_{3.0}$	characteristic residual tensile strength of concrete at a Crack Opening Depth (COD) of 3.0 mm
f'_c	characteristic compressive (cylinder) strength of concrete at 28 days
$f'_{R,1}$	characteristic residual flexural strength of concrete at a Crack Mouth Opening Depth (CMOD) of 0.5 mm
$f'_{R,2}$	characteristic residual flexural strength of concrete at a Crack Mouth Opening Depth (CMOD) of 1.5 mm
$f'_{R,3}$	characteristic residual flexural strength of concrete at a Crack Mouth Opening Depth (CMOD) of 2.5 mm
$f'_{R,4}$	characteristic residual flexural strength of concrete at a Crack Mouth Opening Depth (CMOD) of 3.5 mm
f'_w	fibre stress corresponding to a crack width of w
$f'_{w_{ext}}$	fibre stress corresponding to a crack width of w_{ext}
G_{FM}	fracture energy of concrete
K_f	global orientation factor of fibres
k	a decay factor for the pre- and post-peak stress-strain relationship of concrete
k_g	a factor to take into account for the area of the fracture surface on fibre materials variability (relative to that of the prism bending test)
L	centre-to-centre distance between the supports of a flexural members
l_{ch}	characteristic length of finite element modelling
l_f	length of fibre
M	a moment
M_{el}	linear-elastic bending moment

M_{exp}	experimental bending moment
n	a curve fitting factor for the stress-strain relationship of concrete
P	load on each span
P_{cr}	load on each span at cracking of concrete
P_f	load on each span at fracture of reinforcing bar
P_{y1}	load on each span at first yielding of reinforcement
P_{y2}	load on each span at second yielding of reinforcement
P_p	peak load on each span
$P_{u,bi-linear}$	ultimate load predicted by the bi-linear model
$P_{u,exp}$	ultimate (peak) load from experiments
$P_{u,FEM}$	ultimate (peak) load from finite element modelling
$P_{u,RSB}$	ultimate load predicted by the rectangular stress block model
T_s	tensile force of steel reinforcement
T_f	tensile force of fibres
W_u	total work done up to the ultimate load
W_{y2}	work done up to the second yielding of reinforcement
w	crack width
w_{ext}	crack width at the extreme tension fibre of a cross-section
w_u	ultimate crack width
z_f	lever arm from the compressive force to the tensile force of fibres
z_s	lever arm from the compressive force to the tensile force of reinforcing bars
α_1, α_2, α_3	tension softening parameters of concrete
α_f	aspect ratio of fibre
α_I	fibre engagement parameter
γ	the ratio of the depth of the assumed rectangular compressive stress block to the depth of neutral axis

Δ	a deflection
Δ_{cr}	deflection at cracking of concrete
Δ_f	deflection at fracture of reinforcing bar
Δ_u	deflection at ultimate load
$\Delta_{u,exp}$	defection at ultimate load from experiments
$\Delta_{u,FEM}$	defection at ultimate load from finite element modelling
Δ_{y1}	deflection at first yielding of reinforcement
Δ_{y2}	deflection at second yielding of reinforcement
Δ_p	deflection at peak load
ε	a strain
ε_c	strain of concrete
ε_{cp}	strain corresponding to peak in-situ compressive stress of concrete
ε_{bot}	strain value at extreme bottom (tension) fibre of concrete
ε_{top}	strain value at extreme top (compression) fibre of concrete
ε_{st}	strain of tensile steel reinforcement
ε_{sc}	strain of compressive steel reinforcement
ε_{su}	ultimate strain of steel reinforcement
ε_{sy}	yield strain of steel reinforcement
η_{actual}	actual value of moment redistribution
η_{theo}	theoretical value of moment redistribution
μ_w	ductility factor based on work done
μ_Δ	ductility factor based on displacement
ν	Poisson's ratio
κ	curvature
ρ	reinforcement ratio
ρ_{min}	minimum reinforcement ratio

ρ_f	volumetric ratio of fibres
σ	a stress
τ_b	average bond shear strength at the fibre and concrete matrix interface
$\overline{\phi}$	a safety parameter to take account of the differences in model error and variation between the bar reinforcement and fibres contributions to the flexural strength

Chapter 1

INTRODUCTION

1.1 Background

The fastest and most widely adopted approach for analysis and, accordingly, design of reinforced concrete (RC) members is based on the linear-elastic assumption for materials. In the linear-elastic analysis, it is assumed that both the concrete and the reinforcement behave elastically until the reinforcement yields, and the bending moment and shear force are calculated by assuming a constant flexural stiffness for the member. However, the flexural stiffness of an RC member varies with respect to the level of cracking and thus, in reality, the member behaves non-linearly after the formation of cracks. Moreover, all the sections of a continuous member do not crack and yield at the same time, and the member does not fail as soon as the moment of a particular section exceeds its design moment capacity. If the section has sufficient rotation capacity, a plastic hinge is formed, and the hinge region starts rotating at almost a constant moment. Further application of load will increase the increment of moments at other sections which are not critically loaded; this process is called moment redistribution. The load can be increased until multiple plastic hinges form to develop a failure mechanism.

The incorporation of moment redistribution into linear-elastic analysis has some benefits. The amount of longitudinal reinforcement in congested areas, such as beam-column joint regions, can be reduced by shifting bending moments away from beam-column connection zone toward mid-span that, in turn, can lead to improved concrete compaction and better bonding in those congested areas. The incorporation of moment redistribution into the design also contributes to cost-saving by utilising the full capacity of the member, redistributing moments at different load combinations and resulting in a narrower bending moment envelope [1]. Moreover, the use of linear-elastic analysis in conjunction with moment redistribution is simple and reasonably accurate for practical applications, compared to plastic and nonlinear analyses that require complex calculations.

The capacity of a section to redistribute moment depends mainly on the ductility of the critical sections. Ductility is defined as the capacity of a member to undergo considerable plastic deformation while maintaining its load capacity [2]. Assessing the ductility of RC members is important as it allows adequate deformation at the ultimate limit state to avoid sudden failure of the structure and to resist dynamic loads such as blast and earthquake.

The ductility of concrete can be improved by the inclusion of steel fibres. The inclusion of steel fibres into concrete mix started over half a century ago with the concept of bridging micro and macro cracks that occur in the concrete matrix due to various states of stress [3]. It is now well established that steel fibre reinforced concrete (SFRC) has superior post cracking tensile strength and superior resistance to crack propagation than that of plain concrete [4]. The crack bridging property of SFRC can transform the behaviour from one of quasi-brittle to ductile [5]. Many studies have been conducted to investigate the flexural performance of conventionally reinforced SFRC (R-SFRC) flexural members. The incorporation of steel fibres has been found to improve the deformational and cracking behaviour of RC beams. The inclusion of steel fibres increases both the service and post-peak stiffness of the beams resulting in a substantial reduction of deflection, strain in reinforcing steel, rotation and curvature at all stages of loading [4, 6-15]. The addition of steel fibres inhibits the free propagation of cracks and decreases the width, length and spacing of the cracks at service loading condition; the number of cracks also increases [6-8, 11, 13, 15-20]. Apart from improvements at the service loading condition, the inclusion of steel fibres can improve the yield and ultimate bending moment capacity of the RC beams [5, 6, 8, 10, 11, 14-17, 19, 21-24].

The ductility of R-SFRC flexural members depends on the amount of tensile reinforcement and the dosage of steel fibres. The inclusion of steel fibres has been found to increase the ductility of RC beams when the tensile reinforcement ratios are more than 0.4% [4, 5, 7, 9, 11-14, 19, 20]. However, when the tensile reinforcement ratio is less than 0.4%, the addition of steel fibres may lead to a distinct widening of one or two cracks (crack localisation) leading to a post-peak softening behaviour and fracture of tensile reinforcing bars at relatively low displacements [14, 15, 22-25]. Crack localisation in R-SFRC flexural members is caused by the improved bond between the reinforcing bars and the surrounding concrete due to the influence of fibres and enhanced control of microcracking [23]. Low ductility can also result from using steel fibres with high flexural toughness, or using reinforcement with a low hardening ratio [12].

Few studies are found in the literature on the flexural performance of R-SFRC continuous members that allow for moment redistribution. Hassoun and Sahebjam [26] studied the cracking behaviour of R-SFRC continuous beams. Pfyl and Marti [25] investigated the flexural behaviour of lightly reinforced SFRC one-way slabs that were designed for 0% of moment redistribution. Iskhakov et al. [27] studied the moment redistribution of two-layer R-SFRC beams placing steel fibres in the compression zone which is not a common sort of practice. Küsel and Kearsley [28] investigated the moment redistribution of R-SFRC continuous beams with high fibre dosages (1-2%).

Although SFRC has been researched for over 50 years, guidelines available for the design of SFRC remain limited. The first international standard to introduce fibres in a comprehensive way was the New Zealand standard NZS 3101: Part 1-2006 [29]. Since this time, a number of other international standards have evolved that deal with fibre reinforced concrete in some way, including *fib* Model Code 2010 [30], ACI 318-14 [31], DAfStb Guideline [32], AS 5100.5:2017 [33] and AS 3600-2018 [34].

AS 5100.5:2017 [33] and AS 3600:2018 [34] are the two standards in Australia to include design procedures for SFRC. While rules have been introduced for flexure and shear design of SFRC, limitations are placed on the application of steel fibres where large plastic rotations are expected because of lack of testing undertaken on R-SFRC continuous members to clearly show that SFRC moment hinges can maintain their capacity during large rotations and moment redistributions. The limitations placed in AS 3600:2018 [34] are:

(a) For SFRC members designed for moment redistribution, the tensile reinforcement ratio for steel reinforcement and tendons is not less than 0.004.

(b) For SFRC ordinary moment-resisting frames forming part of the seismic-force-resisting system, the tensile reinforcement ratio for steel reinforcement and tendons is not less than 0.004.

(c) For SFRC intermediate moment-resisting frames, the tensile reinforcement ratio for steel reinforcement and tendons is not less than 0.006.

1.2 Motivation

Research on the flexural performance of R-SFRC continuous members that allow for moment redistribution is limited. No study has investigated the ability of R-SFRC continuous members to achieve the maximum amount of moment redistribution (generally ±30%) allowed by current design standards [30, 33-35] and the ability of R-SFRC continuous members with tensile reinforcement ratios less than 0.004 to redistribute moment. Moreover, the effect of tensile reinforcement volume and fibre dosage on the post-peak behaviour and ductility of R-SFRC flexural members needs to be investigated to understand the relevant mechanism. Furthermore, no guidelines are available in the standards on the requirements for minimum tensile reinforcement for which R-SFRC flexural members will show a sufficient level of ductility.

1.3 Objectives and scope of the thesis

The objectives of this study are to:

- investigate the effect of the inclusion of steel fibres on the cracking behaviour, load-carrying capacity and ductility of RC continuous members.
- investigate the ability of R-SFRC continuous members to achieve the maximum amount of moment redistribution (both positive and negative) allowed by current design standards.
- investigate the ability of R-SFRC continuous members with tensile reinforcement ratios less than 0.004 to redistribute moment.
- investigate the effect of moment redistribution on the ductility of R-SFRC continuous members.

- investigate the effect of tensile reinforcement volume and fibre dosage on the post-peak behaviour and ductility of R-SFRC flexural members.
- formulate the post-peak behaviour of R-SFRC flexural members.
- develop relationships for minimum reinforcement for which R-SFRC flexural members will show a sufficient level of ductility.

To achieve the above-mentioned objectives, two sets of experiments are designed. The first set of experiments includes six full-scale (8.2 m long, 250 mm wide and 400 mm deep) two-span continuous RC beams with and without steel fibres. The beam specimens are reinforced with conventional steel reinforcing bars with tensile reinforcement ratios of between 0.0069 and 0.0138; four of the six beams also contain either 30 or 60 kg/m^3 of steel fibres. The beams are designed for 30% of positive and negative moment redistribution with respect to the linear-elastic condition, the maximum allowed by different codes and standards.

The second set of experiments comprises of six full-scale (8.2 m long, 800 mm wide and 220 mm deep) two-span continuous one-way RC slabs with low reinforcement ratios. Four of the six slabs contain 60 kg/m^3 of steel fibres. The tensile steel reinforcement ratios are between 0.0021 and 0.0042 to provide 0 to 30% of positive moment redistribution with respect to the linear-elastic condition.

Finally, finite element (FE) models will be developed and validated using the test data in this study. The validated FE models will be used to undertake parametric studies for the formulation of post-peak behaviour and the development of comprehensive design rules for R-SFRC flexural members.

1.4 Organization of the thesis

The rest of the thesis is organized as follows:

Chapter 2 provides an extensive literature review on the flexural performance of R-SFRC flexural members, especially the effect of the inclusion of steel fibres on the cracking and deformation behaviour, load-carrying capacity and ductility of RC flexural members. The effect of tensile reinforcement volume and fibre dosage on the ductility and mechanism of crack localisation are discussed. The available literature on the moment redistribution of R-SFRC continuous members is also reviewed. Finally, the gaps in the current research are identified to be fulfilled by this study.

Chapter 3 describes the experimental program of six full-scale two-span continuous RC beams with and without steel fibres. The effect of the inclusion of steel fibres on the cracking behaviour, load-carrying capacity and ductility of RC continuous members are studied. The ability of R-SFRC continuous members to achieve the maximum amount of moment redistribution allowed by current design standards is also investigated.

Chapter 4 details the experimental program of six full-scale two-span continuous one-way RC and R–SFRC slabs with low reinforcement ratios. The effect of low reinforcement ratios and moment redistribution on the post-peak behaviour and ductility of R-SFRC continuous slabs are studied. The ability of R-SFRC continuous members with tensile reinforcement ratios less than 0.004 to redistribute moment is also investigated.

Chapter 5 presents the FE modelling of R-SFRC continuous members. The FE models are validated using the test data from this study, and the validated FE models are then used to undertake parametric studies to determine the effect of the dosage of fibres, the degree of hardening of reinforcement and the type of loading on the post-peak behaviour of R-SFRC flexural members.

Chapter 6 presents the design of R-SFRC flexural members. The ultimate strength results of the tests are compared with predictions using (1) the rectangular stress block design model of AS 3600:2018 [34] and (2) a bi-linear model to describe the SFRC stress-COD relationship. The effect of tensile reinforcement volume and fibre dosage on the ductility of R-SFRC flexural members is studied using the test data available in the literature. The parametric studies in Chapters 5 and 6 are used to formulate the post-peak behaviour of R-SFRC flexural members and develop relationships for minimum tensile reinforcement ratio for which R-SFRC flexural members will show a sufficient level of ductility.

Chapter 7 summarizes the results of the study. Some conclusions are drawn based on the results. The limitations of the study and the recommendations for future investigations are also discussed.

Chapter 2

LITERATURE REVIEW

2.1 Introduction

The history of the use of fibres to reinforce weak brittle materials is quite ancient, dating back to the 8th and 7th millennia BCE with the reinforcement of mud using straws [36, 37]. The incorporation of randomly distributed short, discontinuous steel fibres in concrete started in the 1970s to compensate for the low tensile strength of concrete [38]. One of the early studies to characterise the material properties of SFRC was by Shah and Rangan [39]. It was found that fibres have negligible effect on the load at which cracks initiate in the matrix. However, the resistance of concrete to crack propagation and flexural strength and toughness of concrete are considerably increased by the inclusion of steel fibres. The post-cracking resistance provided by fibres were considerably influenced by their aspect ratio, orientation with respect to the cracking direction and their stress-strain curves. Later a lot of research [40-67] confirmed the improvement of mechanical performance of concrete with regard to its crack resistance, tensile and flexural strengths, toughness, ductility, energy absorption and resistance to fatigue, impact and cyclic loading by the addition of steel fibres. Although the inclusion of steel fibres has marginal effect on compressive strength of concrete, high post-peak strain and a gradual slope in the descending part of the stress-strain curve of SFRC indicates improved spalling resistance, ductility, energy absorption capacity and fracture toughness in compression [68-73]. Swamy [74] predicted that SFRC would find extensive and advantageous applications through its unusual properties such as impact resistance, thermal shock resistance, wear and spall resistance and energy absorption.

In the beginning, steel fibres were mainly used in large concrete pavements [75-80], precast concrete decking panels [81, 82], unreinforced tunnel linings [83-85], mines [86, 87] and bridge decks [88, 89] to prevent the propagation of micro-cracks that eventually lead to failure. Slowly SFRC finds its way to RC structural elements like beam [4, 90-98], column [99-103], beam-column joint [104-112] and slab [113-118] not only to reduce shrinkage and microcracking but also to improve overall cracking and deformational behaviour, to enhance the flexural, shear, fatigue and impact performances, and also as a replacement of tensile and shear reinforcement.

As the research and use of steel fibres in RC structural members have flourished over the last two decades, some of the researchers [14, 15, 22-25] noticed the negative effect of steel fibres on the ductility on RC flexural members. The inclusion of steel fibres has been found to reduce the ductility of lightly RC flexural members. The following section reviews the flexural performance of SFRC beams and slabs, especially the effect of tensile reinforcement ratio on the ductility of SFRC flexural members. Since different studies used different criteria to quantify ductility, a line corresponding to a displacement of span/100 is plotted on the load-deflection curves (where available) of the studies reviewed. This point (displacement of span/100) is considered as corresponding to sufficient ductility for observation of serious distress in the member [119].

2.2 Flexural performance of R-SFRC beams and slabs

2.2.1 Effect of the depth of fibre placement

Swamy et al. [4] studied the cracking and deformational behaviour of R-SFRC beams and also investigated the possibility of using higher strength steel reinforcement in SFRC than that of allowed in RC during that time. The authors tested two series of ten specimens. In one series, reinforcing bars with 460 MPa of yield stress were used whereas reinforcing bars with 605 MPa of yield stress were used in another series. The beam specimens were 2.5 m long (effective span = 2.25 m), 130 mm wide and 200 mm deep. The tensile reinforcement ratio was 1%. Crimpled steel fibres with a length of 50 mm and an aspect ratio of 100 were used either throughout the whole depth of the beam or only in the effective tension zone surrounding the reinforcing bars. The dosages of steel fibres were 0.5 and 1.0% by volume, the average compressive strength (cubes) of plain and steel fibre reinforced concrete varied from 37 to 41 MPa and the load was applied at the mid-span of the beams.

Swamy et al. found that the inclusion of steel fibres in RC increased the service stiffness by 50 to 70% resulting in substantial reductions of deflection, steel strain, rotation and curvature. The presence of fibres also increased the stiffness of the beams considerably at ultimate state. Steel reinforcement with 605 MPa of yield stress could control cracking and deformation at service loads to within acceptable limits and developed adequate plastic deformation at failure. Beams with fibres throughout their whole depth performed slightly better in the ultimate limit state than beams with fibres in the effective tension zone only.

From the load versus deflection curves of Swamy et al. for the beam specimens that had fibres throughout the whole depth of the beam (Figure 2.1), it is evident that the inclusion of steel fibres in RC beams with 460 MPa steel improved the ductility. At the ultimate load, the deflection of the R-SFRC beams was more than the span/100 value demonstrating a high level of ductility for the reinforcement ratio tested. Although there was also a modest increase in ultimate flexural strength with the inclusion of steel fibres, the authors commented that from a design point of view the influence of steel fibres on cracking and deflection is more significant than that on strength.

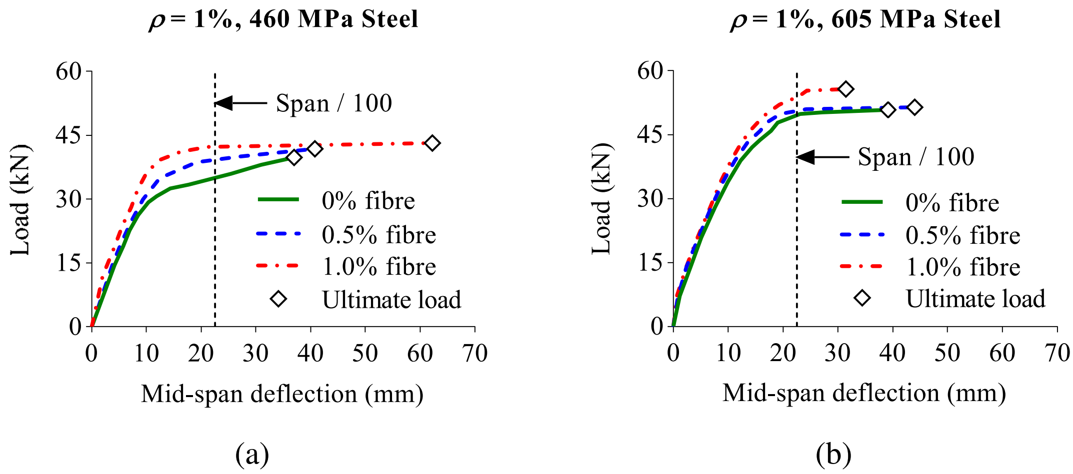

Figure 2.1: Load versus deflection curves in tests by Swamy et al. [4] for (a) 460 MPa steel and (b) 605 MPa steel.

Bentur and Mindess [8] investigated the flexural performance of R-SFRC beams with low yield strength conventional steel. The beam specimens were 1.0 m long with a cross-section of 100 mm × 100 mm and reinforced with 220 MPa steel bars at a ratio of 0.5%. Deformed steel fibres with a length of 50 mm and an aspect ratio of 100 mm were used at a volume fraction of 1.5% over the full depth of the beam in one specimen and at 1.0% and 1.5% by volume in the lower half (tension side) of the beam only in two specimens. The specimens were tested in third-point point loading with a span of 0.9 m.

The test results of Bentur and Mindess showed that R-SFRC beams had higher post-cracking rigidity than that of RC beams. The number of cracks was increased, and the width and length of the cracks were reduced by the inclusion of steel fibres. Beam with fibres throughout the full depth of the cross-section showed better performance in terms of load-carrying capacity and ductility than that of beams with fibres in the tension side of the cross-section only. The ultimate load increased by 55.4% for the beams with steel fibres over the full depth. For the beam with steel fibres in the tension side only, the increase in ultimate load was 32.5%. Beam with steel fibres over the full depth had almost the same ductility of the beam without steel fibres with respect to the span/100 value (see Figure 2.2). However, incorporating steel fibres in just the tension side of the beam decreased the ductility.

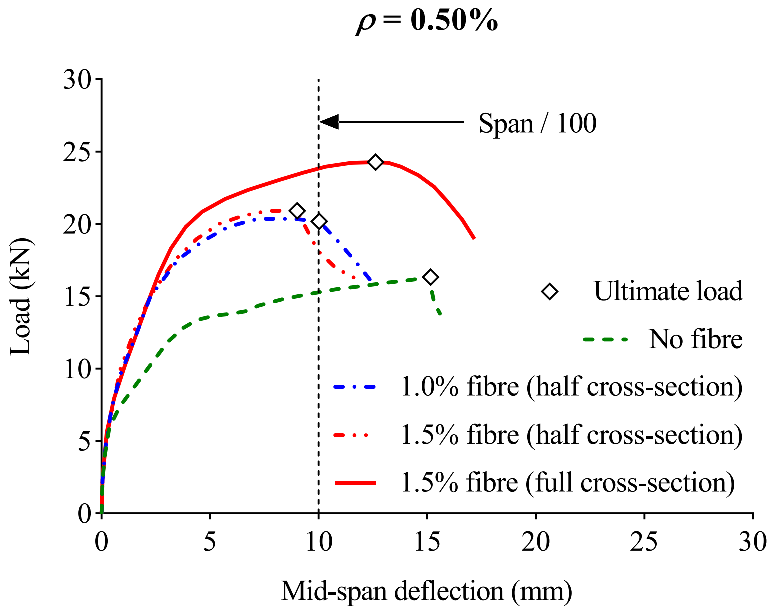

Figure 2.2: Load versus deflection curves in tests by Bentur and Mindess [8].

Swamy and Al-Ta'an [7] presented an extensive study on the performance of R-SFRC beams in flexure. The authors tested three series of 15 specimens. The specimens were 2.5 m long (effective span = 2.25 m), 130 mm wide and 203 mm deep. In series 1, steel reinforcement with 460 MPa of yield stress was used at a ratio of 0.99 %. Series 2 had 1.74% of 460 MPa reinforcing bars whereas 617 MPa reinforcing bars were used at a ratio of 0.94% in the last series. The average compressive strength (cubes) of plain and steel fibre reinforced concrete varied from 37 to 41 MPa. Crimped steel fibres with a length of 50 mm and aspect ratio of 100 were used at dosages 0.5 and 1.0% by volume either over the whole depth of the beam or over the effective tension zone (i.e., over an area with the steel bars as the centroid) of the beam only.

Swamy and Al-Ta'an found that steel fibres were effective on resisting deformation at all stages of loading, and steel fibre reinforced concrete beams showed significant inelastic deformations and ductility at failure. Beams with fibres throughout their depth were more effective in resisting deformation than beams with fibres in the effective tension zone only. The inclusion of steel fibres resulted in closely spaced narrower cracks. The maximum increase in ultimate flexural strength by the addition of steel fibres was just 10.5%.

Swamy and Al-Ta'an commented that the increase in ultimate flexural strength of a conventionally reinforced concrete beam with the inclusion of steel fibres is limited. However, fibres play an important role by improving cracking and deformational behaviour at all stages of loading, and by increasing the stiffness at service loads and ductility at failure. Moreover, steel reinforcement with higher yield stress than typically used for RC can be used with steel fibres without the fear of excessive cracking and deflection, and lack of ductility.

Dwarakanath and Nagaraj [10] studied the deformational behaviour of R-SFRC beams in pure bending. The authors tested two groups of beams. In one group, steel fibres were dispersed in the entire depth of the beams and in another group, steel fibres were dispersed over the half of the beam on the tension side. The beam specimens were 1.8 m long with a cross-section of 100 mm $\times$ 208 mm. The tensile reinforcement ratios varied from 0.77 and 1.28%. The average yield strength of tensile reinforcing steel was 500 MPa. The average compressive strength of concrete was 25.5 MPa. Hooked-end steel fibres a nominal length of 36 mm and an aspect ratio of 72 were used at dosages 0.75 and 1.5% by volume. The beam specimens were tested under four-point bending with a simply supported length of 1.5 m and a shear span-depth ratio of 3.3.

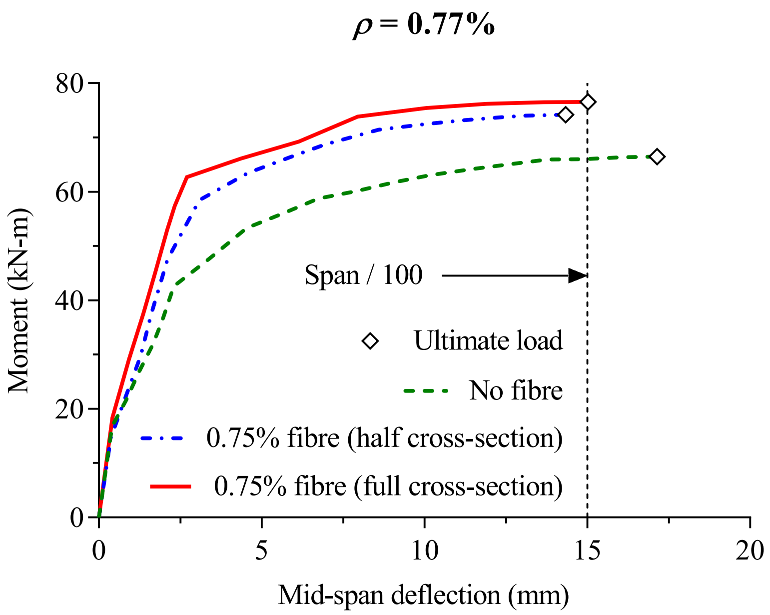

Figure 2.3: Moment versus deflection curves in tests by Dwarakanath and Nagaraj [10].

The test results of Dwarakanath and Nagaraj showed that the inclusion of steel fibres increased the load-carrying capacity and reduced the strains in reinforcing steel, curvatures and deflections of the RC beams at any given load level. The ultimate moment was increased by 15% by the addition of 0.75% of steel fibres over the full-depth of the cross-section. Half-depth fibre inclusion, requiring only half the quantity of fibres of full-depth inclusion, was practically as effective as full-depth fibre inclusion in improving the deformational behaviour of beams. Moreover, increasing fibre content from 0.75% to 1.5% did not improve the performance significantly.

Figure 2.3 shows the moment versus deflection curves of Dwarakanath and Nagaraj for the beam specimens with 0.77% reinforcement ratio. Although the inclusion of steel fibres decreased the ductility slightly, the deflection at the ultimate load of the R-SFRC beams was very close to the span/100 value indicating sufficient ductility for observation of serious distress in the member.

2.2.2 Effect of fibre dosage

Lim et al. [9] presented the test results of three full-scale beam specimens with varying fibre dosage. The beam specimens were 2.5 m long, 152 mm wide and 254 mm deep. The tensile reinforcement ratio was 1.2%. The average yield strength of tensile reinforcing steel was 450 MPa. The average compressive strength of concrete was 34.0 MPa. Hooked-end steel fibres with a nominal length of 30 mm and an aspect ratio of 60 were used at dosages 0.5 and 1% by volume. The beam specimens were tested under four-point bending with a simply supported length of 2.20 m and a shear span-depth ratio of 3.9.

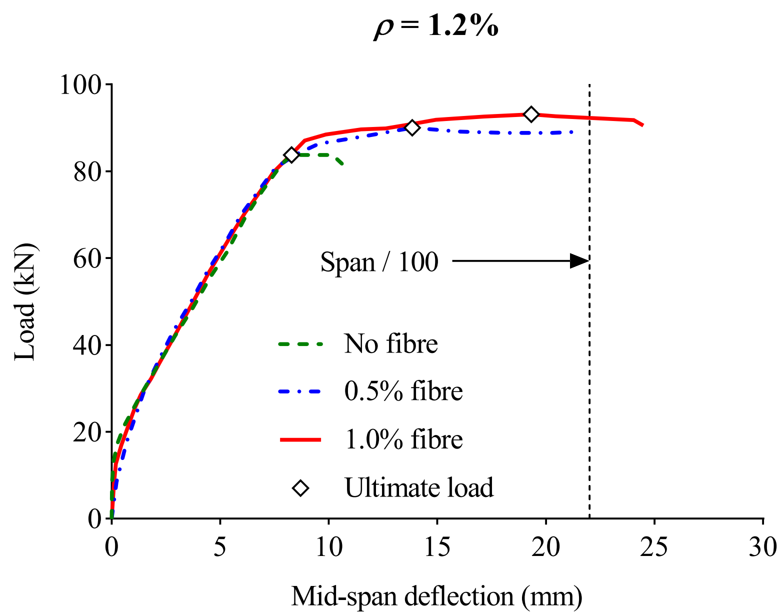

Figure 2.4: Load versus deflection curves in tests by Lim et al. [9]

Lim et al. found that the inclusion of steel fibres did not increase the load-carrying capacity significantly. From the load-displacement curves of the tested beam specimens (see Figure 2.4), it is evident that none of the RC or R-SFRC beams had sufficient ductility with respect to the span/100 value. However, the R-SFRC specimens had better ductility than that of the RC specimen for the reinforcement ratio tested.

Ashour and Wafa [11] investigated the effect of the inclusion of steel fibres on the flexural behaviour of high-strength concrete beams. The authors tested eight full-scale beam specimens with a cross-section of 170 mm × 300 mm. The span of the beams was varied as 2.62 and 3.68 m to have two different shear span-depth ratios (a/d) of 4 and 6. The amount of tensile reinforcement was 1.39%. The average yield strength of tensile reinforcing steel was 437 MPa. The average compressive strength of concrete was 88.0 MPa. Hooked-end steel fibres with a nominal length of 60 mm and an aspect ratio of 75 were used in the study. The dosage of steel fibres varied from 0.5 to 1.5% by volume.

The test results of Ashour and Wafa showed that the addition of steel fibres enhanced the post-cracking stiffness, flexural strength, ductility and energy absorption capacity of the tested beams. The presence of fibres also reduced the crack width and increased the number of cracks. The addition of 1.5% of steel fibres increased the flexural strength by 20.7 and 15.5% for the shear span-depth ratio of 4 and 6, respectively. The inclusion of 1.5% of steel fibres increased the displacement ductility, the rotational ductility and the energy absorbed by 120, 107 and 147%, respectively for the shear span-depth ratio of 4 and by 45, 39, 64%, respectively for the shear span-depth ratio of 6 (see Figure 2.5). The fibre enhancements of deflection, rotation and energy absorbed were greater at ultimate load than that of at yield load. It was found that increasing fibre dosage did not improve the performance significantly.

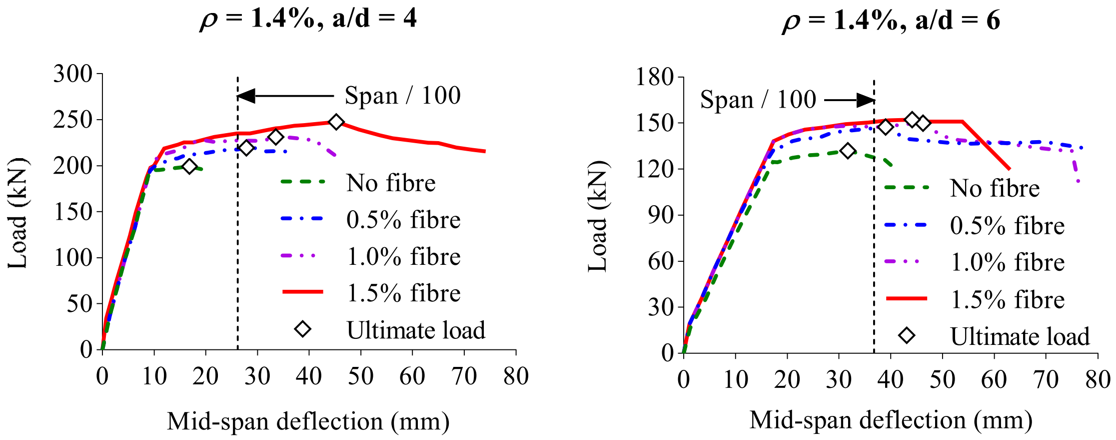

(a) (b)

Figure 2.5: Load versus deflection curves in tests by Ashour and Wafa [11] for (a) a/d = 4 and (b) a/d = 6.

Altun et al. [19] studied the effect of the inclusion of steel fibres in two different strength of concrete (C20 and C30). The authors tested eighteen full-scale beam specimens with a length of 2 m and a cross-section of 300 mm × 300 mm. The average measured compressive strength of C20 and C30 concrete were 24.4 and 34.8 MPa, respectively. The amount of tensile reinforcement was 0.5%. Hooked-end steel fibres with a nominal length of 60 mm and an aspect ratio of 80 were used at dosage 30 and 60 kg/m^3.

Altun et al. found that the inclusion of steel fibres increased the ultimate load, flexural toughness and ductility. The presence of steel fibres in C20 concrete did not increase the ultimate load significantly. However, the ultimate load increased by 30 and 41% by the addition of 30 and 60 kg/m^3 of steel fibres, respectively, in C30 concrete. The flexural toughness increased by 391 and 166% by the addition of 30 kg/m^3 of steel fibres in C20 and C30 concrete, respectively. The R-SFRC beams showed a good level of ductility for the reinforcement ratio tested (see Figure 2.6). It was found that increasing fibre dosage, did not improve the performance significantly.

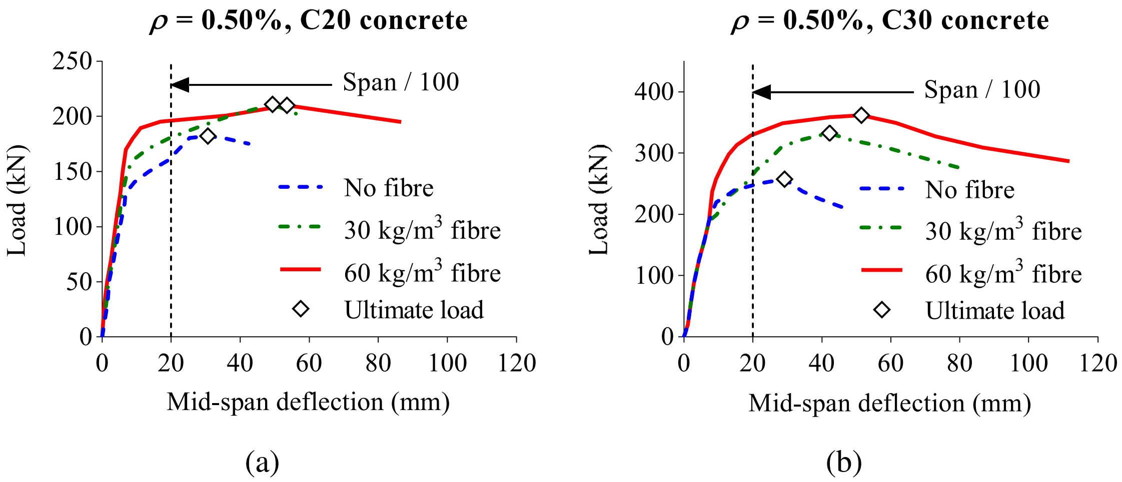

Figure 2.6: Load versus deflection curves in tests by Altun et al. [19] for (a) C20 concrete and (b) C30 concrete.

Aoude et al. [20] studied the cracking and deformational behaviour of R-SFRC beam specimens with varying fibre dosage. The authors tested three full-scale beam specimens with a length of 4.4 m and a cross-section of 300 mm × 500 mm. Hooked-end steel fibres with a nominal length of 30 mm and an aspect ratio of 55 were used at dosages 0.5 and 1.0% by volume. The amount of tensile reinforcement was 1.5%, the average yield strength of tensile reinforcing steel was 429 MPa and the average compressive strength of concrete was 23.3 MPa. The beam specimens were tested under four-point bending with a simply supported length of 3.7 m and a shear span-depth ratio of 3.1.

The test results of Aoude et al. showed that the inclusion of 0.5% and 0.1% by volume of steel fibres increased the ultimate displacement by 50% and 90%, respectively. R-SFRC specimens had better post-peak residual strength response than that of RC specimens (see Figure 2.7). The presence of fibres resulted in a reduction of crack widths and the crack patterns were diffused with many secondary cracks growing out of the primary cracks. The load-carrying capacity did not increase significantly by the addition of steel fibres.

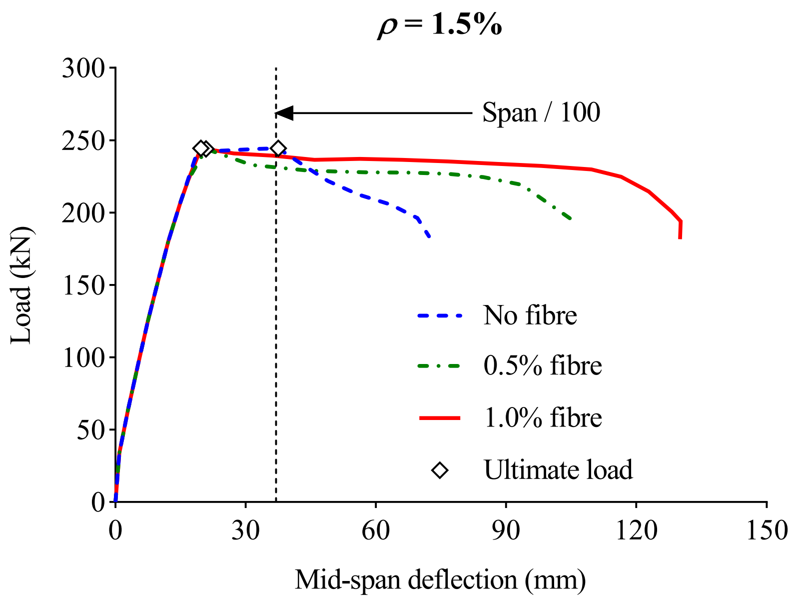

Figure 2.7: Load versus deflection curves in tests by Aoude et al. [20].

Sahoo et al. [120] tested three full-scale beam specimens with a length of 2.0 m and a cross-section of 150 mm × 200 mm. Hooked-end steel fibres with a nominal length of 60 mm and an aspect ratio of 80 were used at dosages 0.5 and 1% by volume. The amount of tensile reinforcement was 1.35%, the nominal yield strength of tensile reinforcing steel was 500 MPa and the average measured compressive strength of concrete was 35.5 MPa. The beams were tested under four-point bending with a simply supported length of 1.8 m with a shear span-depth ratio of 3.0. The authors found that the increase in ultimate strength by the addition of steel fibres was marginal (approximate 6%). However, the R-SFRC specimens had better post-peak residual strength and larger ultimate deflection than that of RC specimens (see Figure 2.8).

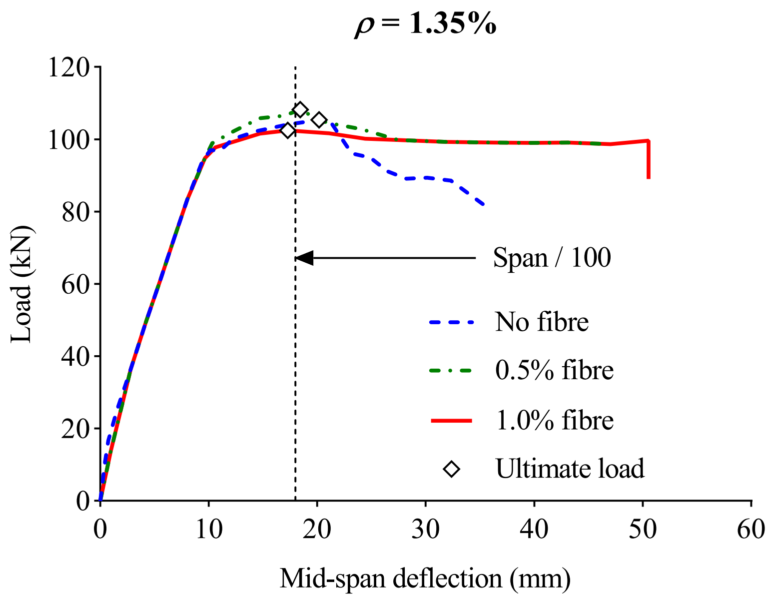

Figure 2.8: Load versus deflection curves in tests by Sahoo et al. [120]

2.2.3 Effect of fibre length and aspect ratio

Vandewalle [18] studied the effect of fibre aspect ratio on the cracking behaviour of R-SFRC beams. The authors tested five full-scale beam specimens with a length of 3.6 m and a cross-section of 200 mm × 350 mm. Hooked-end steel fibres with different lengths and aspect ratios were used at dosages of 30 and 45 kg/m^3. One type of fibres had a nominal length of 35 mm with an aspect ratio of 65; the other type of fibres had a nominal length of 50 mm with an aspect ratio of 80. The amount of tensile reinforcement was 1.03%, the nominal yield strength of tensile reinforcing steel was 500 MPa and the average compressive strength of concrete was 42.0 MPa. The beam specimens were tested under four-point bending with a simply supported length of 3.25 m. Test results showed that the inclusion of steel fibres decreased the crack spacing and crack width. At service load, the distinct influence of two different types of fibres was not clear. However, at larger bending moments, a greater reduction in crack width and crack spacing was evident when fibres with a higher aspect ratio were used.

Alsayed [21] investigated the effect of fibre dosage and aspect ratio on the flexural strength and ductility of R-SFRC beams. The authors tested ten full-scale beam specimens with a length of 2.5 m and a cross-section of 250 mm × 250 mm. Hooked-ends steel fibres with same length but different aspect ratios were used at dosages of 0.5, 1.0 and 1.5% by volume. The nominal length of the fibres was 60 mm and the aspect ratios were 60 and 75. The amount of tensile reinforcement was 0.75%, the average yield strength of tensile reinforcing steel was 470 MPa and the average compressive strength of concrete was 35.0 MPa. The beam specimens were tested under four-point bending with a simply supported length of 2.3 m. It was found that the beams containing steel fibres with higher aspect ratio exhibited higher flexural strength and ductility. Increasing fibre content did not improve the load-carrying capacity or ductility significantly (see Figure 2.9).

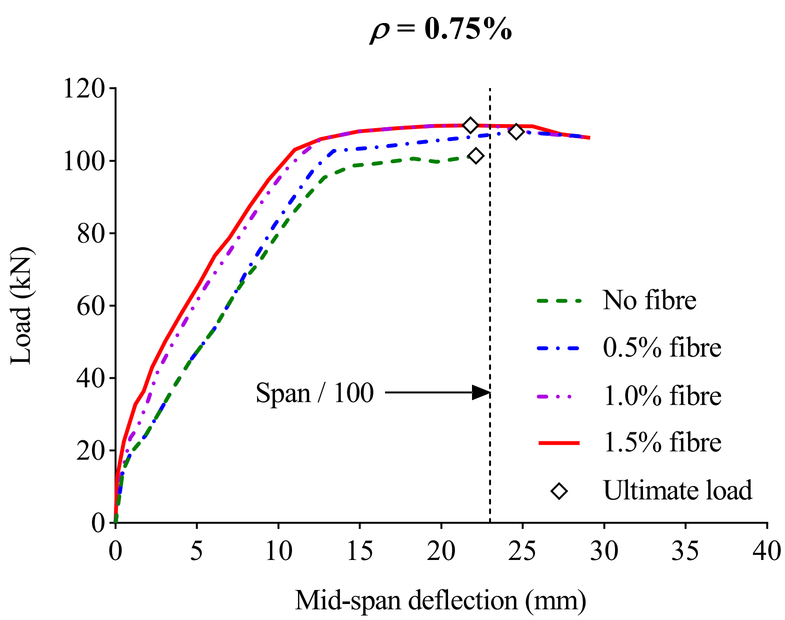

Figure 2.9: Load versus deflection curves in tests by Alsayed [21].

Pujadas et al. [13] studied the effect of fibre length and aspect ratio on the cracking and deformational behaviour of R-SFRC one-way slabs. The authors tested eighteen full-scale slab specimens with a length of 3 m and a cross-section of 1000 mm × 200 mm. Hooked-end steel fibres with different lengths and aspect ratios were used at volumetric ratios of 0.25 and 0.5%. One type of steel fibres (SF1) had a nominal length of 35 mm with an aspect ratio of 64; the second type of steel fibres (SF2) had a nominal length of 60 mm with an aspect ratio of 80. The amount of tensile reinforcement was 0.85%, the nominal yield strength of tensile reinforcing steel was 500 MPa and the strength class of the FRC was C25/30. The beams were tested under four-point bending with a simply supported length of 2.7 m and a shear span-depth ratio of 5.5.

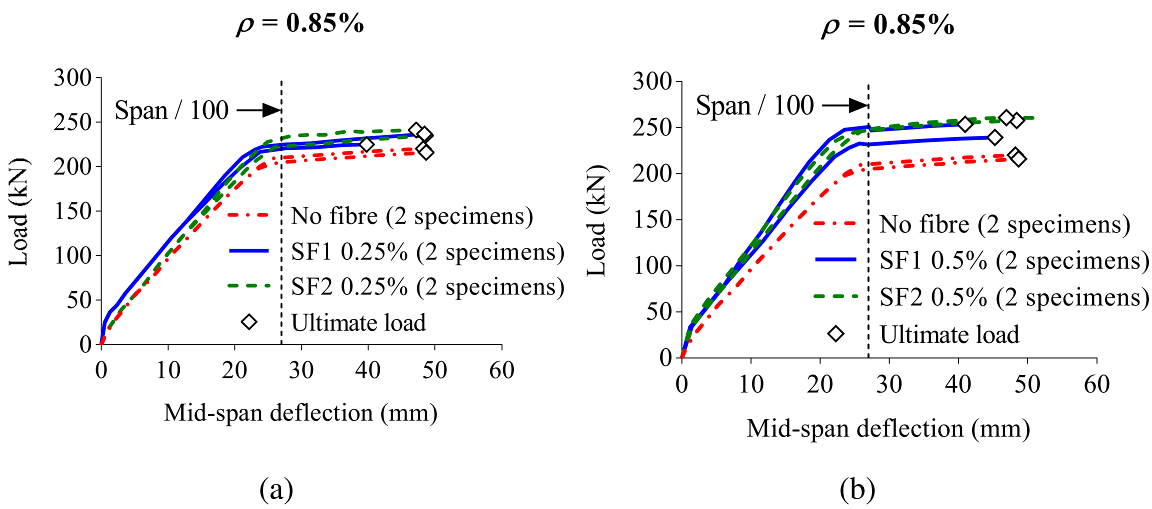

Figure 2.10: Load versus deflection curves in tests by Pujadas et al. [13] for (a) 0.25% fibre and (b) 0.50% fibre.

Pujadas et al. found that the inclusion of steel fibres increased the number of cracks and decreased the spacing of cracks. There was no crack localisation. However, for specimens with a higher dosage of fibres, ramification was observed in many of the cracks. The shorter fibres were found to be more effective in controlling cracks whereas the increase in ultimate strength was more with the longer ones. The R-SFRC slab specimens showed a good level of ductility with respect to the span/100 value. However, the ductility did not vary significantly with fibre dosage and aspect ratio (see Figure 2.10).

2.2.4 Effect of the amount of tensile reinforcement

Kormeling et al. [6] studied the effect of the amount of tensile reinforcement on the ultimate strength and cracking behaviour of R-SFRC beams. The beam specimens were 2.2 m long, 100 mm wide and 152 mm deep. The tensile reinforcement ratios varied from 0.17 to 2.09%. The highest reinforcement ratio corresponds to about the maximum amount and the lowest reinforcement ratio was substantially below the minimum amount used in that time's design practice. The yield strength of the tensile reinforcement varied from 460 to 716 MPa, and the average compressive strengths of plain and steel fibre reinforced concrete were 40.7 and 43.3 MPa, respectively. Three different types of steel fibres: straight, hooked-end and paddled-end were used at dosages of 1.27, 0.89 and 1.54% by volume, respectively. The length and aspect ratio of the fibres varied from 24 to 50 mm and 60 to 77.5, respectively. The beams were tested in four-point loading with a span of 2.0 mm and a shear span-depth ratio of 4.2.

The test results of Kormeling et al. showed that the addition of steel fibres increased the ultimate bending moment, and decreased the deflection, crack width, crack spacing and strain in reinforcement steel. However, the beneficial influences of the inclusion of steel fibres decreased with increased reinforcement ratio. The inclusion of steel fibres increased the ultimate load from 20 to 63% for the beams with 0.17% reinforcement ratio, whereas for the beams with 2.09% reinforcement ratio the increase was only from 2 to 9%. Also, the reduction in crack spacing was highest with the lowest amount of reinforcement.

Oh [16] investigated the flexural behaviour of singly and doubly reinforced concrete beams containing steel fibres. The authors tested two series of six singly reinforced concrete beams and one series of three doubly reinforced concrete beams with a length of 2.0 m and a cross-section of 120 mm $\times$ 180 mm. The main parameters of the study were the amount of tensile reinforcement and the dosage of steel fibres. The amount of tensile reinforcement varied from 1.5 to 3.4%, the nominal yield strength of the tensile reinforcing steel was 420 MPa and the average compressive strength of concrete was 40.3 MPa. Round and straight steel fibres with a length of 40 mm and an aspect ratio of 57 were used at volumetric ratios of 1 and 2%. The beams were tested under four-point bending with a simply supported length of 1.8 m and a shear span-depth ratio of 4.3.

Oh found that the inclusion of steel fibres decreased the crack width and crack spacing, and increased the load-carrying and energy absorption capacity. However, the increase in load-carrying capacity was more pronounced in beams with lower reinforcement ratio. The addition of 2% of steel fibres increased the ultimate load by 50% when the reinforcement ratio was 1.5%. However, the increases were 18.6% and 1.3% when the reinforcement ratios were 2.4% and 3.4%, respectively. From the load versus deflection curves of the tested beam specimens (see Figure 2.11), it is evident that the deflection at the ultimate load of all R-SFRC specimens was more than the span/100 value indicating a good level of ductility, and the ductility of the R-SFRC beams improved with the increase of reinforcement ratio. However, increasing fibre dosage did not improve the performance significantly.

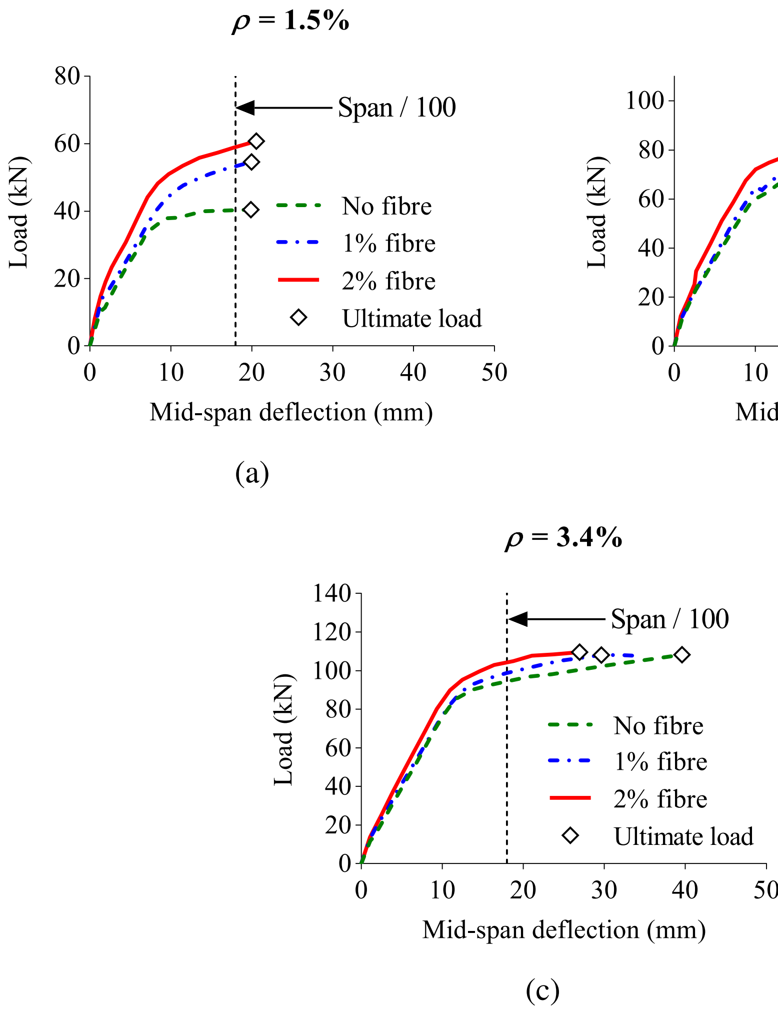

Figure 2.11: Load versus deflection curves in tests by Oh [16] for (a) ρ = 1.5%, (b) ρ = 2.4% and (c) ρ = 3.4%.

Espion et al. [22] studied the effect of the inclusion of steel fibres on the ductility and cracking behaviour of RC beams with low reinforcement ratios. The beam specimens were 1.4 m long, 250 mm wide and 150 mm deep. The amount of tensile reinforcement varied from 0.33 to 0.75%, the average yield strength of tensile reinforcing steel was 577 MPa and the average compressive strength of concrete was 32.0 MPa. The steel fibres used were conical ends at 0.4% by volume. These fibres had a nominal length of 60 mm with an aspect ratio of 60. The beam specimens were tested under four-point bending with a shear span-depth ratio of 3.8.

Figure 2.12 shows the moment versus deflection curves of Espion et al. for the reinforcement ratio of 0.52%. Although the deflection at the ultimate load of R-SFRC specimen was more than the span/100 value indicating a good level of ductility, the ductility was lower than that of the RC beam. The displacement ductility decreased by 65, 56 and 78% for the reinforcement ratios of 0.33, 0.52 and 0.75%, respectively by the addition of steel fibres. It was observed that for the RC beams with fibres, the inelastic deformation at failure was concentrated in one large crack, while the inelastic deformation was more evenly distributed in several cracks for RC beams without fibres.

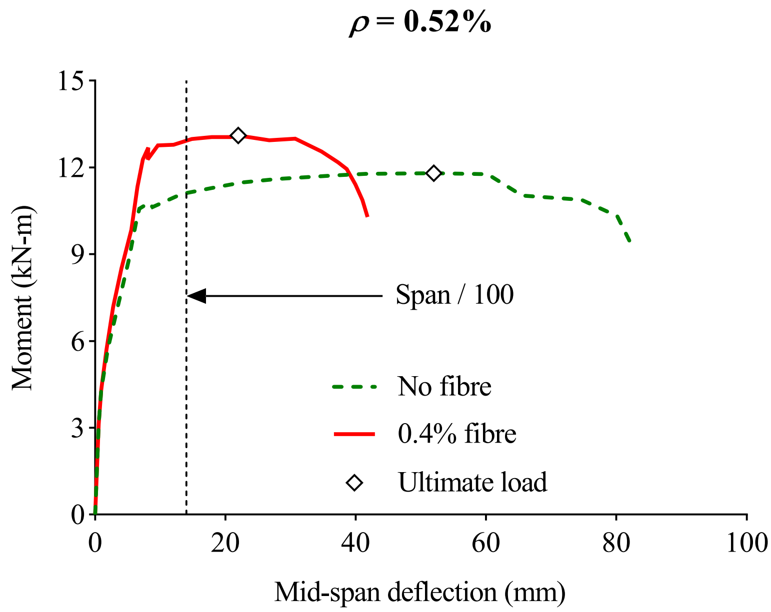

Figure 2.12: Moment versus deflection curves in tests by Espion et al. [22].

Ashour et al. [17] investigated the effect of concrete strength and tensile reinforcement ratio on the flexural behaviour of R-SFRC beams. The experimental study included 27 full-scale beam specimens with a length of 3.4 m and a cross-section of 200 mm × 250 mm. The compressive strengths of concrete varied from 49 to 102 MPa and the tensile reinforcement ratios varied from 1.18 to 2.37%. The average yield strength of tensile reinforcing steel was 530 MPa. Hooked-end steel fibres with a nominal length of

60 mm and an aspect ratio of 75 were used were at 0.5 and 1.0% by volume. The beam specimens were tested under four-point bending with a simply supported length of 3.08 m with a shear span-depth ratio of 6.0.

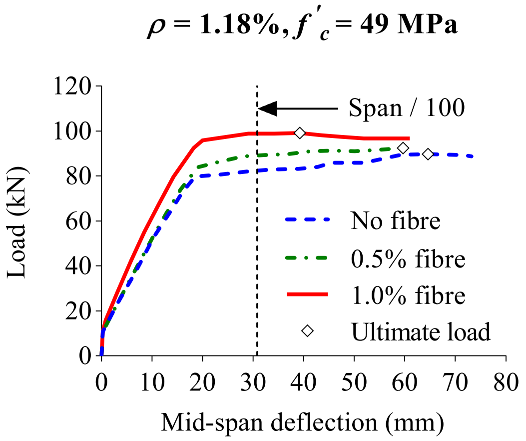

(a) ρ = 1.18%, f_c' = 49 MPa

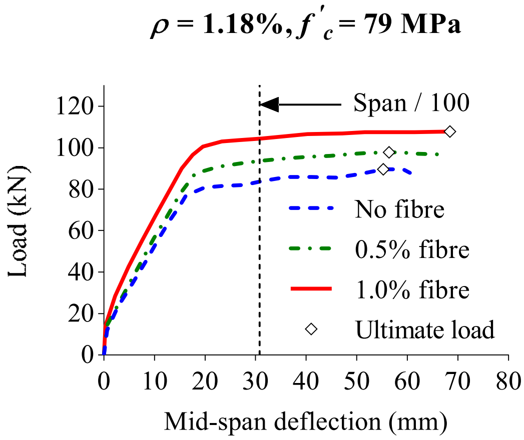

(d) ρ = 1.18%, f_c' = 79 MPa

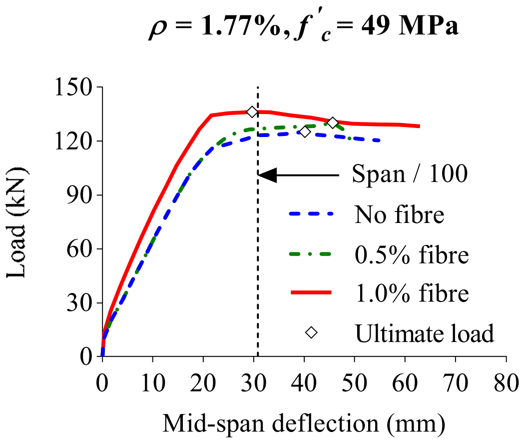

(b) ρ = 1.77%, f_c' = 49 MPa

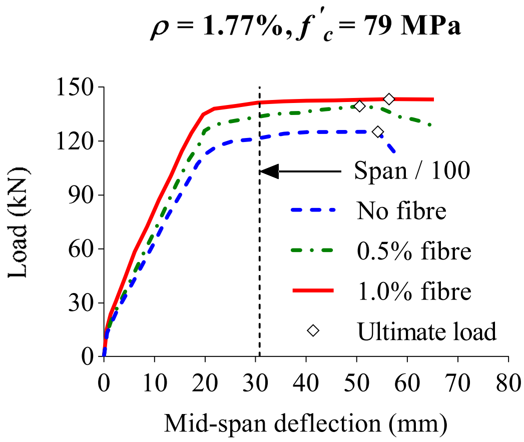

(e) ρ = 1.77%, f_c' = 79 MPa

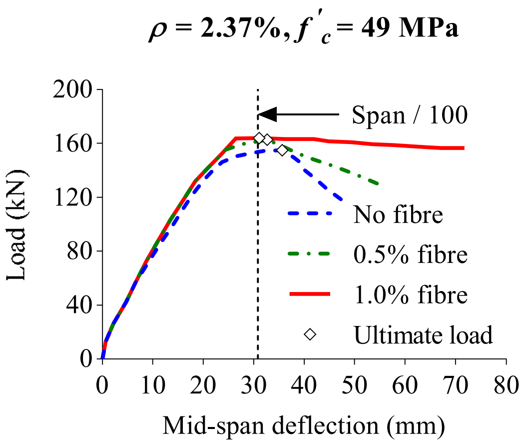

(c) ρ = 2.37%, f_c' = 49 MPa

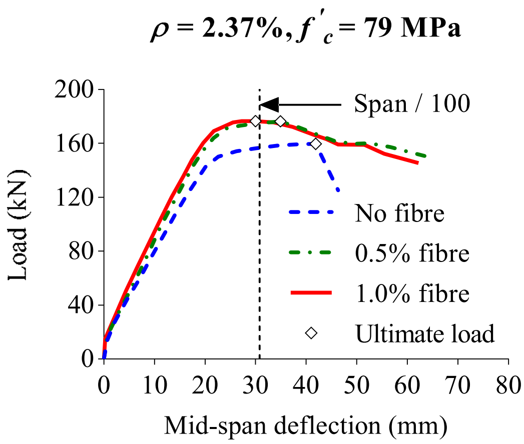

(f) ρ = 2.37%, f_c' = 79 MPa

Figure 2.13: Load versus deflection curves in tests by Ashour et al. [17].

Ashour et al. found that the presence of fibres reduced the crack width and increased the number of cracks. The addition of steel fibres increased the post-cracking stiffness and ultimate strength. The additional moment capacity provided by fibres was not affected by the amount of tensile reinforcement ratio. However, the concrete compressive strength influenced the fibre contribution significantly. The flexural rigidity was increased as the concrete compressive strength and steel fibre content increased.

Figure 2.13 shows the load versus displacement curves of Ashour et al. for concrete strengths of 49 and 79 MPa. From the figure, it is evident that the R-SFRC beam specimens had a good level of ductility for the reinforcement ratios tested. However, the R-SFRC specimens with higher reinforcement ratio showed a softening behaviour after the peak load.

Dancygier and Savir [23] studied the flexural behaviour of high strength R-SFRC beams with low reinforcement ratios. The authors tested nine full-scale beam specimens with a length of 3.9 m and a cross-section of 200 mm $\times$ 300 mm. The amount of tensile reinforcement varied from 0.28 to 0.56%. The measured yield strength of tensile reinforcing steel ranged from 480 to 616 MPa. The average measured compressive strength of concrete was 118 MPa. Hooked end steel fibres with two different lengths (60 and 35 mm) were used at a volumetric ratio of 0.75%. The aspect ratio of the fibres was 65. The beam specimens were tested under four-point bending with a simply supported length of 3.5 m and the shear span-depth ratios varied from 3.5 to 5.3.

Test results of Dancygier and Savir showed that the addition of fibres reduced the ductility of lightly reinforced beams (see Figure 2.14). For the beams without steel fibres, the cracks in the constant moment zone were distributed evenly and the widening of cracks was almost uniform. However, for the beams with steel fibres, out of the several cracks developed at the initial stage of loading, one or two cracks widened distinctly leading to the fracture of steel bar at relatively low displacement. The authors suggested that the minimum tensile reinforcement ratio in flexure in high strength R-SFRC beams should be higher than that of conventionally reinforced members to achieve sufficient ductility.

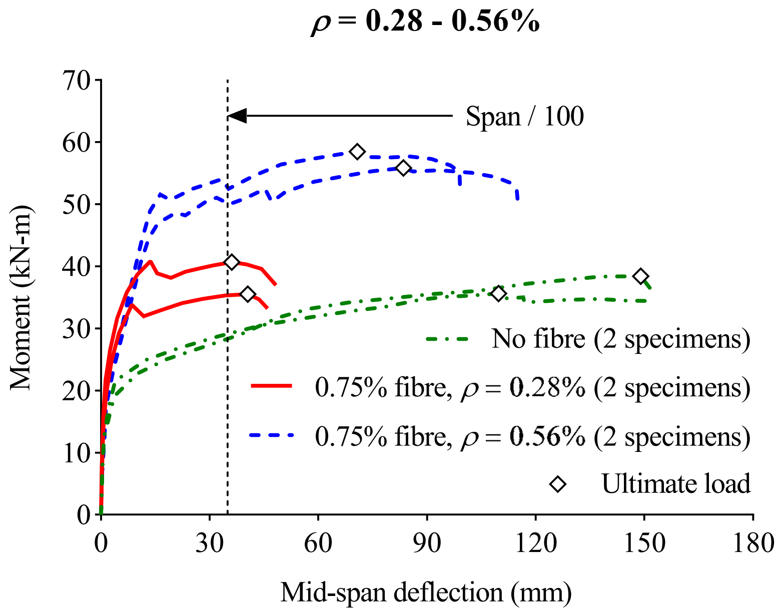

Figure 2.14: Moment versus deflection curves in tests by Dancygier and Savir [23].

Meda et al. [12] studied the amount and bond of tensile reinforcement on the flexural performance of R-SFRC beams. Seven full-scale beam specimens with a length of 4.0 m, a cross-section of 200 × 300 mm were tested in this study. In two of the seven specimens, the bond of the reinforcement was released in the central portion of the beam through plastic pipes. The amount of tensile reinforcement varied from 0.75 to 1.5%, the average yield strength of tensile reinforcing steel was 534 MPa and the average compressive strength (cubes) of concrete was 40 MPa. The steel fibres used were hooked ends at dosages of 30 and 60 kg/m^3. These fibres had a nominal length of

50 mm with an aspect ratio of 50. The beam specimens were tested under four-point bending with a simply supported length of 3.60 m and a shear span-depth ratio of 4.6.

Meda et al. found that the inclusion of steel fibres provided a limited enhancement in load-carrying capacity. The maximum increase was 6.7% by the addition of 30 kg/m^3 of steel fibres in beams with 0.75% of reinforcement. Increasing fibre dosage did not provide any further improvement. The R-SFRC specimens with a reinforcement ratio of 0.75% have a good level of ductility (see Figure 2.15). The beams with higher reinforcement ratio (1.5%) failed by concrete crushing. However, the presence of fibres converted the explosive concrete crushing to a progressive concrete crushing (see Figure 2.15b). When the bond of the reinforcement was released, the beneficial effect of fibres decreased by the formation of fewer and wider cracks.

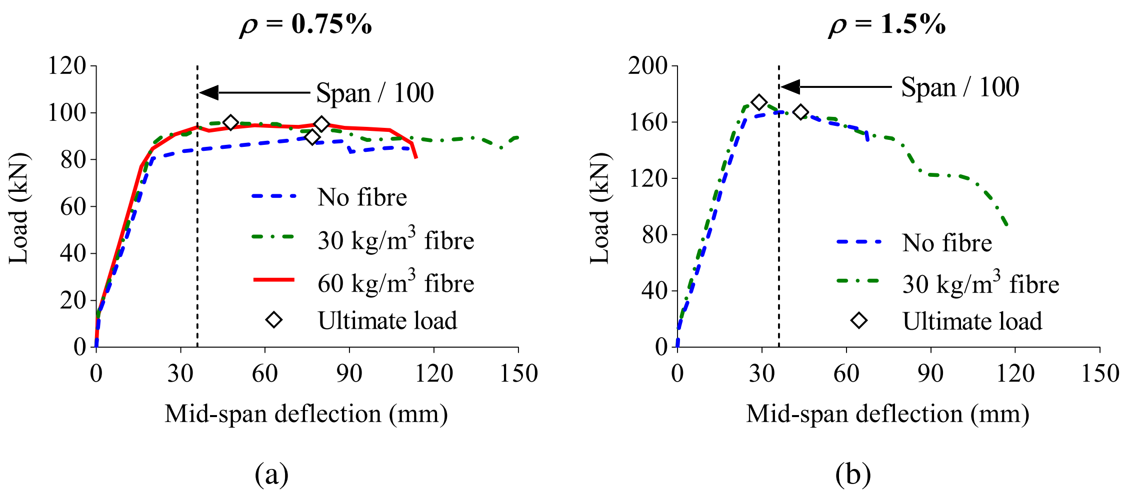

Figure 2.15: Load versus deflection curves in tests by Meda et al. [12] for (a) ρ = 0.75% and (b) ρ = 1.5%.

Dancygier and Berkover [24] performed an extensive experimental study to investigate the flexural performance of R-SFRC beam specimens. The beam specimens were 3.2 m long, 240 mm wide and 300 mm deep. The amount of tensile reinforcement varied from 0.15 to 3.27%. The measured yield strength of tensile reinforcing steel ranged from 409 to 508 MPa. The measured compressive strength of concrete ranged from 26.9 to 37.5 MPa. The steel fibres used were hooked ends at dosages of 40 and 60 kg/m^3. These fibres had a nominal length of 35 mm with an aspect ratio of 64. The beams were tested under four-point bending with a shear span-depth ratio of 3.1. It was found that the addition of steel fibres leads to a significant reduction (50-80%) in flexural ductility of beams with reinforcement ratios less than 0.5% (see Figure 2.16). It was observed that for the beams without fibres, the cracks widened almost uniformly in the constant moment zone. However, for the fibrous specimens with low conventional reinforcement ratios, one or two cracks widened distinctly.

In the Dancygier and Berkover tests, the load-carrying capacities of beams with reinforcement ratios lower than 0.5% were increased up to 25%; at larger reinforcement ratios, the improvement was not significant. Although no significantly different results were observed from two different fibre dosages, the flexural performance was slightly better with lower fibre dosage. The authors commented that although the reduced ductility by the addition of steel fibres in beams with low reinforcement ratios suffice for design purposes, it is important to understand the phenomenon of crack localisation in order to set a minimum reinforcement ratio for R-SFRC beams.

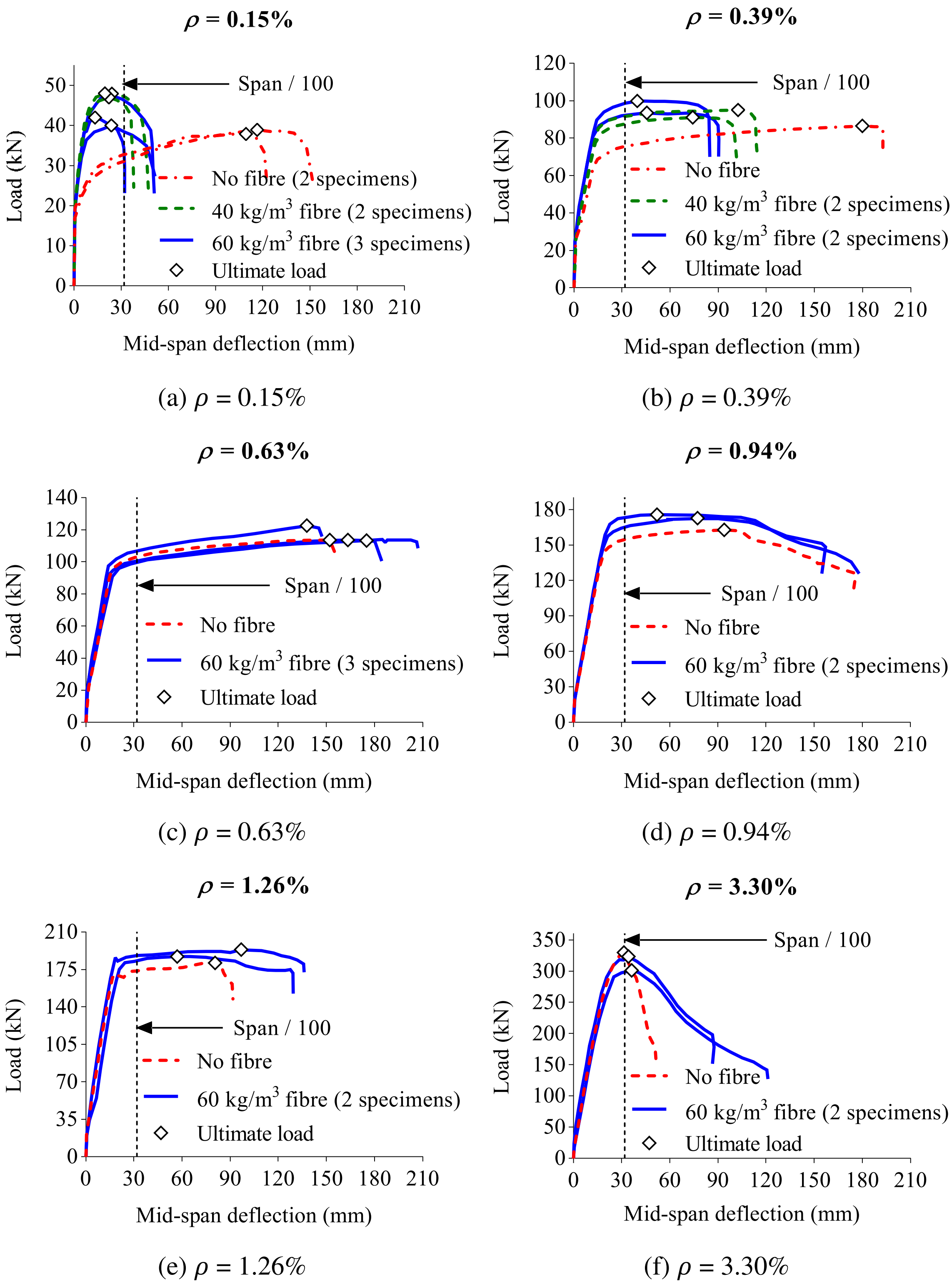

Figure 2.16: Load versus deflection curves in tests by Dancygier and Berkover [24].

The experimental study of Mertol et al. [14] included twenty full-scale beam specimens with a length of 3.5 m and a cross-section of 180 mm × 350 mm. The amount of tensile reinforcement was varied from 0.2 to 2.5% covering the range from under-reinforced to over-reinforced beam behaviour. The average yield strength of tensile reinforcing steel was 420 MPa and the average compressive strength of concrete was 31 MPa. Hooked-end steel fibres with a nominal length of 30 mm and an aspect ratio of 60 were used were at a volumetric ratio of 1.0%. The beams were tested under four-point bending with a simply supported length of 3.30 m and a shear span-depth ratio of 6.5.

The test results of Mertol et al. showed two contrasting behaviours of the addition of steel fibres. At low reinforcement ratios, there were significant increases in ultimate strength but decreases in ductility by the addition of steel fibres. However, as the reinforcement ratio was increased, the increase in ultimate strength became less significant and the R-SFRC specimens became more ductile than that of RC beams (see Figure 2.17). The post-peak stiffness of over-reinforced R-SFRC specimens was observed to be significantly lower than that of RC specimens which indicates that the load in the post-peak region of R-SFRC specimens dropped at a slower rate than that of RC specimens. The flexural toughness of R-SFRC specimens was greater than that of RC specimens with the difference being significantly larger for over-reinforced sections.

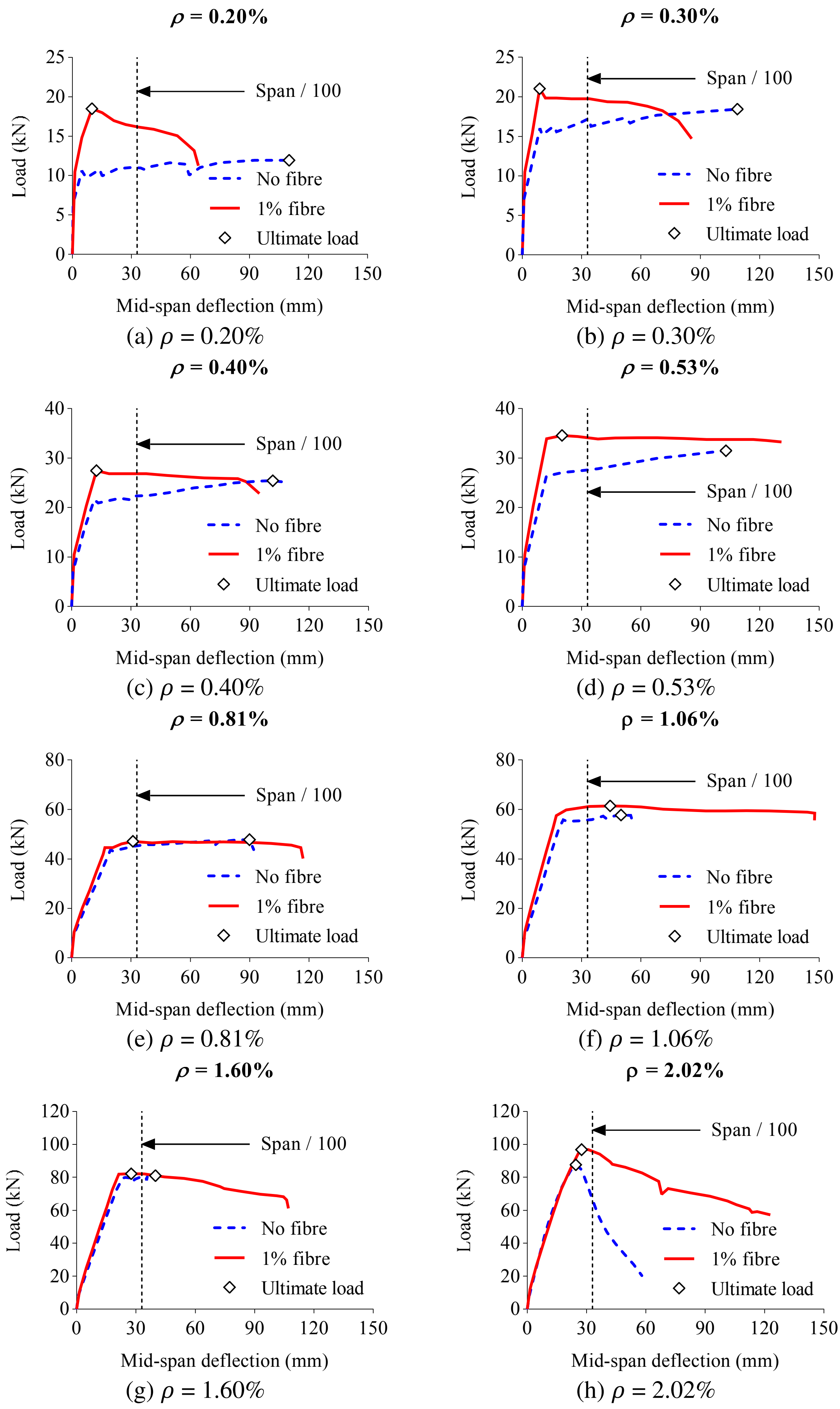

Figure 2.17: Load versus deflection curves in tests by Mertol et al. [14].

Yoo and Moon [15] studied the effect of the addition of steel fibres on the flexural performance of RC beams with low reinforcement ratios. The authors tested twenty-four full-scale beam specimens with a length of 3.0 m and a cross-section of 320 mm × 300 mm. The amount of tensile reinforcement varied from 0.18 to 0.41%; the tensile reinforcement ratios were 44, 66, 78 and 100% of the minimum reinforcement ratio based on ACI318-14 code. The nominal yield strength of tensile reinforcing steel was 500 MPa and the average measured compressive strength of concrete was 43 MPa. Hooked-end steel fibres with a nominal length of 35 mm and an aspect ratio of 64 were used in the study. The dosage of steel fibres varied from 0.25 to 1.0% by volume. The specimens were tested under four-point bending with a simply supported length of 2.6 m and a shear span-depth ratio of 4.0.

The test results of Yoo and Moon showed that the inclusion of steel fibres increased the cracking load, post-cracking stiffness and yield load. Although the ultimate load was also increased by the addition of steel fibres, the improvement was not significant and the improvement became even less significant at higher reinforcement ratios. Moreover, the R-SFRC beams with a fibre volume fraction more than 0.5% showed a softening behaviour after the peak load for whereas the RC beams exhibited a continuous and gradual increase in the flexural load due to hardening of steel reinforcing bars until the ultimate load at which the reinforcing bars fractured (see Figure 2.18).

In terms of ductility, Yoo and Moon found that the addition of steel fibres leads to a significant reduction in flexural ductility of beams, and RC beams with lower reinforcement ratios and higher fibre volume fractions resulted in lower ductility. Although the number of cracks increased by the addition of steel fibres, the crack localisation phenomenon (widening of a single crack) was observed for fibre volume fractions equal to or greater than 0.75%. However, for fibre volume fractions less than 0.5%, the crack localisation phenomenon was barely observed.

Based on the test results, Yoo and Moon concluded that replacing tensile steel reinforcing bars with steel fibres is not favourable in terms of ultimate load-carrying capacity, ductility and maintaining flexural strength margin up to the failure.

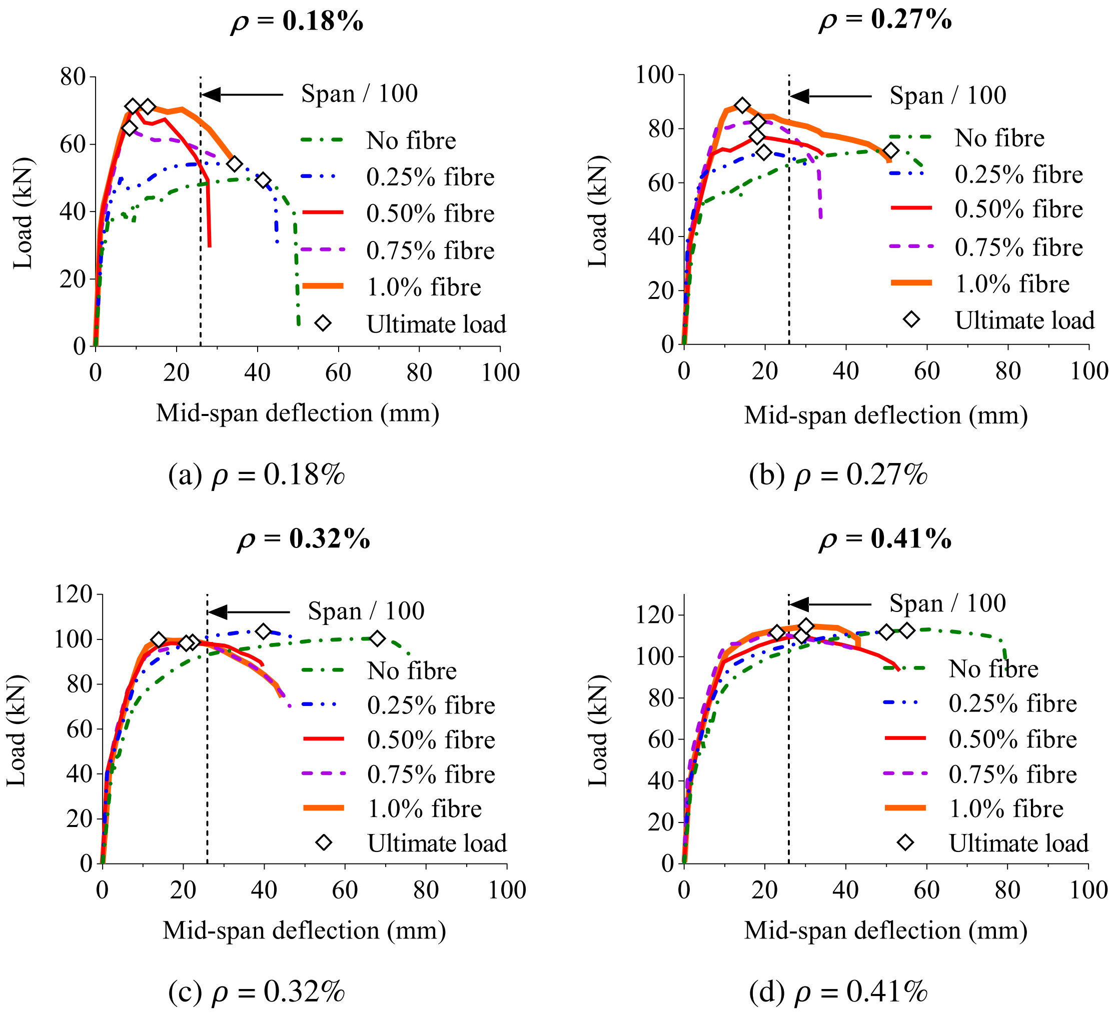

(a) $\rho = 0.18\%$ (b) $\rho = 0.27\%$

(c) $\rho = 0.32\%$ (d) $\rho = 0.41\%$

Figure 2.18: Load versus deflection curves in tests by Yoo and Moon [15].

2.2.5 Effect of the presence of compressive reinforcement

Craig et al. [5] studied the effect of the inclusion of steel fibres in RC beams with and without compressive reinforcement. The authors tested four full-scale beam specimens with a length of 3.66 m and a cross-section of 178 mm $\times$ 381 mm. The amount of tensile reinforcement was 1.8%, the average yield strength of tensile reinforcing steel was 448 MPa and the average compressive strength of concrete was 28 MPa. Crimped-end steel fibres with a length of 50 mm and an aspect ratio of 100 were used at a dosage of 1.75% by volume. The beam specimens were tested under four-point bending with a simply supported length of 2.74 m and a shear span-depth ratio of 2.8. Test results showed that the inclusion of steel fibres increased the load-carrying capacity and ductility of the RC beams. The ultimate moment was increased by 27% by the addition of steel fibres in RC beam with compressive reinforcement.

Figure 2.19 shows the results of Craig et al. tests for moment versus deflection curves. From the figure, it is evident that the beams with compressive reinforcement had better ductility than that of beams without compression reinforcement. The beams with compressive reinforcement showed hardening behaviour after the yielding of reinforcement and the deflection at ultimate load was more than the span/100 value demonstrating a high level of ductility. Although the R-SFRC beam without compressive reinforcement showed a softening behaviour after the peak load, the softening was more ductile than that of the beam without steel fibres.

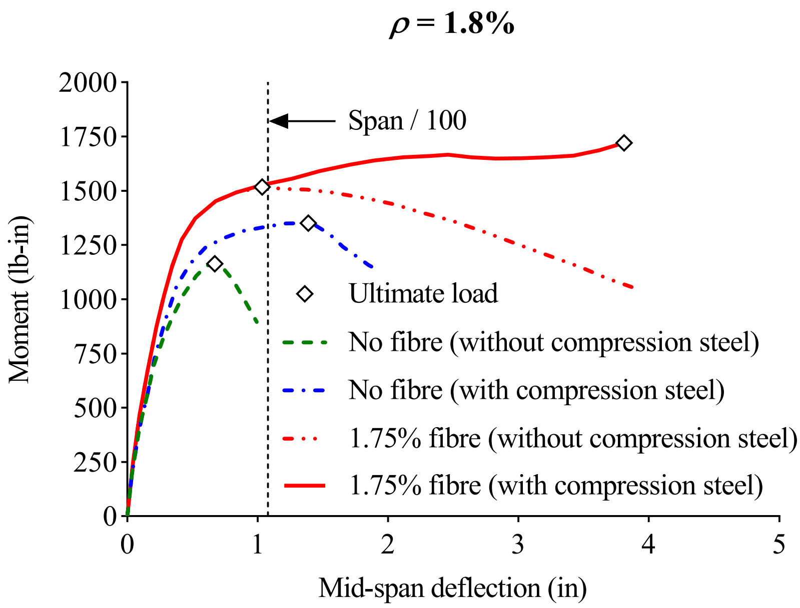

Figure 2.19: Moment versus deflection curves in tests by Craig et al. [5].

2.3 Crack localisation in SFRC flexural members

After reviewing the performance of R-SFRC flexural members, it is evident that the inclusion of steel fibres can lead to a reduction in deformation capacity and ductility of R-SFRC flexural members when the amount of tensile reinforcement is very low (less than 0.4%). This decrease in deformational capacity and ductility is caused by the localisation of plastic deformation in one or two cracks compared to more even distribution in several cracks in case of RC flexural members [15, 22-24, 121]. This phenomenon is called “crack localisation”.

The inclusion of steel fibres increases the load-carrying capacity of R-SFRC flexural members. Due to crack localisation, fibres bridging the highly stressed cracks start to pull out from the concrete at the surface of the localised cracks and the additional load carried by the fibres transferred to the tensile steel reinforcement. If the stress released by the fibres cannot be picked up by the reinforcement, the load-carrying capacity of the member decreases. Moreover, crack localisation causes the reinforcement strain to concentrate at the localised cracks leading to early strain hardening and premature fracture of the reinforcement, causing a reduction in ultimate deflection and flexural ductility. Crack localisation was also observed in R-SFRC tension members [122, 123].

Dancygier and Savir [23] suggested that the increased bond between the tensile reinforcing bars and concrete caused by the confining action of the steel fibres may cause the crack localisation. The relative confining effect of fibres is anticipated to be reduced with the increase of tensile reinforcement, thus reducing the localisation effect and increasing the ductility.

Schumacher et al. [121] reported that crack localisation depends on the combined effects of steel fibres (amount, geometry, orientation, bond properties) and reinforcing bars (amount, hardening properties). The response of a R-SFRC member depends on the stress-strain behaviour of steel reinforcing bars and stress-crack opening behaviour of SFRC. The overall behaviour depends on the resultant of the hardening of the reinforcing steel and the softening of the SFRC. A high fibre dosage and/or pronounced softening of SFRC and a low conventional reinforcement ratio and/or reinforcing steel with low hardening ratio can cause the softening of the tensile/flexural member.

Walraven [124] and Yuguang et al. [125] implied that crack localisation resulted from the variation of the concentration and orientation of fibres in the different cross-sections. Increasing fibre content increases the probability of scattering and thus increasing the probability of localisation in one crack.

Deluce and Vecchio [122] described the crack localisation as the formation of "the weakest section". At the weakest section, once the crack width progressed beyond a certain threshold, fibres began to pull out, and the ability of the fibres to bridge the cracks began to decrease. This essentially caused the weakest section of the specimen to become even weaker, ensuring further local yielding of the reinforcing bar at this crack location. However, the authors did not discuss the possible factors of the formation of the weakest section.

Dancygier and Karinski [126] proposed a quantitative, probabilistic model of crack localisation in axially loaded R-SFRC prismatic specimens. The model is based on the hypothesis that the "weak sections" as referred by Deluce and Vecchio [122] are the results of non-uniform distribution of fibres. Based on a probability function of the fibres distribution, the model is said to predict the number of significantly widened cracks than others out of a given number of cracks. The authors performed a case study and found that the probability of widening only one or two cracks increases with the reduction of tensile reinforcement ratios, and as the conventional reinforcement increases, this phenomenon diminishes and the crack widths become more uniform.

Karinski and Dancygier [127] and Karinsrki et al. [128] studied the effect of the amount of tensile reinforcement and the dosage of steel fibres on fibre distribution along R-SFRC prismatic specimens. The specimens were 1.05 m long with a cross-section of 80 mm × 80 mm. The specimens had a single, centrally located deformed bar except for the control specimens. The diameter of the tensile reinforcement varied from 8 to 20 mm representing tensile reinforcement ratios of 0.8 to 5%. Hooked-end steel fibres with a length of 35 mm and an aspect ratio of 64 were used at dosages of 30 and 60 kg/m^3. Each specimen was sawed into equal segments where the width of each segment was equal to the length of a single fibre and the number of fibres appearing at the cross-sections was counted.

Karinsrki et al. and Karinski and Dancygier found that the as the conventional reinforcement increased, the distribution of steel fibres became more uniform and for a given amount of tensile reinforcement, the distribution became less uniform with the increase of fibre dosage. A reasonable good agreement was obtained between the experimental results and the results predicted by the model proposed by Dancygier and Karinski [126].

2.4 Moment redistribution of R-SFRC flexural members

Few studies are found in the literature on the moment redistribution performance of R-SFRC flexural members. Liu et al. [129] studied the moment redistribution of fully and partially prestressed high strength SFRC beams with a varying height of box section. Hooked-end steel fibres with a volumetric ratio of 1% were used in their study. The ratio of the bending moment at the intermediate support to that of at the mid-span was used to reflect the moment redistribution. The authors found that the moment redistribution occurred in two stages. In the first stage, the critical section in the mid-span cracked first and the stiffness at the mid-span section became lower than that of the intermediate support. Consequently, moment redistribution occurred from mid-span to intermediate support. As loading continued, the prestressing tendons and the reinforcing bars at the intermediate support yielded leading to the formation of a plastic hinge at the intermediate support and moment redistribution occurred from intermediate support to mid-span. Although the amount of moment redistribution was not quantified in this study, the authors commented that SFRC specimens exhibited an excellent capacity for moment redistribution.

Abas et al. [130] investigated the moment redistribution of composite slabs fabricated with deep trapezoidal steel decks and SFRC. Two different types of hooked-end steel fibres were used at dosages varied from 0 to 40 kg/m^3. The authors used the ratio of the bending moments at the intermediate support to that of at the mid-span to indicate moment redistribution. Further, the sudden changes in moment redistribution due to cracking and bond-slip at the steel-concrete interface were found to be less evident in the SFRC slabs than that of in the plain concrete slab.

Iskhakov et al. [27] studied the moment redistribution of two-layer SFRC beams. The authors used normal strength plain concrete in the tension zone and high strength SFRC in the compression zone to increase the concrete capacity in the compression zone to withstand relatively large bending moments resulting from longer beam span and increased service load. Hooked end steel fibres with a length of 50 mm and an aspect ratio of 50 were used at a dosage of 40 kg/m^3. Experimental results confirmed the formation of a plastic hinge at the intermediate support followed by the formation of two more hinges at the mid-spans, which implies that the full moment redistribution potential was realised.

Küsel and Kearsley [28] investigated the effect of the inclusion of steel fibres on moment redistribution in reinforced concrete beams. In their study, the amount of tensile reinforcement varied from 0.7 to 2.2%. Hooked-end steel fibres with a length of 30 mm and an aspect ratio of 55 were used at dosages varying from 1 to 2%. The authors used the rate of deviation of the experimental moment from the theoretical elastic moment to quantify moment redistribution. The test results indicated the occurrence of significant moment redistribution before the plastic behaviour. A fibre dosage of 1.5% was found to be optimum in terms of moment redistribution corresponded to a flatter post-peak moment-curvature relationship. The effect of fibres was found to decrease with increased reinforcement ratio.

2.5 Conclusions

It is unanimously agreed in the literature that the inclusion of steel fibres can significantly improve the cracking and deformational behaviour of RC beams at service loading condition. The presence of steel fibres increases the number of cracks and decreases their width, length and spacing. The addition of steel fibres increases the service stiffness of the RC beams resulting in a substantial reduction of deflection, strain in reinforcing steel bars, rotation and curvature.

Apart from improvements at the service the loading condition, the inclusion of steel fibres increases the load-carrying capacity and ductility of RC beams. However, the improvements in load-carrying capacity and ductility have been found to be dependent on the amount of tensile reinforcement and the dosage of steel fibres. The increase in load-carrying capacity by the addition of steel fibres is more significant in beams with low reinforcement ratios. As the reinforcement ratio increases, combined with limits on the dosage of fibres, the improvement in load-carrying capacity becomes marginal. On the other hand, the addition of steel fibres leads to a reduction in ductility of RC beams with low reinforcement ratios (less than 0.4%) combined with high dosages of fibres. The presence of steel fibres enhances the ductility of RC beams with high reinforcement ratios. For over-reinforced concrete beams, the inclusion of steel fibres converts dynamic concrete crushing to progressive concrete crushing.

The reduction in ductility and deformational capacity by the addition of steel fibres is caused by the localisation of plastic deformation in one or two cracks compared to more even distribution in several cracks in case of RC flexural members. Crack localisation in R-SFRC flexural members is caused by the improved bond between reinforcing bars and the surrounding concrete due to the influence of fibres and enhanced control of microcracking.

Although limited research has been conducted on the flexural performance of R-SFRC simply supported members, few studies are found in the literature on the flexural performance and moment-redistribution capacity of R-SFRC continuous members, and no prior studies have investigated the ability of R-SFRC continuous members with low reinforcement ratios (less than 0.4%) to redistribute loads, or if the achievement of the maximum moment redistribution in design standards (generally ±30%) is possible. Because of the lack of research in this area, limitations are placed in design standards on the application of steel fibres in locations where large plastic rotations are expected because of moment redistribution, and no guidelines are available in the standards on the requirement for minimum reinforcement ratio for which R-SFRC flexural members will show a sufficient level of ductility. Therefore, there is a need to investigate the moment redistribution capacity of R-SFRC continuous members, study the effect of reinforcement ratio and fibre dosage on the ductility and post-peak behaviour of R-SFRC flexural members, and develop relationships for minimum reinforcement ratio for which R-SFRC flexural members will show a sufficient level of ductility.

Chapter 3

FLEXURAL PERFORMANCE OF R-SFRC CONTINUOUS BEAMS

3.1 Introduction

An experimental study to investigate the ability of R-SFRC continuous members to achieve the maximum amount of moment redistribution allowed by current design standards [30, 33-35] is presented in this chapter. The experimental study consisted of six tests, four full-scale two-span continuous R-SFRC beams and two control RC beams. The beam specimens were designed for nominally ±30% of moment redistribution with respect to the linear-elastic condition. The specimens were tested under monotonically increasing displacement-controlled load up to a displacement of 50 mm. The improvements in cracking behaviour, load-carrying capacity and ductility of the R-SFRC beams are evaluated with respect to the control RC beams. The laboratory test results are further analysed to determine if internal forces can be redistributed to under-utilised regions of the member and if R-SFRC moment hinges can maintain their capacity during large plastic rotations and moment redistribution.

3.2 Experimental investigation

3.2.1 Description of test specimens

The details of the test specimens are shown in Table 3.1. The geometry, loading, boundary conditions and arrangement of longitudinal and transverse reinforcements for the tested specimens are shown in Figure 3.1. The primary variables within different test specimens were the volume of tensile steel reinforcement and the dosage of steel fibres. The tensile reinforcement ratios varied between 0.69% and 1.38%, and the nominal dosages of steel fibres were 0, 30 and 60 kg/m^3. The beams were nominally designed for ±30% redistribution of moment with respect to the linear-elastic condition, the maximum moment redistribution allowed by *fib* Model Code 2010 [30], AS 5100.5:2017 [33], AS 3600:2018 [34] and Eurocode 2 [35]. Accordingly, the designation BW(±30) for specimens is used with respect to 'B' the member type (Beam) and 'W' the dosage of steel fibres (in kg/m^3) and '(±30)' denote the nominal percentage of moment redistribution with respect to the linear-elastic condition.

The specimens in Series A were designed for negative moment redistribution (from mid-span to intermediate support) by increasing the negative moment at the intermediate support by the given percentage with respect to the linear-elastic condition and, consequently, decreasing the positive moment at the mid-spans, while keeping the total static moment unchanged. In Series B, the specimens were designed for positive moment redistribution (from intermediate support to mid-span) by decreasing the negative moment at the intermediate support by the given percentage with respect to the linear-elastic condition and, consequently, increasing the positive moment at the mid-spans, again while keeping the total static moment unchanged.

The specimens without steel fibres (RC specimens) were designed first for 30% of negative and positive moment redistribution with respect to linear-elastic condition based on AS 3600:2018 [34]. In the calculation of the flexural strength of the RC specimens, the compressive strength of concrete and the yield strength of steel were taken as 40 MPa and 500 MPa, respectively. The flexural strength of the specimens with steel fibres (R-SFRC specimens) was determined assuming the contribution of fibres to the flexural strength based on the rectangular stress block (RSB) model of AS 3600:2018 [34]. The RSB model has been demonstrated to provide a good balance between model simplicity and reliability [131]. In the calculation of the flexural strength of the R-SFRC specimens, the residual tensile strength of SFRC for 1.5 mm crack opening depth ($f'_{1.5}$) for 30 kg/m^3 and 60 kg/m^3 of fibres were taken as 0.8 MPa and 1.6 MPa, respectively. Since the steel reinforcement ratios in specimens with or without steel fibres were kept constant in a series, the inclusion of steel fibres slightly changed the designed amount of moment redistribution of R-SFRC beams from that of RC beams. Detail calculations of the design of the beam specimens are provided in Appendix A.

Table 3.1: Specimen details.

Series	Specimen	Fibre dosage (kg/m^3)	Negative reinforcement at intermediate support (mm^2)	Positive reinforcement at mid-span (mm^2)	Nominal amount of moment redistribution (%)
A	B00(−30)	0	1240 (1.38%)	620 (0.69%)	−30
	B30(−30)	30 (0.4%)			
	B60(−30)	60 (0.8%)			
B	B00(+30)	0	620 (0.69%)	930 (1.03%)	+30
	B30(+30)	30 (0.4%)			
	B60(+30)	60 (0.8%)			

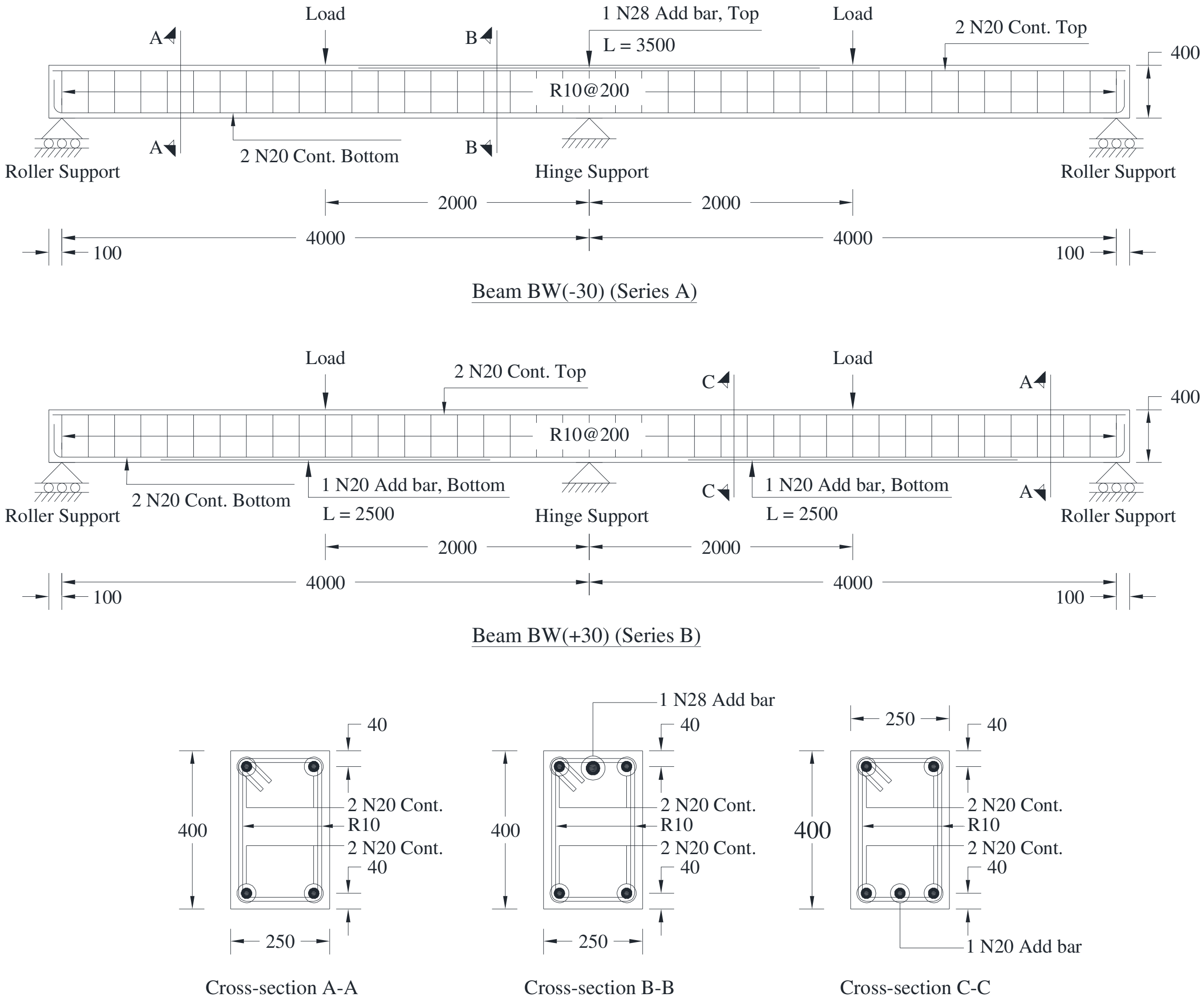

Figure 3.1: Details of specimens and arrangements for continuous two-span beam tests (all dimensions in mm).

3.2.2 Preparation of test specimens and material properties

In all specimens, D500N (D-deformed, N-normal ductility) grade steel bars with a nominal yield strength of 500 MPa were used for tensile reinforcement, and R250N (R-round, N-normal ductility) grade steel bars with a nominal yield strength of 250 MPa were used for stirrups. The average measured yield strength of N20 (20 mm diameter), N28 (28 mm diameter) and R10 (10 mm diameter) bars were 520, 540 and 325 MPa, respectively. The average measured elastic modulus of N20, N28 and R10 bars were 196, 197 and 210 GPa, respectively. The uniaxial stress-strain curves for the reinforcing bars tested to AS 1391-2007 [132] are shown in Figure 3.2.

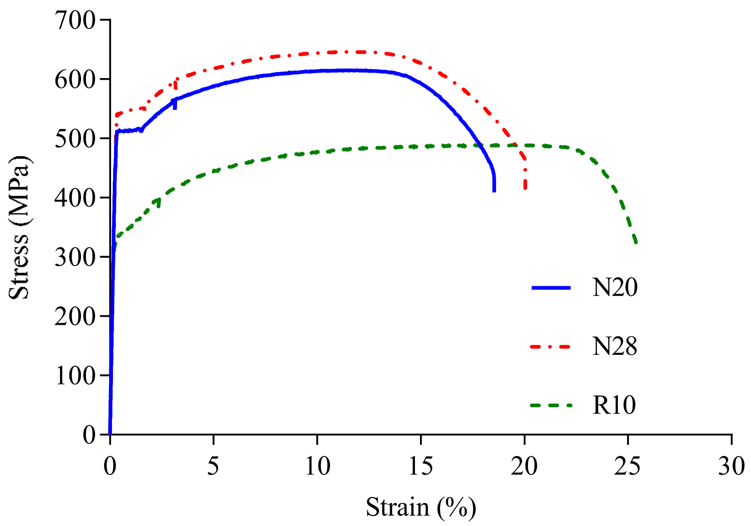

Figure 3.2: Uniaxial stress versus strain curves for reinforcing bars in tension.

The steel fibres used in this study were 0.9 mm in diameter, 60 mm long double end-hooked fibres (Dramix®5D-65/60-BG) (see Figure 3.3) and were manufactured from high ductility wire with a high tensile strength of 2300 MPa.

Figure 3.3: Dramix®5D-65/60-BG steel fibres.

The plain concrete was commercially batched with a maximum aggregate size of 10 mm, a slump of 200 mm and design compressive strength of 40 MPa at 28 days. The aggregate size and slump were chosen to ensure the workability of the concrete after the inclusion of steel fibres. The specimens without fibres were cast first and then the required amount of steel fibres were added to the plain concrete and mixed in the agitator for a minimum of 10 minutes before the casting of the SFRC specimens. The plain concrete was compacted using a poker vibrator, and the SFRC specimens were compacted using external vibrators attached to the sides of the formwork to ensure a uniform distribution of steel fibres (see Figure 3.4b).

For each pour of SFRC, the as-cast dosages of steel fibres were determined by collecting SFRC samples in three 150 mm diameter and 300 mm high cylinders at the start, middle and end of the pour. Standard wash-out test and magnetic separation were performed to extract the fibres from the concrete mix, with the fibres dried before weighing. For the mix with nominally 30 kg/m^3 of steel fibres, the average dosages of fibres at the start, middle and end of the pour were 26, 30 and 26 kg/m^3, respectively. For the mix with nominally 60 kg/m^3 of steel fibres, the average dosages of fibres at the start, middle and end of pour were 49, 47 and 59 kg/m^3, respectively.

(a)

(b)

Figure 3.4: (a) Formwork for the casting of beam specimens; (b) external vibrators.

Along with beams, companion specimens were cast to determine the material properties of the plain concrete and SFRC. These specimens included 150 mm diameter and 300 mm high cylinders for the determination of compressive strength as per AS 1012.9:2014 [133], splitting tensile strength as per AS 1012.10-2000 [134] and stress-strain relationship of concrete in compression, dogbone specimens (see Figure 3.5) tested to AS 3600:2018 [34] to determine the residual direct tensile stress of the SFRC and 150 x 150 x 600 mm prism specimens (see Figure 3.6) tested to EN 14651-2005 [135] to determine the flexural tensile stress of the SFRC. The companion cylinder, dogbone and prism samples were tested on the testing day of the respective beam specimens.

The stress-strain curves for plain and SFRC are shown in Figure 3.7. The mean compressive strength of the concrete with 0, 30 and 60 kg/m^3 of steel fibres were 57, 66.1 and 57.4 MPa, respectively. The mean splitting tensile strength of the concrete with 0, 30 and 60 kg/m^3 of steel fibres were 4.7, 6.8 and 6.4 MPa, respectively.

The full stress-COD (σ–w) and stress-CMOD (crack mouth opening displacement) results are given in Figures 3.8 and 3.9, respectively, and a summary of prism test results is provided in Table 3.2. The mean residual tensile stress determined by the direct tensile test method was 2.23 MPa for 0.5 mm crack opening depth (COD) ($f'_{0.5}$) for SFRC with 60 kg/m^3 of steel fibres. The value of $f'_{0.5}$ for SFRC with 30 kg/m^3 of steel fibres could not be determined as the crack widths at the cracking of concrete were more than 0.5 mm (see Figure 3.8a). The mean residual tensile stress determined by the direct tensile test method were 1.83 MPa and 2.02 MPa for 1.5 mm COD ($f'_{1.5}$) for SFRC with 30 and 60 kg/m^3 of steel fibres, respectively. These compare to $f'_{0.5}$ = 2.68 and 3.20 MPa and $f'_{1.5}$ = 2.98 and 3.19 MPa for SFRC with 30 and 60 kg/m^3 of steel fibres, respectively, when determined by the AS 3600:2018 [34] inverse analysis method on prism bending tests.

Table 3.2: Summary of flexural tensile strength test results and calculated tensile strengths (according to EN 14651-2005 [135] test procedure and determined by AS 3600:2018 [34] analysis).

Fibre dosage (kg/m^3)	$f'_{R,1}$ (MPa)	$f'_{R,2}$ (MPa)	$f'_{R,3}$ (MPa)	$f'_{R,4}$ (MPa)	$f'_{0.5}$ (MPa)	$f'_{1.5}$ (MPa)
30	6.17 (0.314)	8.84 (0.164)	9.69 (0.154)	9.57 (0.166)	2.68 (0.169)	2.98 (0.175)
60	8.53 (0.303)	11.26 (0.148)	12.04 (0.140)	11.48 (0.188)	3.20 (0.055)	3.19 (0.110)

Notes: 1. Mean values of 5 specimens with COV's in ().

2. $f'_{R,1}, f'_{R,2}, f'_{R,3}$ and $f'_{R,4}$ are residual flexural tensile strength of SFRC corresponding to CMODs of 0.5, 1.5, 2.5 and 3.5 mm, respectively.

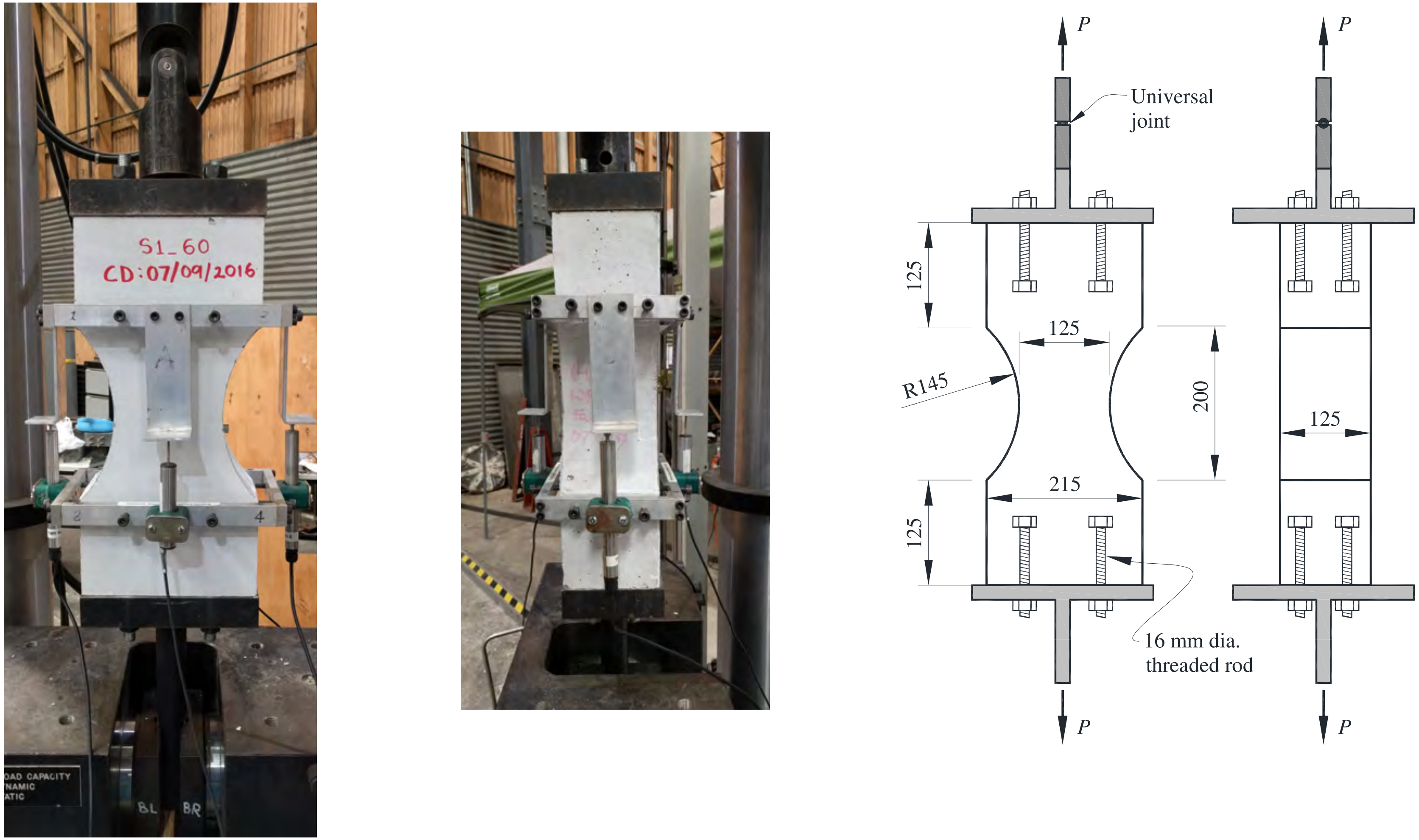

(a) **(b)** **(c)**

Figure 3.5: Test setup for dogbone specimens – (a) elevation; (b) side view; (c) dimensions [34].

Figure 3.6: Test setup for prism specimens.

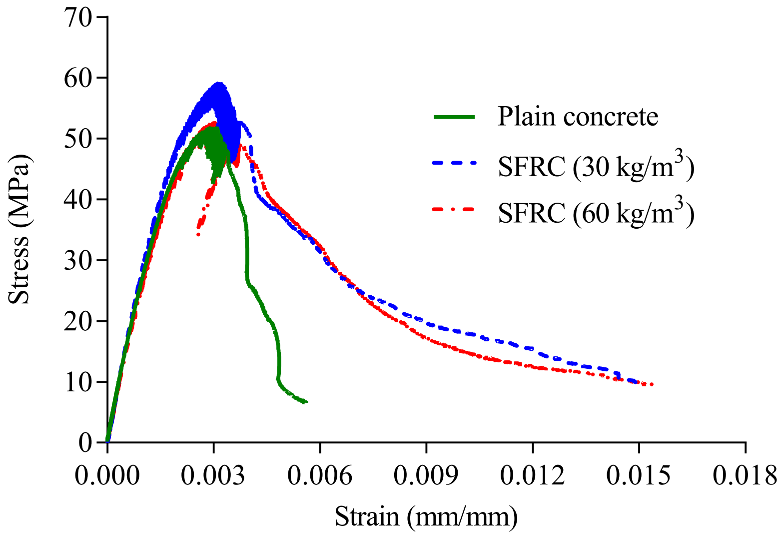

Figure 3.7: Compressive stress-strain curves for plain concrete and SFRC mixes.

(a)

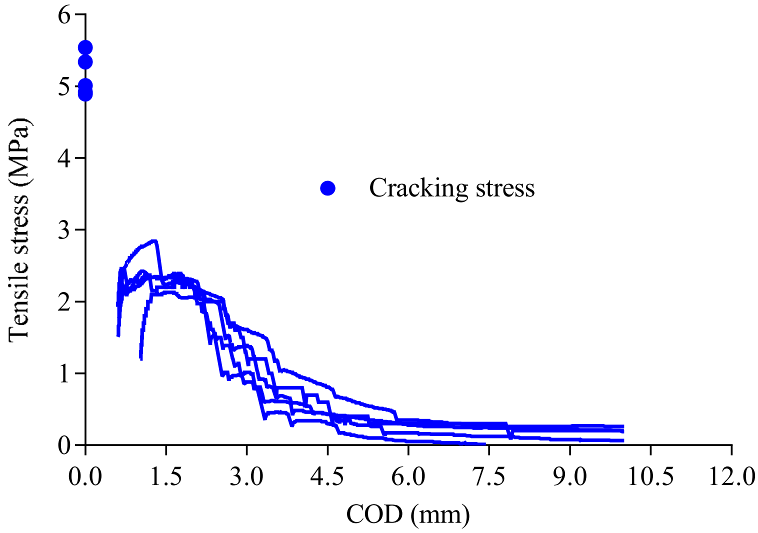

(b)

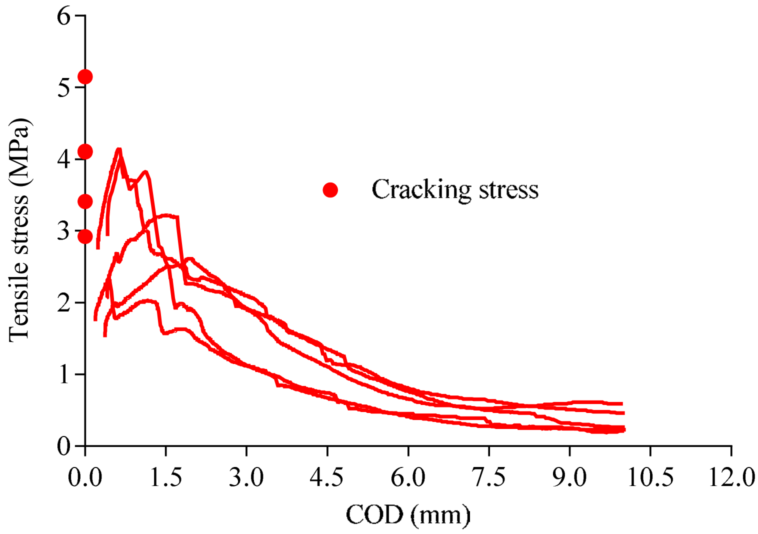

Figure 3.8: Tensile stress versus COD for fibre dosages of (a) 30 kg/m^3 and (b) 60 kg/m^3.

(a)

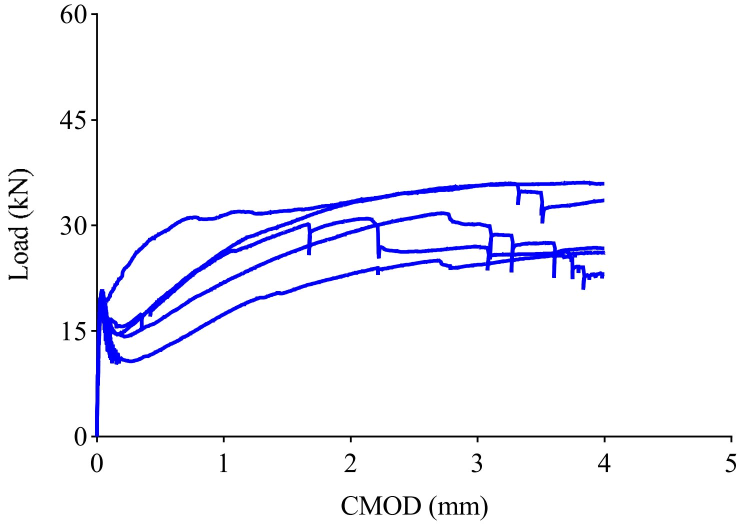

(b)

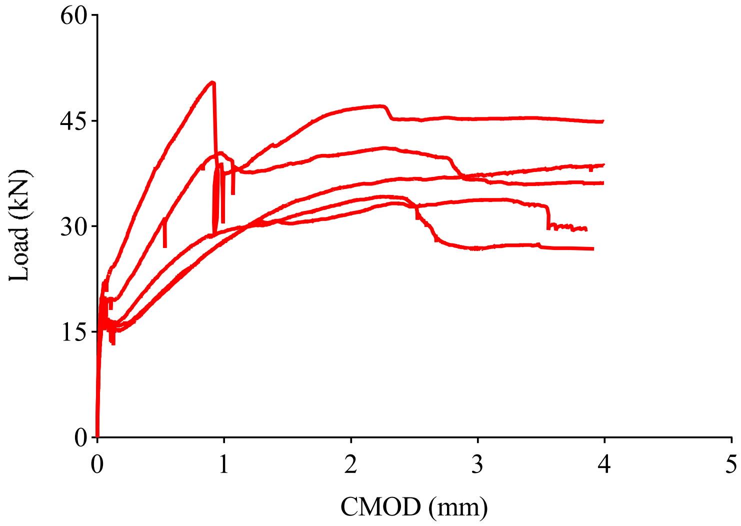

Figure 3.9: Load versus CMOD for fibre dosages of (a) 30 kg/m^3 and (b) 60 kg/m^3.

3.2.3 Experimental setup and instrumentation

The experimental setup and a schematic diagram of the loading arrangement and instrumentation are shown in Figures 3.10 and 3.11, respectively. A 5000 kN capacity hydraulic jack was used to apply the load on the spreader beam (see Figure 3.10) that, in turn, transferred the load evenly to each span. The applied load was recorded by the installed load cell within the testing apparatus, and linear variable displacement transducers (LVDTs) were placed at mid-spans (see Figure 3.10) to measure the deflection of the beams. Load cells were placed at two ends of the beams (see Figure 3.10) to measure the end support reactions. The reaction at the mid support was determined by deducting the sum of two end support reactions from the applied load.

The concrete strains were measured on the sides of specimens at the intermediate support and mid-spans using a 250 mm demountable mechanical (Demec) strain gauge and a grillage of Demec targets (see Figure 3.12a). Three 250 mm Pi-gauges were also installed at the location of intermediate support on the tension side of specimens to monitor crack width growth (see Figure 3.12b). Strains in the tensile reinforcement were measured by 5 mm electronic strain gauges installed (glued after polishing the surface and protected by silicon sealant) on the reinforcement at the mid-spans under the load points and at the intermediate support before the casting of concrete (see Figure 3.12c). Additional strain gauges were installed at an interval of 200 mm on the left and right of the intermediate support (see Figure 3.12c). The data from strain gauges were used to determine the yielding of reinforcement and the formation and development of plastic hinges.

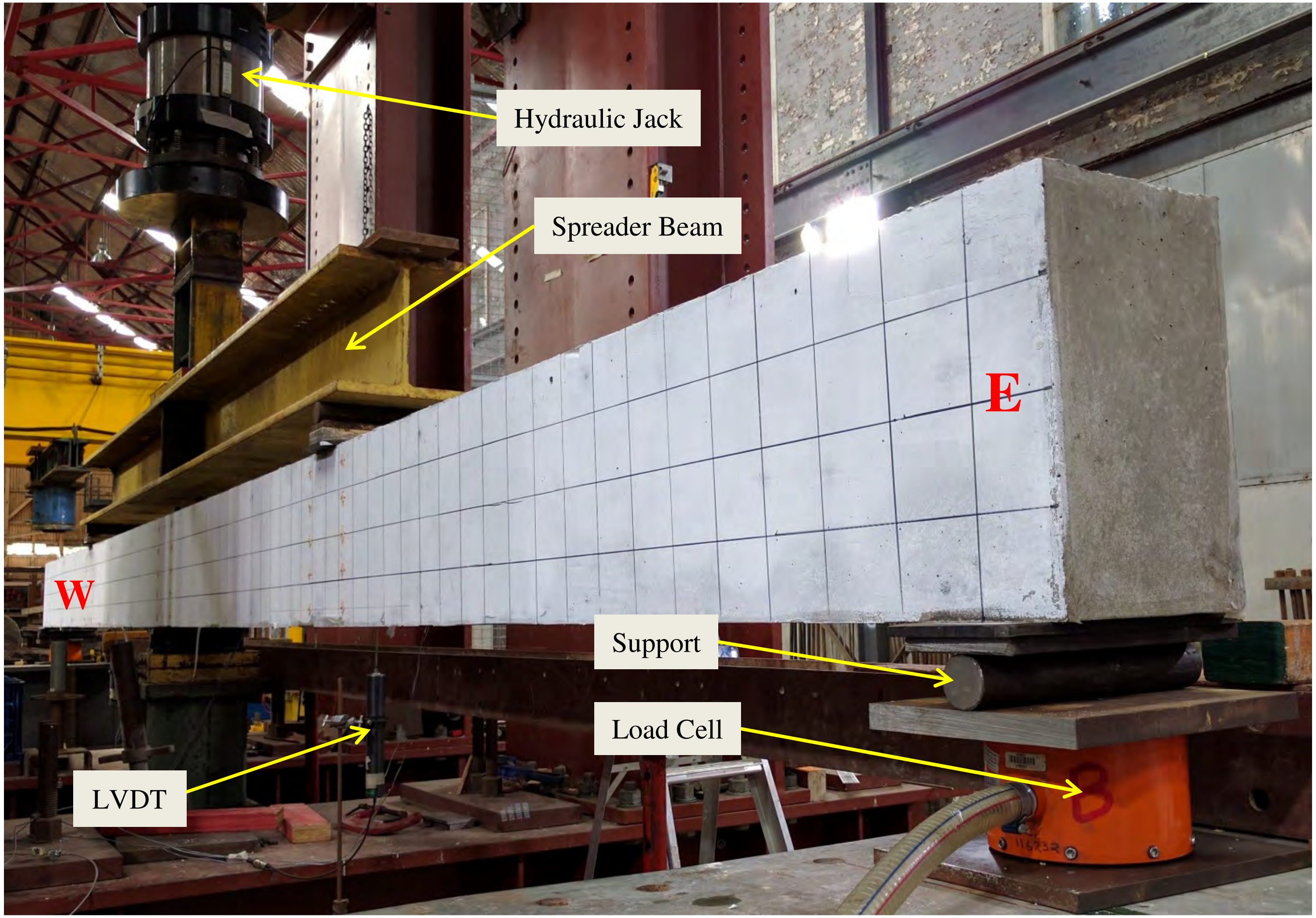

Figure 3.10: Experimental setup (E = East; W = West).

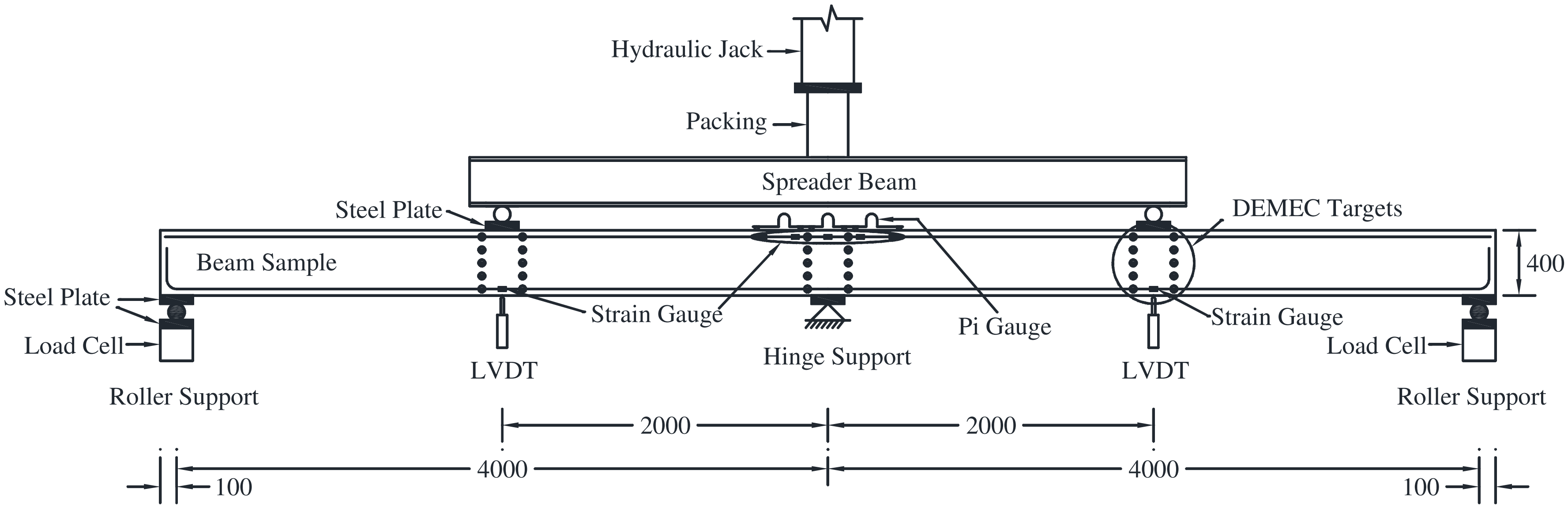

Figure 3.11: Schematic outline of the experimental setup and instrumentation.

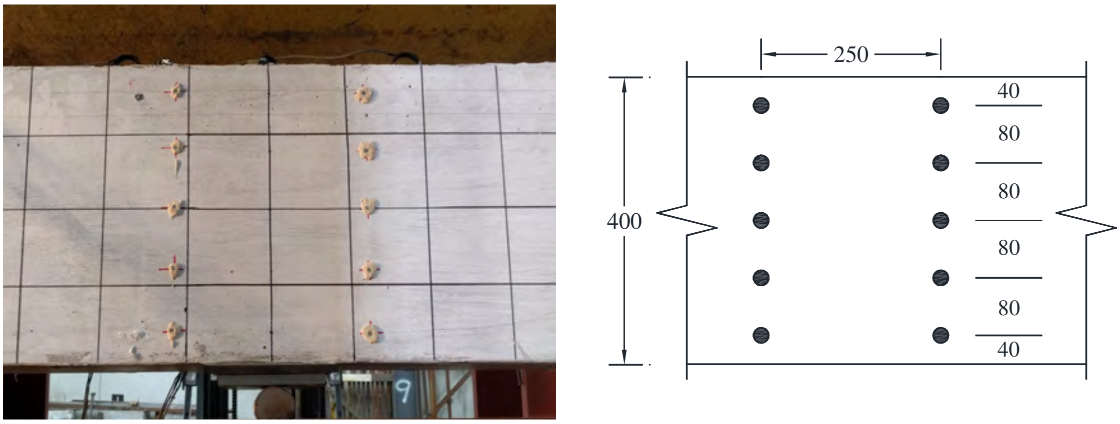

(a)

(b)

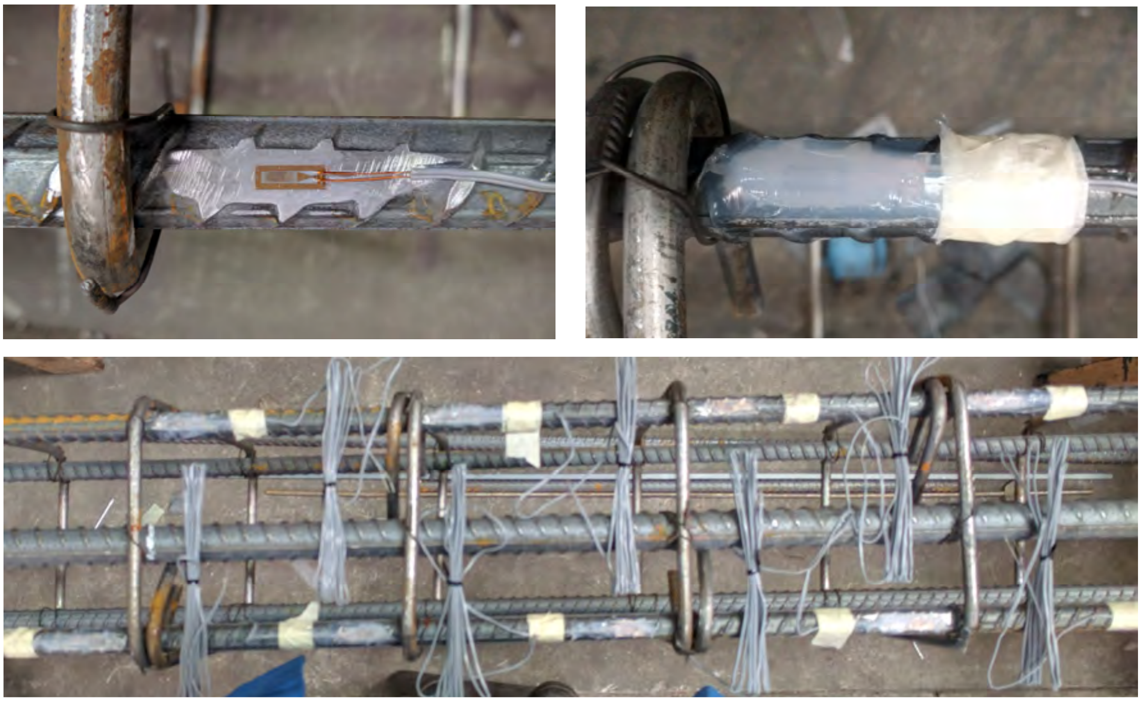

(c)

Figure 3.12: Instrumentation – (a) Demec targets; (b) Pi-gauges; (c) installation of strain gauges.

3.2.4 Testing procedure

The beam specimens were tested under monotonically increasing displacement-control load at a rate of 0.50 mm/min up to peak load. After the peak load was attained, the loading rate was increased to 1 mm/min. At every 4 mm displacement increment, up to a displacement of 24 mm, the loading was paused to mark the progress of cracks and measure the concrete strains at the mid-spans and intermediate support sections. Testing was continued to a deflection of 50 mm or failure, whichever occurred first. The applied load, support reactions, mid-span deflection, strain gauge readings and Pi-gauge readings were recorded via data logger continuously throughout the test.

3.3 Results and discussion

3.3.1 Behaviour under load

The total load on each span versus mid-span deflection curves for the tested specimens in Series A are shown in Figure 3.13. The total load on the beam includes the load applied by the hydraulic actuator, the weight of the packing (11.7 kN) and spreader beam (7.1 kN), and the self-weight of the beam (2.3 kN/m).

For the specimens in Series A, first cracking occurred at the intermediate support. The cracking was determined by the sudden change of the strain values measured by the Pi-gauges. Cracking then continued both in the intermediate support and mid-span regions until the yielding of reinforcement at the mid-spans. The yielding of reinforcing bars was determined from the strain values measured by the strain gauges (see Figure 3.14). In the load versus reinforcing bar strain graphs, the onset of yielding was taken as the point where the strain in steel bars exceeded their measured yield strain (i.e., $\varepsilon_{sy} = 0.00265$ for N20 bars and $\varepsilon_{sy} = 0.00275$ for N28 bars). As loading continued, a hinge formed in the vicinity of the mid-span in the critical member (see Figures 3.14 and 3.15). The final defining event was the yielding of reinforcement and the formation of a second plastic hinge over the intermediate support (see Figures 3.14 and 3.15). The load continued to increase slowly until the peak load, which was attributed to strain hardening of the reinforcement. Noting that the strain gauges failed at strains less than 1.25%, the strain gauges could not capture the complete hardening of the reinforcing bars.

Specimens B30(−30) and B60(−30) maintained the peak load up to a deflection of 50 mm. Specimen B00(−30) failed in a shear-tension mode shortly after reaching the peak load, with the formation of a major shear crack (see Figure 3.16). Post analysis of the results indicates that the shear capacity of the specimen was exhausted before crushing of the compressive concrete, defining the ultimate failure mechanism.

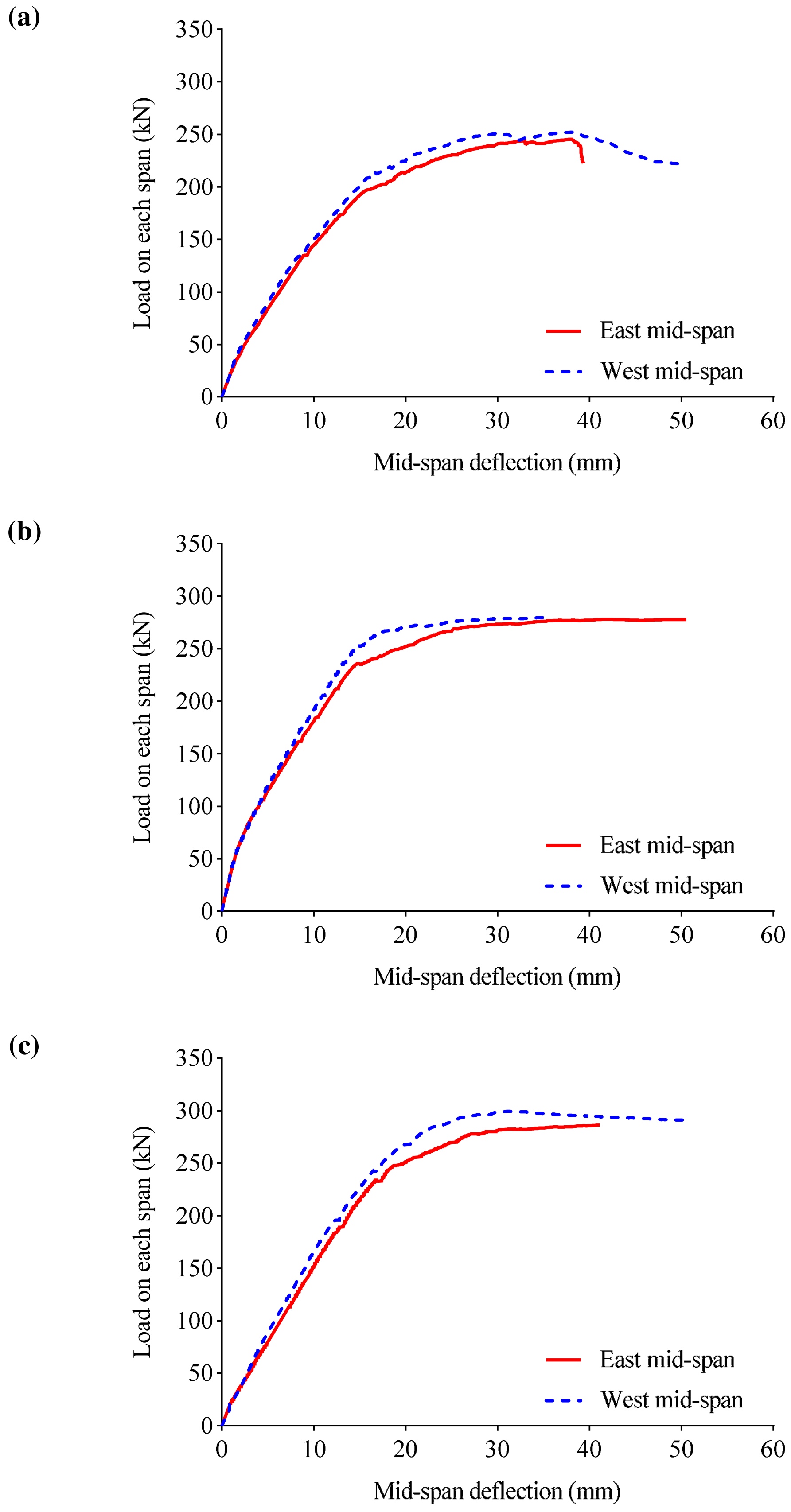

Figure 3.13: Load versus mid-span deflection for Series A specimens - (a) B00(−30), (b) B30(−30) and (c) B60(−30).

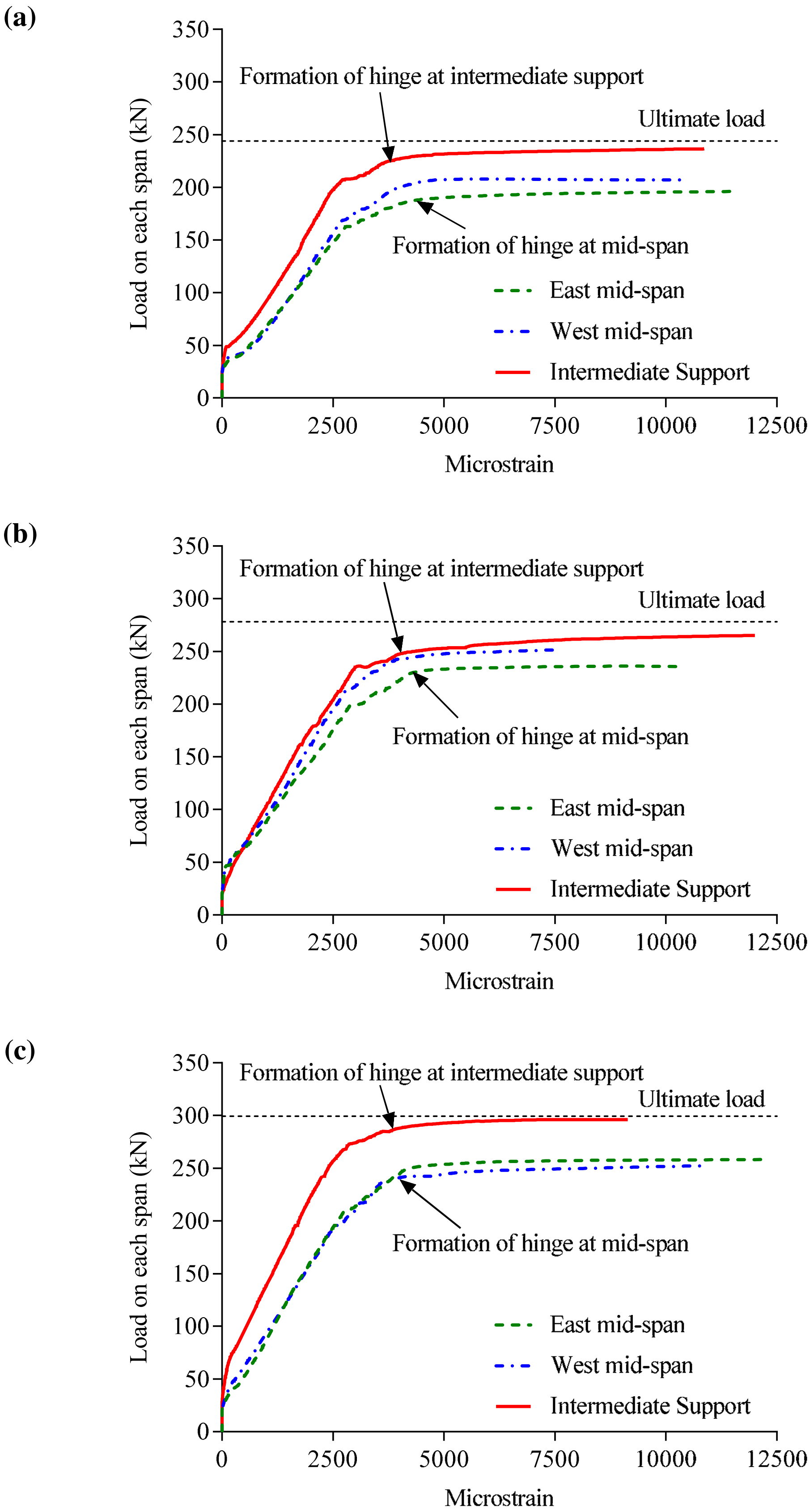

Figure 3.14: Load versus strain of reinforcing bars for Series A specimens - (a) B00(−30), (b) B30(−30) and (c) B60(−30).

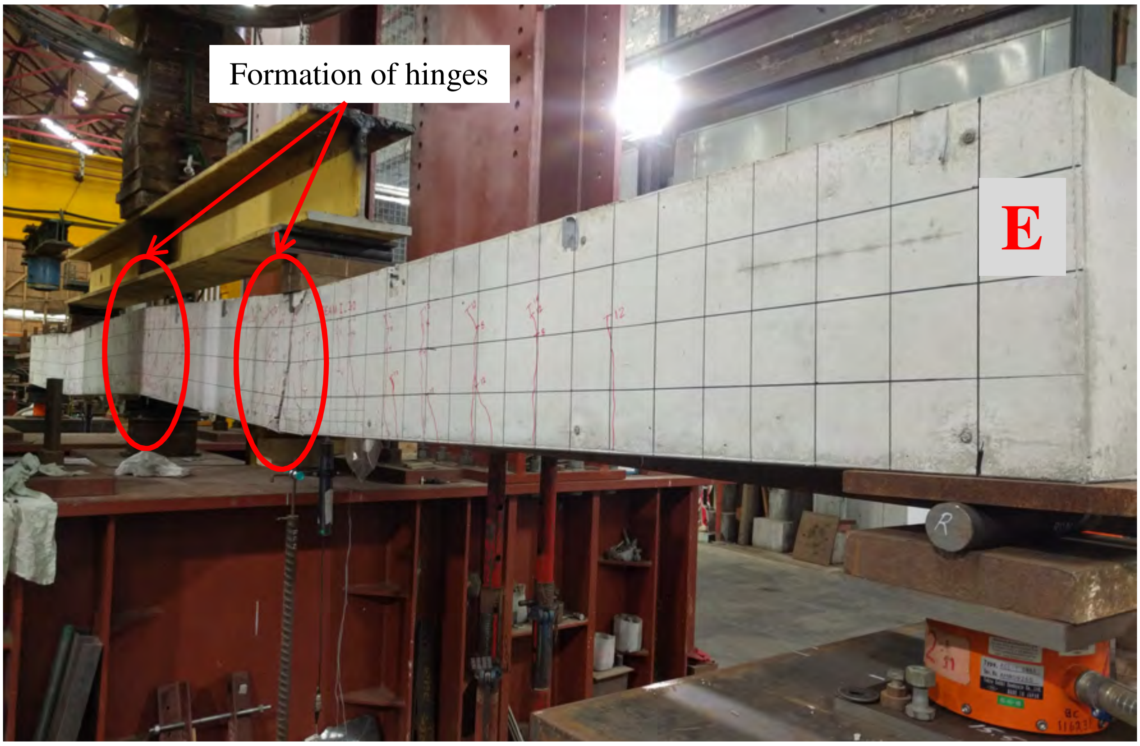

Figure 3.15: Representative picture of the formation of plastic hinges for specimens in Series A.

Figure 3.16: Formation of shear crack in specimen B00(–30).

The load versus mid-span deflection and load versus strain of reinforcing bars at the critical sections for the specimens in Series B are shown in Figures 3.17 and 3.18, respectively. For the specimens in Series B, after cracking over the intermediate support, cracking developed both over the intermediate support and at the mid-span regions of the beams. First reinforcement yielding occurred over the intermediate support (see Figure 3.18), and a plastic hinge formed in the vicinity of the intermediate support (see Figure 3.18). The final defining event was the yielding of reinforcement and formation of second hinge in the critical mid-span (see Figure 3.18), followed by a period of reinforcement strain hardening before attainment of the peak load. Noting that the strain gauges failed at strains less than 1.25%, the strain gauges could not capture the complete hardening of the reinforcing bars.

A summary of the loads and corresponding mid-span deflections at different stages of loading (i.e. the formation of first crack, yielding of tensile reinforcement and peak state) are provided in Table 3.3. A comparison of load versus mid-span deflection curves of the beams is shown in Figure 3.19. Of the two spans of the beams, the span where the critical mid-span hinge formed, providing the mechanism was considered in the analysis. The loads and corresponding mid-span deflections at the formation of first crack, yielding of tensile reinforcement and peak are also marked on the graph.

From the figure, we see that the inclusion of steel fibres increased the load-carrying capacity of the beams. The peak load increased by 12–14% for fibre dosage of 30 kg/m^3 and 12–23% for fibre dosage of 60 kg/m^3. For the specimens in Series B, increasing the fibre dosage from 30 kg/m^3 to 60 kg/m^3 did not increase the capacity.

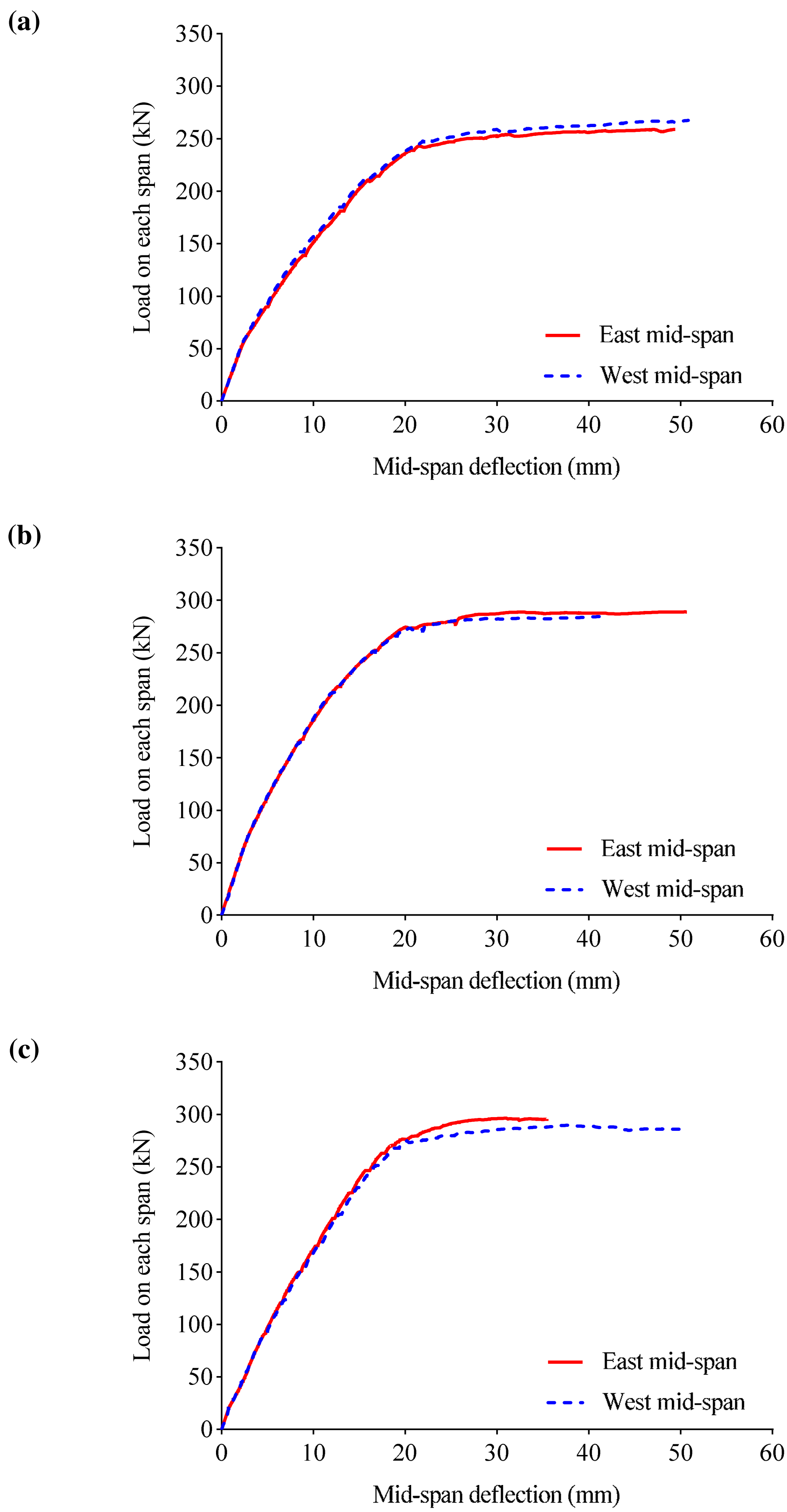

Figure 3.17: Load versus mid-span deflection for Series B specimens - (a) B00(+30), (b) B30(+30) and (c) B60(+30).

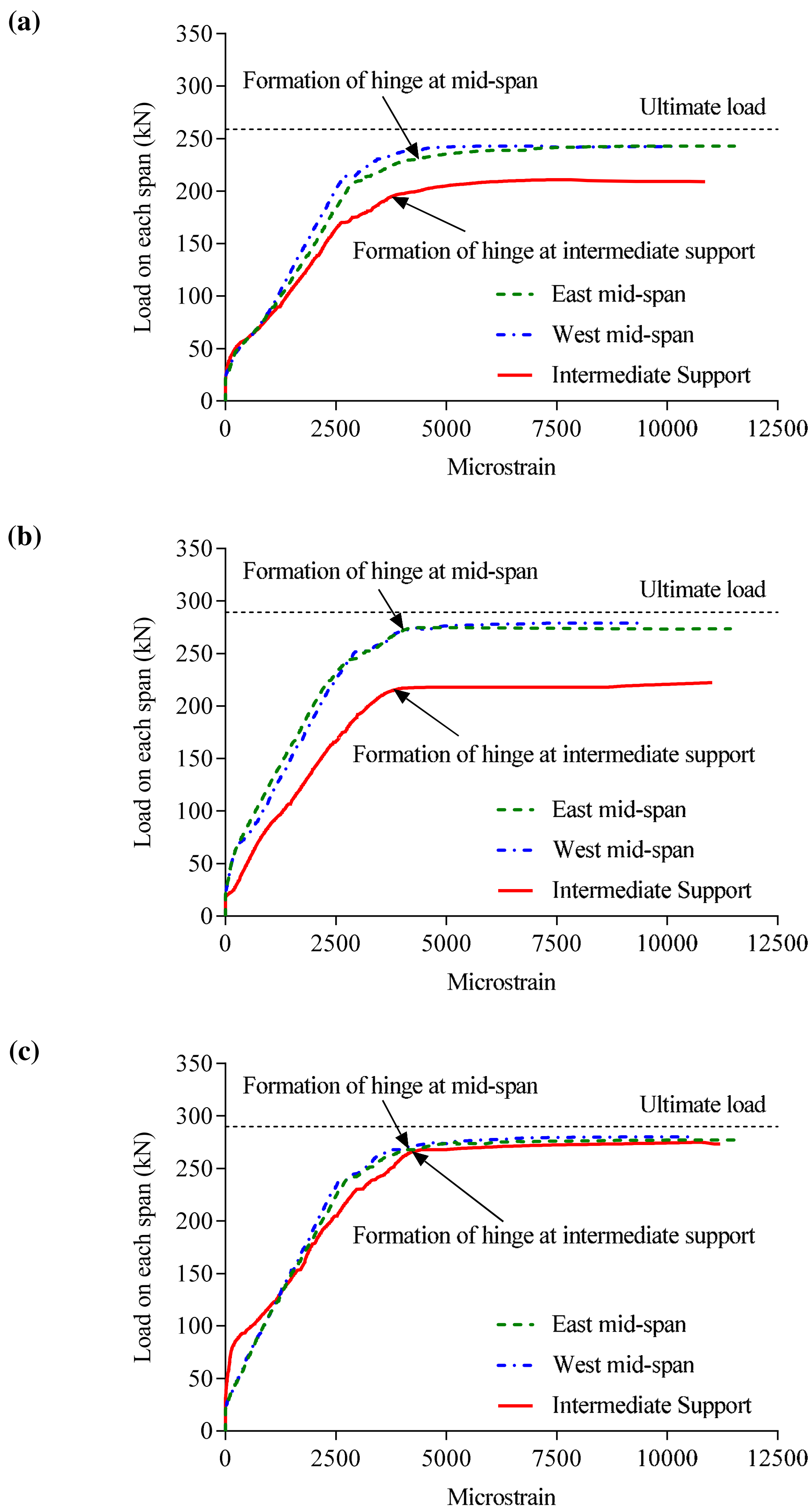

Figure 3.18: Load versus strain of reinforcing bars for Series B specimens - (a) B00(+30), (b) B30(+30) and (c) B60(+30).

Table 3.3: Summary of results.

Series	Specimen	Cracking		First yield		Second yield		Peak		At deflection = 40 mm
		P_{cr} (kN)	Δ_{cr} (mm)	P_{y1} (kN)	Δ_{y1} (mm)	P_{y2} (kN)	Δ_{y2} (mm)	P_p (kN)	Δ_p (mm)	P_{40} (kN)
A	B00(−30)	48.8	2.44	162.6	11.80	207.8	18.77	243.9	32.7	-
	B30(−30)	56.4	1.62	199.4	11.48	235.8	15.37	278.1	41.7	277.9
	B60(−30)	64.3	3.56	195.2	12.34	262.1	18.91	299.2	31.2	294.8
B	B00(+30)	47.2	2.00	170.0	11.93	208.4	15.68	258.8	49.4	258.8
	B30(+30)	42.7	1.61	173.0	9.12	244.1	15.64	289.2	50.0	289.2
	B60(+30)	51.1	2.52	223.9	14.28	236.9	15.47	289.7	37.9	288.8

Notes: 1. P_{cr}, P_{y1}, P_{y2}, P_p and P_{40} are loads on each span corresponding to cracking of the concrete, at first yielding of the reinforcement, at second yielding of the reinforcement, at the peak load and at a deflection of 40 mm.

2. Δ_{cr}, Δ_{y1}, Δ_{y2} and Δ_p are deflections at mid-span corresponding to cracking of the concrete, at first yielding of the reinforcement, at second yielding of the reinforcement and at the peak load.

(a)

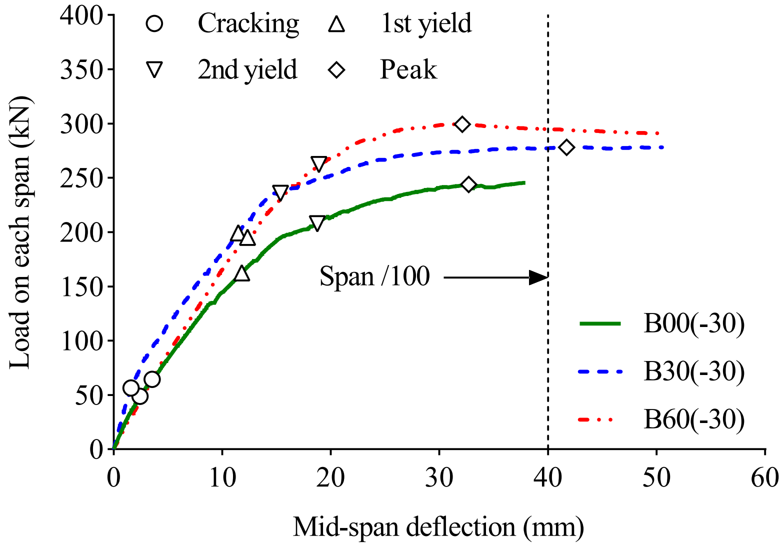

(b)

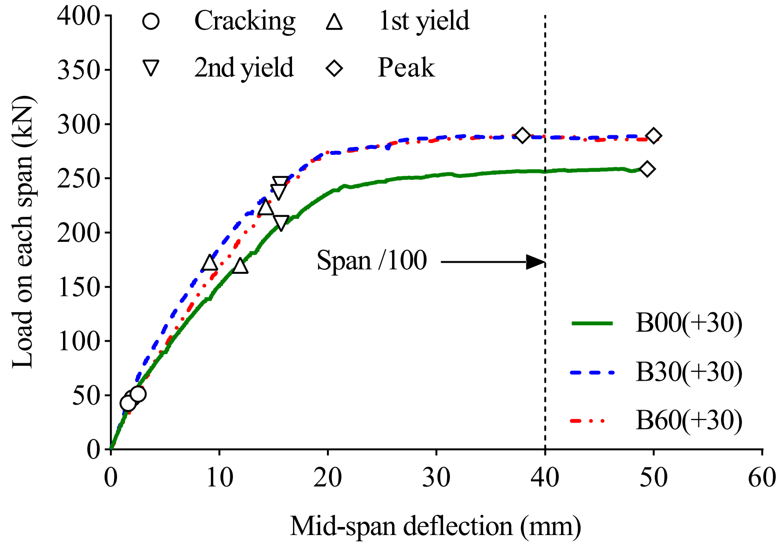

Figure 3.19: Comparison of load versus mid-span deflection for (a) Series A and (b) Series B specimens.

3.3.2 Cracking behaviour

During the tests, the cracks were marked at deflection intervals of 4 mm to establish the patterns of cracks at different stages of loading (see Figure 3.20). The crack patterns at the mid-span and intermediate support (i.e. at the location of the formation of plastic hinges) for Series A and Series B specimens are shown in Figures 3.21 and 3.22, respectively. Pictures of crack patterns for the tested specimen are provided in Appendix B (see Figures B1 to B6). The cracks were distributed evenly along the length of the beams. In specimen B00(−30), a major shear crack developed near to the mid-span. It is evident from Figures 3.21 and 3.22 that the inclusion of steel fibres increased the number of cracks and decreased the crack spacing.

The crack widths over the intermediate support (negative moment) determined by the Pi-gauges are plotted in Figure 3.23, noting that the gauges were removed at 24 mm of displacement to prevent their damage during the final stages of testing. From the figure, it is evident that the inclusion of steel fibres decreased the crack width over the intermediate support for the specimens in Series B (moment redistribution from intermediate support to mid-span). However, for the specimens in Series A (moment redistribution from mid-span to intermediate support), the inclusion of steel fibres did not have a significant effect on the crack width over the intermediate support.

Figure 3.20: Representative picture of crack patterns for specimen B00(−30).

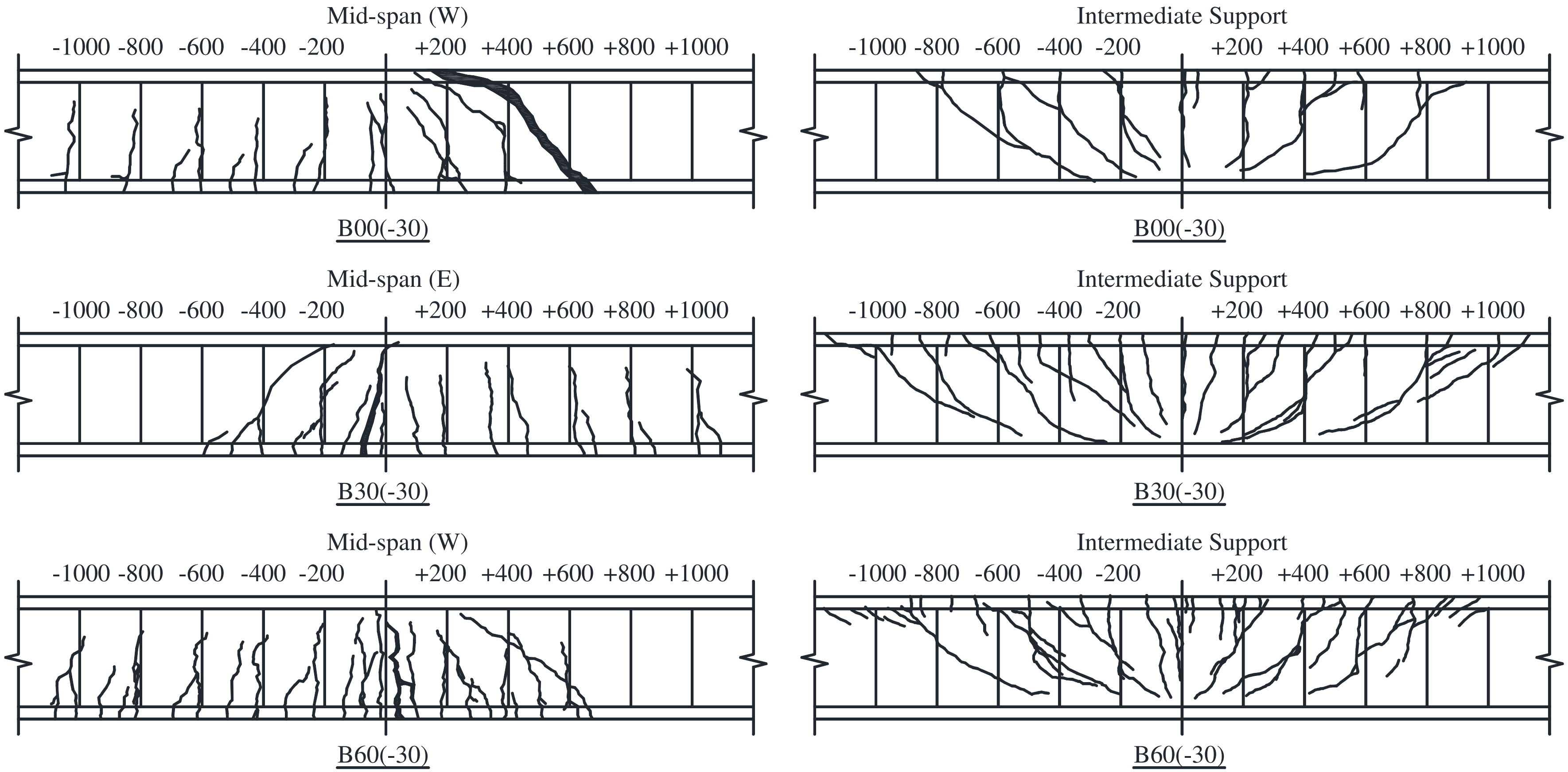

Figure 3.21: Crack patterns for Series A specimens (E = East; W = West).

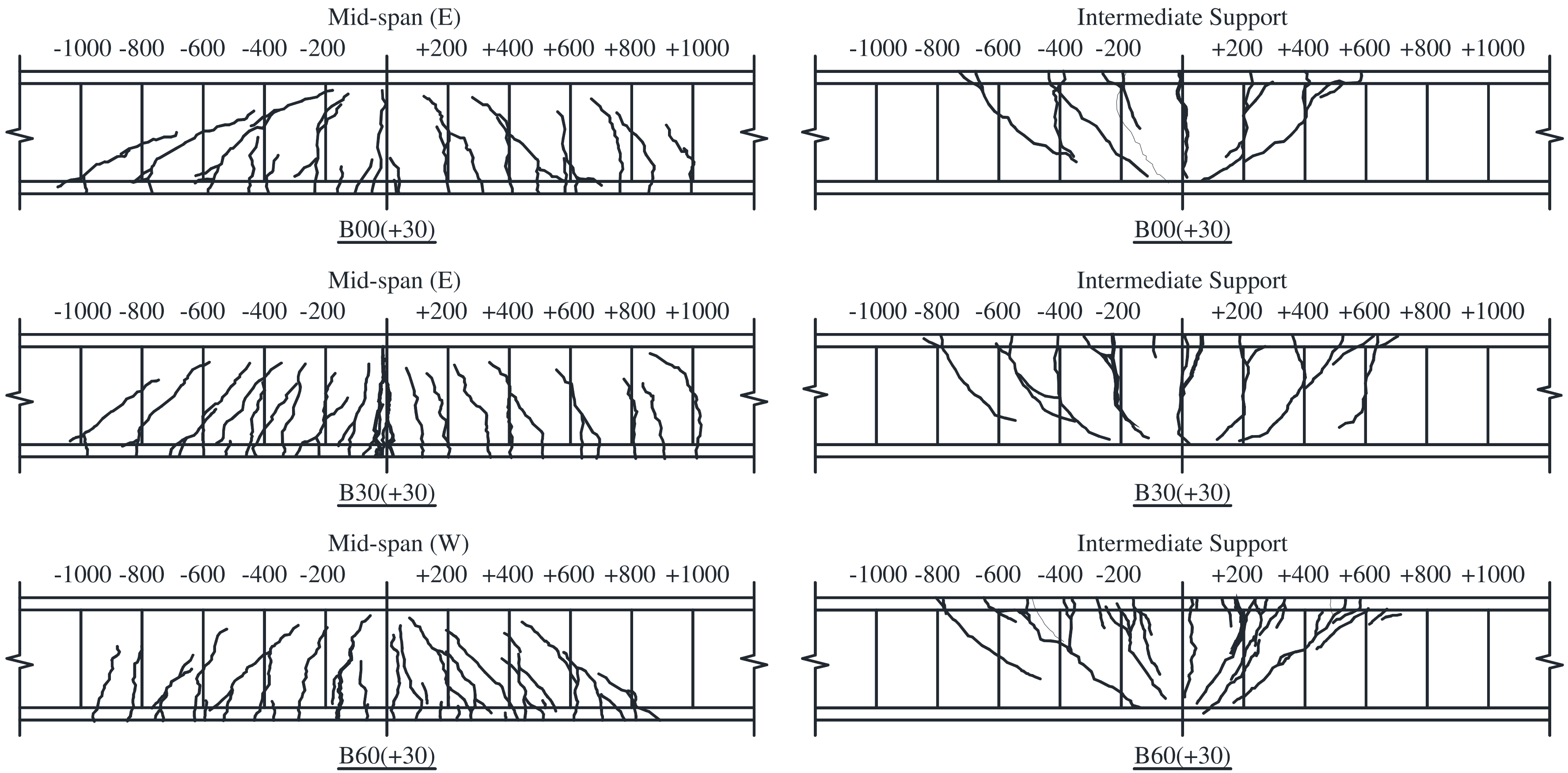

Figure 3.22: Crack patterns for Series B specimens (E = East; W = West).

(a)

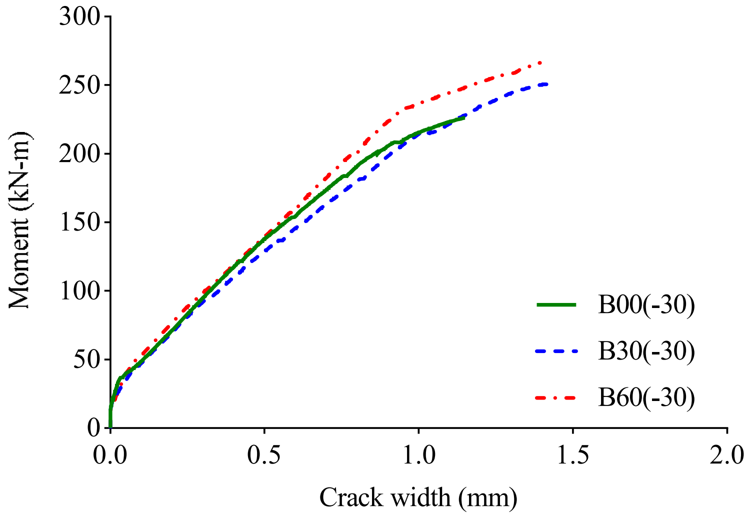

(b)

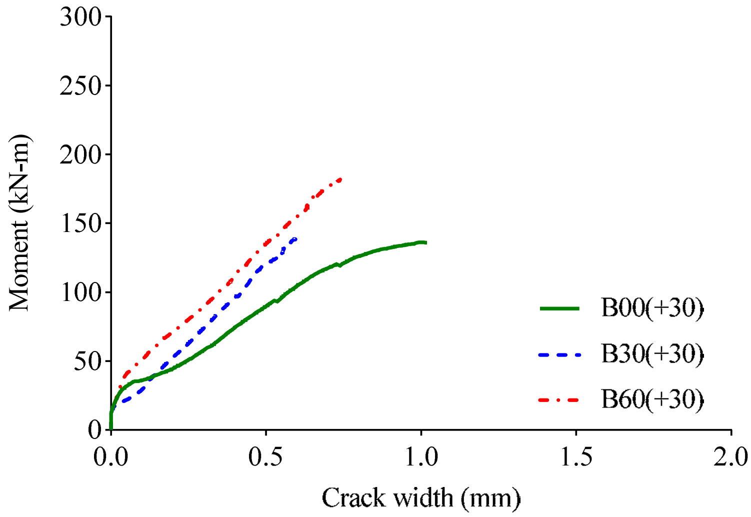

Figure 3.23: Moment versus crack width at intermediate support for (a) Series A and (b) Series B specimens (up to deflection = 24 mm).

3.3.3 Curvature

The curvature (κ) values at the intermediate support and mid-spans of the specimens are determined from the Demec strain gauge measurements by:

$$\kappa = \left(DR_{bot} - DR_{top}\right)/y \tag{3.1}$$

where DR_{bot} and DR_{top} are the Demec readings at the bottom and top reinforcement level, respectively, and y is the distance between the bottom and top gauges. The Demec strain values are provided in Appendix B (see Figures B7 to B12). The moment versus curvature diagrams are plotted in Figure 3.24, noting that the Demec readings were suspended after 24 mm of displacement for safety; the sequence of the formation of plastic hinges, discussed above, is evident from the moment versus curvature diagrams.

Figure 3.25 shows a comparison of the experimental and theoretical moment versus curvature curves for the beams in Series A. The theoretical curvature (κ) values were calculated at key points (i.e. cracking, yielding and ultimate moments) from:

$$\kappa = \left(\varepsilon_{bot} - \varepsilon_{top}\right)/D \tag{3.2}$$

where ε_{bot} and ε_{top} are the theoretical strain values at extreme fibres (bottom and top) of the beam specimens and D is the depth of the specimen. The theoretical strain values at the yielding of reinforcement and at the ultimate load were determined using rectangular stress blocks for the concrete in compression and SFRC in tension as per AS 3600:2018 [34] model. Figure 3.25 shows that the theoretical values of moment-curvatures determined at the key points are close to the experimental ones.

(a)

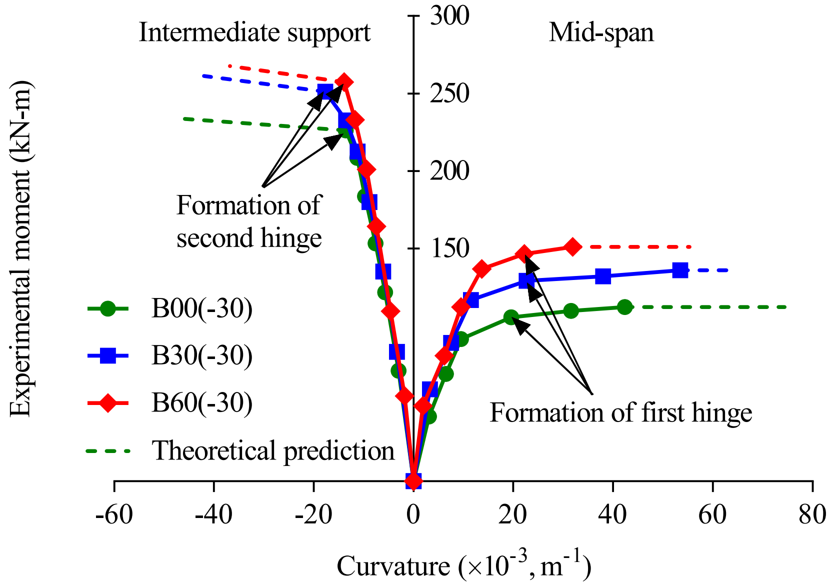

(b)

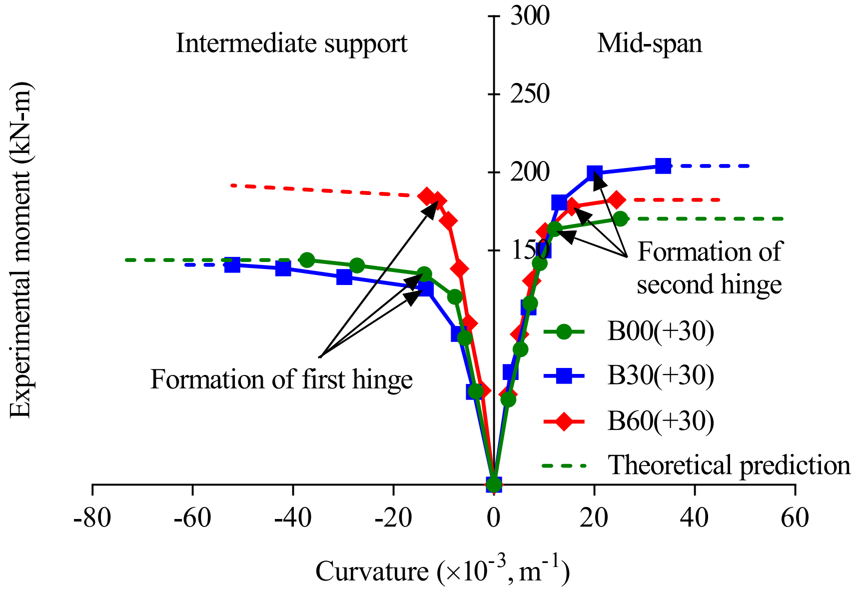

Figure 3.24: Moment versus curvature for (a) Series A and (b) Series B specimens (up to deflection = 24 mm).

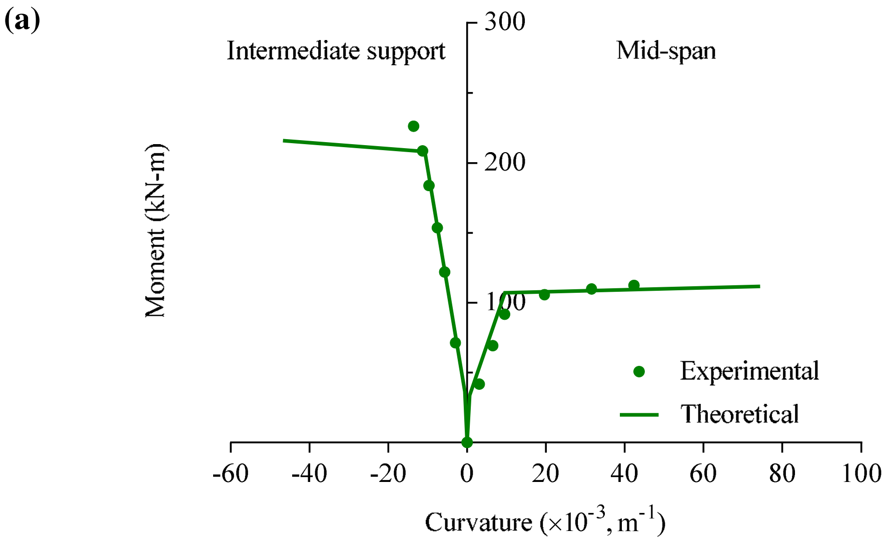

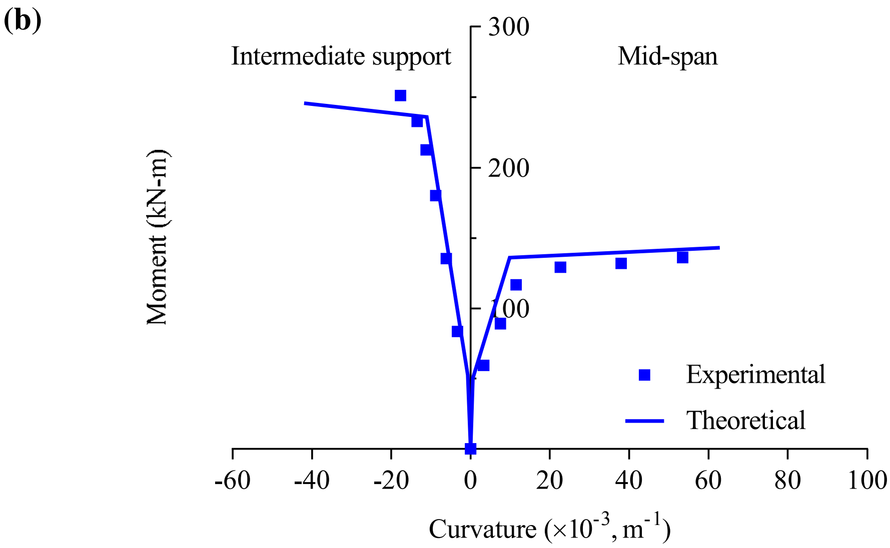

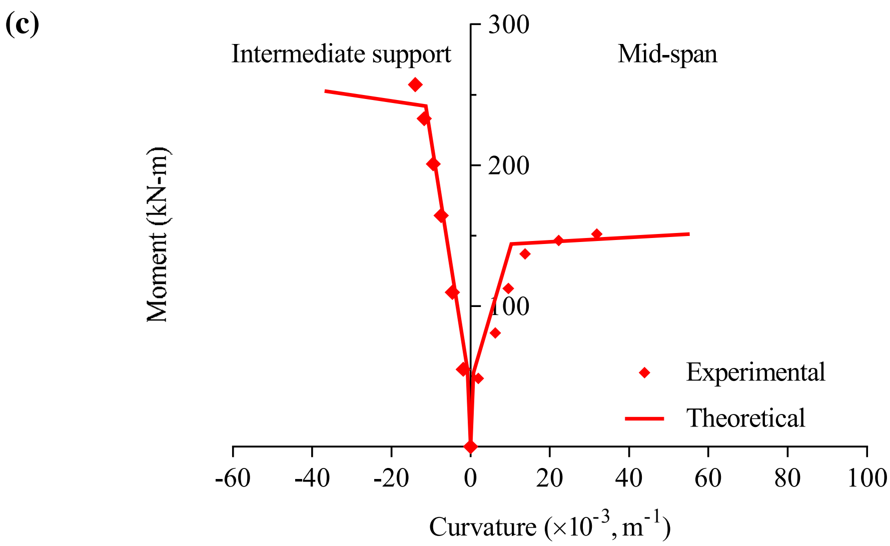

Figure 3.25: Comparison of experimental and theoretical moment versus curvature for the beams in Series A (a) B00(−30), (b) B30(−30) and (c) B60(−30).

3.3.4 Ductility

The ductility of a structure can be evaluated quantitatively in terms of deflection or work done. The ductility factor based on deflection (μ_{Δ}) is the ratio of ultimate mid-span deflection (Δ_u) to the mid-span deflection at the yielding of reinforcement (second yielding in the case of continuous members with moment redistribution), i.e. $\mu_{\Delta} = \Delta_u/\Delta_{y2}$ [136]. The ultimate deflection can be considered as the point at which the load decreases sharply [137, 138], or drops to 80% of the peak load [139, 140]. The ductility factor based on work done is the ratio of the total work done up to the ultimate load (W_u) to the work done up to the second yielding of reinforcement (W_{y2}) for continuous members with moment redistribution, i.e. $\mu_w = W_u/W_{y2}$ [141]. The area under the load-deflection curve up to the second yielding of reinforcement is defined as W_{y2}; similarly, the area under the load-deflection curve up to the ultimate load is W_u.

In this study, the specimens were tested up to a deflection of 50 mm (span/80) to avoid potential fracture of tensile reinforcing bars. A line corresponding to a displacement of span/100 (i.e. 40 mm) is plotted in Figure 3.19. This point is considered as corresponding to sufficient ductility for observation of serious distress in the member [119]. Although for specimens B00(-30), B60(-30) and B60(+30), the point corresponding to the peak (ultimate) load occurred slightly before the span/100 deflection, with the exception of beam B00(−30) that failed in a shear mode after reaching its flexural strength (i.e. diagonal-tension failure mechanism after yielding of the tensile steel), the load in the beams did not fall below 99% of their load at peak at the deflection of span/100. Thus, it is concluded that, with the exception of specimen B00(−30), the beams were highly ductile. To provide an indication on the ductility of the tested specimens, the value of the deflection of span/100 (i.e. 40 mm) was used as the ultimate deflection to calculate the ductility factors, and the ductility factor values are shown in Table 3.4. A value of ductility factor greater than 2.0 indicates good ductility [141], so all R-SFRC beams tested were indeed ductile.

Table 3.4: Ductility factor values.

Series	Specimen	μ_{Δ}	μ_{w}
A	B00(−30)	1.7	2.3
	B30(−30)	2.6	3.9
	B60(−30)	2.1	3.2
B	B00(+30)	2.6	4.2
	B30(+30)	2.6	4.0
	B60(+30)	2.6	4.4

3.3.5 Moment redistribution

Moment redistribution is the ability of a member to transfer forces from a section that is critically loaded to others that are not, and the transfer continues until multiple plastic hinges formed to develop a failure mechanism. As two full plastic hinges formed in all tests, one at the mid-span of the critical member and one over the intermediate support, before the peak (ultimate) load was reached, the specimens achieved their full moment redistribution capacities.

The degree of moment redistribution at a section of a flexural member is usually calculated as the ratio of the deviation of the experimental moment (M_{exp}) from the theoretical linear-elastic moment (M_{el}) with respect to the theoretical linear-elastic moment [142]. This is termed as theoretical moment redistribution (η_{theo}) and given by:

$$\eta_{theo}(\%) = \frac{M_{el} - M_{exp}}{M_{el}} \times 100\% \quad (3.3)$$

Figure 3.26 shows a comparison of the experimental load versus bending moment diagrams at the intermediate support with the theoretical load versus bending moment predicted by the linear-elastic analysis. The nonlinear behaviour and deviation from the linear-elastic behaviour after the cracking of concrete are evident from Figure 3.26. It is seen that the experimental moment followed the linear-elastic moment at the earlier stages of the loading process. After the formation of cracks, the experimental moment started deviating from the linear-elastic moment. As loading continued, the crack formation stabilised and the rate of change in bending moment became almost constant. The experimental moment started deviating again from the linear-elastic moment after the yielding of reinforcement and formation of first plastic hinge. The applied load continued to increase until the formation of second plastic hinge, which theoretically constituted the collapse mechanism. As noted above, a small increase in load was attained due to the onset of strain hardening in the reinforcing steels.

The deviation of the experimental moment from the linear-elastic behaviour at the earlier stage of loading (after the formation of cracks and before the yielding of reinforcement) is due to continual adjustments in stiffnesses as cracks form and the ratios of the load distributed to each support continually adjust. Therefore, the calculation of moment redistribution with respect to the linear-elastic moment incorporates the distribution of forces due to cracking.

(a)

(b)

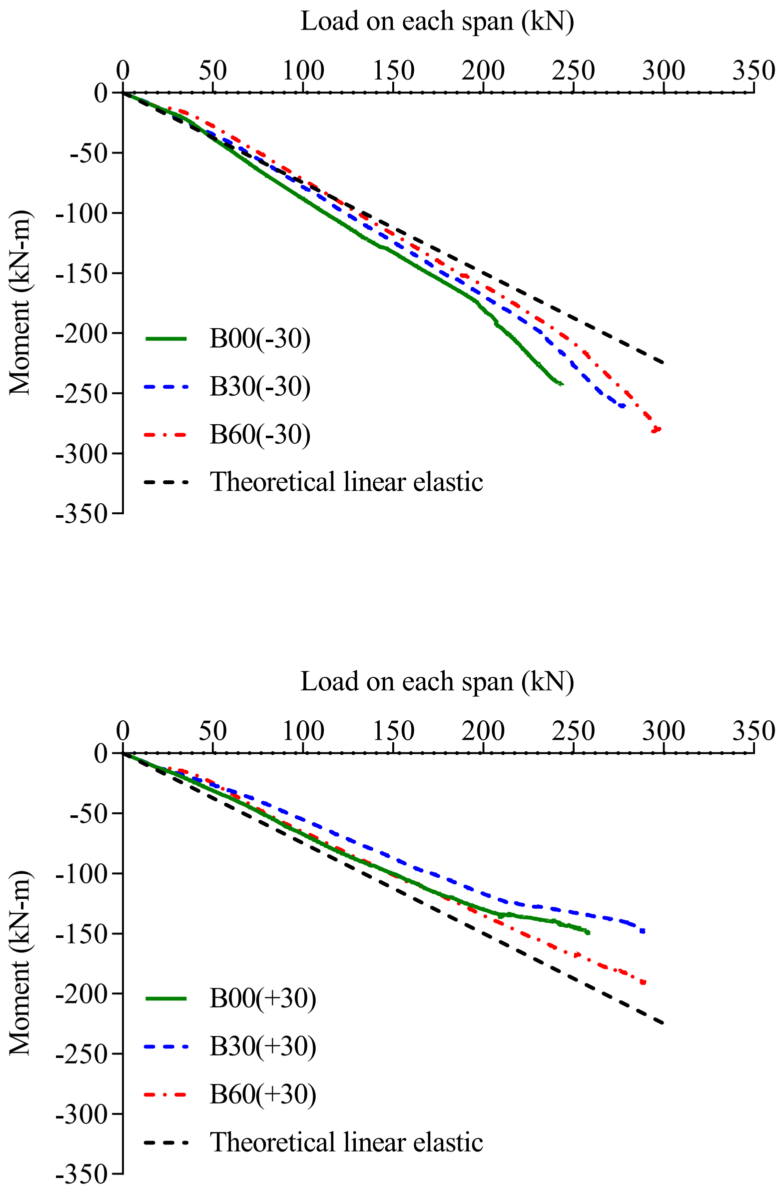

Figure 3.26: Moment versus load at the intermediate support for (a) Series A and (b) Series B specimens.

The "actual" (plastic) moment redistribution starts when the critical section of a member reaches its capacity and a plastic hinge is formed, i.e. after the first yielding of reinforcement at the critical section of the member. The actual moment redistribution (η_{actual}) is determined from the ratio of support moment to load at the time of measurement of first yield, to that attained of the full formation of the second plastic hinge and is given by:

$$\eta_{actual}(\%) = \frac{(M/P)_{y1} - (M/P)_{exp}}{(M/P)_{y1}} \times 100\% \tag{3.4}$$

Table 3.5 shows a summary of the moment at intermediate support to load on each span at the key points from first yield. Figure 3.27 shows a comparison of theoretical and actual moment redistribution for specimen B00(-30). The difference between the values of "actual" and "theoretical" moment redistribution is due to their different starting points.

Table 3.5: Ratios of moment at intermediate support to load on each span.

Series	Specimen	Linear elastic $(M/P)_{LE}$	Experimental $(M/P)_{exp}$		
			First yield $(M/P)_{y1}$	Second yield $(M/P)_{y2}$	Peak $(M/P)_{p}$
A	B00(-30)	-0.75	-0.877	-0.919	-0.984
	B30(-30)		-0.857	-0.884	-0.937
	B60(-30)		-0.817	-0.879	-0.962
B	B00(+30)		-0.662	-0.637	-0.569
	B30(+30)		-0.589	-0.543	-0.518
	B60(+30)		-0.683	-0.680	-0.652

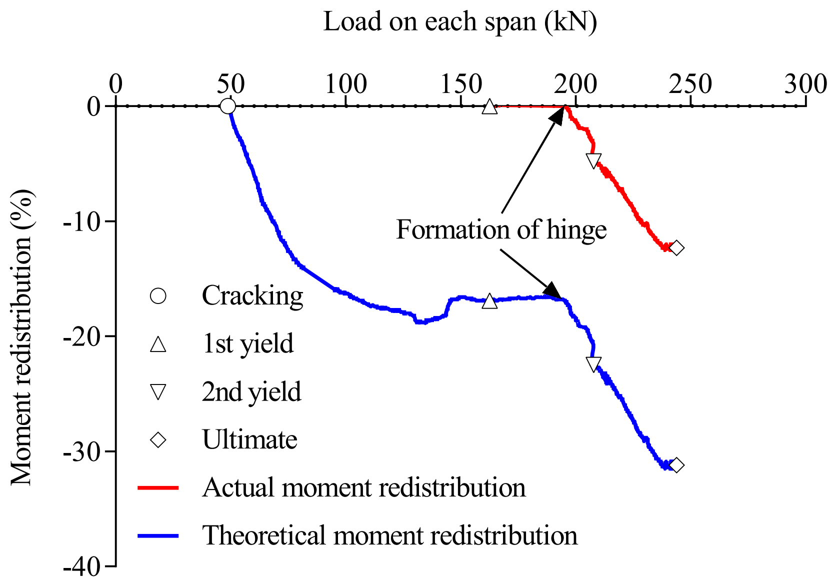

Figure 3.27: Comparison of theoretical and actual moment redistribution for specimen B00(−30).

The moment redistributions at the key points from first yield are presented in Table 3.6 and Figure 3.28. For the specimens in Series A, yielding of the reinforcement at the mid-span of the critical member resulted in negative moment redistribution (from mid-span to intermediate support). After the yielding of reinforcement at mid-span, the degree of moment redistribution increased slightly until the formation of first hinge at mid-span. After the formation of first hinge, rapid strain development led to the yielding of negative reinforcement at the intermediate support and formation of second plastic hinge. A sharp increase in the amount of redistributed moment is a characteristic of this stage. A similar pattern for specimens in Series B was observed with the yielding of tensile reinforcement at the intermediate support resulting in positive moment redistribution (from intermediate support to mid-span).

Specimens B00(−30), B30(−30) and B60(−30) (i.e. Series A) achieved −31.2%, −24.9% and −28.2% of moment redistribution, respectively, at the peak load based on the theoretical linear-elastic moment. The actual (plastic) moment redistributions at peak load after first yield were −12.3%, −9.3% and −17.7%. As described above, the difference between the theoretical moment redistribution and the actual moment redistribution is due to the formation of cracks and the progressive adjustment to stiffness in different regions of the member.

Specimens B00(+30), B30(+30) and B60(+30) (i.e. Series B) achieved 24.1%, 30.9% and 13.1% of moment redistribution, respectively, at the peak based on theoretical linear-elastic analysis results. The actual moment redistributions were 14.0%, 12.0% and 4.5%, respectively.

Table 3.6: Amount of moment redistribution (in %) at different stages of loading.

Series	Specimen	First yield		Second yield		Peak	
		η_{theo}	η_{actual}	η_{theo}	η_{actual}	η_{theo}	η_{actual}
A	B00(−30)	-16.9	0.0	-22.5	-4.8	-31.2	-12.3
	B30(−30)	-14.3	0.0	-17.9	-3.1	-24.9	-9.3
	B60(−30)	-9.0	0.0	-17.2	-7.5	-28.2	-17.7
B	B00(+30)	11.7	0.0	15.0	3.7	24.1	14.0
	B30(+30)	21.5	0.0	27.5	7.7	30.9	12.0
	B60(+30)	9.0	0.0	9.3	0.4	13.1	4.5

Notes: 1. $\eta_{theo}(\%) = \frac{(M/P)_{LE} - (M/P)_{exp}}{(M/P)_{LE}} \times 100\%$

2. $\eta_{actual}(\%) = \frac{(M/P)_{y1} - (M/P)_{exp}}{(M/P)_{y1}} \times 100\%$

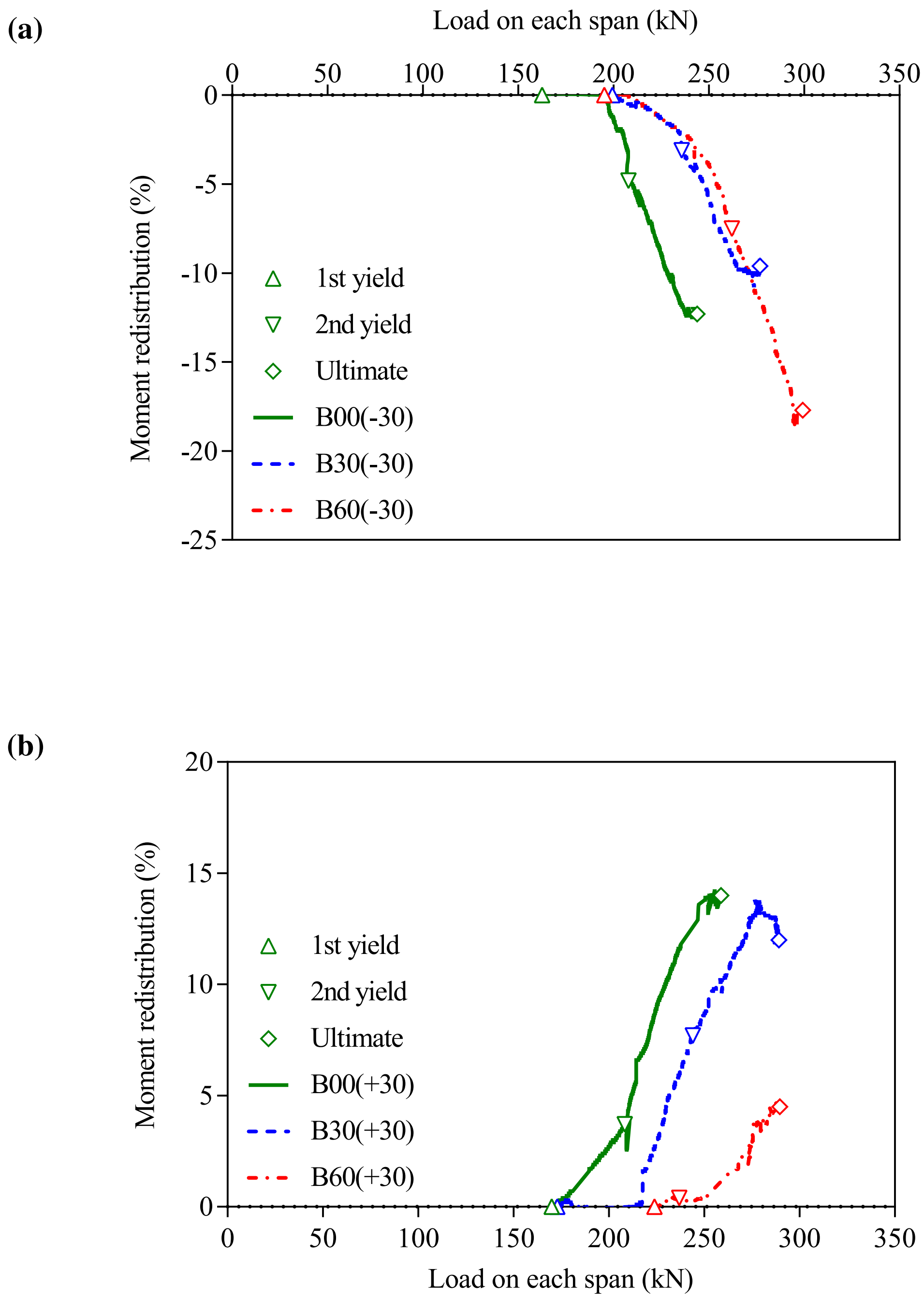

Figure 3.28: Actual moment redistribution versus load for specimens in (a) Series A and (b) Series B.

Of all specimens tested, B60(+30) had the lowest plastic moment redistribution demand. The bending moment versus deflection (Figure 3.29) and strain versus load (Figure 3.18c) graphs of the beam B60(+30) revealed that for the beam, both the mid-span and intermediate support sections had almost the same bending moment capacity, and the plastic hinges at mid-span and intermediate support formed almost at the same load level. A possible explanation for this is that the steel fibres were not distributed evenly throughout the length of the specimen, and there were more fibres at the intermediate support section than in theory, resulting in an increase in the stiffness and load-carrying capacity at the intermediate support section. This is evidenced by the variability observed in the wash-out test data for the 60 kg/m^3 tests (being 53 ±6 kg/m^3).

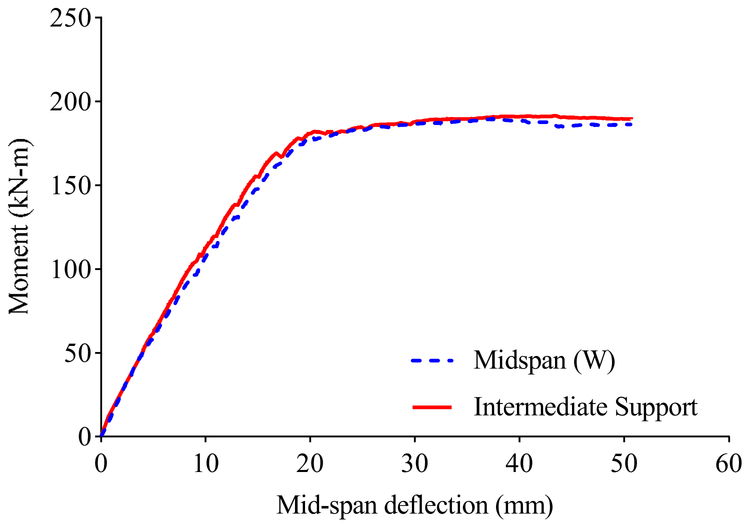

Figure 3.29: Moment versus deflection for specimen B60(+30).

3.4 Conclusions

An experimental study was undertaken to investigate the moment redistribution and post-peak behaviour of R-SFRC continuous beams with tensile reinforcement ratios varied between 0.69% and 1.38%. Two series, with three specimens in each series, of two-span continuous beams were cast and tested under monotonically increasing displacements. The beam specimens were 250 mm wide, 400 mm deep and 8.2 mm long (4.0 mm span). One series was designed for 30% of negative moment redistribution from the linear-elastic condition, the other for 30% of positive moment redistribution. Nominal fibre dosages of 0, 30 and 60 kg/m^3 were considered in each series (average as-cast fibre dosages were 0, 27.3 and 51.7 kg/m^3).

The inclusion of steel fibres increased the load-carrying capacity of the beams. The peak load increased by 12-14% for fibre dosage of 30 kg/m^3 and 12-23% for fibre dosage of 60 kg/m^3. The loads corresponding to the onset of steel yielding and formation of first plastic hinge were also increased by the addition of steel fibres. It was also observed that the crack widths and crack spacings were reduced with the inclusion of the steel fibres, and the number of cracks increased. This observation is consistent with that of previous studies.

The specimens in this study had tensile reinforcement ratios of between 0.69% and 1.38%. For these tests, it was observed that for the specimens in Series A, the addition of steel fibres increased the ductility of the beams over that of similarly reinforced beams without fibres. For the specimens in Series B, since the load did not drop to lower than 99 per cent of the peak load up to a displacement of span/100 (i.e. 40 mm) for any of the specimens, no relative conclusion is drawn in comparing ductility of the R-SFRC beams with the RC beams, other than to say that both the conventionally reinforced concrete beams and the beams with both conventional and steel fibre reinforcement were found to have good ductility for the steel reinforcement ratios tested.

In all tests, two plastic hinges fully formed, one at the mid-span of the critical member and one over the internal support. Thus, it is concluded that the full design moment redistribution of ±30% was achieved in all cases. At peak (ultimate) load, the theoretical moment redistributions based on the theoretical linear-elastic moment were −31.2%, −24.9% and −28.2% for specimens B00(−30), B30(−30) and B60(−30), respectively and 24.1%, 30.9% and 13.1% for specimens B00(+30), B30(+30) and B60(+30), respectively. The actual moment redistributions after first yield were -12.3%, -9.3% and -17.7% for specimens B00(−30), B30(−30) and B60(−30), respectively and 14.0%, 12.0% and 4.5% for specimens B00(+30), B30(+30) and B60(+30), respectively.

The difference between the theoretical moment redistribution, based on linear-elastic theory, and the actual moment redistribution (demand) is due to the influence of cracking and the constant adjustment in stiffnesses of RC members during cracking. The ductility demand in the real system is less than the theoretical elastic demand due to the inelastic realities that occur in reinforced concrete members and structures. This behaviour is consistent for RC beams with and without steel fibres. Therefore, the design of RC and R-SFRC continuous beams for moment redistribution based on elastic analysis has some limitations.

Chapter 4

FLEXURAL PERFORMANCE OF R-SFRC CONTINUOUS SLABS

4.1 Introduction

An experimental study to investigate the moment redistribution capability and post-peak behaviour of R-SFRC two-span one-way slabs with low reinforcement ratios is presented in this chapter. In Chapter 3, the flexural performance of RC and R-SFRC beams having the same amount of tensile reinforcement was compared. However, adding steel fibres increases the flexural capacity, which makes the specimens non-equivalent. In this chapter, the flexural performance of equivalent (same design flexural capacity and the same amount of moment redistribution) RC and R-SFRC slab specimens is compared. The specimens were made equivalent by increasing the amount of tensile reinforcement, with consideration of the predicted (design) fibres' component to flexural strength. The specimens were tested under monotonically increasing displacement-controlled load up to the failure of the specimens. The post-peak behaviour and ductility of equivalent RC and R-SFRC slabs are compared. The laboratory test results are further analysed for the ability of R-SFRC continuous members with less than 0.4% of tensile reinforcement to redistribute moments, and the effect of low reinforcement ratios and moment redistribution on the ductility of R-SFRC continuous members are also discussed.

4.2 Experimental investigation

4.2.1 Description of test specimens

The experimental study consisted of six full-scale two-span continuous slabs. The variables within different test specimens are shown in Table 4.1. Figure 4.1 shows the geometry, loading, boundary conditions and arrangement of longitudinal and transverse reinforcement for the tested specimens. The clear cover to the reinforcing steel bars was 20 mm and 25 mm at top and bottom, respectively. The specimens are designated as SW(+MR), where 'S' is the member type (Slab), 'W' is the dosage of steel fibres (in kg/m^3) and '(+MR)' is the nominal design value of moment redistribution (from the negative moment at the intermediate support to the positive moments at mid-span).

Table 4.1: Specimen details.

Series	Specimen	Fibre dosage (kg/m^3)	Negative reinforcement at intermediate support (mm^2)	Positive reinforcement at mid-span (mm^2)	Nominal amount of moment redistribution (%)
A	S60(+00)	60 (0.8%)	440 (0.28%)	320 (0.21%)	+00
	S60(+10)		320 (0.21%)	320 (0.21%)	+10
	S60(+20)		320 (0.21%)	440 (0.29%)	+20
	S60(+30)		320 (0.21%)	620 (0.42%)	+30
B	S00(+00)	0	760 (0.51%)	620 (0.42%)	+00
	S00(+30)		620 (0.41%)	910 (0.61%)	+30

The specimens in Series A contained 60 kg/m^3 of steel fibres. The tensile reinforcement ratios varied between 0.21% and 0.42% to provide nominally 0 to 30% redistribution of moment from that of the elastically determined bending moments from the intermediate support to the mid-spans. The flexural strength of the specimens with steel fibres (R-SFRC specimens) was determined assuming the contribution of fibres to the flexural strength based on the rectangular stress block (RSB) model of AS 3600:2018 [34]. In the calculation of the flexural strength of the slab specimens, the compressive strength of concrete, the yield strength of steel and the residual tensile strength of SFRC for 1.5 mm crack opening depth ($f'_{1.5}$) were taken as 32 MPa, 500 MPa and 1.6 MPa, respectively.

The specimens S00(+00) and S00(+30) in Series B were designed to have equivalent flexural strength and moment redistribution to the specimens S60(+00) and S60(+30), respectively. This was done by increasing the amount of tensile reinforcement, with consideration of the predicted fibres' contribution to flexural strength based on the rectangular stress block (RSB) model of AS 3600:2018 [34]. Detail calculations for the design of the slab specimens are provided in Appendix C.

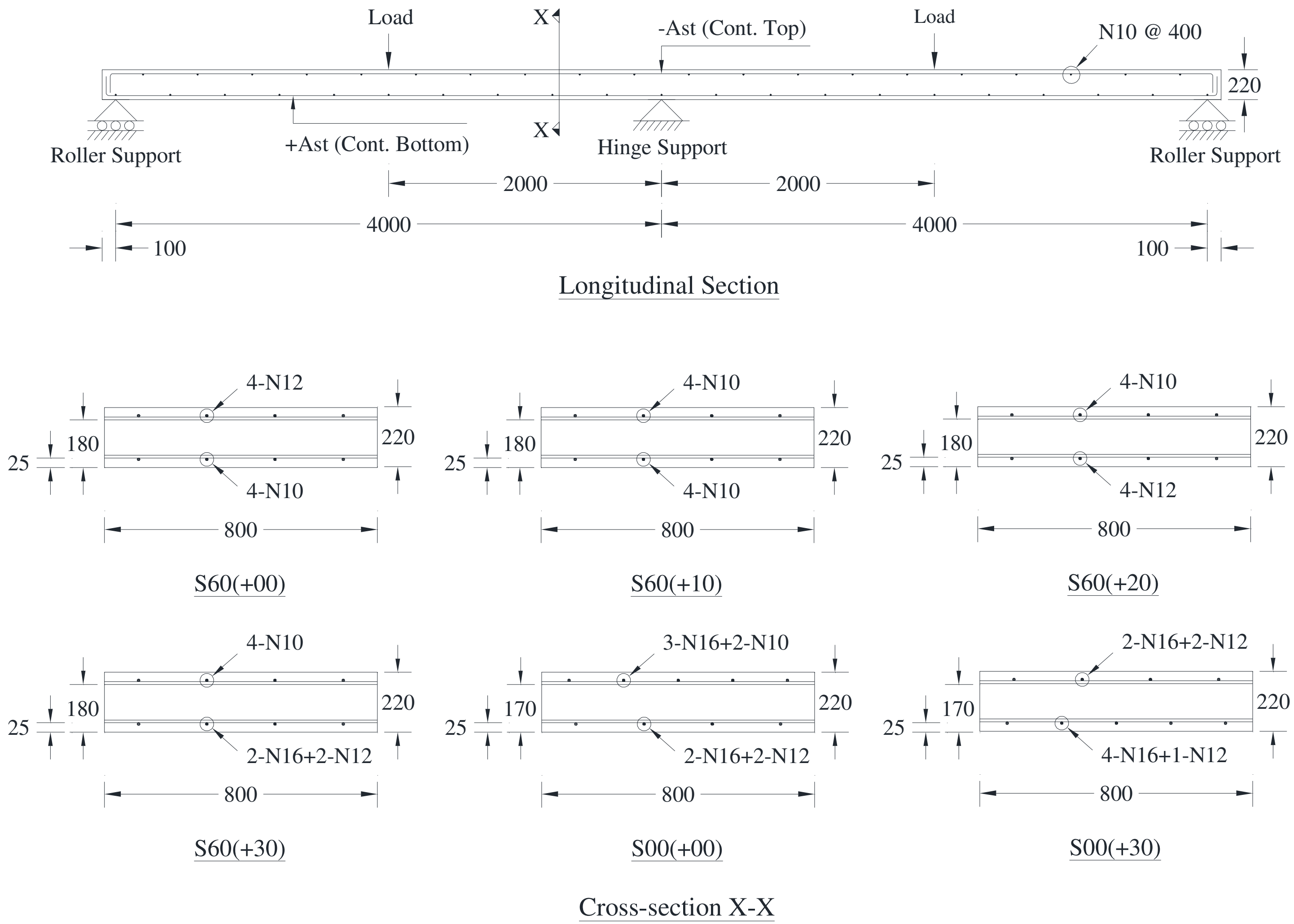

Figure 4.1: Details of specimens and arrangements for two-span continuous slab tests (all dimensions in mm).

4.2.2 Preparation of test specimens and material properties

The reinforcing steel meshes of the specimens were prepared with nominally 500 MPa deformed steel bars. The average measured yield strengths of N10 (normal ductility, 10 mm diameter), N12 (normal ductility, 12 mm diameter) and N16 (normal ductility, 16 mm diameter) bars were 505, 605 and 560 MPa, respectively. The average measured elastic modulus of N10, N12 and N16 bars were 196, 207 and 196 GPa, respectively. Figure 4.2 shows the uniaxial stress-strain curves for the reinforcing bars used in this study tested to AS 1391-2007 [132].

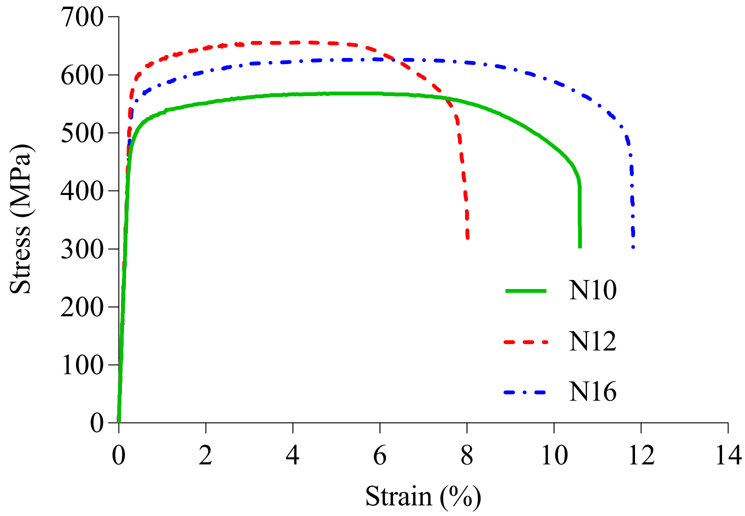

Figure 4.2: Uniaxial stress versus strain curves for reinforcing bars in tension.

Single end-hooked steel fibres (Dramix®3D-65/60-BG) (see Figure 4.3) with a diameter of 0.9 mm and a length of 60 mm were used in this study. The manufacturer provided tensile strength of the steel fibres is 1160 MPa.

Figure 4.3: Dramix®3D-65/60-BG steel fibres.

The specimens were cast in three pours using commercially batched plain concrete and SFRC. The specimens S00(+00) and S00(+30) were cast in the first pour (plain concrete) followed by the specimens S60(+20) and S60(+30) in the second (SFRC Batch 1) and specimens S60(+00) and S60(+10) in the third pour (SFRC Batch 2). The design compressive strength of the concrete at 28 days was 32 MPa. To ensure the workability of the concrete after the inclusion of steel fibres, the maximum aggregate size and slump were chosen to be 10 mm and 150 mm, respectively. The uniform distribution of the steel fibres was ensured by compacting the SFRC specimens using external vibrators attached to the sides of the formwork (see Figure 4.4a).

During the casting of the SFRC specimens, three 150 mm diameter and 300 mm high cylinders were collected at the start, middle and end of the pours to determine the as-cast dosages of steel fibres. Fibres were extracted from the concrete mix using a magnet after washing out the cement paste. For the specimens S60(+20) and S60(+30), the average dosages of fibres at the start, middle and end of the pour were 84, 58 and

57 kg/m^3, respectively. For the specimens S60(+00) and S60(+10), the average dosages of fibres at the start, middle and end of pour were 60, 57 and 49 kg/m^3, respectively.

(a) (b)

Figure 4.4: (a) Formwork and (b) casting of the slab specimens.

To determine the material properties of the plain concrete and the SFRC, companion cylinder, dogbone and prism samples were also cast with the slab specimens. The companion samples were tested on the testing day of the respective slab specimens.

The stress-strain curves for the plain and the SFRC are shown in Figure 4.5. The mean compressive strength of the plain concrete and batches 1 and 2 of the SFRC tested to AS 1012.9:2014 [133] were 38.6, 46.3 and 31.2 MPa, respectively. The mean splitting tensile strength of the plain concrete and batches 1 and 2 of the SFRC tested to AS 1012.10-2000 [134] were 4.0, 6.3 and 3.8 MPa, respectively.

The stress-COD (σ–w) and the stress-CMOD relationship of SFRC were determined by testing dogbone specimens to AS 3600:2018 [34] and prism specimens to EN14651 [135]; the results are given in Figures 4.6 and 4.7. The mean residual tensile stresses from five specimens for each batch determined by the direct tensile test method were 1.82 MPa and 0.87 MPa for 0.5 mm COD ($f'_{0.5}$) and 1.71 MPa and 0.99 MPa for 1.5 mm COD ($f'_{1.5}$) for SFRC batches 1 and 2, respectively. These compare to $f'_{0.5}$ = 2.40 and 1.63 MPa and $f'_{1.5}$ = 2.54 and 1.69 MPa for batches 1 and 2, respectively, when determined by the AS 3600:2018 [34] inverse analysis method on prism bending tests. A summary of prism bending test results is given in Table 4.2.

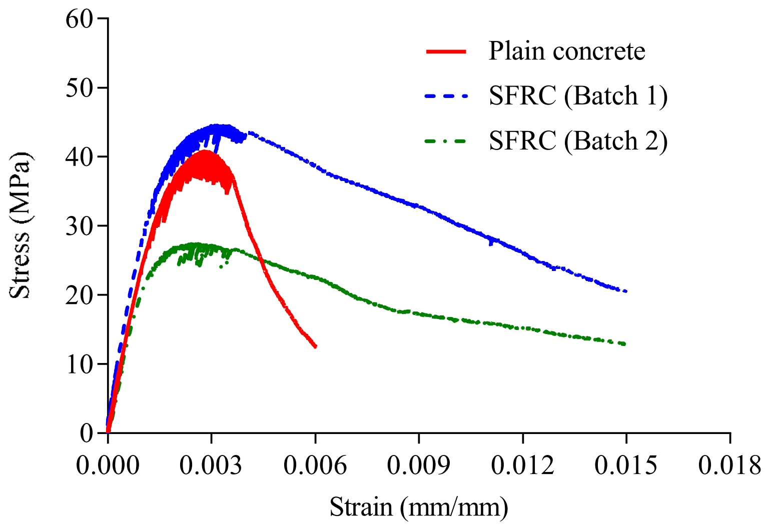

Figure 4.5: Compressive stress-strain curves for the plain concrete and SFRC mixes.

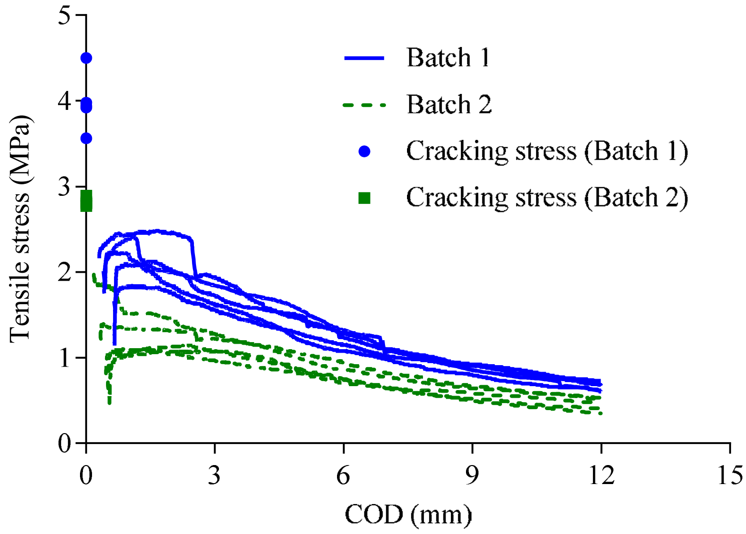

Figure 4.6: Tensile stress versus COD for SFRC dogbone specimens.

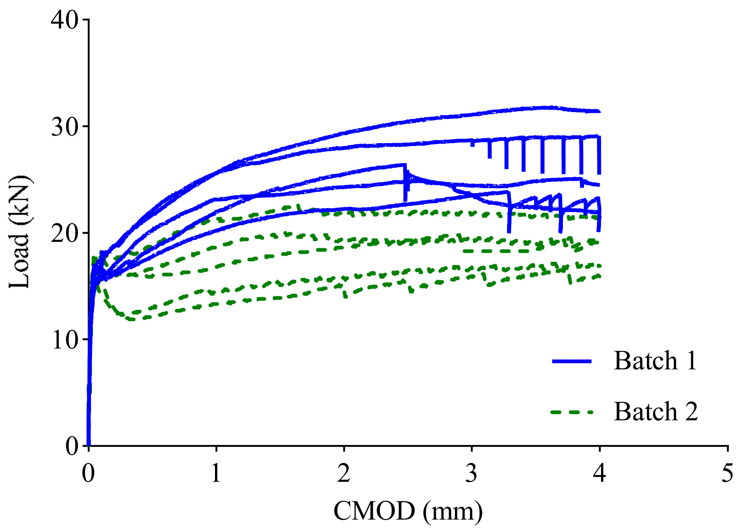

Figure 4.7: Load versus CMOD for SFRC prism specimens.

Table 4.2: Summary of flexural tensile strength test results and calculated tensile strengths (according to EN 14651-2005 [135] test procedure and determined by AS 3600:2018 [34] analysis).

Batch	$f'_{R,1}$ (MPa)	$f'_{R,2}$ (MPa)	$f'_{R,3}$ (MPa)	$f'_{R,4}$ (MPa)	$f'_{0.5}$ (MPa)	$f'_{1.5}$ (MPa)
1	6.36 (0.102)	7.87 (0.105)	8.35 (0.116)	8.26 (0.158)	2.40 (0.099)	2.54 (0.161)
2	4.59 (0.171)	5.34 (0.183)	5.49 (0.123)	5.48 (0.111)	1.63 (0.192)	1.69 (0.098)

Notes: 1. Mean values of 5 specimens with COV's in ().

2. $f'_{R,1}, f'_{R,2}, f'_{R,3}$ and $f'_{R,4}$ are residual flexural tensile strength of SFRC corresponding to CMODs of 0.5, 1.5, 2.5 and 3.5 mm, respectively.

4.2.3 Experimental setup and instrumentation

The experimental setup and a schematic diagram of the setup and instrumentation are shown in Figures 4.8 and 4.9, respectively. The load was applied using a 500 kN capacity hydraulic jack. An equal distribution of the load at the mid-span of each span of the specimen was ensured by a steel spreader beam placed on the specimen. External load cells were placed under the supports to measure the support reactions (see Figure 4.8). The mid-span deflections were measured by linear variable displacement transducers (LVDTs) (see Figure 4.8). LVDTs were also placed directly above each support to detect any support settlement.

A grillage of Demec targets (see Figure 4.10a) was installed on the side of the specimens at the critical sections (mid-spans and intermediate support) to measure the concrete strains using a 250 mm Demec strain gauge. Pi-gauges (gauge length = 150 mm) were installed on the tension side of the specimens at the critical sections to monitor the growth of crack widths (see Figure 4.10b). Before the casting of the concrete, electronic strain gauges (gauge length = 5 mm) were installed on the tensile reinforcement at the critical sections and at 100 mm intervals on each side of the critical sections to measure the strain of reinforcing bars (see Figure 4.10c).

4.2.4 Testing procedure

The tests were performed using displacement-control load at a rate of 0.60 mm/min up to a deflection of 24 mm. The loading was paused at deflection intervals of 4 mm to mark the progress of cracks and measure the concrete strains. After 24 mm deflection, the load was applied uninterruptedly at a rate of 1.2 mm/min until the failure of the specimens. A data logger was used to monitor and record the applied load, support reactions, mid-span deflections, strain gauge readings and Pi-gauge readings continuously throughout the test.

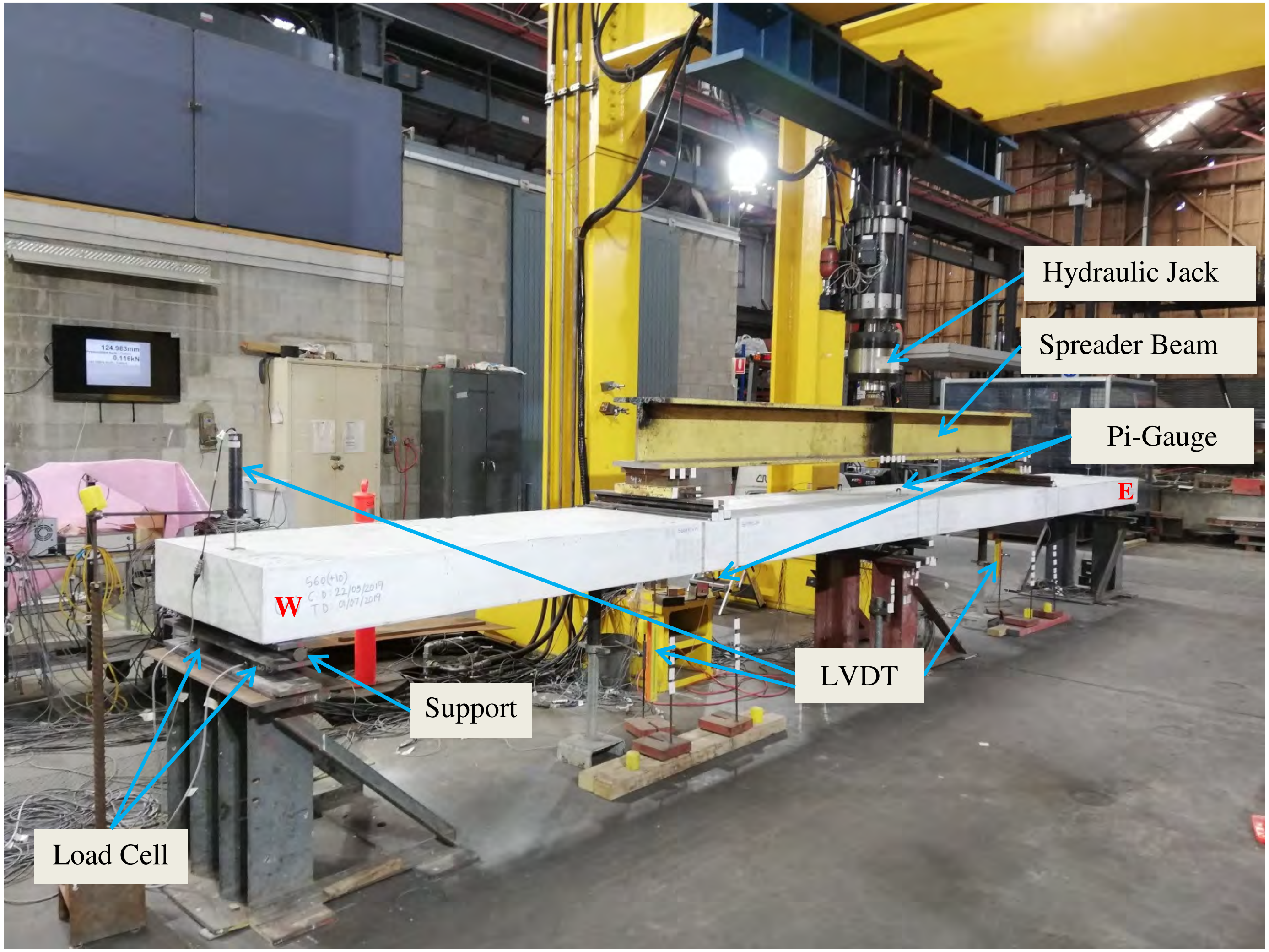

Figure 4.8: Experimental setup (E = East; W = West).

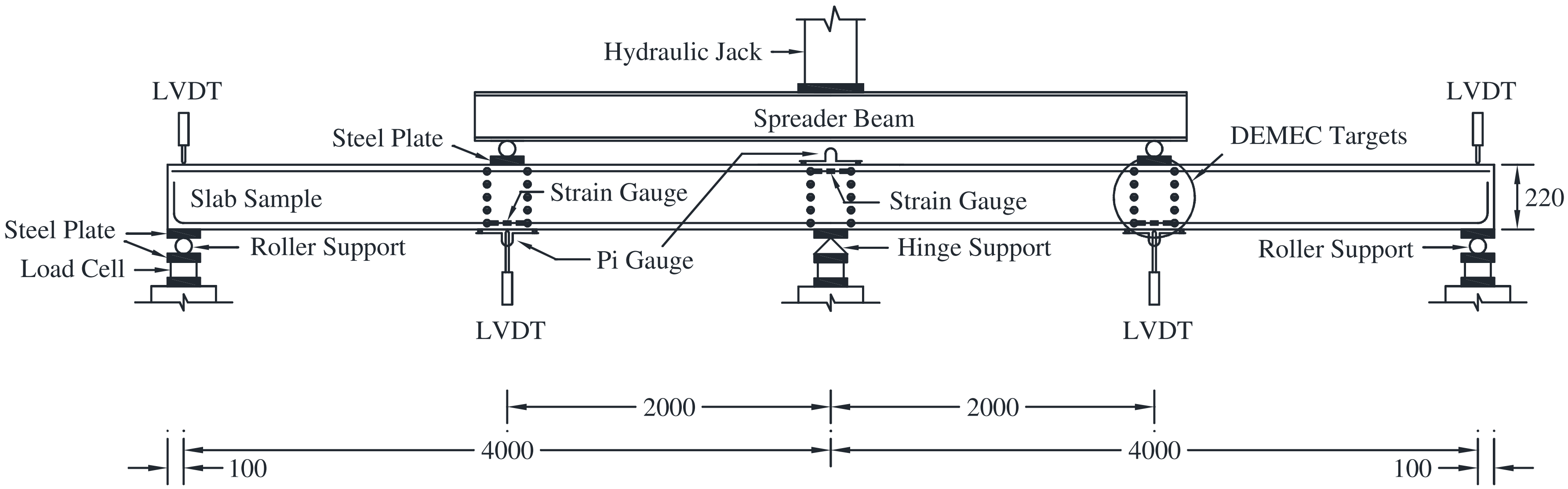

Figure 4.9: Schematic outline of the experimental setup and instrumentation.

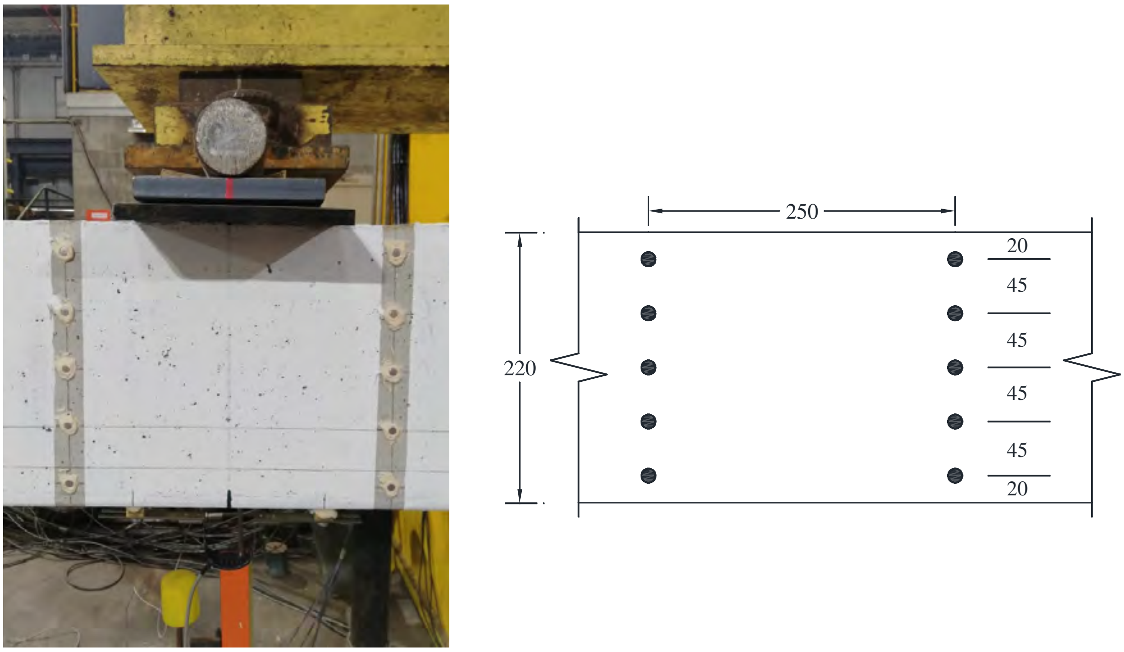

(a)

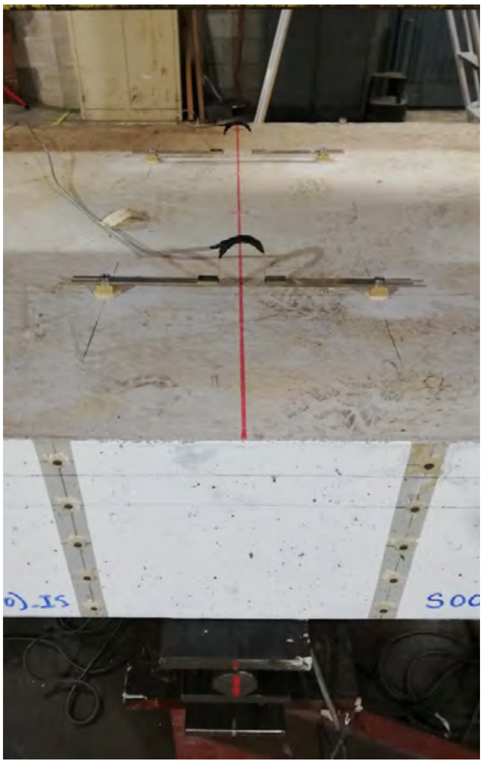

(b) **(c)**

Figure 4.10: Instrumentation – (a) Demec targets; (b) Pi-gauges; (c) strain gauges.

4.3 Results and discussion

4.3.1 Behaviour under load

Specimen S60(+00)

Specimen S60(+00) was designed for 0% of moment redistribution with respect to the linear-elastic condition. The total load on each span versus mid-span deflection curves for the tested specimen are shown in Figure 4.11. The self-weight of the specimen (4.4 kN/m) and the weight of the spreader beam (8.6 kN) are included in the total load.

For specimen S60(+00), the cross-section at the intermediate support cracked first. The cracking was determined by the sudden change of the strain values measured by the Pi-gauges. Cracking then continued both in the intermediate support and the mid-span regions. As loading continued, the reinforcement at the east mid-span yielded first, followed by the yielding of reinforcement at the west mid-span and intermediate support. The yielding of reinforcement was determined from the strain gauge measurements (see Figure 4.11) and was taken as the point where strain in reinforcing bars exceeded their measured yield strain (i.e., ε_{sy} = 0.00258 for N10 bars, ε_{sy} = 0.00292 for N12 bars and ε_{sy} = 0.00286 for N16 bars). As loading continued, hinges formed at the east mid-span first and then at the intermediate support (see Figure 4.12). Figure 4.13 shows the location of the formation of hinges. After the formation of hinges, the peak load was reached, and the load dropped by 12% to the point of fracture of the tensile reinforcement in the east mid-span.

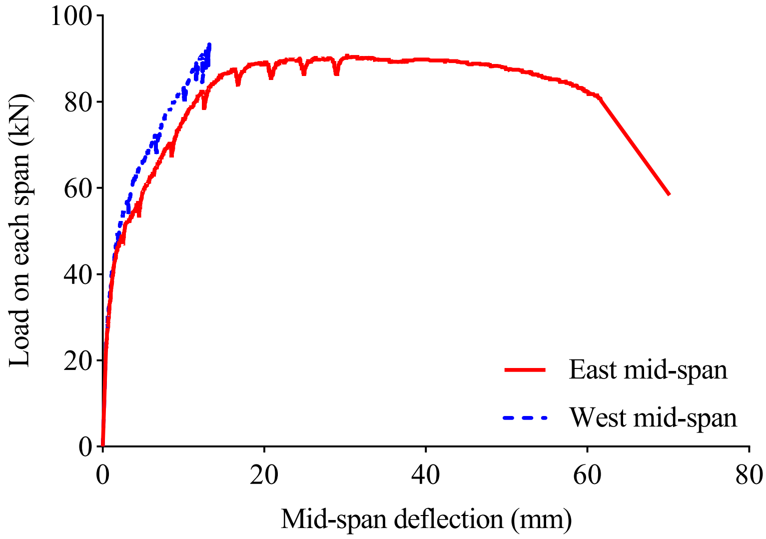

Figure 4.11: Load versus mid-span deflection for specimen S60(+00).

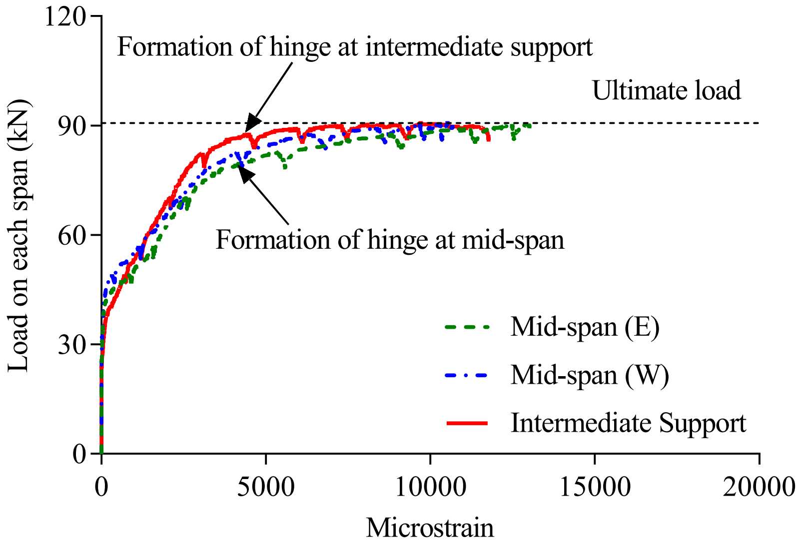

Figure 4.12: Load versus strain of reinforcing bars for specimen S60(+00).

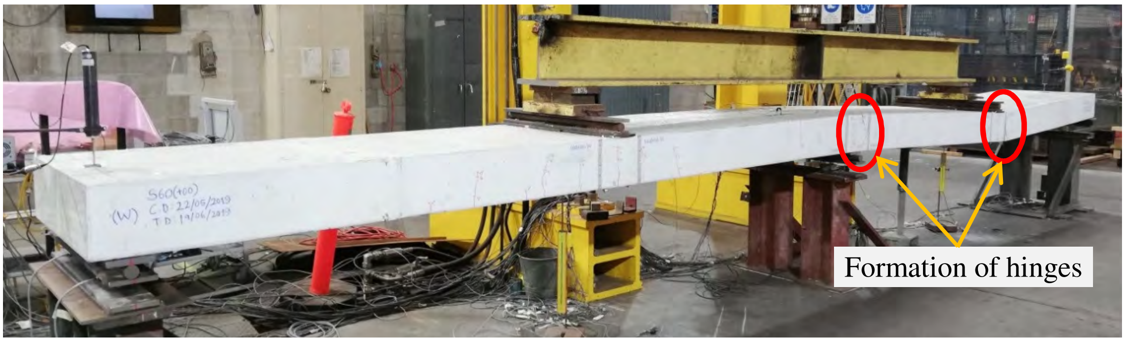

(a) Formation of hinges

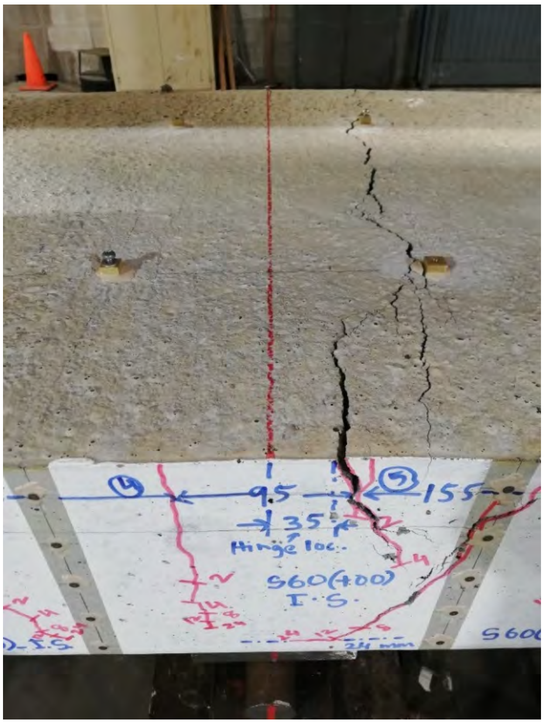

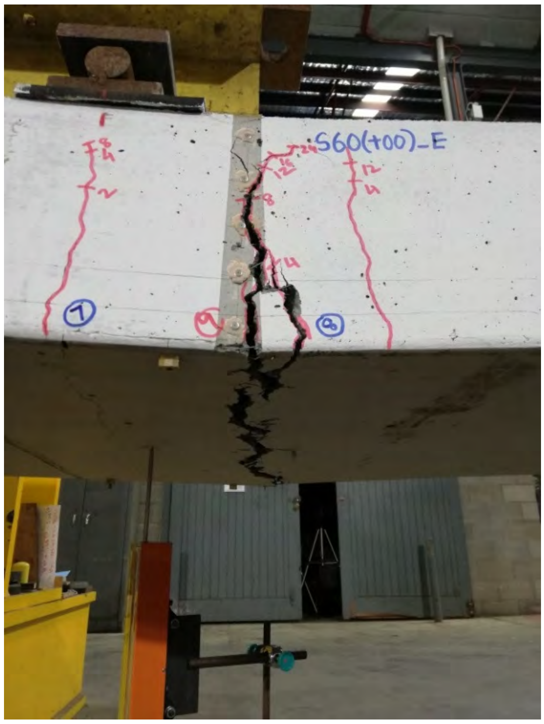

(b) Intermediate support

(c) East mid-span

Figure 4.13: Location of the formation of plastic hinges for specimen S60(+00).

Specimen S60(+10)

Specimen S60(+10) was designed for 10% of positive moment redistribution with respect to the linear-elastic condition. The load versus mid-span deflection and load versus strain of reinforcing bars curves for the specimen are shown in Figures 4.14 and 4.15, respectively.

For specimen S60(+10), the cross-section at the intermediate support cracked first. Cracking then continued both in the intermediate support and the mid-span regions, and the reinforcement at the west mid-span yielded first followed by the yielding of reinforcement at the intermediate support and the east mid-span. As loading continued, hinges formed at the west mid-span first and then at the intermediate support (see Figure 4.15). After the formation of hinges, the peak load was reached, and the load dropped by 11% after to the point of fracture of the tensile reinforcement in the west mid-span.

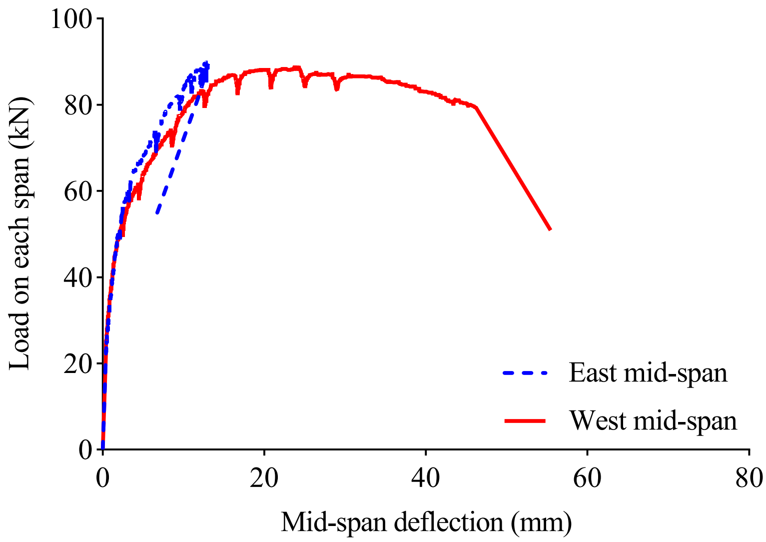

Figure 4.14: Load versus mid-span deflection for specimen S60(+10).

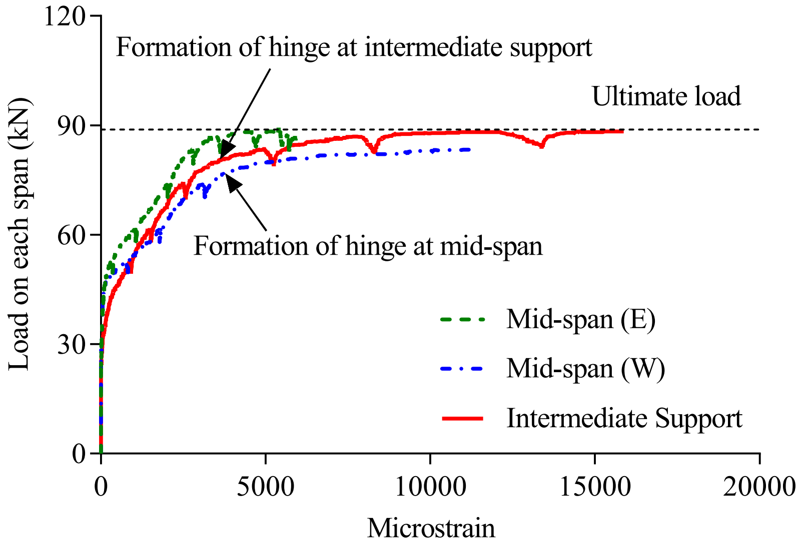

Figure 4.15: Load versus strain of reinforcing bars for specimen S60(+10).

Specimen S60(+20)

Specimen S60(+20) was designed for 20% of positive moment redistribution with respect to the linear-elastic condition. The load versus mid-span deflection and load versus strain of reinforcing bars curves for the specimen are shown in Figures 4.16 and 4.17, respectively.

For specimen S60(+20), the cross-sections at the intermediate support and mid-spans cracked almost at the same load. Cracking then continued both in the intermediate support and the mid-span regions, and the reinforcement at the intermediate support yielded first followed by the yielding of reinforcement at the east and west mid-span. The yielding of reinforcement at the east and west mid-span occurred almost at the same load. As loading continued, hinges formed at the intermediate support first and then at the east mid-span (see Figure 4.17). After the formation of hinges, the peak load was reached, and the load dropped by 14% to the point of fracture of the tensile reinforcement in the east mid-span.

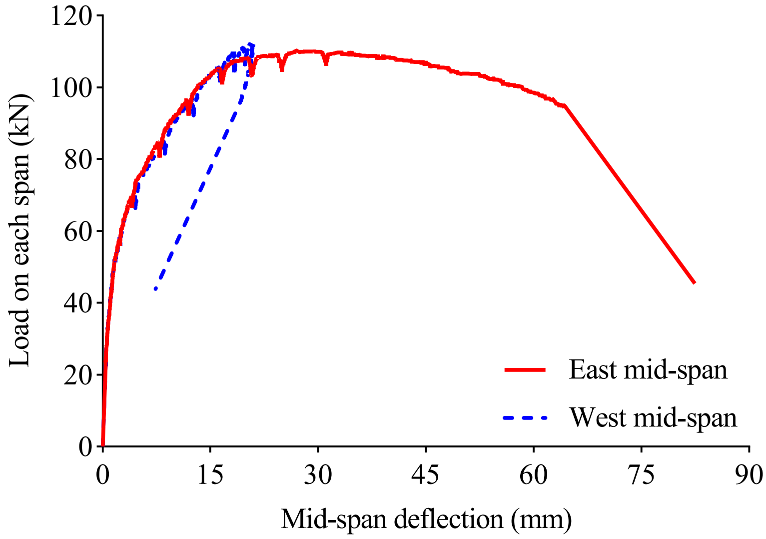

Figure 4.16: Load versus mid-span deflection for specimen S60(+20).

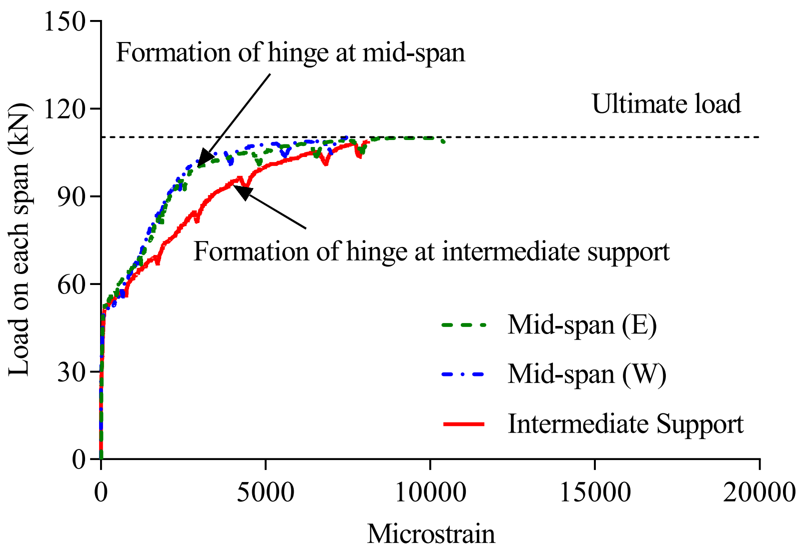

Figure 4.17: Load versus strain of reinforcing bars for specimen S60(+20).

Specimen S60(+30)

Specimen S60(+30) was designed for 30% of positive moment redistribution with respect to the linear-elastic condition. The load versus mid-span deflection and load versus strain of reinforcing bars curves for the specimen are shown in Figures 4.18 and 4.19, respectively.

For specimen S60(+30), the cross-section at the intermediate support cracked first. Cracking then continued both in the intermediate support and the mid-span regions, and the reinforcement at the intermediate support yielded first followed by the yielding of reinforcement at the west and east mid-span. The yielding of reinforcement at the west and east mid-span occurred almost at the same load. As loading continued, a hinge formed at the intermediate support followed by the formation of hinges at the west and east mid-span (see Figure 4.19). After the formation of hinges, the peak load was reached and the load dropped by 23% to the point of fracture of the tensile reinforcement in the east mid-span.

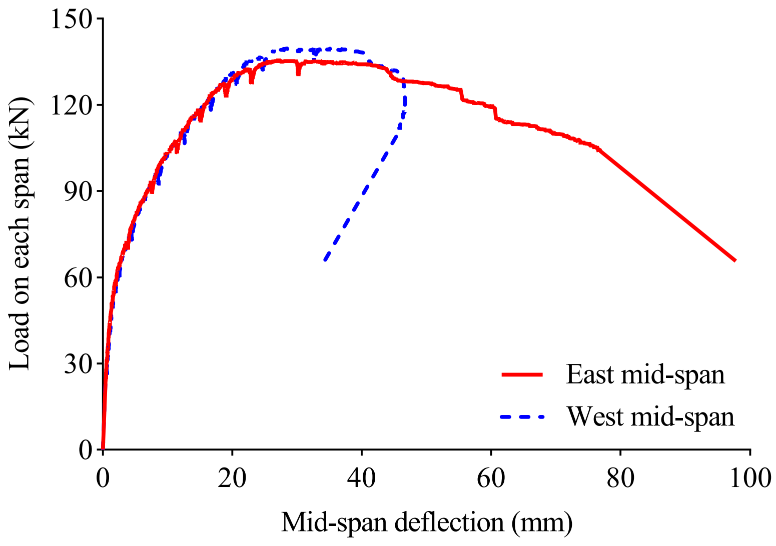

Figure 4.18: Load versus mid-span deflection for specimen S60(+30).

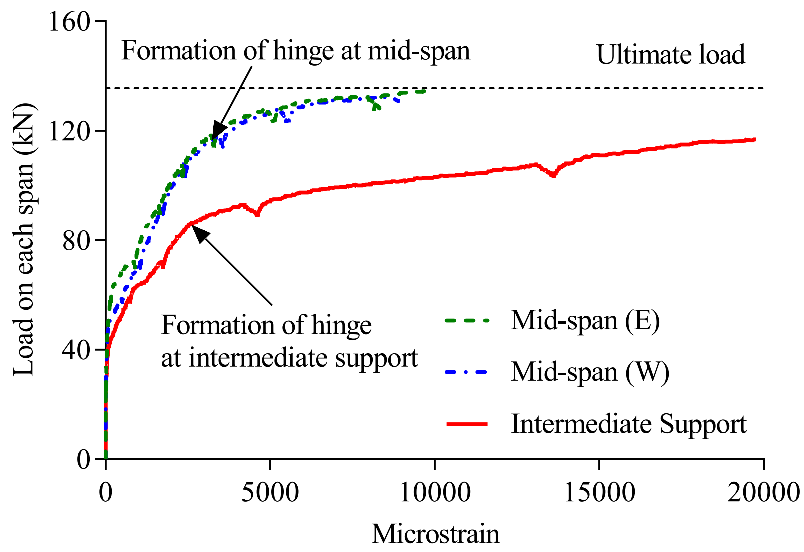

Figure 4.19: Load versus strain of reinforcing bars for specimen S60(+30).

Specimen S00(+00)

Non-fibre specimen S00(+00) was designed as equivalent to the fibre-reinforced specimen S60(+00), with 0% of moment redistribution with respect to the linear-elastic condition. The load versus mid-span deflection and load versus strain of reinforcing bars curves for the specimen are shown in Figures 4.20 and 4.21.

For specimen S00(+00), the cross-section at the intermediate support and the mid-spans cracked almost at the same load. Cracking then continued both in the intermediate support and the mid-span regions, and the reinforcement at the west mid-span yielded first followed by the yielding of reinforcement at the intermediate support and east mid-span. As loading continued, hinges formed at the west mid-span first and then at the intermediate support (see Figure 4.21). After the formation of hinges, the load increased due to hardening of reinforcement before failing by fracture of the tensile reinforcement at the east mid-span. Noting that the strain gauges failed at strains less than 1.50%, the strain gauges could not capture the complete hardening of the reinforcing bars.

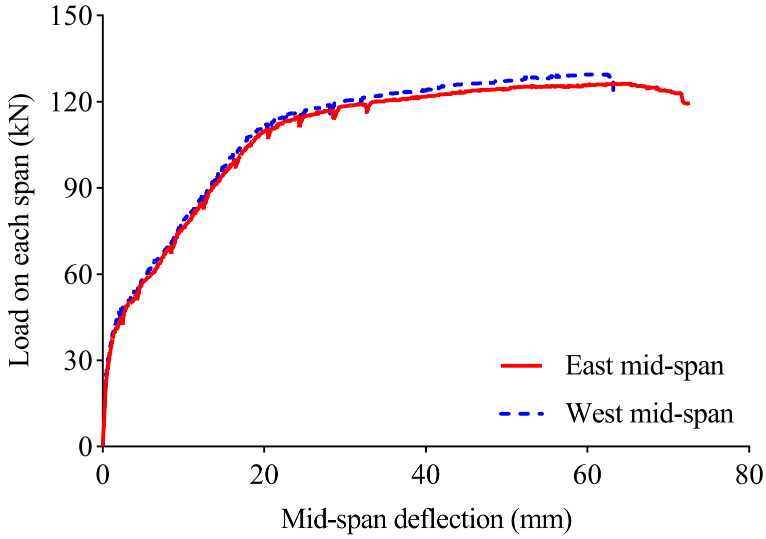

Figure 4.20: Load versus mid-span deflection for specimen S00(+00).

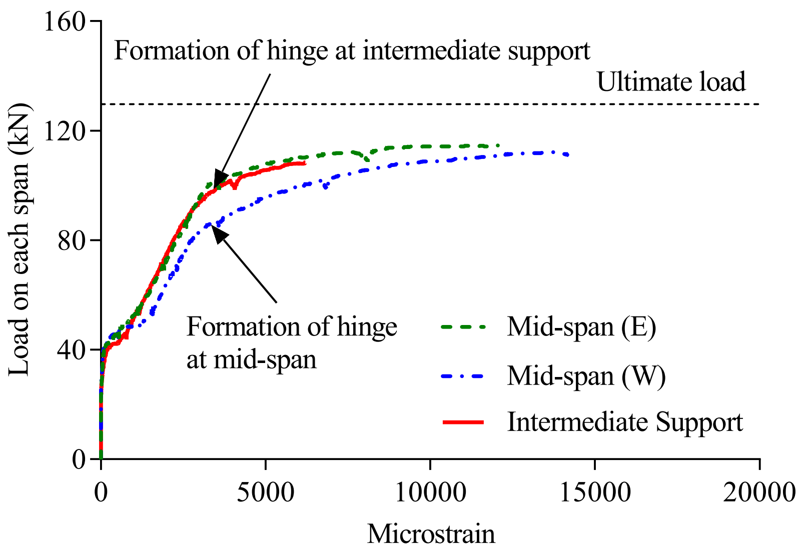

Figure 4.21: Load versus strain of reinforcing bars for specimen S00(+00).

Specimen S00(+30)

Non-fibre specimen S00(+30) was designed as equivalent to the fibre-reinforced specimen S60(+30), with 30% of positive moment redistribution with respect to the linear-elastic condition. The load versus mid-span deflection and load versus strain of reinforcing bars curves for the specimen are shown in Figures 4.22 and 4.23.

For specimen S00(+30), the cross-section at the intermediate support cracked first. Cracking then continued both in the intermediate support and the mid-span regions, and the reinforcement at the intermediate support yielded first followed by the yielding of reinforcement at the east and west mid-span. As loading continued, hinges formed at the intermediate support first and then at the west and east mid-span (see Figure 4.23). After the formation of hinges, the load increased due to hardening of reinforcement before failing by fracture of the tensile reinforcement in the west mid-span. Noting that the strain gauges failed at strains less than 1.50%, the strain gauges could not capture the complete hardening of the reinforcing bars.

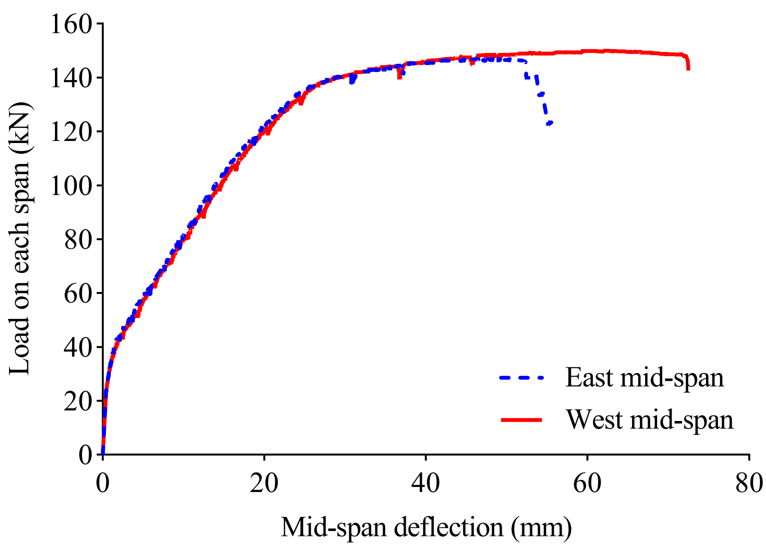

Figure 4.22: Load versus mid-span deflection for specimen S00(+30).

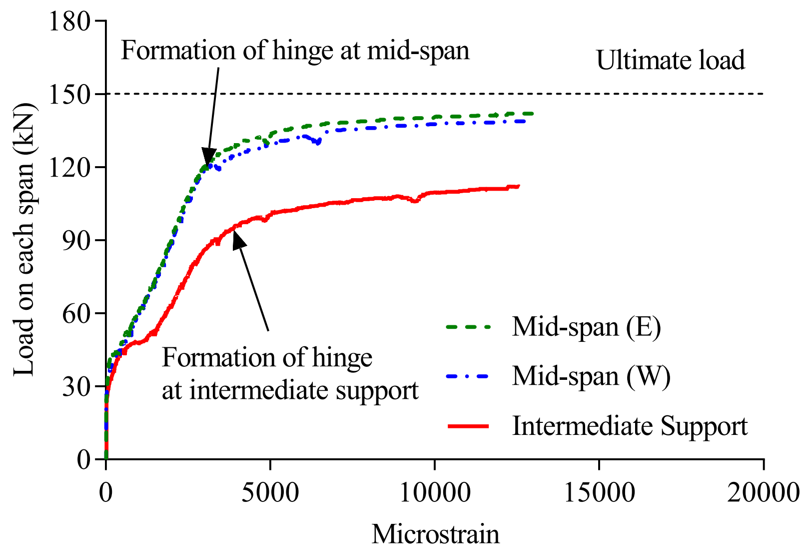

Figure 4.23: Load versus strain of reinforcing bars for specimen S00(+30).

Table 4.3 provides a summary of the loads and corresponding critical mid-span (the span which failed by the formation of plastic hinges) deflections at the formation of first crack, at yielding of tensile reinforcement, at the peak and at fracture of the reinforcing bars. A comparison of load versus mid-span deflection curves for the R-SFRC and RC specimens are shown in Figure 4.24. The loads and corresponding mid-span deflections at the formation of first crack, at yielding of tensile reinforcement, at the peak load and at fracture of the reinforcing bars are also marked on the graph.

Since the actual material properties were different than the design material properties, to accurately compare the results, in the following discussion, the load is normalised with respect to the design capacity predicted by the AS 3600:2018 [34] model. Figure 4.25 shows a comparison of normalised load versus deflection curves for equivalent RC and R-SFRC specimens. From the figure, it is evident that the R-SFRC specimens had higher stiffness in the service load than that of the equivalent RC specimens. The peak load occurred at a lower displacement in the R-SFRC slabs than that in the RC slabs.

Table 4.3: Summary of load-deflection results.

Series	Specimen	Cracking		First yield		Second yield		Peak		Reinforcing bar fracture	
		P_{cr} (kN)	Δ_{cr} (mm)	P_{y1} (kN)	Δ_{y1} (mm)	P_{y2} (kN)	Δ_{y2} (mm)	P_p (kN)	Δ_p (mm)	P_f (kN)	Δ_f (mm)
A	S60(+00)	37.0	1.1	70.2	8.3	76.0	10.1	90.7	30.2	80.2	61.7
	S60(+10)	43.2	1.4	70.3	7.0	74.2	9.0	88.8	23.9	79.3	46.2
	S60(+20)	51.5	1.6	81.5	6.8	99.7	13.1	110.3	26.8	94.4	64.5
	S60(+30)	41.0	1.0	85.8	5.9	116.0	13.9	135.5	27.0	103.8	76.9
B	S00(+00)	40.6	1.3	72.3	8.8	81.9	11.2	129.7	61.7	129.2	62.7
	S00(+30)	35.4	1.1	83.1	10.9	115.5	18.6	150.1	61.8	147.8	72.2

Notes: 1. P_{cr}, P_{y1}, P_{y2}, P_p and P_f are loads on each span corresponding to cracking of the concrete, at first yielding of the reinforcement, at second yielding of the reinforcement, at the peak load and at fracture of the reinforcement.

2. Δ_{cr}, Δ_{y1}, Δ_{y2}, Δ_p and Δ_f are deflections at mid-span corresponding to cracking of the concrete, at first yielding of the reinforcement, at second yielding of the reinforcement, at the peak load and at fracture of the reinforcement.

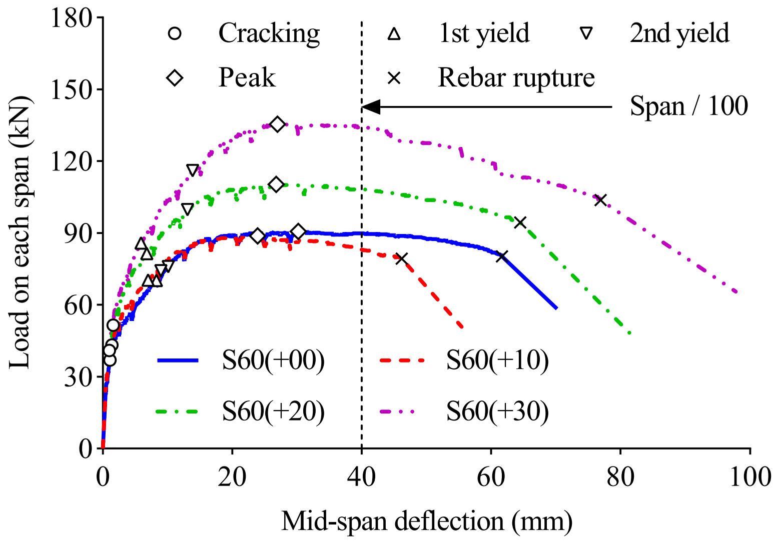

(a)

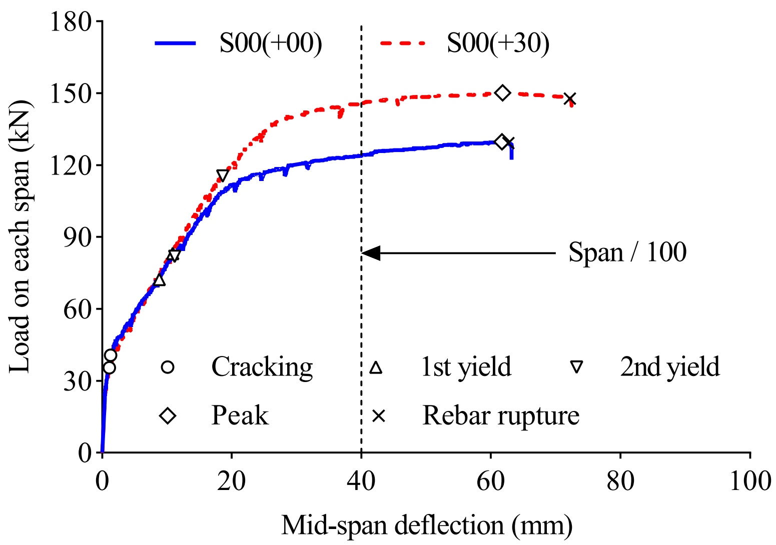

(b)

Figure 4.24: Comparison of load versus mid-span deflection curves for the (a) R-SFRC specimens and (b) RC specimens.

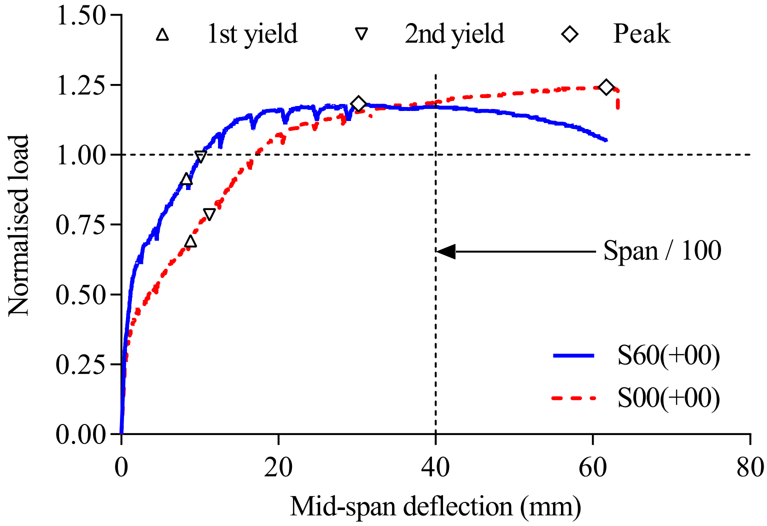

(a) Comparison between S60(+00) and S00(+00)

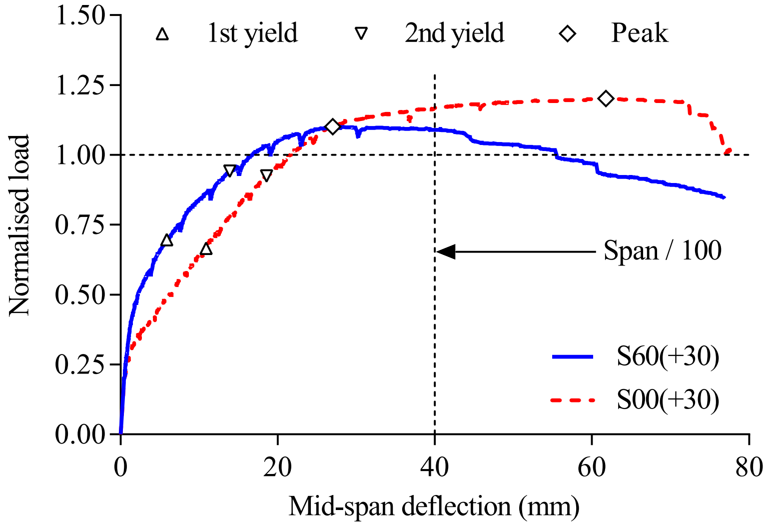

(b) Comparison between S60(+30) and S00(+30)

Figure 4.25: Comparison of normalised load versus mid-span deflection curves for equivalent RC and R-SFRC specimens.

4.3.2 Cracking behaviour

During the tests, the development and progress of cracks were monitored and marked at deflection intervals of 4 mm. A comparison of crack patterns at the intermediate support and mid-span (the critical span) of the tested specimens are shown in Figure 4.26. Pictures of crack patterns of the tested specimen are provided in Appendix D (see Figures D1 to D6).

The distribution of cracks was uniform within the critical length of the specimens. A decrease in crack spacing by the inclusion of steel fibres is evident from Figure 4.26. Since the load was applied at the mid-span, crack localisation (significant widening of one single crack) happened in both R-SFRC and RC specimens.

Figure 4.27 shows a comparison of crack widths over the intermediate support (negative moment) and below the mid-span (positive moment) of equivalent RC and R-SFRC specimens up to a deflection of 24 mm. Since the actual material properties were different than the design material properties, for an accurate comparison, the resulting moment is normalised with respect to the design capacity predicted by the AS 3600:2018 [34] model. From the figure, it is evident that for the service load condition, the R-SFRC specimens had smaller crack widths than that of the equivalent RC specimens.

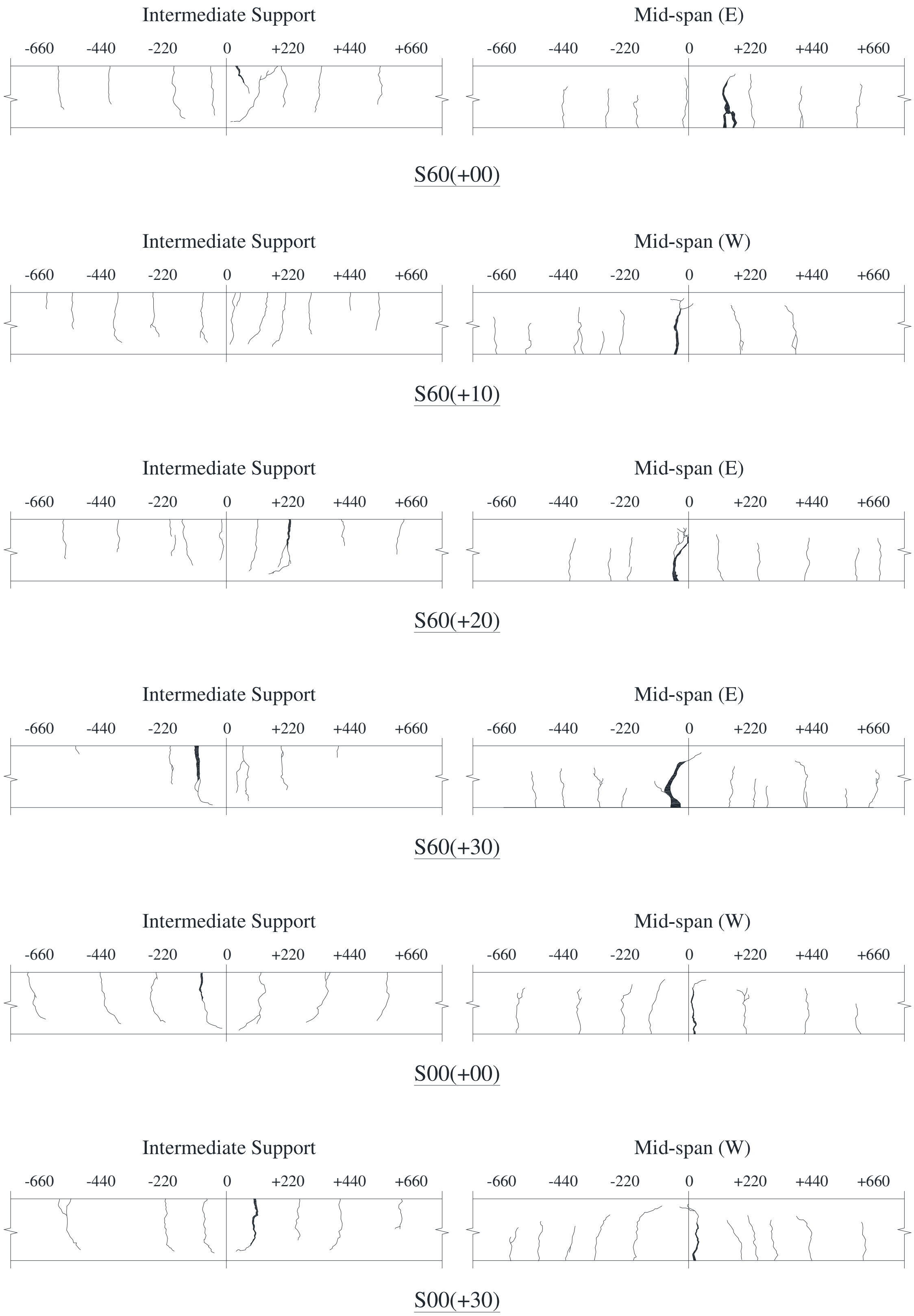

Figure 4.26: Crack patterns for the slab specimens (E = East; W = West).

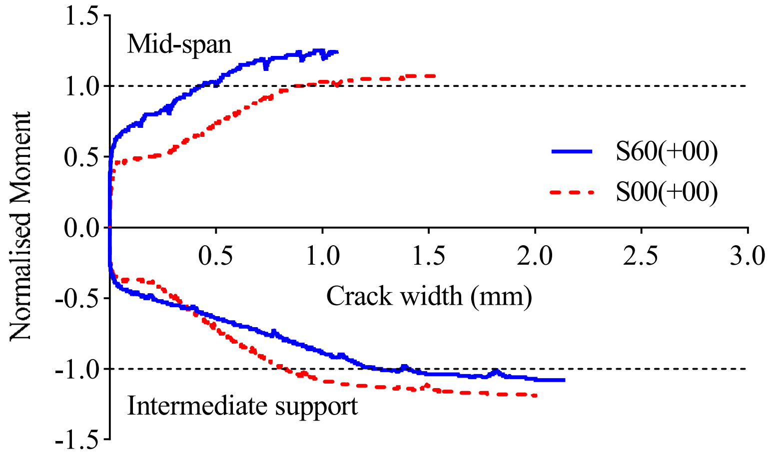

(a) Comparison between S60(+00) and S00(+00)

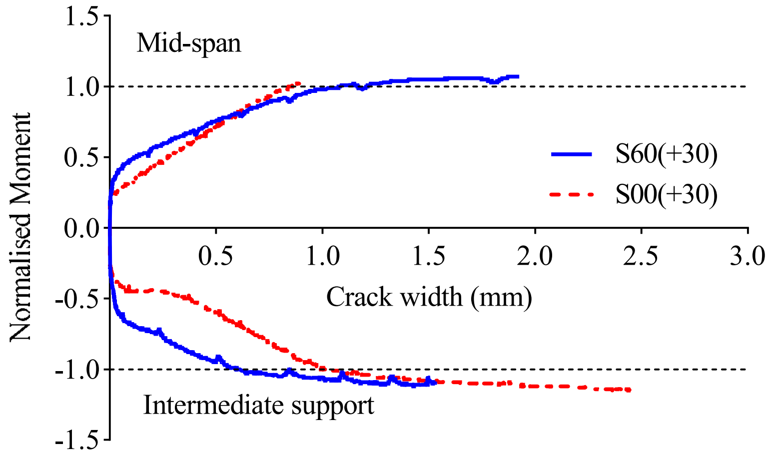

(b) Comparison between S60(+30) and S00(+30)

Figure 4.27: Comparison of normalised moment versus crack width at critical sections for equivalent RC and R-SFRC specimens (up to deflection = 24 mm).

4.3.3 Curvature

The curvature (κ) values at the critical sections of the specimens were determined from the Demec strain gauge measurements using the formula in Section 3.3.3. The Demec strain values are provided in Appendix D (see Figures D7 to D12). The moment versus curvature diagrams are plotted in Figure 4.28.

For safety, the Demec readings were suspended after 24 mm of displacement. Also, in some cases (at east mid-span for specimen S60(+00), at intermediate support for specimens S60(+10) and S60(+20)), the hinges formed outside the Demec gauged region (see Figures D1 to D6 in Appendix D).

The normalised moment versus curvature diagrams of equivalent R-SFRC and RC specimens are plotted in Figure 4.29. A reduction in curvature by the inclusion of steel fibres is evident from the figure. Since the Demec strain readings were not measured after 24 mm of displacement, it is not possible to comment on the post-peak curvature of the specimens from the Demec strain readings.

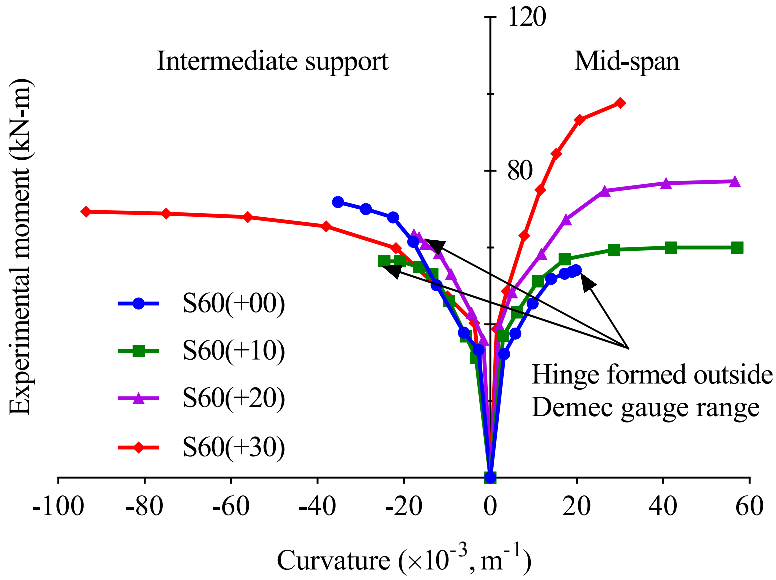

(a)

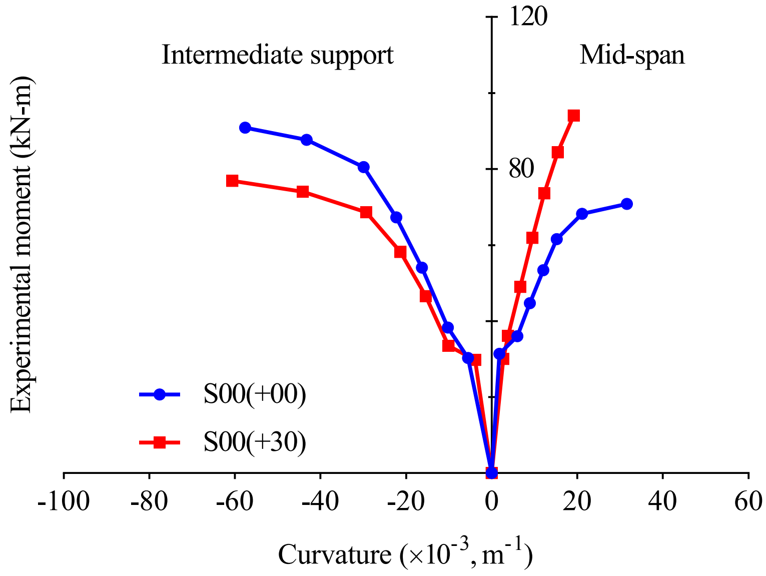

(b)

Figure 4.28: Moment versus curvature curves at critical sections for the (a) R-SFRC and (b) RC specimens.

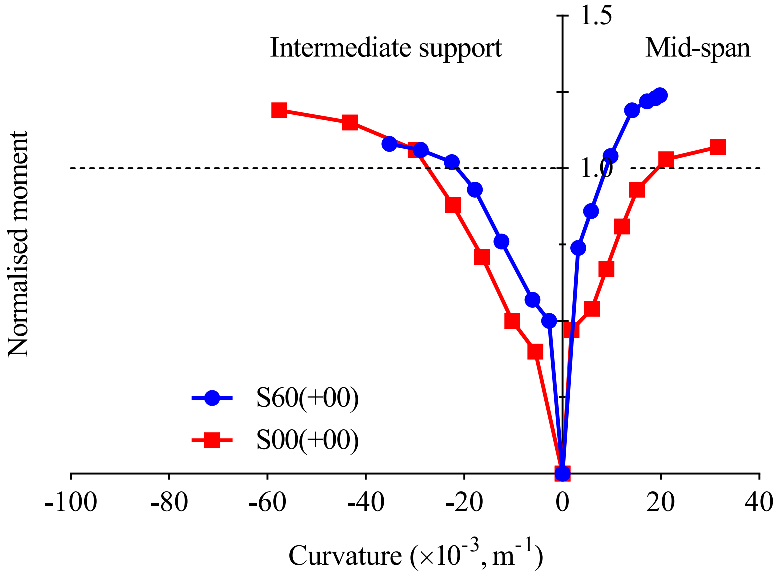

(a) Comparison between S60(+00) and S00(+00)

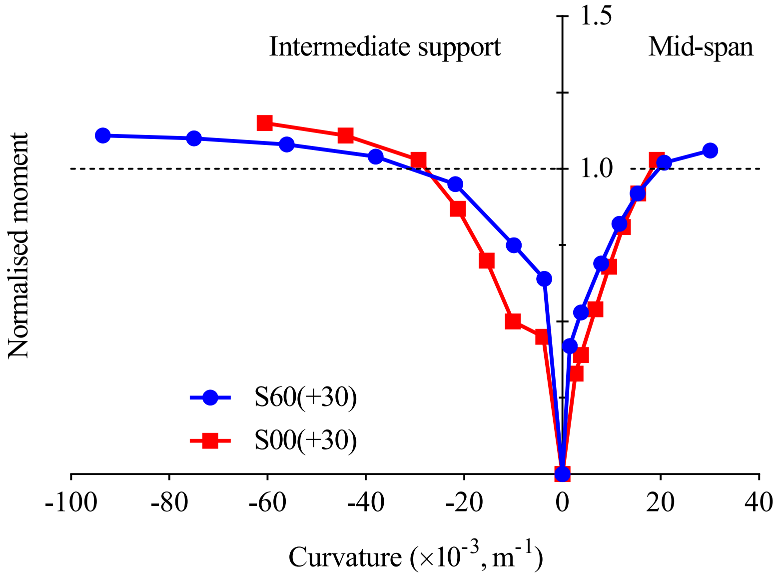

(b) Comparison between S60(+30) and S00(+30)

Figure 4.29: Comparison of normalised moment versus curvature at critical sections for equivalent RC and R-SFRC specimens (up to deflection = 24 mm).

4.3.4 Ductility

The ductility of the specimens was evaluated quantitatively in terms of deflection and work done using the formulas in Section 3.3.4. Table 4.4 shows the values of the ductility factors based on displacement and work done. Using the measure of a ductility factor value greater than 2 indicates good ductility [141], good ductility was exhibited by all the slabs tested. It is recognised, however, that the peak (ultimate) load for the R-SFRC specimens was obtained at a lower deflection than that for the similar RC specimens (see Figure 4.25).

A line corresponding to a displacement of span/100 (i.e. 40 mm) is plotted in Figure 4.24. This point is considered as corresponding to sufficient ductility for observation of serious distress in the member [119]. The point corresponding to the ultimate capacity of the R-SFRC slabs occur slightly before the span/100 deflection and, thus, some limitations in reinforcement are appropriate for R-SFRC flexural members to ensure sufficient ductility up to a displacement of span/100. The ductility factor values for both R-SFRC and RC specimens decreased with increased moment redistribution.

Table 4.4: Ductility factor values.

Series	Specimen	μ_Δ	μ_w
A	S60(+00)	6.1	4.1
	S60(+10)	5.1	3.4
	S60(+20)	4.9	2.5
	S60(+30)	5.3	2.4
B	S00(+00)	5.5	10.2
	S00(+30)	3.3	5.4

4.3.5 Moment redistribution

A comparison of the experimental moment to the theoretical linear-elastic moment at the intermediate support with respect to load is shown in Figure 4.30. For the specimens with no moment redistribution, the moments in the tests were almost that determined by linear-elastic moment calculations. For the specimens designed for moment redistribution, the experimental moment deviated from the linear-elastic moment after the formation of cracks. As loading continued, the crack formation stabilised and the rate of change of bending moment became almost constant. The experimental moment started deviating again from the linear-elastic moment after the yielding of reinforcement and formation of first plastic hinge. The deviation continued until a second plastic hinge formed, and the section reached its ultimate capacity.

The deviation of the experimental moment from the linear-elastic moment at the earlier stage of loading (after the formation of cracks and before the yielding of steel) is due to continual adjustments in stiffness that occurred due to progressive cracking under increasing load. The deviation of the experimental moment from the linear-elastic moment at the later stage of loading (after steel yielding) is due to transferring of forces from a section that is critically loaded to others that are not.

As explained in Chapter 3, the actual moment redistribution differs from the theoretical moment redistribution calculated based on linear-elastic values. The theoretical moment redistribution incorporates the distribution forces due to changes in stiffnesses as cracks form and develop. The actual moment redistribution starts after the yielding of reinforcement at the critical section of a member and is determined from the ratio of support moment to load at the time of measurement of first yield, to that attained of the full formation of the second plastic hinge. Table 4.5 shows a summary of the ratios moment at intermediate support to load on each span at the key points from first yield. The redistributions of moment with respect to load for the R-SFRC and RC specimens are shown in Figure 4.31. The theoretical (based on linear-elastic) and actual values of moment redistribution at the key points from the first yield are presented in Table 4.6.

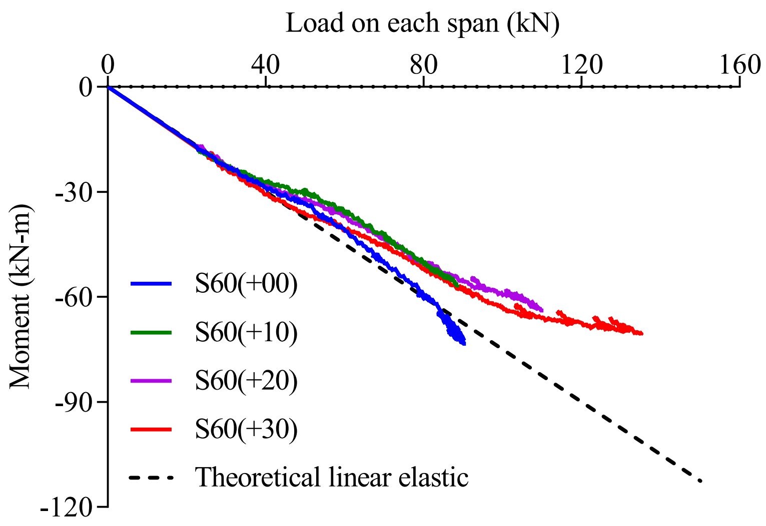

(a)

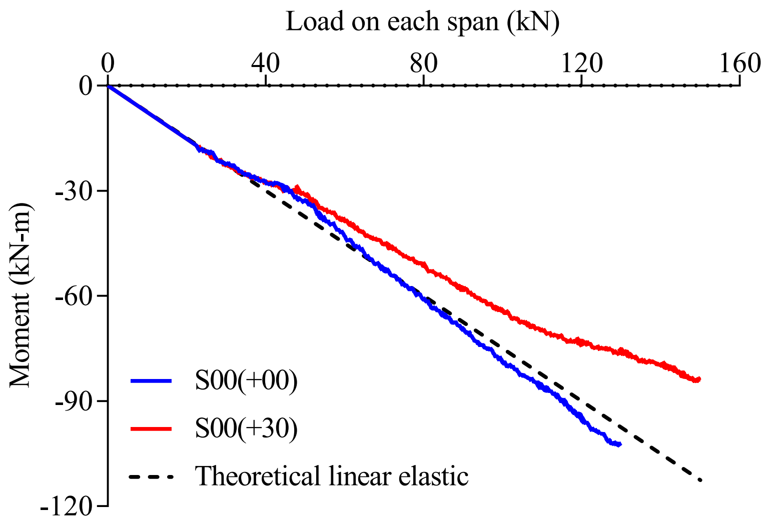

(b)

Figure 4.30: Load versus moment curves for the (a) R-SFRC and (b) RC specimens.

Table 4.5: Ratios of moment at intermediate support to load on each span.

Series	Specimen	Linear elastic $(M/P)_{LE}$	Experimental $(M/P)_{exp}$		
			First yield $(M/P)_{y1}$	Second yield $(M/P)_{y2}$	Peak $(M/P)_{p}$
A	S60(+00)	-0.75	-0.719	-0.727	-0.809
	S60(+10)		-0.601	-0.619	-0.638
	S60(+20)		-0.631	-0.591	-0.579
	S60(+30)		-0.646	-0.579	-0.521
B	S00(+00)		-0.751	-0.772	-0.789
	S00(+30)		-0.647	-0.628	-0.555

Table 4.6: Amount of moment redistribution (in %) at different stages of loading.

Series	Specimen	First yield		Second yield		Peak	
		η_{theo}	η_{actual}	η_{theo}	η_{actual}	η_{theo}	η_{actual}
A	S60(+00)	4.1	0	3.1	−1.1	−7.9	−12.6
	S60(+10)	19.9	0	17.5	−3.1	15.0	−6.2
	S60(+20)	15.9	0	21.2	6.3	22.8	8.2
	S60(+30)	13.9	0	22.8	10.3	30.5	19.3
B	S00(+00)	−0.1	0	−3.0	−2.9	−5.3	−5.2
	S00(+30)	13.7	0	16.3	3.0	26.0	14.2

Notes: 1. $\eta_{theo}(\%) = \frac{(M/P)_{LE} - (M/P)_{exp}}{(M/P)_{LE}} \times 100\%$

2. $\eta_{actual}(\%) = \frac{(M/P)_{y1} - (M/P)_{exp}}{(M/P)_{y1}} \times 100\%$

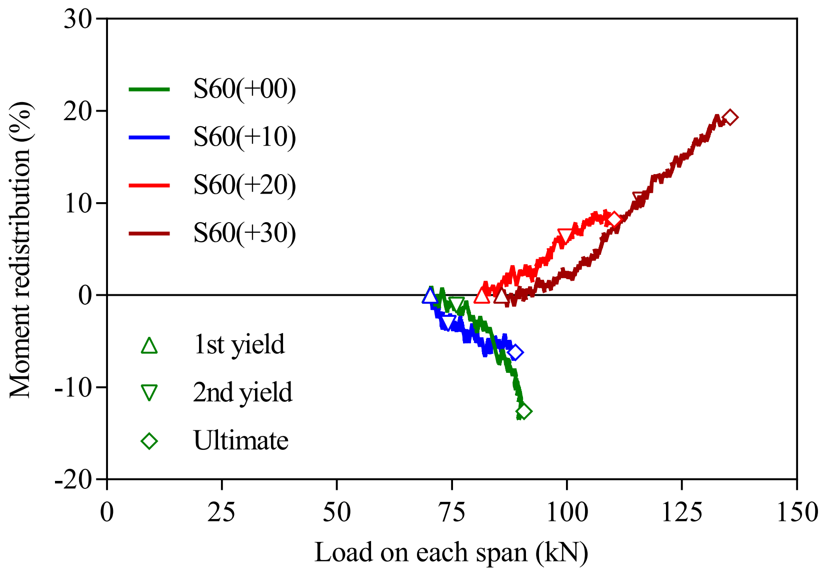

(a)

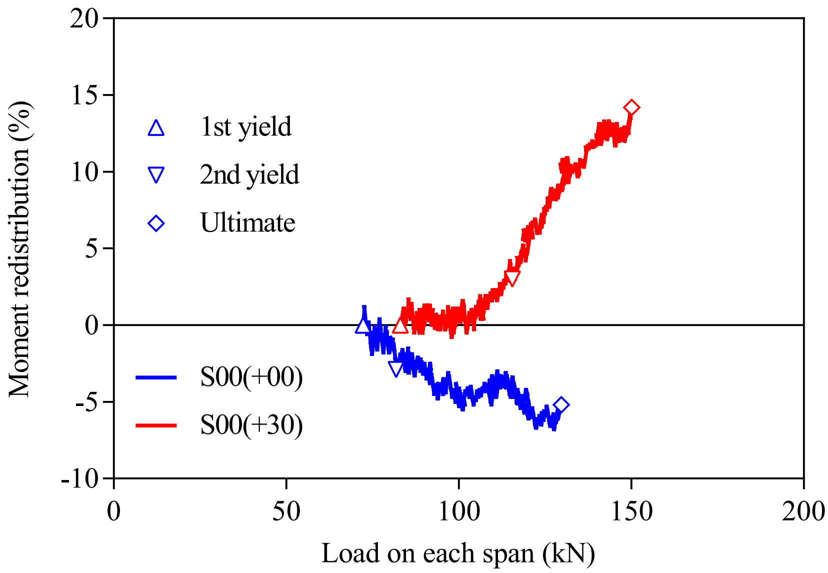

(b)

Figure 4.31: Load versus moment redistribution for the (a) R-SFRC and (b) RC specimens.

Specimens S60(+00), S60(+10), S60(+20) and S60(+30) (i.e. Series A specimens) were designed to have nominally 0, +10 +20 and +30% of moment redistribution, respectively, based on the design material properties. As two full plastic hinges formed in all tests, one at the mid-span of the critical member and one over the intermediate support, the full moment redistribution capabilities were attained as designed.

Specimens S60(+00), S60(+10), S60(+20) and S60(+30) achieved −7.9%, 15.0%, 22.8% and 30.5% moment redistribution, respectively, at the peak load based on the theoretical linear-elastic moments. The actual (plastic) moment redistributions after the first yield were −12.6%, −6.2%, 8.2% and 19.3%.

Although specimens S60(+00) and S60(+10) were designed for positive moment redistribution based on the design material properties, the moment redistribution demands were slightly negative based on the actual material properties. The negative moment redistribution of specimens S60(+00) and S60(+10) is also evident from the load versus strain diagrams, as the hinges formed at the critical mid-span first and then at the intermediate support (see Figures 4.12 and 4.15).

Specimens S00(+00) and S00(+30) (i.e. Series B specimens) achieved −5.3% and 26.0% moment redistribution, respectively, at peak load based on the theoretical linear-elastic analysis results. The actual moment redistributions after the first yield were −5.2% and 14.2%, respectively.

4.4 Conclusions

An experimental study was undertaken to investigate the moment redistribution capability and post-peak behaviour of R-SFRC continuous one-way slabs with low tensile reinforcement ratios. The experimental study included six specimens; four specimens with both fibres and conventional reinforcement, and two specimens with just conventional reinforcement. The specimens were 800 mm wide, 220 mm deep and 8.2 m long (4.0 m spans). The nominal dosage of steel fibres in the R-SFRC specimens was 60 kg/m^3 (average as-cast fibre dosages were 66.4 and 54.9 kg/m^3 for two different batches). The R-SFRC specimens were designed for 0 to 30% of positive moment redistribution with respect to the linear-elastic condition by varying the tensile reinforcement ratios between 0.21% and 0.42%.

The behaviour of two R-SFRC specimens was compared with equivalent RC specimens having the same design flexural capacity and moment redistribution. The test results show that the R-SFRC specimens had higher service stiffness, smaller crack width and crack spacing, and lower curvature than that of the RC specimens. Although crack localisation happened in both RC and R-SFRC specimens, the RC specimens showed lengthy hardening regions after the formation of second plastic hinge; whereas, the R-SFRC specimens showed a shorter displacement length over which hardening occurred before the peak load was reached, followed by a period of gentle softening. A comparison of ductility based on displacement and work done indicates that all specimens had a good level of ductility; however, the deflection of the R-SFRC specimens was less than the desired span/100 at ultimate. Therefore, some limitations in reinforcement are appropriate for R-SFRC flexural members to ensure sufficient ductility up to a displacement of span/100. It is to be noted that the point loads applied in the tests provide for high moment gradients, enhancing the effects of localisation. The influence of load type will be further investigated through parametric studies in Chapter 5. For both the RC and R-SFRC slabs, the amount of ductility decreased with increasing moment redistribution.

In all tests, two full plastic hinges formed, one at the mid-span of the critical member and one over the intermediate support, before the peak (ultimate) load was recorded. Thus, it is concluded that the full design moment redistribution was achieved in all cases. The ductility demand in the real system is less than that based on linear-elastic theory; this is due to the inelastic realities that occur in reinforced concrete members and structures. The theoretical moment redistributions for the R-SFRC slabs at peak load, based on linear-elastic moment, were −7.9%, 15.0%, 22.8% and 30.5% for specimens S60(+00), S60(+10), S60(+20) and S60(+30), respectively. The actual moment redistributions at peak load, after the first yielding of reinforcement, were −12.6%, −6.2%, 8.2% and 19.3% for specimens S60(+00), S60(+10), S60(+20) and S60(+30), respectively.

Chapter 5

FINITE ELEMENT MODELLING OF R-SFRC FLEXURAL MEMBERS

5.1 Introduction

In this chapter, two-dimensional (2D) finite element (FE) models of R-SFRC flexural members are developed using the FE program RECAP [143, 144]. In the FE modelling, the concrete and the reinforcement are modelled as discrete elements with the concrete being modelled as 2D orthotropic membrane element and the reinforcement being modelled as two-node truss element. The details of finite element formulation and material laws can be found in the works of Foster [143-146]. The constitutive relationship for orthotropic membranes, the constitutive models for the materials and the cracking approach used in the FE modelling are presented briefly in the following sections. Finally, the developed FE models are validated using the test data from this study and the validated FE models are used for parametric studies to determine the effect of the softening of SFRC, the hardening of tensile reinforcement and the type of loading on the post-peak behaviour of R-SFRC flexural members.

5.2 Constitutive relationship for orthotropic membranes

Two-dimensional orthotropic membranes are used to model the concrete elements in the FE modelling. RECAP utilizes the concept of equivalent uniaxial strains developed by Darwin and Pecknold [147] for the analysis of RC membranes subjected to biaxial stresses. The equivalent uniaxial strain approach allows the use of uniaxial stress-strain curves to predict the biaxial behaviour of concrete. The equivalent uniaxial strain can be thought of as the strain that would exist in one direction when the stress in the other direction is zero and can be written as:

$$\begin{Bmatrix} \varepsilon_1 \\ \varepsilon_2 \end{Bmatrix} = \begin{bmatrix} 1 & -\nu_{12} \\ -\nu_{21} & 1 \end{bmatrix} \begin{Bmatrix} \varepsilon_{1u} \\ \varepsilon_{2u} \end{Bmatrix} \tag{5.1}$$

where ε_1 and ε_2 are the strains in the principal directions; ε_{1u} and ε_{2u} are the equivalent uniaxial strains in the principal directions; ν_{12} and ν_{21} are the Poisson's ratio for the strain in the 1- and 2-direction due to a strain in the other direction.

The equivalent uniaxial strains are obtained by inverting the coefficient matrix of Equation 5.1:

$$\begin{Bmatrix} \varepsilon_{1\mathrm{u}} \\ \varepsilon_{2\mathrm{u}} \end{Bmatrix} = \frac{1}{1 - \nu_{12}\nu_{21}} \begin{bmatrix} 1 & \nu_{12} \\ \nu_{21} & 1 \end{bmatrix} \begin{Bmatrix} \varepsilon_1 \\ \varepsilon_2 \end{Bmatrix} \tag{5.2}$$

The stress is then obtained from the uniaxial base material models and given by:

$$\begin{Bmatrix} \sigma_{\mathrm{c}1} \\ \sigma_{\mathrm{c}2} \end{Bmatrix} = \begin{bmatrix} E_{c1} & 0 \\ 0 & E_{c2} \end{bmatrix} \begin{Bmatrix} \varepsilon_{1\mathrm{u}} \\ \varepsilon_{2\mathrm{u}} \end{Bmatrix} \ldots (i = 1{,}2) \tag{5.3}$$

where E_{c1} and E_{c2} are the secant moduli in the principal (1,2) stress directions determined from the appropriate uniaxial stress-strain curve.

Relating the stresses and strains in the familiar manner of $\{\sigma\} = [D]\{\varepsilon\}$, the material elasticity matrix in the material 1-2 coordinate system is taken as that suggested by Darwin and Pecknold [147] and given as:

$$[D]_{c12} = \frac{1}{(1 - \nu_{12}\nu_{21})} \begin{bmatrix} E_{c1} & \sqrt{\nu_{12}E_{c1}\nu_{21}E_{c2}} & 0 \\ \ldots & E_{c2} & 0 \\ sym. & \ldots & (1 - \nu_{12}\nu_{21})G_{c12} \end{bmatrix} \tag{5.4}$$

The shear modulus, G_{c12} is taken as that of Attard et al. [148] and is given by:

$$G_{c12} = \frac{1}{4(1 - \nu_{12}\nu_{21})} \left[E_{c1}(1 - \nu_{12}) + E_{c2}(1 - \nu_{21})\right] \tag{5.5}$$

For cracked concrete, the Poisson's ratios are taken as zero and Equation 5.4 reduces to:

$$[D]_{c12} = \begin{bmatrix} E_{c1} & 0 & 0 \\ 0 & E_{c2} & 0 \\ 0 & 0 & G_{c12} \end{bmatrix} \tag{5.6}$$

For the construction of the element stiffness matrix in global coordinates, the material stiffness is transformed such that:

$$[D]_{cxy} = [T]_{\varepsilon}^{T}[D]_{c12}[T]_{\varepsilon} \tag{5.7}$$

where $[T]_{\varepsilon}$ is the strain transformation matrix.

Finally, the element stiffness matrix is obtained in the usual manner:

$$[k] = t\int_{A} [B]^{T}[D]_{xy}[B]dA \tag{5.8}$$

where t is the element thickness and $[B]$ is the strain displacement matrix.

5.3 Constitutive models for materials

5.3.1 Reinforcing steel

A tri-linear stress-strain relationship as shown in Figure 5.1 is adopted for longitudinal tensile and compressive reinforcement and transverse reinforcement (if any), where E_s is the modulus of elasticity of steel. The stress and strain at the yielding of reinforcement are f_{sy} and ε_{sy}, respectively; f_{sw} is the tensile stress corresponding to a strain of ε_{sw}. The ultimate stress and strain at the point of fracture of reinforcement are f_{su} and ε_{su}, respectively.

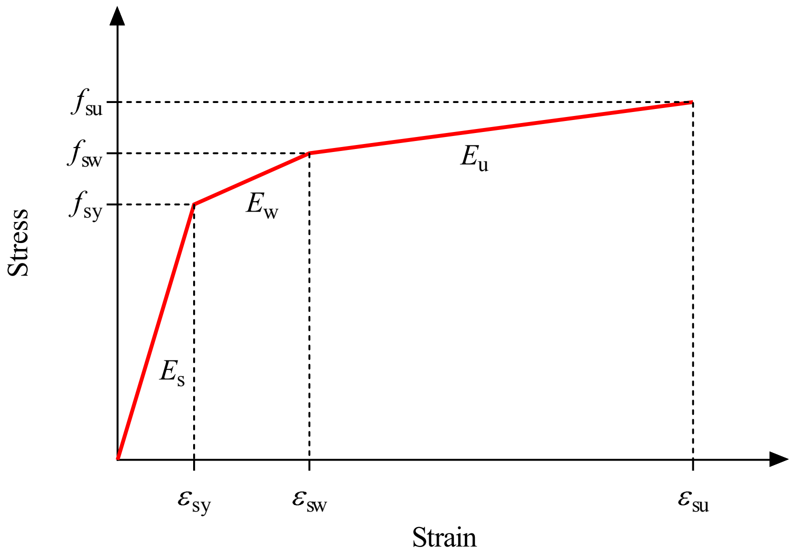

Figure 5.1: Stress-strain relationship for reinforcing bars in tension.

5.3.2 Steel fibre reinforced concrete

In the FE modelling, SFRC is simulated by superposing the contribution of steel fibres to the constitutive law of plain concrete. The compressive properties of concrete are not affected significantly by the inclusion of steel fibres in conventional dosages. Consequently, the stress-strain relationship of plain concrete proposed by Thorenfeldt et at. [149] is used to model the concrete in compression, and is given by:

$$f_c = f_{cp} \frac{n\eta}{n - 1 + \eta^{nk}} \tag{5.9}$$

where $\eta = \varepsilon_c/\varepsilon_{cp}$, ε_c is the concrete strain and ε_{cp} is the strain corresponding to the peak in-situ stress f_{cp}; n is a curve-fitting factor given by $n = E_0/(E_0 - E_{cp})$, E_0 is the initial modulus of elasticity of concrete and $E_{cp} = f_{cp}/\varepsilon_{cp}$ is the secant modulus; and k is a decay factor for the pre- and post-peak responses.

For the stress-strain law of concrete in tension, a bi-linear model proposed by Petersson [150] as shown in Figure 5.2 is used with the tension softening parameters:

$$\alpha_1 = \frac{1}{3};\ \alpha_2 = \frac{2}{9}\alpha_3 + \alpha_1\ ;\ \alpha_3 = \frac{18}{5}\frac{E_0 G_{FM}}{l_{ch} f_{ct}^2} \tag{5.10}$$

where f_{ct} is the tensile strength of plain concrete; E_0 is the initial elastic modulus of concrete; G_{FM} is the fracture energy of concrete; and l_{ch} is the characteristic length of finite element.

The contribution of steel fibres after the cracking of concrete is represented by the Variable Engagement Model (VEM) proposed by Voo and Foster [151, 152]. According to VEM, the tensile strength provided by fibres is given by:

$$f_{tf} = K_f \alpha_f \rho_f \tau_b \tag{5.11}$$

where $\alpha_f = l_f/d_f$ is the aspect ratio of the fibre, l_f is the length of the fibre and d_f is the diameter of the fibre; ρ_f is the fibre volumetric ratio; τ_b is the average bond shear strength at the fibre and matrix interface. The global orientation factor, K_f, is given by:

$$K_f = \frac{\operatorname{atan}[w/\alpha_I l_f)]}{\pi}\left[1 - \frac{2w}{l_f}\right]^2 \tag{5.12}$$

where w is the crack width and α_I is the engagement parameter.

Figure 5.3 shows the resultant tensile stress versus COD of SFRC by adding the contribution of fibres to the constitutive law of plain concrete.

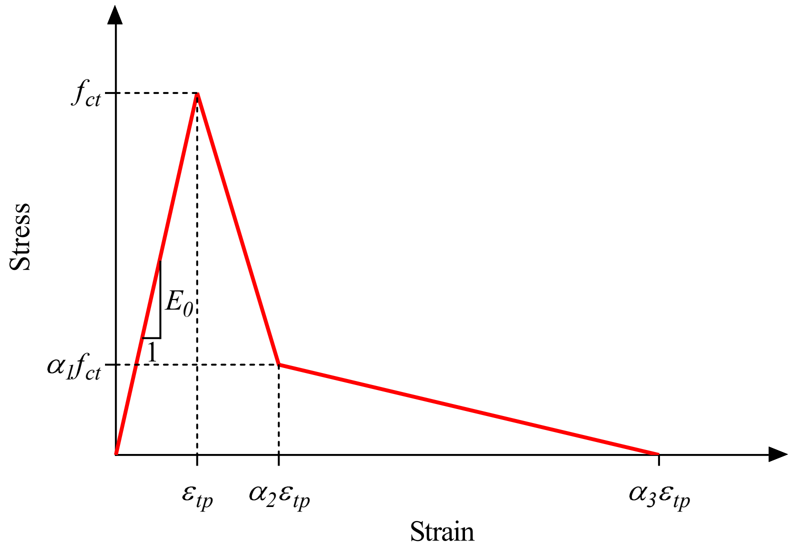

Figure 5.2: Stress-strain relationship for concrete in tension.

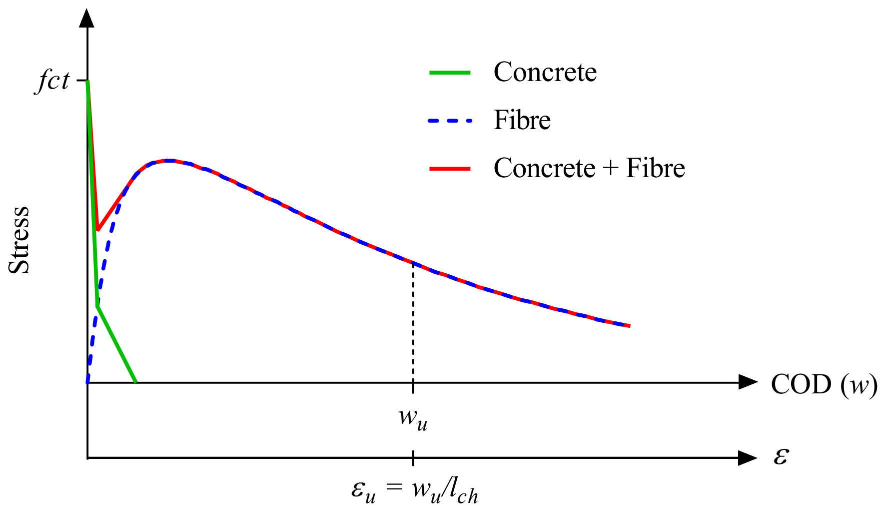

.

Figure 5.3: Stress-COD and stress-strain relationship for SFRC in tension.

5.4 Cracking approach

In the FE modelling, the non-local smeared rotating crack approach is used to simulate the cracking in concrete. Two major approaches, namely the discrete crack approach [153-156] and the smeared crack approach [157, 158], are available in the literature to model the cracking in concrete. In the discrete crack model, cracking is considered as a discontinuity in a structure which propagates through elements. The discrete crack model is limited by predefined crack trajectory and is computationally costly and inefficient due to the generation of additional nodes along the crack faces.

The smeared crack approach is based on the framework of the continuum mechanics where cracking is smeared over a certain volume of material and treated as a reduction of material stiffness in the direction of major principal stresses. The advantage of the smeared crack approach over the discrete crack approach is unchanged mesh topology of a structure during the formation of cracks, which makes numerical implementation convenient. Moreover, the cracking in RC members is usually distributed in nature due to the presence of reinforcement; therefore, the distributed nature of cracking in the smeared crack approach best describes the cracking phenomenon in most RC structures.

Smeared crack approach can be divided into fixed crack models [157, 159, 160] and rotating crack models [145, 158, 161, 162]. In the fixed crack model, the crack initiates normal to the major principal stress and has a fixed direction throughout the loading the process, whereas in the rotating crack model, the crack direction rotates with the principal stress directions during the entire loading process. For flexure, as there is little rotation of cracks, both fixed and rotation crack models give almost the same prediction [163]. In this study, the rotating crack model by Foster et al. [145] is adopted.

The classical smeared crack approach suffers from mesh sensitivity due to localizing crack into a single row of elements. Since the local strain softening constitutive law governs the energy dissipation per unit volume, the energy dissipation decreases to zero as the mesh size reduces to infinitely small causing spurious mesh sensitivity. Moreover, the fracture of concrete involves dense microcracking over a certain length in the fracture zone. Therefore, apart from the mathematical shortcoming, the local continuum models are not able to accurately describe the physical process of fracture in concrete.

In the non-local models [164-167], the stress at a point in a non-local continuum depends on the weighted average of a state variable in the neighbourhood within a distance from that point. A constant energy release rate in the fracture process zone is ensured by introducing an internal length scale [166, 167] or a characteristic length [164, 165] into the constitutive model. In the first non-local model called by “imbricate continuum model” [168], the strain was taken to be the state variable for non-local averaging. Although the model ensures mesh insensitivity, the model involves complicated computations which hinder straightforward numerical implementation [169].

The deficiencies in the “imbricate continuum model” was overcome by the introduction of the concept of non-local continuum with local strain [169]. In the non-local continuum with local strain-based model, the strain at a point in a continuum is kept local while the constitutive relation for strain softening is dependent on the non-local state variable. The drawback of the non-local continuum with local strain-based model is that in some instances, the non-local strain can be lower than the local strain leading to a stress level higher than the tensile strength of the material. Although the formulation does not pose problems in structural fracture analysis, the violation of tensile strength from a structural perspective is undesirable.

In this study, cracking is modelled based on the principle of non-local damage model proposed by Bažant and Pijaudier-Cabot [164]. To avoid tensile stress higher than the tensile strength of concrete, only the strain softening is treated non-locally, while the elastic related variables are treated locally as in the conventional smeared crack model. The total strains are calculated by summing the local elastic component of strain with the non-local plastic component as:

$$\begin{gathered} \bar{\varepsilon}_{iu} = \varepsilon_{iu}, \text{ for } \varepsilon_{iu} \leq \varepsilon_{cr} \\ \bar{\varepsilon}_{iu} = \varepsilon_{iu.e} + \bar{\varepsilon}_{iu.p}, \text{ for } \varepsilon_{iu} > \varepsilon_{cr} \end{gathered} \tag{5.13}$$

where $\varepsilon_{iu.e}$ (i = 1, 2) is the local elastic component of strain, $\bar{\varepsilon}_{iu.p}$ is the non-local plastic component of strain and ε_{cr} is the cracking strain. The local elastic and plastic components are calculated as:

$$\begin{gathered} \varepsilon_{iu.e} = \sigma_1 / E_0 \\ \varepsilon_{iu.p} = \varepsilon_{iu} - \varepsilon_{iu.e} \end{gathered} \tag{5.14}$$

where σ_1 is the local stress corresponding to the local total strain, ε_{iu}, and calculated from the material stress-strain law and E_0 is the initial elastic modulus.

Adopting the methodology of Jirásek and Zimmermann [170], the non-local plastic strains are obtained from the local plastic strains of all source points located within a region A, centred at the target point (Figure 5.4a), such that:

$$\bar{\varepsilon}_{iu.p} = \int_A \gamma'(r)\varepsilon_{iu.p}(r,\theta)dA \tag{5.15}$$

where $\gamma'(r)$ is a spatial weighting factor given by:

$$\gamma'(r) = \frac{\gamma(r)}{\int_A \gamma(r)dA} \tag{5.16}$$

The integral denominator in Equation 5.16 is obtained numerically with the weighting factors taken at the element Gauss points. As these points can be irregularly spaced, the weighting factors are normalized against the sum of the weights for all source points within A so that $\sum\gamma'(r)$ is guaranteed to be unity irrespective of the number of source points or their distribution. Only source points with a positive (tensile) strain in the principal direction being considered are included in the calculation of $\gamma(r)$.

For calculating the weight for each source point the bell-shaped function of Bažant and Ozbolt [165] is used (Figure 5.4b), that is:

$$\gamma(r) = \langle 1-(r/R)^2\rangle^2 \tag{5.17}$$

with $R = 0.9086 l_{ch}$; and l_{ch} is the characteristic length.

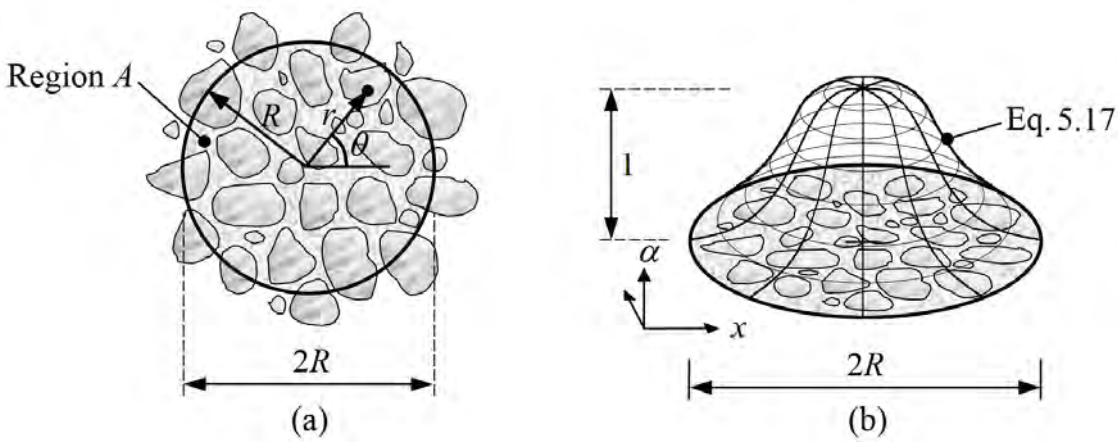

Figure 5.4: (a) Non-local neighbourhood; and (b) bell-shaped weight function [171].

5.5 Experimental verification

5.5.1 R-SFRC beams tested in this study (Chapter 3)

The experimental results of four R-SFRC beam specimens were reported in Chapter 3. Figure 5.5 shows the FE model of the beam specimens. One-half of the specimens are modelled accounting for symmetry. The FE mesh consists of 4-node isoparametric elements for the concrete elements and 4-node stiff elements for the steel plates. The size of the mesh is 20 mm.

The reinforcing steel bars in the specimens are modelled as 2-node bar elements. Perfect bond is assumed between the steel and the concrete. Figure 5.6 shows a comparison of the idealised tensile stress-strain relationships of the reinforcing bars used in the modelling with the test results. The stress-strain values at different points of idealised tensile stress-strain relationships of the reinforcing bars are provided in Table 5.1.

The material parameters used to develop the constitutive law of the SFRC are provided in Table 5.2. The compressive strength and the modulus of elasticity of concrete are determined from the stress-strain test of concrete in compression. To model the stress-strain relationship of concrete in compression based on Thorenfeldt et at. [149], the decay factor k is taken as 1. Figure 5.7 shows a comparison of the idealised stress-strain relationship for concrete in compression used in the modelling with the test results.

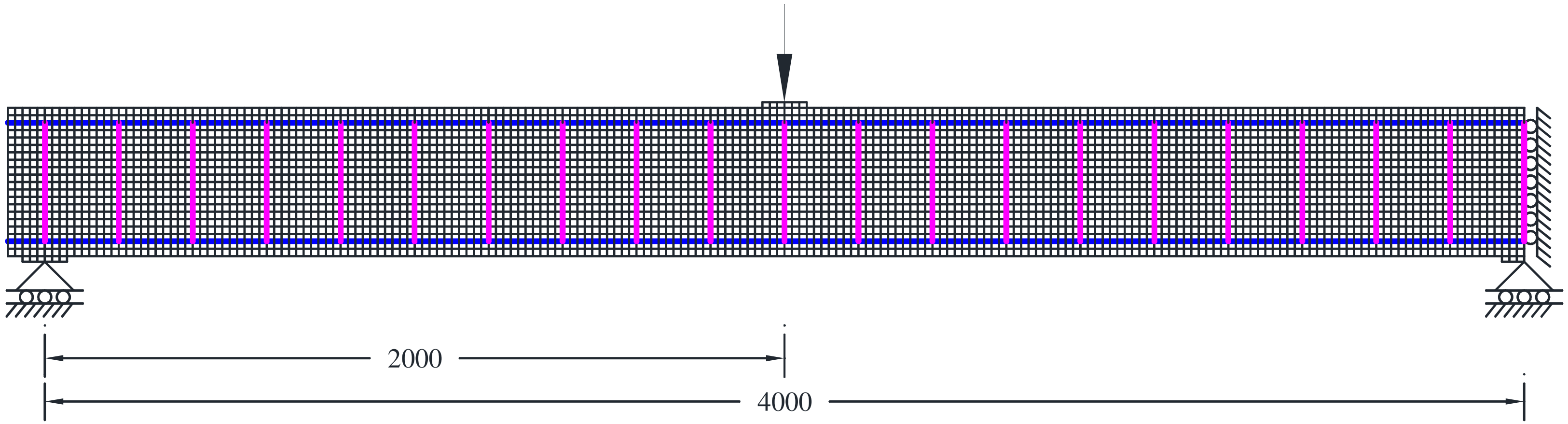

(a) Meshing

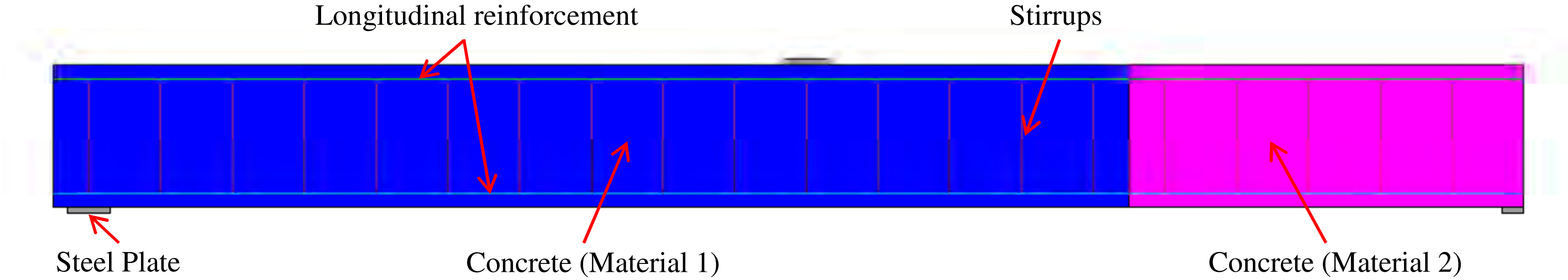

(b) FE modelling

Figure 5.5: Geometric modelling of the tested beam specimen.

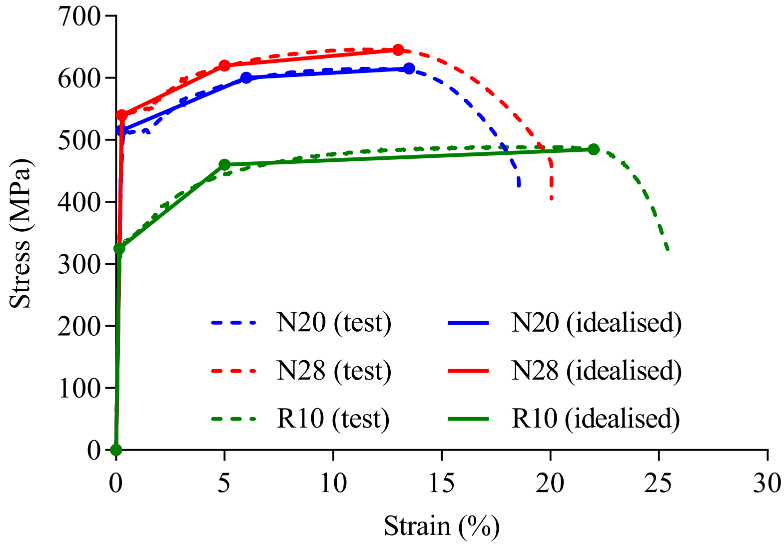

Figure 5.6: Tensile stress-strain relationship for the reinforcing steel bars used in the beam specimens.

Table 5.1: Material properties of the reinforcing bars used in the modelling of the beam specimens tested in this study.

	N20	**N28**	**R10**
E_s (MPa)	196000	197000	210000
ε_{sy} (%)	0.2650	0.2740	0.1550
ε_{sw} (%)	6.0	5.0	5.0
ε_{su} (%)	13.5	13.0	22.0
f_{sy} (MPa)	520	540	325
f_{sw} (MPa)	600	620	460
f_{su} (MPa)	615	645	485

To model the stress-strain relationship of concrete in tension based on Petersson [150], the tensile strength of concrete is taken as $0.36\sqrt{f_{cp}}$, which allows for residual stresses due to shrinkage strains, and the matrix fracture energy is taken as $73f_{cp}^{0.18}$ (N/m) as per *fib* Model Code 2010 [30]. The mean crack spacing is taken as the value of characteristic length for the conversion of crack width to concrete strain [30]. From the crack patterns of the specimens (provided in Chapter 3 and Appendix B), it is evident that the crack spacings at mid-span and intermediate support are different. Thus, to simulate the test responses, the characteristic lengths at mid-span (Material 1) and at intermediate support (Material 2) are varied (see Figure 5.5b). The approximate point of contraflexure is taken as the boundary between the materials of different crack spacings. The crack spacings and the calculated values of α_1, α_2 and α_3 are provided in Table 5.2.

It is noted that no calibration has been undertaken for the VEM for the 5D fibres used in this study. Here the VEM parameters of Equations 5.11 and 5.12 are adjusted to provide a best fit to the tensile stress-COD results obtained from the materials testing, giving an idealised curve of good fit. Figure 5.8 shows a comparison of the idealised stress-COD relationships used in the modelling with the dog-bone test results.

For the non-local crack model, the characteristic length is taken as 30 mm being three times the size of the aggregate size [172].

Table 5.2: Material properties of concrete used in the modelling of the beam specimens tested in this study.

Material properties	**Specimen**							
	B30(−30)		**B30(+30)**		**B60(−30)**		**B60(+30)**	
	Mid-span	Intermediate Support	Mid-span	Intermediate Support	Mid-span	Intermediate Support	Mid-span	Intermediate Support
E_0 (MPa)	30800		30800		28000		28000	
ν	0.20		0.20		0.20		0.20	
f_{cp} (MPa)	59.5		59.5		51.7		51.7	
f_{ct} (MPa)	2.78		2.78		2.59		2.59	
G_{FM} (N/m)	152.3		152.3		148.5		148.5	
ε_{cp}	0.003		0.003		0.003		0.003	
k	1.0		1.0		1.0		1.0	
l_{ch} (mm)	99	101	106	206	69	139	89	188
α_1	0.33	0.33	0.33	0.33	0.33	0.33	0.33	0.33
α_2	5.23	5.14	4.91	2.69	7.52	3.90	5.91	2.97
α_3	22.1	21.6	20.6	10.6	32.3	16.1	25.1	11.9

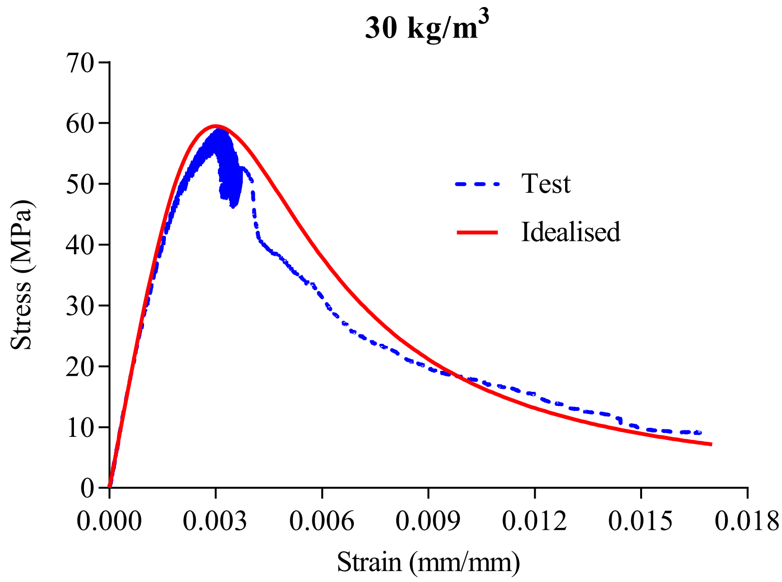

(a)

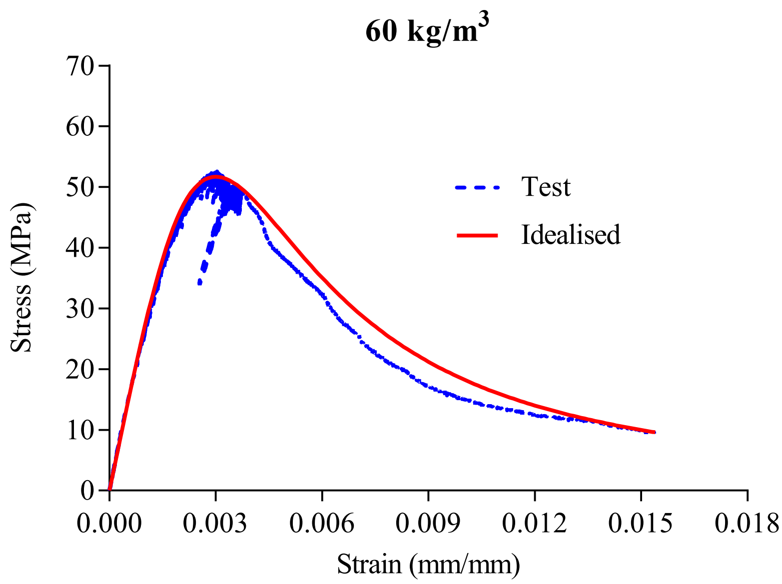

(b)

Figure 5.7: Stress-strain diagram for concrete in compression for fibre dosages of (a) 30 kg/m^3 and (b) 60 kg/m^3.

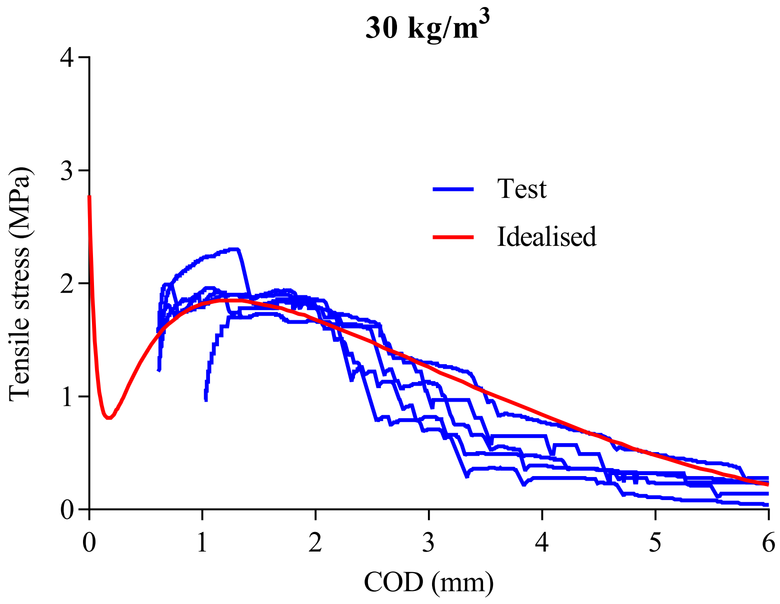

(a)

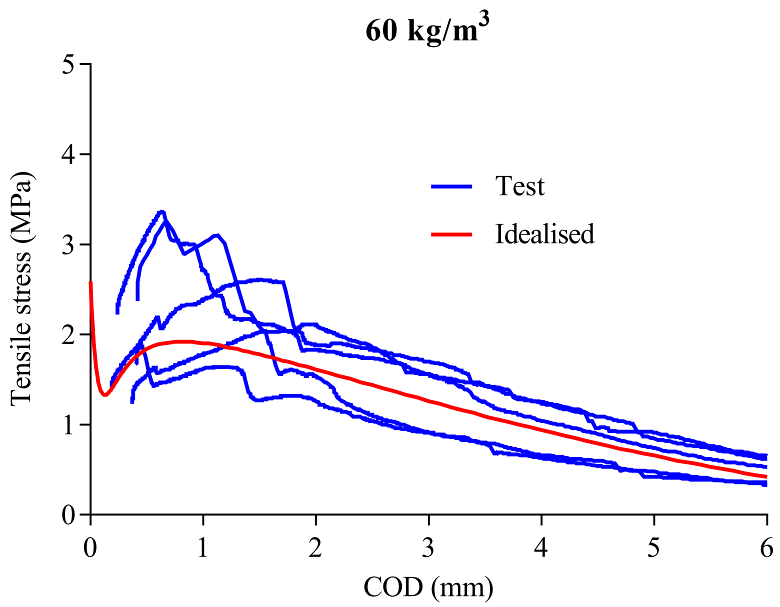

(b)

Figure 5.8: Tensile stress versus COD relationship for fibre dosages of (a) 30 kg/m^3 and (b) 60 kg/m^3.

Table 5.3 shows a comparison of the ultimate loads obtained from the FE modelling with the results from the experimental testing. The mean theoretical to experimental ratio for the ultimate load is 1.01 with a coefficient of variation of 0.022. Figure 5.9 shows that the FE results compared well with the experimental data for the mid-span deflection of the beams.

A comparison of crack patterns from the experiments and FE modelling (principal strains) for the beam specimens at a deflection of 40 mm (span/100) is shown in Figure 5.10. The localisation of cracking at the mid-span and intermediate support is evident from the crack patterns. The direction of moment redistribution is also observed from the crack patterns. For specimen B30(−30) and B60(−30), the strains at the mid-span are higher than that of at the intermediate support indicating the formation of first hinge at mid-span and moment redistribution from mid-span to intermediate support and vice versa for specimens B30(+30) and B60(+30).

Table 5.3: Comparison of experimental ultimate load and deflection with FEM results for the beam specimens.

Specimen	$P_{u,exp}$ (kN)	$\Delta_{u,exp}$ (mm)	$P_{u,FEM}$ (kN)	$\Delta_{u,FEM}$ (mm)	$\frac{P_{u,FEM}}{P_{u,exp}}$
B30(−30)	278.1	41.7	288.4	48.8	1.04
B30(+30)	289.2	50.0	289.0	36.6	1.00
B60(−30)	299.2	31.2	295.0	29.1	0.99
B60(+30)	289.7	37.9	294.7	33.8	1.02
Average (COV)					**1.01 (0.022)**

Notes: 1. $P_{u,exp}$ and $P_{u,FEM}$ are ultimate loads from experiments and FEM, respectively.

2. $\Delta_{u,exp}$ and $\Delta_{u,FEM}$ are ultimate deflections from experiments and FEM, respectively.

Table 5.4 shows a comparison of crack widths obtained from the FE modelling with the test results at the first yielding of reinforcement (at a deflection of 12 mm). The mean model to test ratio for the crack widths is 1.13 with a coefficient of variation of 0.043.

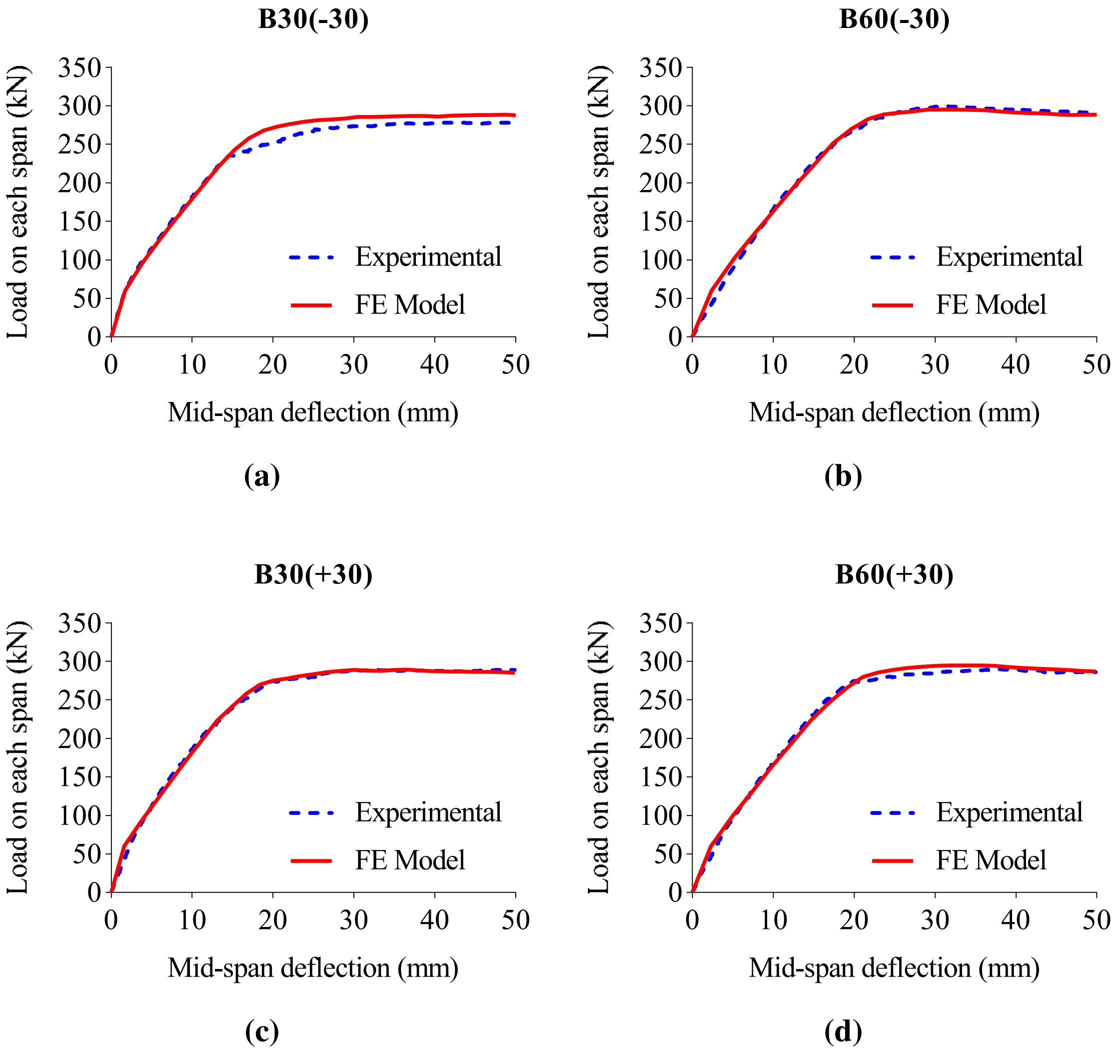

Figure 5.9: Load versus mid-span deflection plots for specimen (a) B30(-30), (b) B60(-30), (c) B30(+30) and (d) B60(-30).

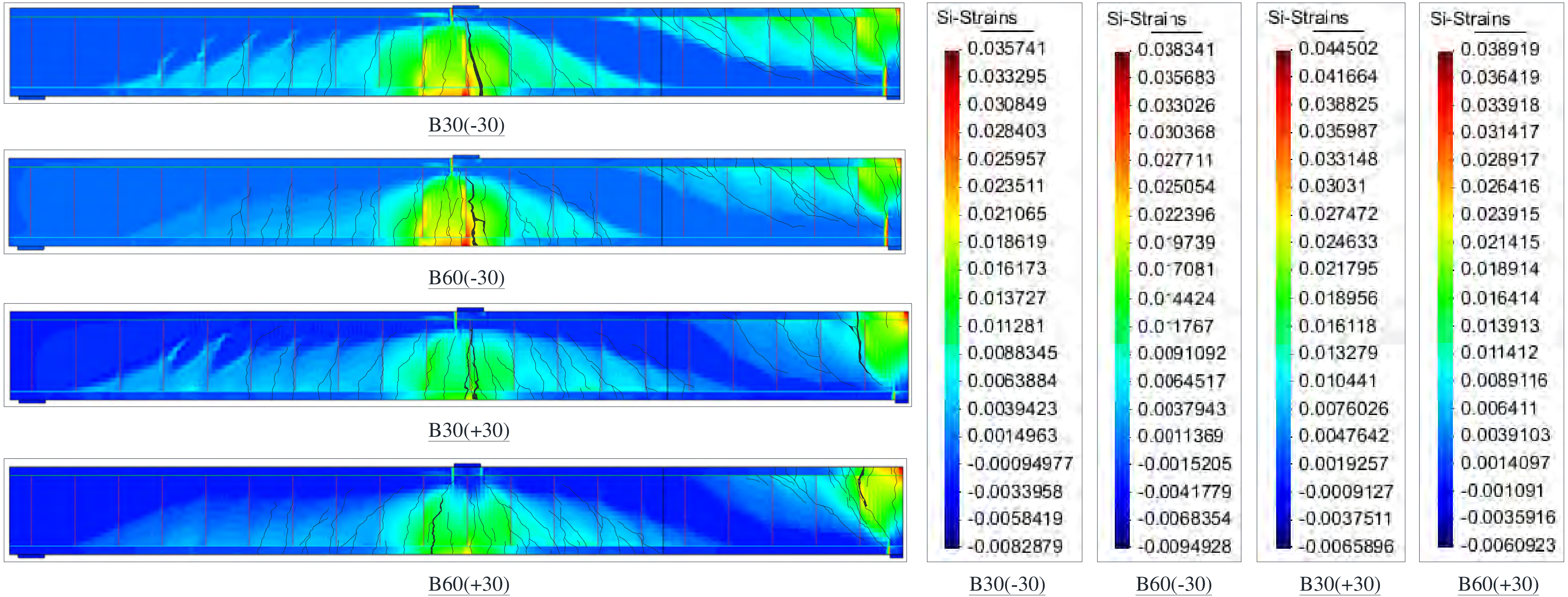

Figure 5.10: Comparison of crack patterns from experiments and FEM for the beam specimens.

Table 5.4: Comparison of experimental crack width with FEM results for the beam specimens.

Specimen	Intermediate support		Mid-span		Intermediate support	Mid-span	Average
	w_{exp} (mm)	w_{FEM} (mm)	w_{exp} (mm)	w_{FEM} (mm)	$\frac{w_{FEM}}{w_{exp}}$	$\frac{w_{FEM}}{w_{exp}}$	$\frac{w_{FEM}}{w_{exp}}$
B30(−30)	0.20	0.25	0.30	0.31	1.23	1.02	1.13
B60(−30)	0.30	0.34	0.20	0.21	1.13	1.07	1.10
B30(+30)	0.72	0.81	0.24	0.26	1.12	1.07	1.09
B60(+30)	0.56	0.76	0.20	0.21	1.36	1.07	1.22
Average (COV)							**1.13 (0.043)**

Note: w_{exp} and w_{FEM} are crack widths from experiments and FEM, respectively.

5.5.2 R-SFRC slabs tested in this study (Chapter 4)

The experimental results of four R-SFRC slab specimens were reported in Chapter 4. The FE modelling approach of the slab specimens is the same as that of the beam specimens reported in Section 5.5.1. Figure 5.11 shows the FE model of the slab specimens. The size of the mesh is 20 mm.

Figure 5.12 shows a comparison of the idealised tensile stress-strain relationships for the reinforcing steel bars used in the modelling with the test results. The stress-strain values at different points of idealised tensile stress-strain relationships of the reinforcing bars are provided in Table 5.5.

The material parameters used to develop the constitutive law of the SFRC are provided in Table 5.6. Figure 5.13 shows a comparison of the idealised stress-strain relationship for concrete in compression used in the modelling with the test results. Figure 5.14 shows a comparison of the idealised stress-COD relationships used in the modelling with the dog-bone test results.

Table 5.7 shows a comparison of the ultimate loads obtained from the FE modelling with the results from the experimental testing. The mean theoretical to experimental ratio for the ultimate load was 1.02 with a coefficient of variation of 0.058. Figure 5.15 shows that the FE results compared well with the experimental data for the mid-span deflection of the slab specimens.

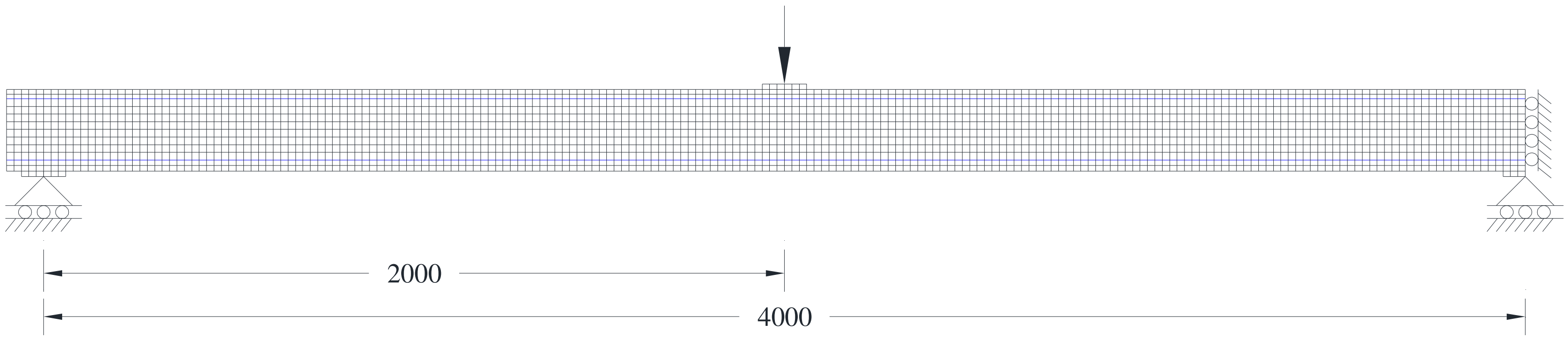

(a) Meshing

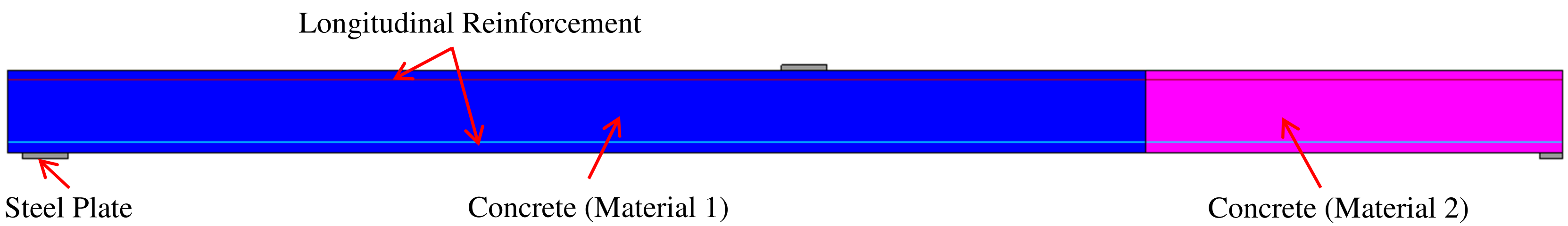

(b) FE modelling

Figure 5.11: Geometric modelling of the tested slab specimen.

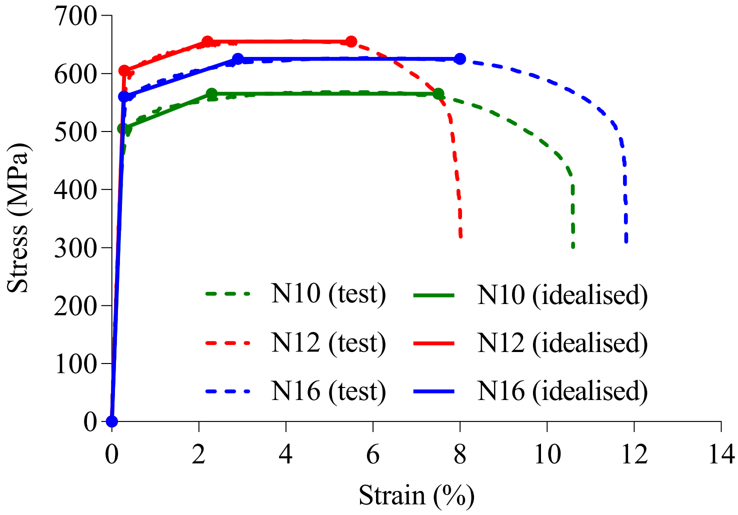

Figure 5.12: Tensile stress-strain relationship for the reinforcing bars used in the slab specimens.

Table 5.5: Material properties of the reinforcing bars used in the modelling of the slab specimens tested in this study.

	N10	**N12**	**N16**
E_s (MPa)	196000	207000	196000
ε_{sy} (%)	0.2575	0.2920	0.2855
ε_{sw} (%)	2.3	2.2	2.9
ε_{su} (%)	7.5	5.5	8.0
f_{sy} (MPa)	505	605	560
f_{sw} (MPa)	565	655	625
f_{su} (MPa)	565	655	625

Table 5.6: Material properties of concrete used in the modelling of the slab specimens tested in this study.

Material properties	Specimen							
	S60(+00)		S60(+10)		S60(+20)		S60(+30)	
	Mid-span	Intermediate Support	Mid-span	Intermediate Support	Mid-span	Intermediate Support	Mid-span	Intermediate Support
E_0 (MPa)	29500		29500		30100		30100	
ν	0.20		0.20		0.20		0.20	
f_{cp} (MPa)	28.1		28.1		41.7		41.7	
f_{ct} (MPa)	1.91		1.91		2.32		2.32	
G_{FM} (N/m)	133.1		133.1		142.9		142.9	
ε_{cp}	0.003		0.003		0.003		0.003	
k	1.0		1.0		1.0		1.0	
l_{ch} (mm)	146	156	174	163	162	173	174	148
α_1	0.33	0.33	0.33	0.33	0.33	0.33	0.33	0.33
α_2	6.23	5.85	5.28	5.62	4.28	4.03	4.01	4.66
α_3	26.5	24.8	22.3	23.8	17.8	16.6	16.5	19.5

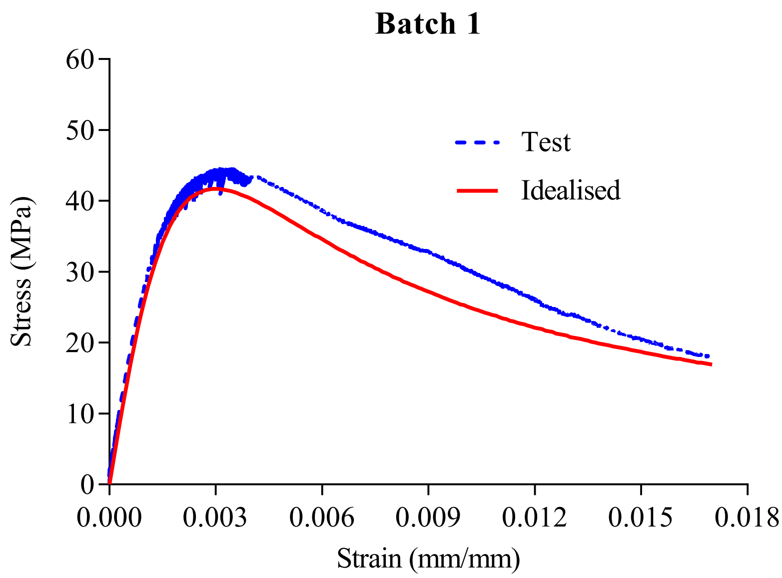

(a)

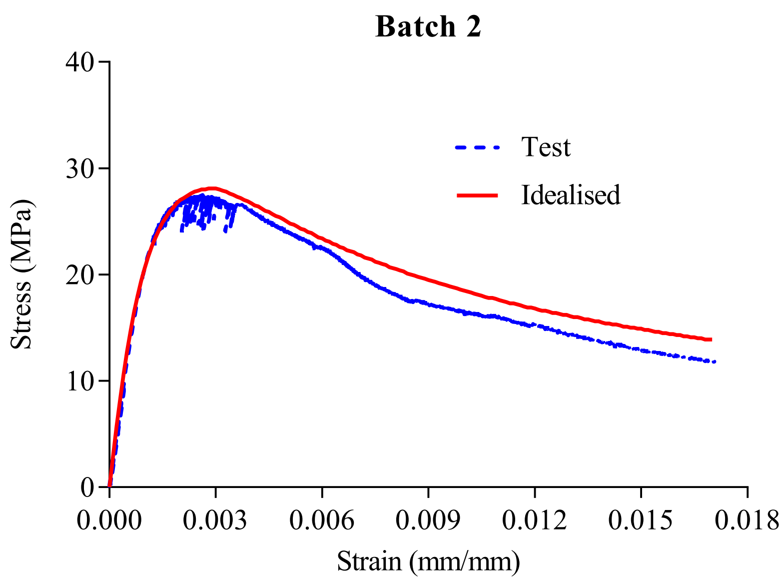

(b)

Figure 5.13: Stress-strain diagram for concrete in compression for SFRC (a) Batch 1 and (b) Batch 2.

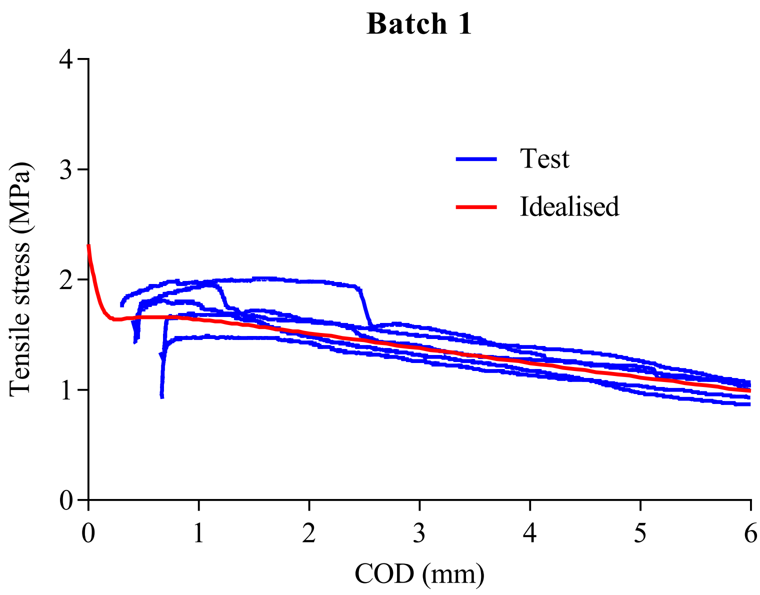

(a)

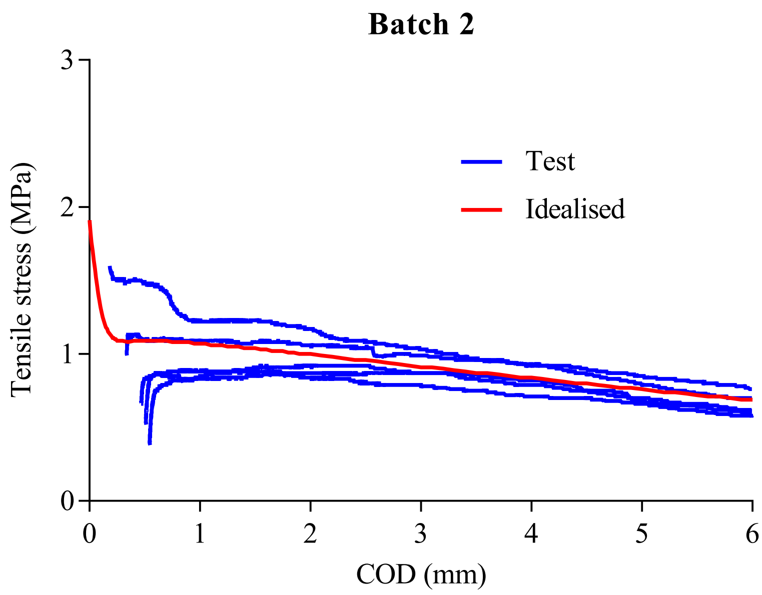

(b)

Figure 5.14: Tensile stress versus COD relationship for SFRC (a) Batch 1 and (b) Batch 2.

Table 5.7: Comparison of experimental ultimate load and deflection with FEM results for the slab specimens.

Specimen	$P_{u,exp}$ (kN)	$\Delta_{u,exp}$ (mm)	$P_{u,FEM}$ (kN)	$\Delta_{u,FEM}$ (mm)	$\frac{P_{u,FEM}}{P_{u,exp}}$
S60(+00)	90.7	30.2	94.2	35.1	1.04
S60(+10)	88.8	23.9	84.2	28.4	0.95
S60(+20)	110.3	26.8	119.9	28.1	1.09
S60(+30)	135.5	27.0	135.4	29.9	1.00
Average (COV)					**1.02 (0.058)**

Notes: 1. $P_{u,exp}$ and $P_{u,FEM}$ are ultimate loads from experiments and FEM, respectively.
2. $\Delta_{u,exp}$ and $\Delta_{u,FEM}$ are ultimate deflections from experiments and FEM, respectively.

A comparison of crack patterns from the experiments and FE modelling (principal strains) for the slab specimens at peak load is shown in Figure 5.16. The localisation of cracking at the mid-span and the intermediate support is evident from the crack patterns. The direction and the amount of moment redistribution are also obvious from the crack patterns. For specimens S60(+10), S60(+20) and S60(+30), the strains at the intermediate support are higher than that of at the mid-span indicating the formation of first hinge at the intermediate support and moment redistribution from the intermediate support to the mid-span, and as the amount of moment redistribution increases, strains are more localized at the intermediate support than that of at the mid-span. The formation of first hinge at the mid-span and negative moment redistribution for specimen S60(+00) also support the test data.

Table 5.8 shows a comparison of crack widths obtained from the FE modelling with the test results at the first yielding of reinforcement (at a deflection of 8 mm). The mean model to test ratio for the crack widths is 0.89 with a coefficient of variation of 0.051.

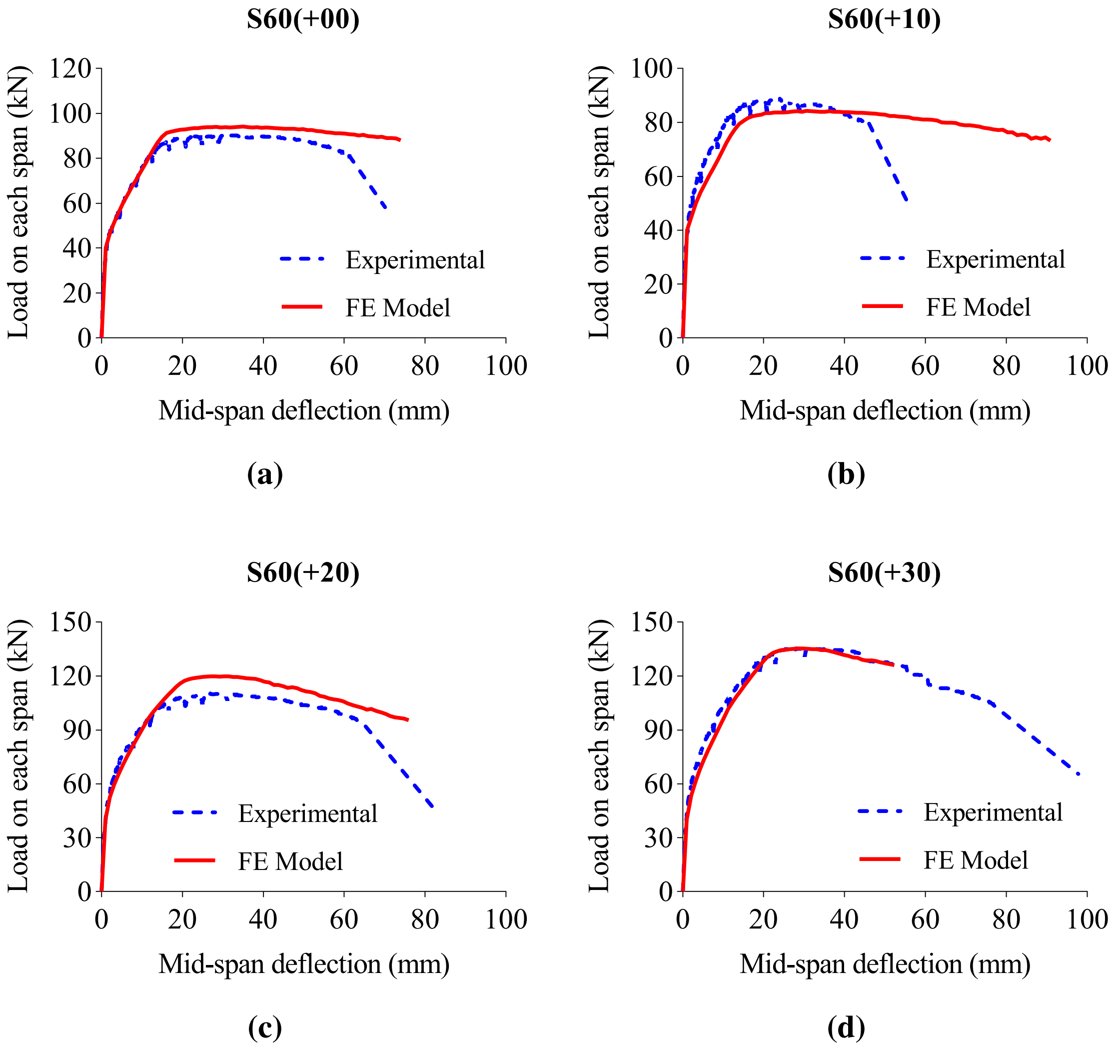

Figure 5.15: Load versus mid-span deflection plots for specimen (a) S60(+00), (b) S60(+10), (c) S60(+20) and (d) S60(+30).

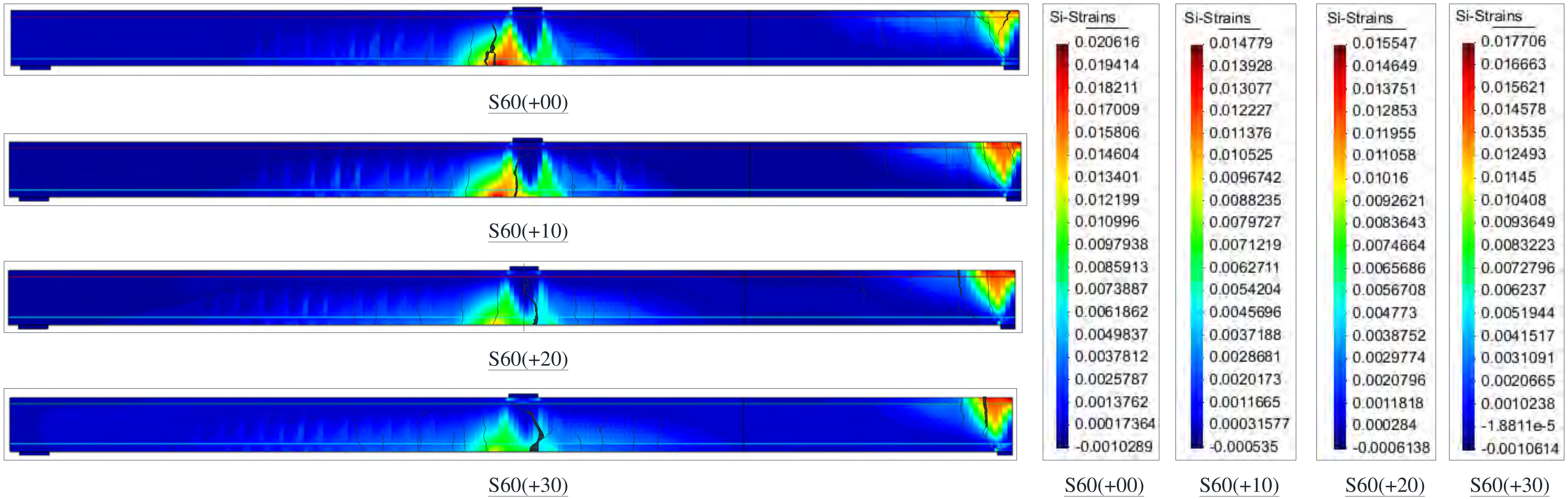

Figure 5.16: Comparison of crack patterns from experiments and FEM for the slab specimens.

Table 5.8: Comparison of experimental crack width with FEM results for the slab specimens.

Specimen	Intermediate support		Mid-span		Intermediate support	Mid-span	Average
	w_{exp} (mm)	w_{FEM} (mm)	w_{exp} (mm)	w_{FEM} (mm)	$\frac{w_{FEM}}{w_{exp}}$	$\frac{w_{FEM}}{w_{exp}}$	$\frac{w_{FEM}}{w_{exp}}$
S60(+00)	0.28	0.25	0.26	0.20	0.88	0.78	0.83
S60(+10)	0.32	0.29	0.30	0.24	0.92	0.79	0.86
S60(+20)	0.36	0.32	0.20	0.19	0.88	0.97	0.92
S60(+30)	0.42	0.30	0.18	0.21	0.71	1.17	0.94
Average (COV)							**0.89 (0.051)**

Note: w_{exp} and w_{FEM} are crack widths from experiments and FEM, respectively.

5.6 Parametric studies

To determine the effect of the softening of SFRC and the hardening of reinforcing steel bars on the post-peak behaviour of R-SFRC flexural members, parametric studies are performed using the validated beam and slab models.

5.6.1 Effect of the softening of SFRC

The slope of the idealised stress-COD relationships based on dog-bone test data is increased and decreased to find the effect of the softening of SFRC on the post-peak behaviour of R-SFRC flexural members. Figures 5.17 and 5.18 show the stress-COD relationships used for the parametric studies for the beam and the slab specimens, respectively. The stress-strain relationships of the reinforcing bars are kept constant among the specimens with different stress-COD relationships.

Figures 5.19 and 5.20 show a comparison of the load-deflection curves for different slopes of stress-COD relationships for the beam and the slab specimens, respectively. From the figures, it is evident that the post-peak behaviour of R-SFRC flexural members depends on the stress-COD relationship of SFRC. For the same stress-strain relationship of reinforcing bars, increasing the slope of the stress-COD relationship softens the post-peak behaviour whereas decreasing the slope of the stress-COD relationship improves the post-peak behaviour.

The effect of the slope of the stress-COD relationship is more pronounced in specimens with low amount of tensile reinforcement. The softening and hardening in the slab specimens, where the tensile reinforcement ratios are less than 0.5%, are more obvious than that of the beam specimens where the tensile reinforcement ratios are more than 0.5%.

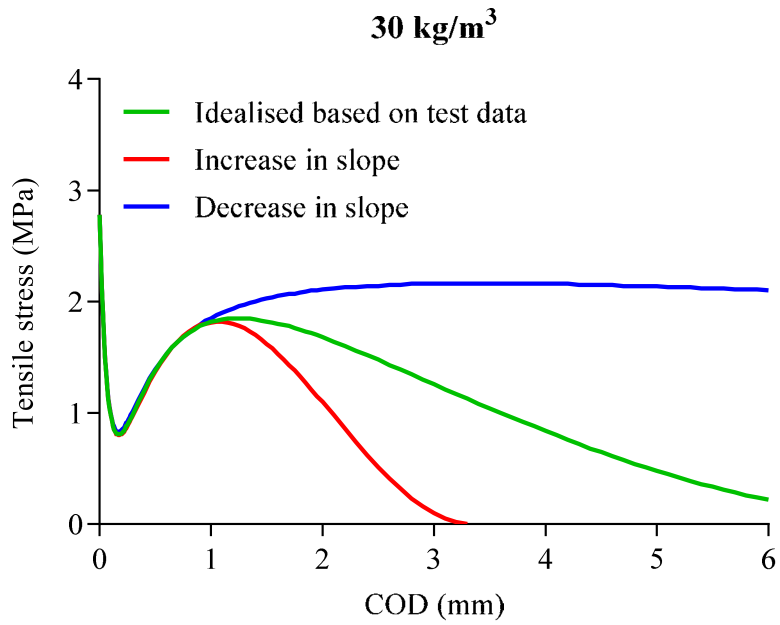

(a)

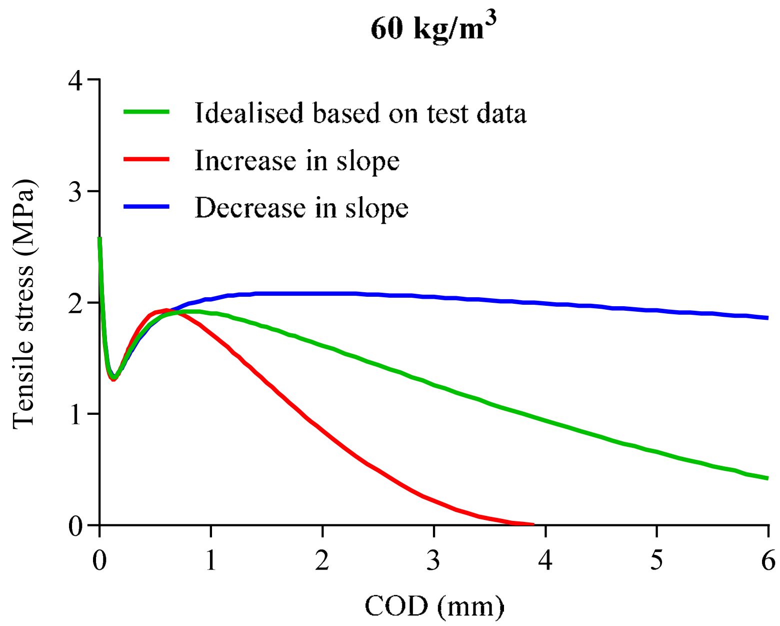

(b)

Figure 5.17: Tensile stress versus COD relationships used for parametric studies for fibre dosages of (a) 30 kg/m^3 and (b) 60 kg/m^3.

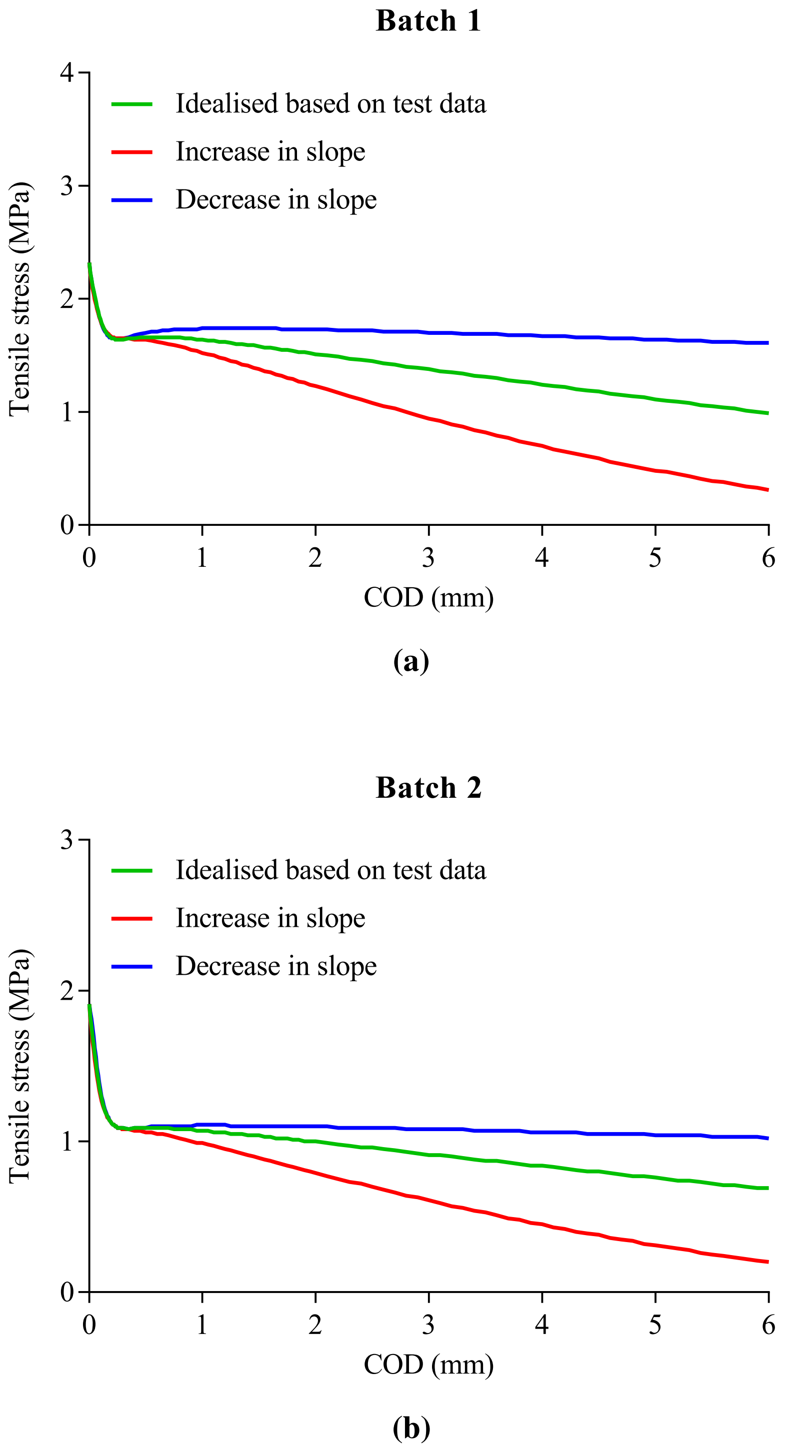

Figure 5.18: Tensile stress versus COD relationships used for parametric studies for SFRC (a) Batch 1 and (b) Batch 2.

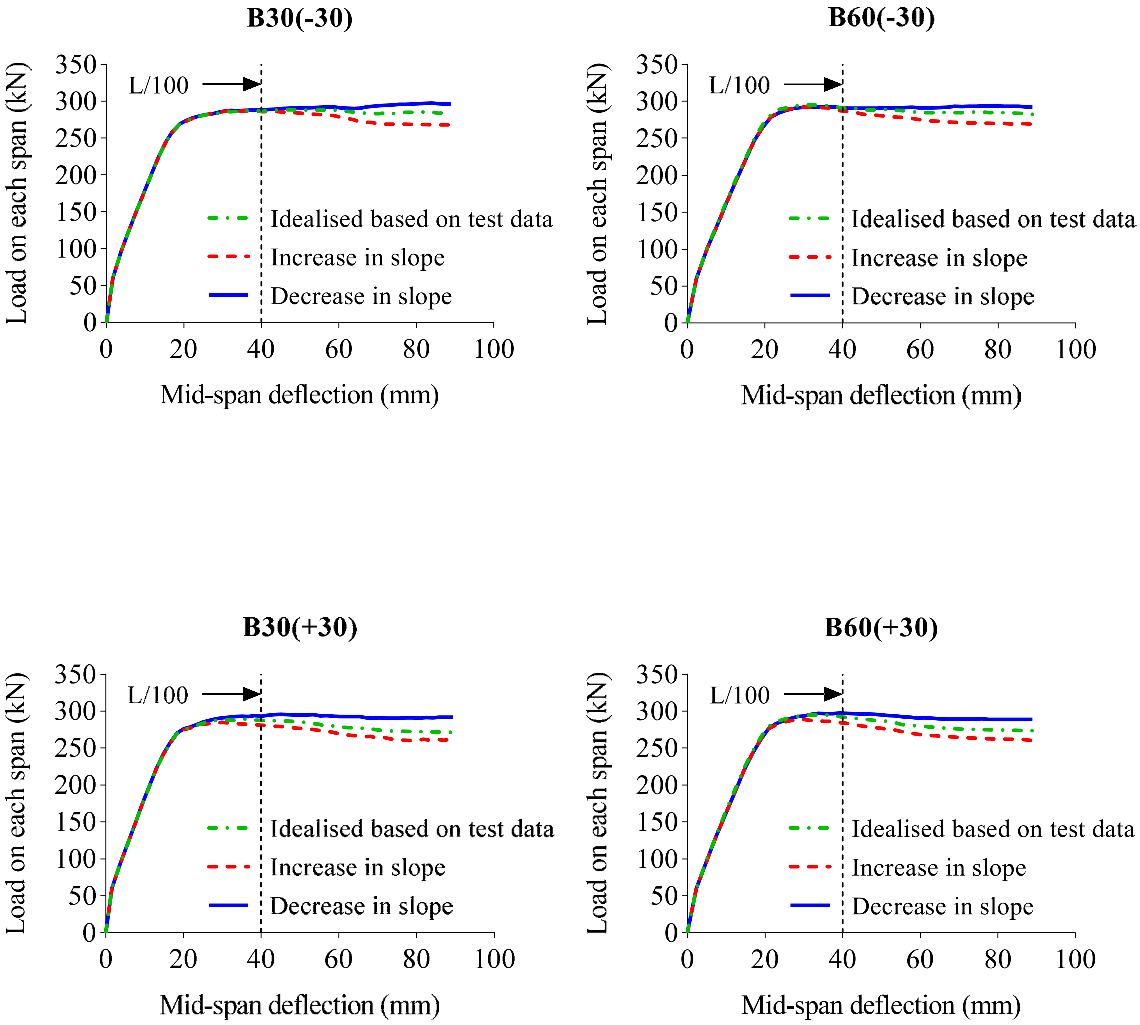

Figure 5.19: Comparison of load versus deflection plots for different stress-COD relationships for the beam specimens.

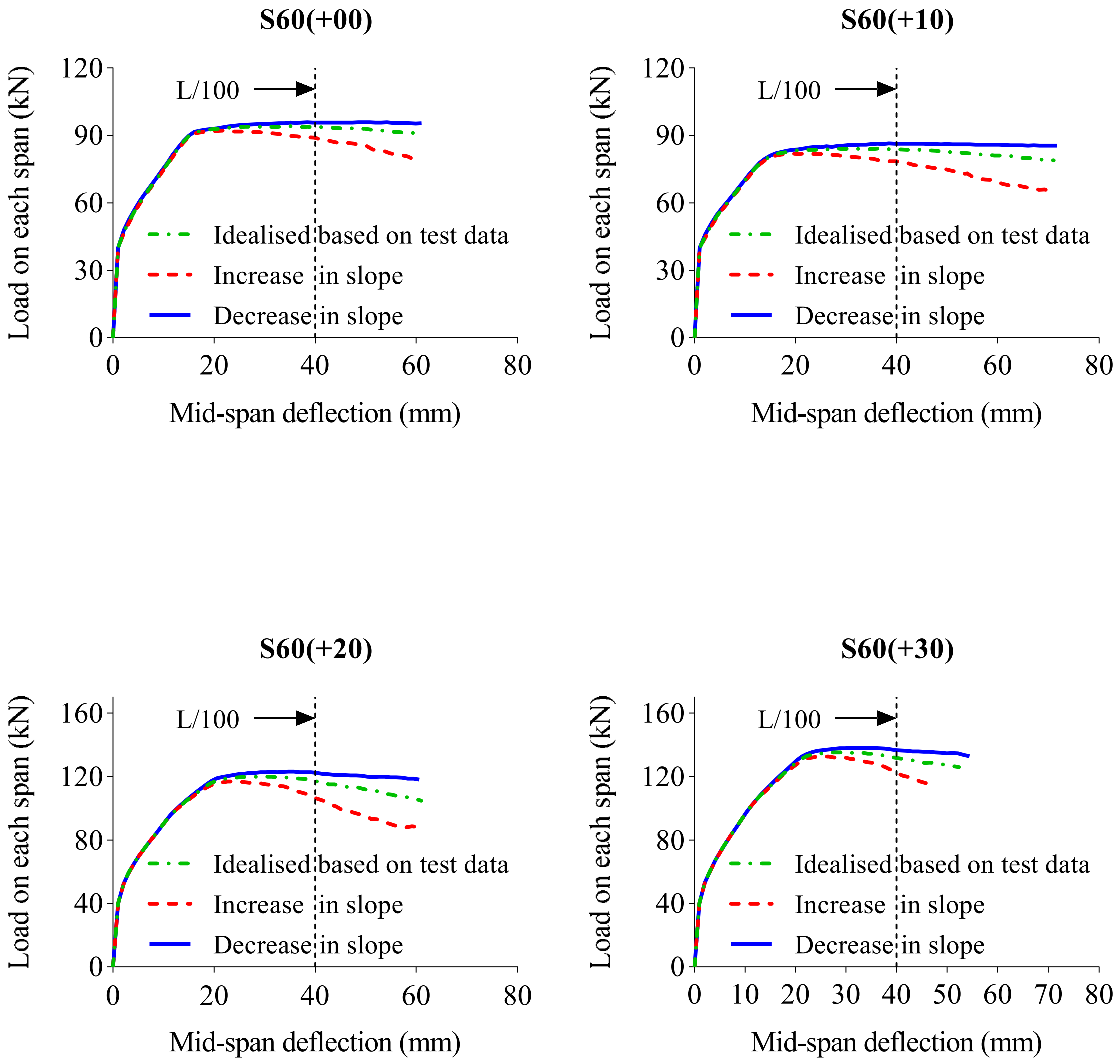

Figure 5.20: Comparison of load versus deflection plots for different stress-COD relationships for the slab specimens.

5.6.2 Effect of the hardening of reinforcing bars

To determine the effect of the degree of hardening of reinforcing steel bars on the post-peak behaviour of R-SFRC flexural members, a parametric study is performed by changing the degree of hardening of reinforcing bars. In the parametric study, the ultimate strengths of reinforcement are taken as $1.10f_{sy}$ and $1.20f_{sy}$. The stress-COD relationship of the SFRC is kept constant between the specimens of different degrees of hardening.

Figures 5.21 and 5.22 show a comparison of the load-deflection curves for different degrees of hardening of reinforcement for the beam and slab specimens, respectively. From the figures, it is evident that the post-peak behaviour of R-SFRC flexural members also depends on the degree of hardening of the reinforcement. For the same stress-COD relationship of SFRC, decreasing the degree of hardening of reinforcement softens the post-peak behaviour whereas increasing the degree of hardening of reinforcement improves the post-peak behaviour.

The effect of the degree of hardening of reinforcement is less pronounced in specimens with low amount of tensile reinforcement. The softening and hardening in the slab specimens, where the tensile reinforcement ratios are less than 0.5%, are less obvious than that of the beam specimens where the tensile reinforcement ratios are more than 0.5%.

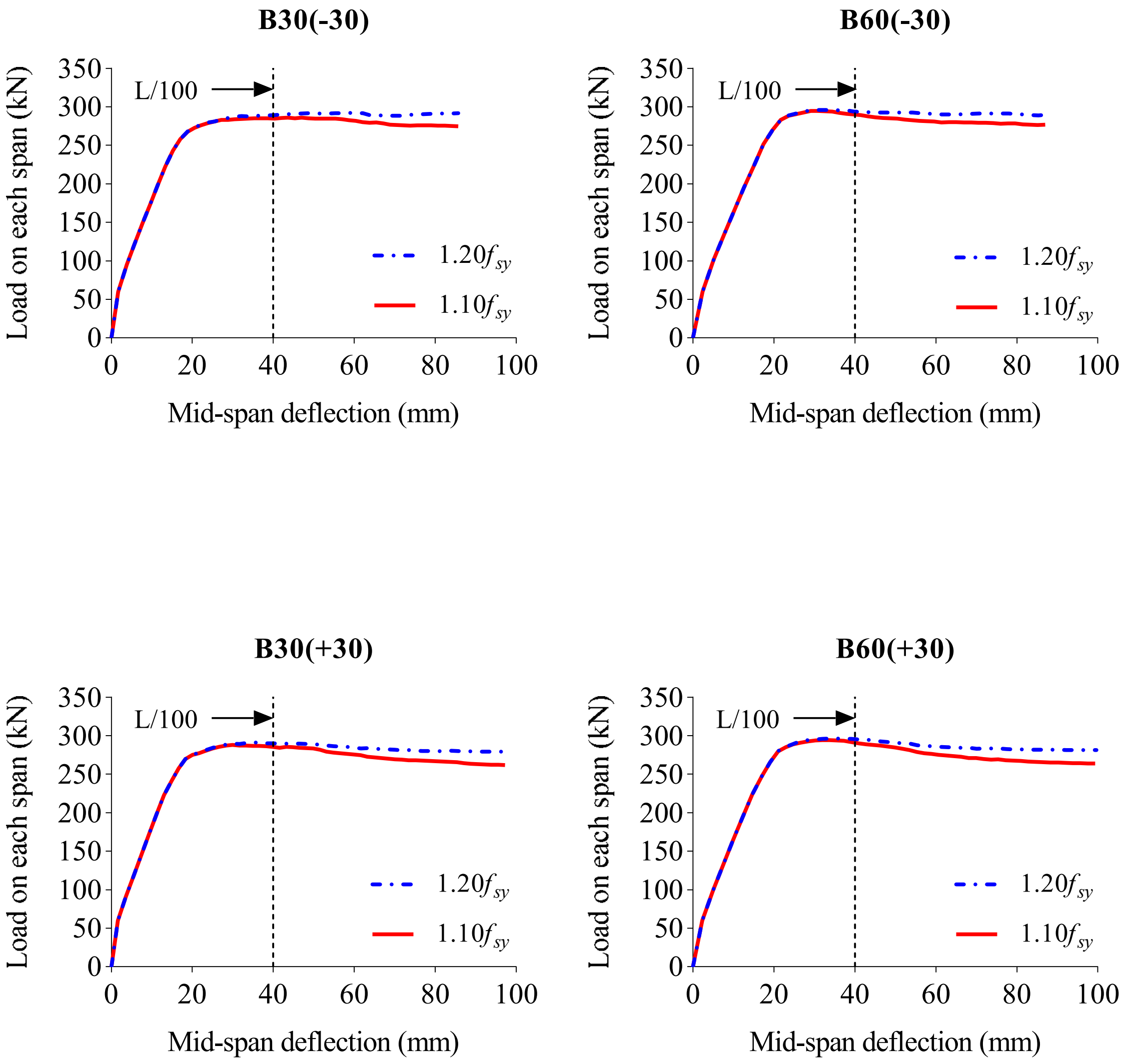

Figure 5.21: Comparison of load versus deflection plots for different degrees of hardening of reinforcing bars for the beam specimens.

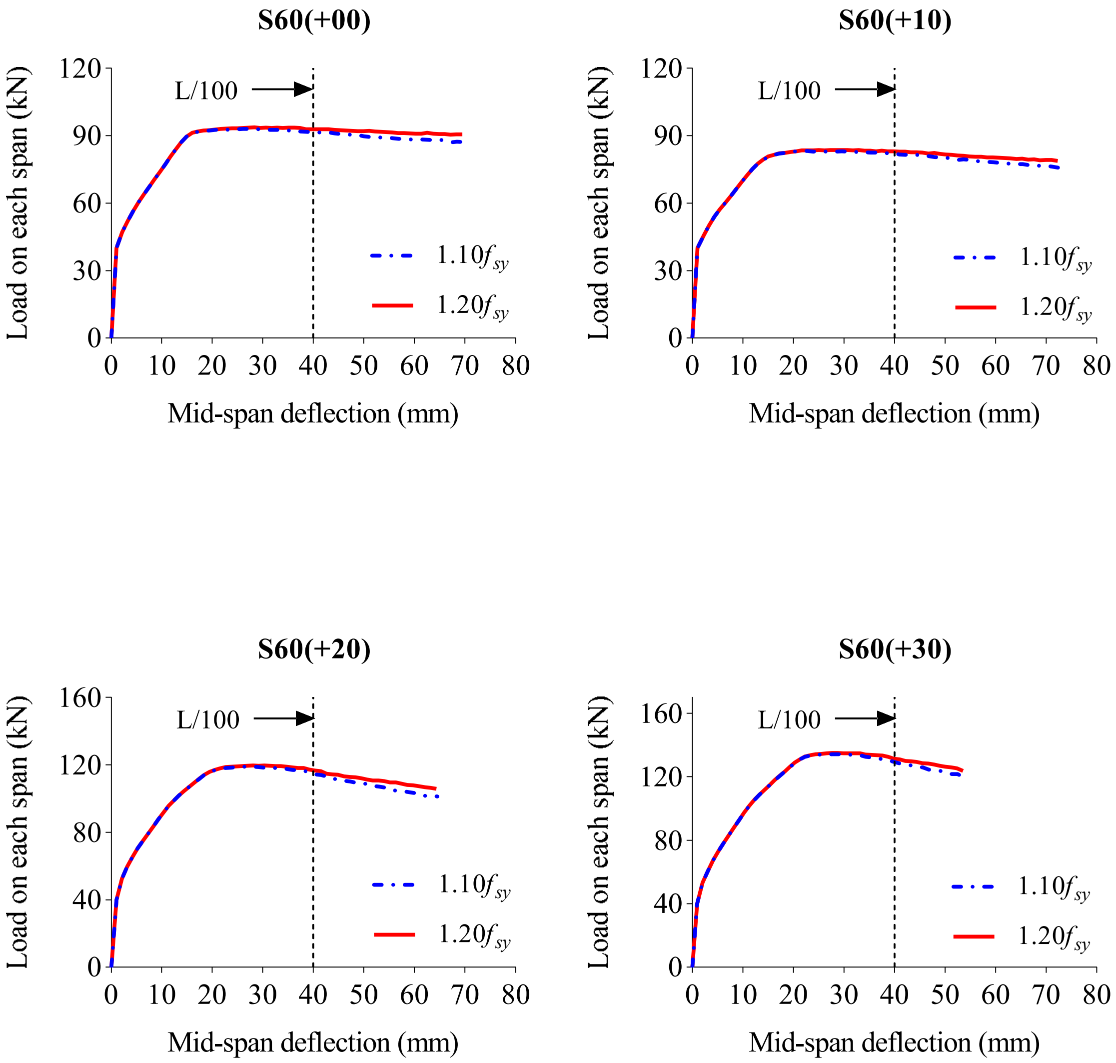

Figure 5.22: Comparison of load versus deflection plots for different degrees of hardening of reinforcing bars for the slab specimens.

5.6.3 Effect of the type of loading

The specimens in this study were tested under point loads. However, real structures are usually subjected to uniform load. To determine the effect of the type of loading on the post-peak behaviour, a uniform load is applied on the slab specimens.

Figure 5.23 shows a comparison of the normalised load versus deflection plots of the slab specimens under point and uniform load. Since the application of uniform load increases the capacity of the specimens, the loads are normalised with respect to the peak load. From the figure, it is evident that the post-peak behaviour of the specimens improves when uniform load is applied on the specimens. This is attributed to the lower moment gradient, resulting in a larger plastic region, particularly in the positive moment zones.

Figure 5.24 shows a representative comparison of crack patterns under point load and uniform load. Under point load, the cracking is localised in one crack in mid-span increasing the crack width and the strain of the reinforcement significantly on that particular crack. However, under uniform load, the crack widths are uniformly distributed which significantly improves the post-peak behaviour.

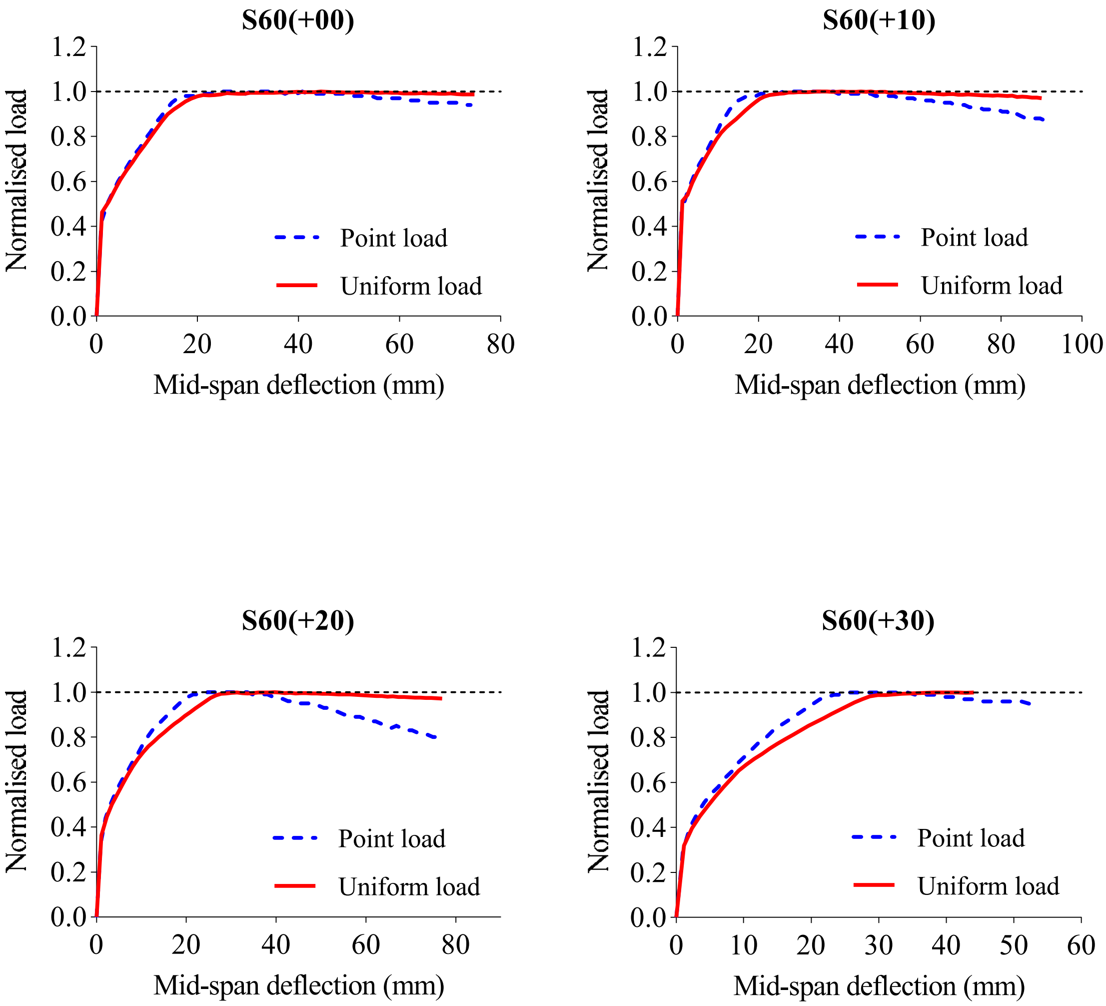

Figure 5.23: Comparison of load versus deflection plots for different types of loading for the slab specimens.

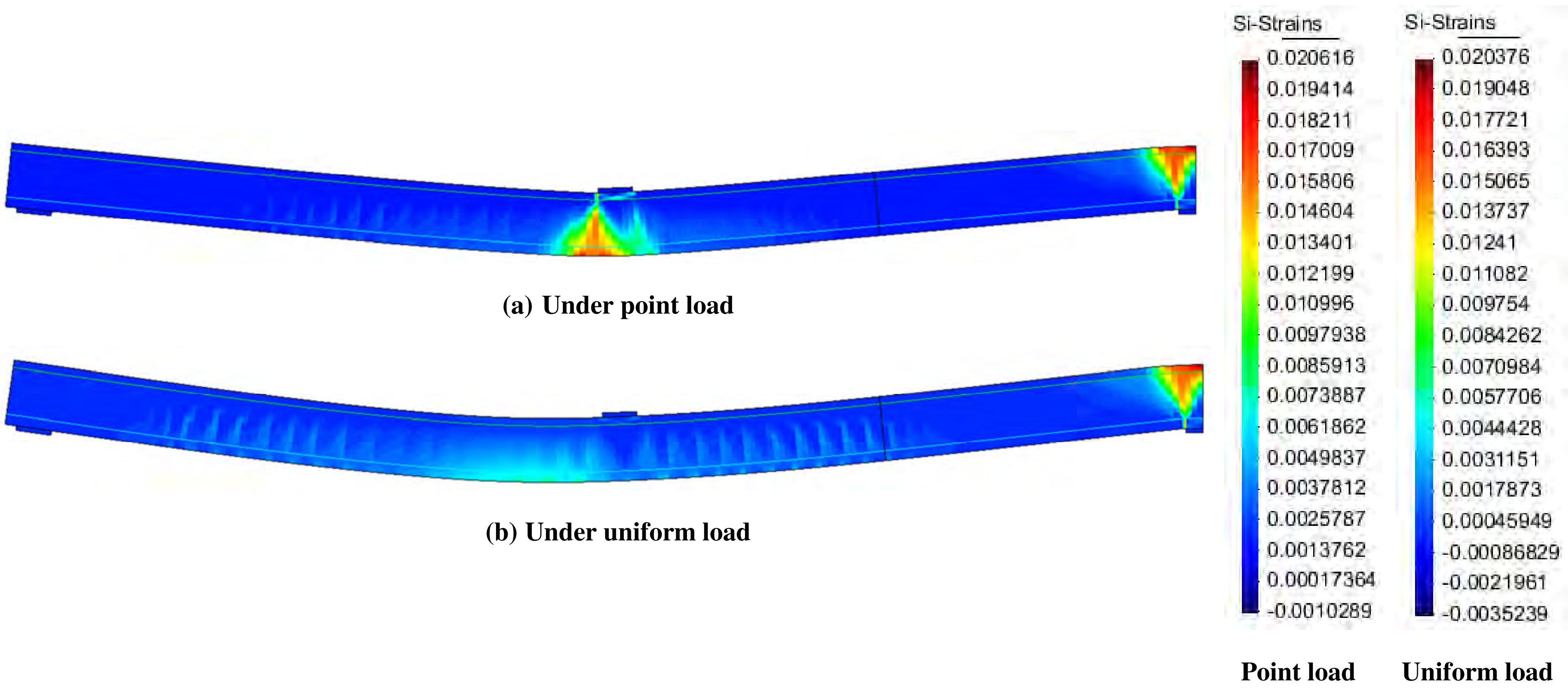

Figure 5.24: Representative comparison of crack patterns under (a) point load and (b) uniform load for the slab specimens.

5.7 Conclusions

In this chapter, the FE program RECAP was used to develop two-dimensional FE models of R-SFRC flexural members. In the FE modelling, the concrete was modelled as 2D orthotropic membrane element and the reinforcement was modelled as two-node truss element. The non-local smeared rotating crack approach was used to simulate the cracking in concrete. The developed FE models showed good correlation with the test data in this study.

The validated FE models were used for parametric studies by varying the slope of the tensile stress-COD of SFRC and the degree of hardening of reinforcement to determine their effect on the post-peak behaviour of R-SFRC flexural members. It is found that the post-peak behaviour of R-SFRC flexural members depends on the combined effect of the rate of softening of SFRC and the degree of hardening of reinforcement. At low reinforcement ratios, the effect of the rate of softening of SFRC is more pronounced than that of the degree of hardening of reinforcement increasing the possibility of post-peak softening behaviour of R-SFRC flexural members.

The slab specimens tested in this study showed post-peak softening behaviour. From the parametric studies, it is found that for the same material properties of SFRC and reinforcement, the slab specimens would have shown relatively flat post-peak behaviour under uniform load. Comparison of crack patterns shows that the cracking is more uniformly distributed rather than localised in one single crack, which decreases the strain of steel and the crack width at critical sections, thus improving the post-peak behaviour.

Chapter 6

DESIGN OF R-SFRC FLEXURAL MEMBERS

6.1 Introduction

In this chapter, the ultimate capacity of R-SFRC flexural members is calculated using two analytical models; a rectangular stress block (RSB) model based on plasticity and a bi-linear model based on crack width to describe the contribution of fibres to flexural strength. The predicted capacities are compared with the results of the beam and slab specimens tested in this study.

Previous studies have reported that the reduction in ductility and the softening behaviour showed by R-SFRC flexural members were due to crack localisation. In this study, although crack localisation happened in both RC and R-SFRC specimens, the R-SFRC specimens showed softening behaviour after a period of hardening, whereas the RC specimens showed extensive hardening behaviour before fracture of the reinforcing bars. To formulate the post-peak behaviour of R-SFRC flexural members, a parametric study is performed using the test data available in the literature to determine the effect of tensile reinforcement ratio and fibre dosage on the ductility of R-SFRC flexural members. A deformation factor is defined for consistent evaluation of the ductility of the flexural members. Based on the parametric study, the post-peak behaviour of R-SFRC flexural members is mathematically formulated, and empirical relationships are developed for minimum reinforcement required for a sufficient ductility of R-SFRC flexural members.

6.2 Ultimate capacity of R-SFRC members in bending

6.2.1 Rectangular stress block model based on plasticity

Calculations of the capacity of R-SFRC cross-sections in bending incorporate the same equilibrium and strain-compatibility considerations of RC cross-sections including the contribution of fibres. Figure 6.1 shows the rectangular stress block (RSB) model of AS 3600: 2018 [34]. The RSB model is founded on the theory of plasticity.

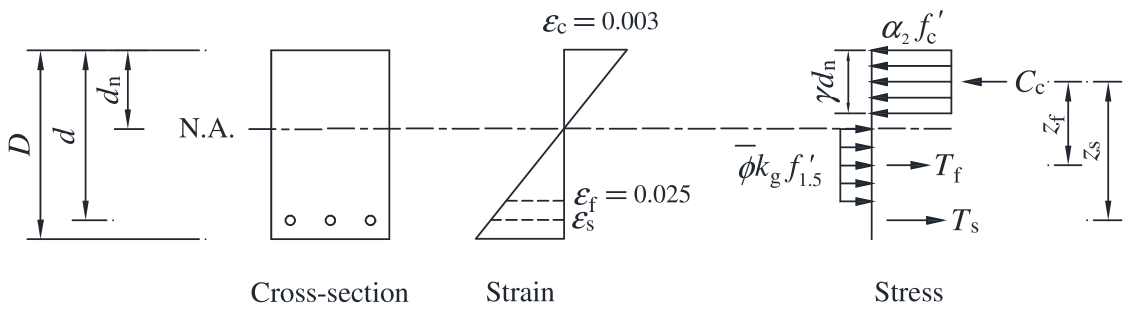

where, $\alpha_2 = 0.85 - 0.0015 f_c'$ ... $\alpha_2 \geq 0.67$

$\gamma = 0.97 - 0.0025 f_c'$ ... $\gamma \geq 0.67$

Figure 6.1: Stress block and forces on R-SFRC section based on RSB model.

In the RSB model, the stress in SFRC in tension is taken to be uniformly distributed and is $\overline{\phi} k_g f_{1.5}'$, where $\overline{\phi}$ is a safety parameter to take account of the differences in model error and variation between the bar reinforcement and fibres contributions to the flexural strength (in order to use a common strength reduction, ϕ, factor), and k_g is a factor to take into account for the area of the fracture surface on fibre materials variability (relative to that of the prism bending test). When comparing model prediction to test results, $\overline{\phi}$ = 1 and k_g = 1 is taken in this study. Lastly, for the AS 3600:2018 RSB model adopted, the contribution of fibres where the tensile strain exceeds 0.025 is ignored in the calculation of moment capacity.

The load-carrying capacity of the beam and slab specimens were determined using a rigid-plastic analysis with the resisting moment at the plastic hinges at mid-span, M^{+}, and at intermediate support, M^{-}, determined based on the RSB model. Since two plastic hinges, one over the intermediate support and one at the critical mid-span, formed in all of the R-SFRC beam and slab specimens for increasing applied load, it is known that the moments can be fully sustained for increasing curvatures to this point. The values of M^{+} and M^{-} were used to calculate the theoretical plastic load ($P_{u.RSB}$) using the formula $P_{u.RSB} = M^{+} + 0.5M^{-}$. These values are compared with the ultimate loads from the experiment ($P_{u.exp}$) in Tables 6.1 and 6.2 for the beam and slab specimens, respectively.

From the analysis results, it is observed that the predicted ultimate loads correlate well with the experimental observations. For the beam specimens, the mean test to model ratios are 1.09 and 1.03, and coefficients of variation are 0.027 and 0.022, using $f'_{1.5}$ determined from the dogbone tests and $f'_{1.5}$ determined by the AS 3600:2018 inverse analysis method on prism bending tests, respectively.

For the slab specimens, the mean test to model ratios are 1.22 and 1.01, and coefficients of variation are 0.153 and 0.061, using $f'_{1.5}$ determined from the dogbone tests and $f'_{1.5}$ determined by the AS 3600:2018 inverse analysis method on prism bending tests, respectively.

Table 6.1: Comparison of experimental loads with predicted loads based on RSB model for the beam specimens.

Specimen	$P_{u.exp}$ (kN)	Using $f'_{1.5}$ from dogbone tests		Using $f'_{1.5}$ from prism tests	
		$P_{u.RSB}$ (kN)	$\frac{P_{u.exp}}{P_{u.RSB}}$	$P_{u.RSB}$ (kN)	$\frac{P_{u.exp}}{P_{u.RSB}}$
B30(−30)	278.1	265.4	1.05	278.6	0.99
B60(−30)	299.2	267.4	1.12	286.3	1.05
B30(+30)	289.2	264.0	1.10	277.3	1.04
B60(+30)	289.7	266.2	1.09	285.2	1.02
Average (COV)			**1.09 (0.027)**		**1.03 (0.022)**

Note: $P_{u.exp}$ = ultimate load from experiments; $P_{u.RSB}$ = ultimate load predicted by RSB model.

Table 6.2: Comparison of experimental loads with predicted loads based on RSB model for the slab specimens.

Specimen	$P_{u.exp}$ (kN)	Using $f'_{1.5}$ from dogbone tests		Using $f'_{1.5}$ from prism tests	
		$P_{u.RSB}$ (kN)	$\frac{P_{u.exp}}{P_{u.RSB}}$	$P_{u.RSB}$ (kN)	$\frac{P_{u.exp}}{P_{u.RSB}}$
S60(+00)	90.7	71.4	1.27	91.2	0.99
S60(+10)	88.8	60.6	1.47	82.5	1.08
S60(+20)	110.3	105.7	1.04	119.0	0.93
S60(+30)	135.5	121.5	1.12	133.3	1.02
Average (COV)			**1.22 (0.153)**		**1.01 (0.061)**

Note: $P_{u.exp}$ = ultimate load from experiments; $P_{u.RSB}$ = ultimate load predicted by RSB model.

6.2.2 Bi-linear model based on crack width

To check the validity of the RSB model of AS 3600:2018 [34] for the design of R-SFRC flexural member, a more detailed bi-linear model based on crack width is used in this section to predict the capacity of the R-SFRC flexural members. Figure 6.2 shows the bi-linear model of determining the capacity of R-SFRC section at the ultimate strength.

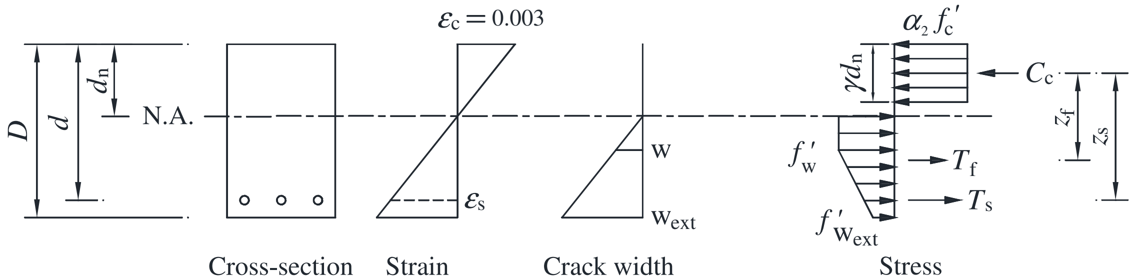

Figure 6.2: Stress block and forces on R-SFRC section based on bi-linear model.

The residual tensile stress of SFRC is a function of crack width. The crack width is assumed to be linear, zero at neutral axis and maximum at the extreme tension fibre. The ultimate load is the point when concrete strain reaches its ultimate value (ε_{cu}). The ultimate strain of concrete is taken as 0.003 as per AS 3600:2018 [34]. The maximum crack width at ultimate can be determined from the crack spacing.

The residual tensile stress of SFRC corresponding to the crack width can be determined from the stress-COD relationship. The stress-COD results from the companion dogbone specimens tested with the beam and slab specimens are shown in Figures 6.3 and 6.4, respectively. The stress-COD relationships predicted by different standards are also shown in the figures.

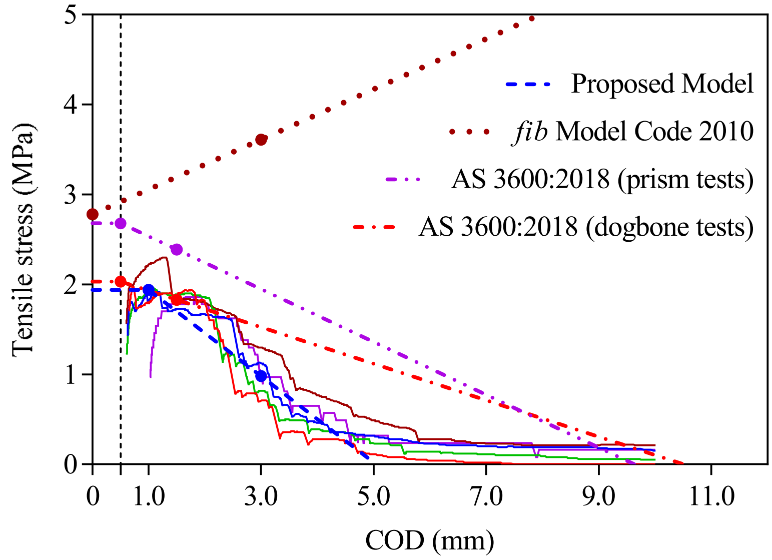

Proposed Model:
$f'_{1.0}$ = 1.94 MPa
$f'_{3.0}$ = 0.98 MPa

(a)

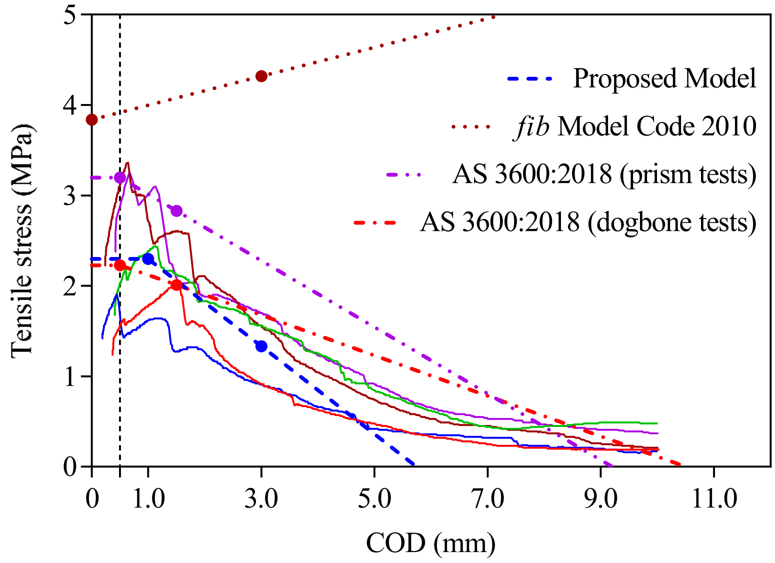

Proposed Model:
$f'_{1.0}$ = 2.30 MPa
$f'_{3.0}$ = 1.33 MPa

(b)

Figure 6.3: Tensile stress versus COD for the beam specimens for fibre dosages of (a) 30 kg/m^3 and (b) 60 kg/m^3.

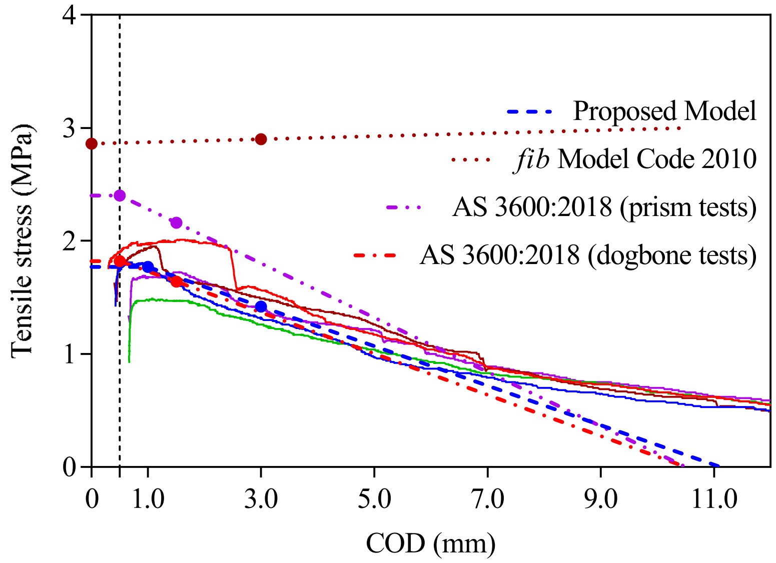

Proposed Model:
$f'_{1.0} = 1.77$ MPa
$f'_{3.0} = 1.42$ MPa

(a)

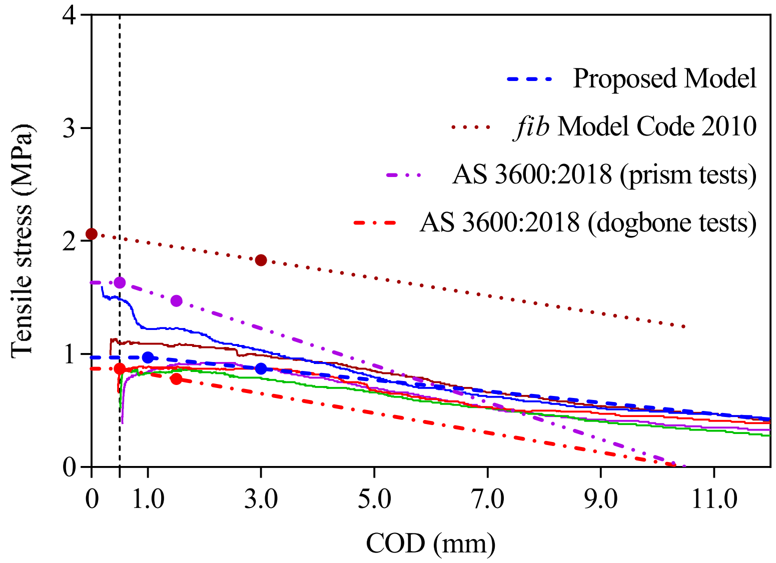

Proposed Model:
$f'_{1.0} = 0.97$ MPa
$f'_{3.0} = 0.87$ MPa

(b)

Figure 6.4: Tensile stress versus COD for the slab specimens for (a) Batch 1 and (b) Batch 2 of SFRC.

From the figures, it is evident that the linear stress-COD relationship determined by the *fib* Model Code 2010 [30] inverse analysis method on prism bending tests not only significantly over-predicts the stress-COD results from the dogbone tests, but also shows a hardening behaviour. The bi-linear stress-COD relationship determined by the AS 3600:2018 [34] inverse analysis method on prism bending tests also over-predicts the stress-COD results from the dogbone tests.

The bi-linear stress-COD relationship determined by the AS 3600:2018 [34] based on dogbone tests gives a reasonable correlation with the dogbone test results. However, the AS 3600:2018 uses the limitation of $f'_{1.5} \leq 0.9 f'_{0.5}$ to ensure the softening behaviour and can over-predict or under-predict the stress-COD results based on the determination of $f'_{0.5}$. For example, in some cases of this study, the $f'_{0.5}$ values could not be determined since the initial crack widths after the cracking of concrete were more than 0.5 mm, and even the determined values of $f'_{0.5}$ showed large variability (see Figures 6.3 and 6.4). Therefore, a new bi-linear stress-COD relationship based on $f'_{1.0}$ and $f'_{3.0}$ (given in Equation 6.1) is used in this study and plotted in Figures 6.3 and 6.4:

$$
\begin{aligned}
f'_w &= f'_{1.0}, \; w = 0 \text{ to } 1.0 \text{ mm} \\
f'_w &= \frac{f'_{1.0}}{w_u - 1.0}(w_u - w), \; 1.0 \leq w \leq w_u \\
w_u &= 1.0 + \frac{2.0 f'_{1.0}}{f'_{1.0} - f'_{3.0}}, \; f'_{3.0} \leq 0.9 f'_{1.0}
\end{aligned}
\tag{6.1}
$$

where w is the crack width and w_u is the ultimate crack width at zero residual tensile stress.

Tables 6.3 and 6.4 show a comparison of the experimental loads with the loads predicted by the bi-linear model for the beam and slab specimens, respectively. In the bi-linear model, the crack widths are calculated from the experimental crack spacing and also from the crack spacing predicted by AS 3600:2018 [34].

The bi-linear model shows reasonable performance in predicting the ultimate capacity. For the beam specimens, the mean test to model ratios are 1.09 and 1.07, and coefficients of variation are 0.029 and 0.021, using experimental crack spacings and crack spacings predicted by AS 3600:2018 [34], respectively.

For the slab specimens, the mean test to model ratios are 1.17 and 1.15, and coefficients of variation are 0.082 and 0.099 using experimental crack spacings and crack spacings predicted by AS 3600:2018 [34], respectively.

In comparison with the RSB model, the proposed bi-linear model gives similar predictions for the beam specimens and slightly better predictions for the slab specimens tested in this study. It must be recognised, however, that the accuracy of the bi-linear model is strongly dependent on knowing the crack spacing to, then, determine the crack width. If the crack spacings are under-predicted, the model will provide non-conservative results, with the degree of non-conservatism dependent on the slope of the residual tensile stress diagram for increasing w (fibre mixes with higher post-cracking residual strength slopes being more prone to error if the crack spacing is inaccurately predicted). Noting that the more complex bi-linear model does not show significantly improved accuracy over that of the simpler plasticity-based RSB model, and the danger of non-conservative results if crack spacings are under predicted, the RSB model is recommended for design.

Table 6.3: Comparison of experimental loads with predicted loads based on bi-linear model for the beam specimens.

Specimen	Experimental	Bi-linear model							
		Experimental crack spacing				Crack spacing based on AS 3600:2018 [34]			
	$P_{u.exp}$ (kN)	Mid-span crack spacings (mm)	Interior-support crack spacings (mm)	$P_{u.bi-linear}$ (kN)	$\frac{P_{u.exp}}{P_{u.bi-linear}}$	Mid-span crack spacings (mm)	Interior-support crack spacings (mm)	$P_{u.bi-linear}$ (kN)	$\frac{P_{u.exp}}{P_{u.bi-linear}}$
B30(-30)	278.1	99	101	263.6	1.06	79	58	265.9	1.05
B60(-30)	299.2	69	139	272.9	1.10	64	47	273.8	1.09
B30(+30)	289.2	106	206	255.4	1.13	64	79	265.6	1.09
B60(+30)	289.7	89	188	266.3	1.09	51	64	272.8	1.06
Average (COV)					**1.09 (0.029)**				**1.07 (0.021)**

Note: $P_{u.exp}$ = ultimate load from experiments; $P_{u.bi-linear}$ = ultimate load predicted by bi-linear model.

Table 6.4: Comparison of experimental loads with predicted loads based on bi-linear model for the slab specimens.

Specimen	Experimental	Bi-linear model							
		Experimental crack spacing				Crack spacing based on AS 3600:2018 [34]			
	$P_{u.exp}$ (kN)	Mid-span crack spacings (mm)	Interior-support crack spacings (mm)	$P_{u.bi-linear}$ (kN)	$\frac{P_{u.exp}}{P_{u.bi-linear}}$	Mid-span crack spacings (mm)	Interior-support crack spacings (mm)	$P_{u.bi-linear}$ (kN)	$\frac{P_{u.exp}}{P_{u.bi-linear}}$
S60(+00)	90.7	146	156	78.0	1.16	187	148	77.5	1.17
S60(+10)	88.8	174	163	68.5	1.30	188	174	68.3	1.30
S60(+20)	110.3	162	173	103.4	1.07	110	114	106.9	1.03
S60(+30)	135.5	174	148	119.2	1.14	97	114	122.6	1.11
Average (COV)					**1.17 (0.082)**				**1.15 (0.099)**

Note: $P_{u.exp}$ = ultimate load from experiments; $P_{u.bi-linear}$ = ultimate load predicted by bi-linear model.

6.3 Parametric study based on test data

A parametric study is performed with the test data available in the literature to find the effect of tensile reinforcement volume and fibre dosage on the ductility of R-SFRC flexural members. The parametric study includes 135 beam and slab specimens with the details of the specimens are provided in Table 6.5. All of the specimens are simply supported. The specimens differ in span, cross-section, concrete strength, reinforcement ratio, yield and ultimate strength of reinforcement and fibre type, dosage, length and aspect ratio.

The displacement ductility of a flexural member is generally evaluated as the ratio of mid-span displacement at ultimate to the mid-span displacement at the yielding of reinforcement. However, in the literature, in most of the cases, the load corresponding to the yielding of reinforcement was not reported for the tested specimens. Moreover, different studies used different criteria for ultimate displacement (i.e., displacement corresponding to 75-85% of peak load). For a consistent evaluation of the ductility of the tested specimens, a plastic deformation factor is defined as the ratio of the deformation at peak load (Δ_{peak}) to the deformation of span/100 (L/100). This point (deformation of span/100) is considered as corresponding to sufficient deformation for observation of serious distress in the member [119], and a member is considered to have sufficient ductility if the value of plastic deformation factor is more than or equal to 1.0.

The plastic deformation factor values of the tested specimens in Table 6.5 are determined and plotted in Figure 6.5. “Blue” markers are used for deformation factor values more than or equal to 1.0, whereas the deformation factor values less than 1.0 are plotted in “Red” markers. From the figure, it is evident that the plastic deformation factor values of RC flexural members decrease with the increase of reinforcement ratios, whereas the plastic deformation factor values of R-SFRC flexural members increase with the increase of reinforcement ratios which implies that the ductility of RC flexural members decreases with the increase of reinforcement ratios whereas the ductility of R-SFRC flexural members increases with the increase of reinforcement ratios.

In most cases, plastic deformation factor values of less than 1.0 are found when the reinforcement ratios are less than 0.4% which indicates that the members did not have sufficient deformation for observation of serious distress in the members. Moreover, a high fibre dosage (1%) also results in deformation factor values of less than 1.0 even at higher reinforcement ratios (see Figure 6.5).

Based on the parametric study, it is evident that the post-peak behaviour of R-SFRC flexural members depends on the combined effect of the volume of tensile reinforcement and the dosage of steel fibres. A low reinforcement ratio combined with a high dosage of fibre can decrease the ductility of R-SFRC flexural members.

Table 6.5: Details of test specimens from the literature for parametric study.

Reference	No. of specimens	Span length (m)	Cross-section $(b \times D)$ (mm × mm)	Average concrete strength (MPa)	Reinforcement ratios (%)	f_{sy} (MPa)	f_{su} (MPa)	Fibre dosage (%)	Fibre type	Fibre length (mm)	Fibre aspect ratio
Swamy et al. [4]	6	2.25	130 × 200	40	1.0	460 605	NA	0, 0.5, 1	Crimpled	50	100
Dwarakanath and Nagaraj [10]	2	1.5	100 × 208	25	0.77	500	585	0, 0.75	Hooked-end	36	72
Oh [16]	4	1.8	120 × 180	40	1.5, 2.4	420	545	0, 1	Straight	40	57
Alsayed [21]	3	2.3	250 × 250	35	0.75	470	NA	0, 0.5, 1.0	Hooked-end	60	75
Ashour and Wafa [11]	6	2.6, 3.7	170 × 300	90	1.4	440	NA	0, 0.5, 1.0	Hooked-end	60	75
Espion et al. [22]	2	1.4	250 × 150	30	0.5	580	NA	0, 0.4	Hooked-end	60	75
Ashour et al. [17]	18	3.1	200 × 250	50, 80	1.2, 1.8, 2.4	530	NA	0, 0.5, 1.0	Hooked-end	60	75
Dancygier and Savir [23]	6	3.5	200 × 300	120	0.28, 0.56	550	720	0, 0.75	Hooked-end	35, 60	65

Altun et al. [19]	6	2.0	300 × 300	25, 35	0.5	NA	NA	0, 0.4, 0.75	Hooked-end	60	80
Meda et al. [12]	5	3.6	200 × 300	40	0.75, 1.5	535	630	0, 0.4, 0.75	Hooked-end	50	50
Pujadas et al. [13]	12	2.7	1000 × 200	30	0.85	500	NA	0, 0.25, 0.50	Hooked-end	35, 60	64, 80
Mertol et al. [14]	20	3.3	180 × 350	30	0.20-2.5	420	NA	0, 1	Hooked-end	30	60
Sahoo et al. [120]	3	1.8	150 × 200	35	1.35	500	NA	0, 0.5, 1.0	Hooked-end	60	80
Dancygier and Berkover [24]	22	3.2	240 × 300	35	0.15-1.3	460	558-693	0, 0.5, 0.75	Hooked-end	35	64
Yoo and Moon [15]	20	2.6	320 × 300	45	0.18-0.41	500	NA	0, 0.25, 0.5, 0.75, 1.0	Hooked-end	35	64

Note: b = width of specimen; D = depth of specimen; f_{sy} = yield strength of steel; f_{su} = ultimate strength of steel.

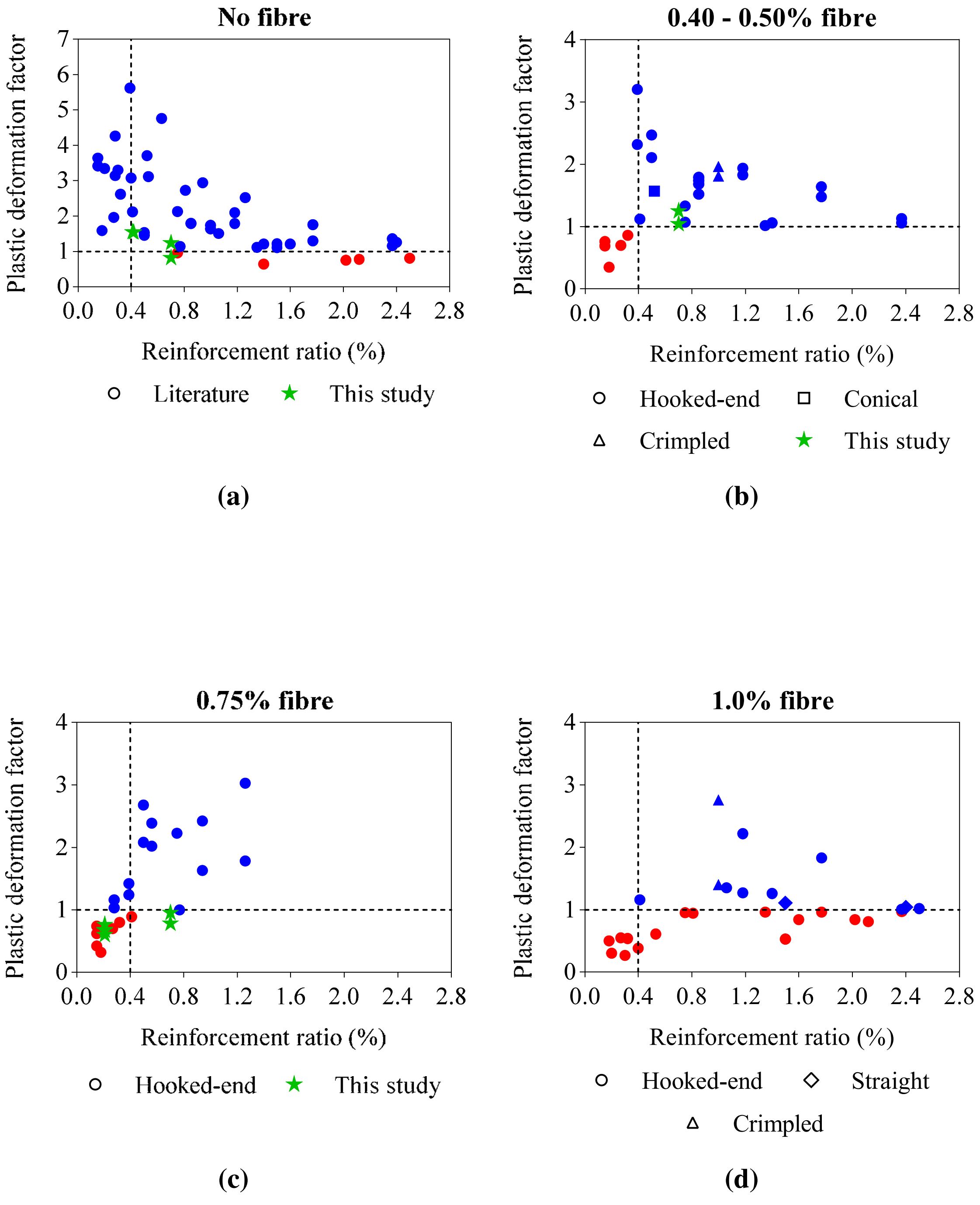

Figure 6.5: Plastic deformation factors versus reinforcement ratios for fibre dosages of (a) 0%, (b) 0.4-0.5%, (c) 0.75% and (d) 1%.

6.4 Post-peak behaviour and minimum reinforcement ratio

The parametric studies, based on the FE models (in Chapter 5) and using the test data (in Section 6.3), indicate that the post-peak behaviour of R-SFRC flexural members depends on the combined effect of the hardening of reinforcement and the softening of SFRC. The post-peak behaviour of R-SFRC flexural members can be explained by Figure 6.6. The steel reinforcing bar shows strain hardening after yield whereas the SFRC softens as the crack width increases. When these two materials are combined, the post-peak behaviour is dictated by the relative change in moment due to the hardening of reinforcing bars and the softening of SFRC.

The capacity of a R-SFRC section is given by:

$$M = T_s z_s + T_f z_f \tag{6.2}$$

where T_s = tensile force in the steel, T_f = tensile force in the fibre, z_s = lever arm from the compressive force to T_s, and z_f = lever arm from the compressive force to T_f. The change in moment after peak load is given by:

$$\Delta M = \Delta(T_s z_s) + \Delta(T_f z_f) \tag{6.3}$$

The flexural member will show an elasto-plastic behaviour when the change in moment due to hardening of steel and softening of fibres is zero. That is:

$$\Delta(T_s z_s) + \Delta(T_f z_f) = 0; \text{ or } \Delta(T_s z_s) = -\Delta(T_f z_f) \tag{6.4}$$

The flexural member will show strain hardening behaviour when $\Delta(T_s z_s) > -\Delta(T_f z_f)$ and strain softening behaviour when $\Delta(T_s z_s) < -\Delta(T_f z_f)$.

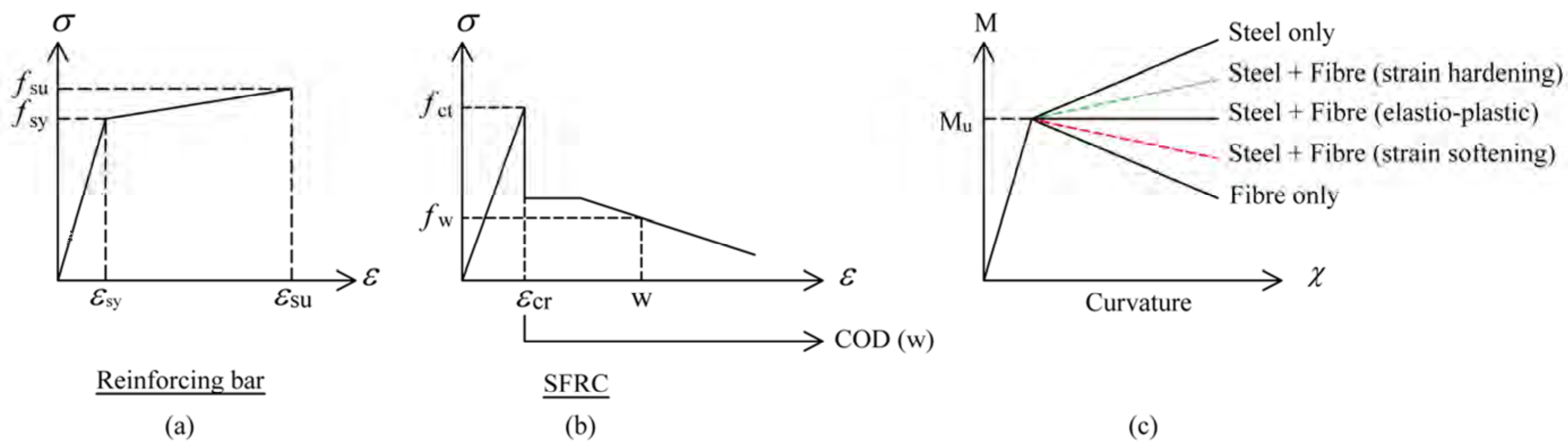

Figure 6.6: (a) Stress-strain behaviour of steel reinforcing bar, (b) stress-strain and stress-COD behaviour of SFRC in tension, and (c) moment-curvature relationship of steel, fibre and steel-fibre combined.

Based on the bi-linear stress-COD relationship of SFRC in Equation 6.1, the R-SFRC flexural member shows a brief hardening after the yielding of reinforcement up to a crack width of 1 mm. After the crack width of 1 mm, the post-peak behaviour largely depends on the relative change in moment by the hardening of reinforcement and the softening of SFRC. To develop an empirical relationship for minimum reinforcement ratio required for a sufficient ductility of R-SFRC beams and slabs, the minimum reinforcement ratio is calculated based on Equation 6.4 for 100 beam and slab specimens by varying the depth of the cross-section and the slope of the descending branch of SFRC between $f'_{1.0}$ and $f'_{3.0}$.

In the parametric study, the depths of the beams and slabs are varied from 400 to 800 mm and 100 to 300 mm, respectively, and the slopes of the descending branch of SFRC between $f'_{1.0}$ and $f'_{3.0}$ are taken over the range of -0.125 to -0.50. In the calculation of the capacity of the cross-section, the values of the compressive strength (f'_C), tensile strength and elastic modulus are taken as 40 MPa, 2.3 MPa ($0.36\sqrt{f'_C}$) and 30000 MPa, respectively. The yield strength (f_{sy}) and ultimate strength (f_{su}) of reinforcing bars are taken as 500 MPa and 540 MPa ($1.08f_{sy}$), respectively. The yield strain (ε_{sy}) and ultimate strain (ε_{su}) of reinforcing bars are taken as 0.0025 and 0.05, respectively. For the beam and slab specimens, the centroid of tensile reinforcement is taken as 60 mm and 30 mm, respectively, from the tension face. The diameters of the reinforcing bars are chosen to be 20 mm and 10 mm for the beams and slabs, respectively.

Tables 6.6 and 6.7 show the calculated values of minimum reinforcement ratio for the beam and slab specimens, respectively. From the tables, it is evident that the minimum reinforcement ratio is directly proportional to the slope of the softening of SFRC and inversely proportional to the depth of the cross-section and the value of $f'_{1.0}$. As expected, for the same depth of cross-section and the same value of $f'_{1.0}$, increasing the difference in $f'_{1.0}$ and $f'_{3.0}$ values (i.e. the slope of the softening of SFRC) increases the value of minimum reinforcement ratio as more reinforcement will be required to overcome the softening of SFRC.

As the depth of the cross-section increases, the lever arm for both reinforcement and fibre contribution increase. However, the increase in lever arm for the reinforcement is more than that of the fibre contribution; therefore for the same fibre contribution, less reinforcement will be required for a flat post-peak behaviour with the increase in the depth of cross-section.

For the same depth of cross-section and the same slope of the softening of SFRC (same difference in $f'_{1.0}$ and $f'_{3.0}$ values), the higher the value of $f'_{1.0}$, the lower the value of minimum reinforcement ratio. SFRC with a higher residual strength ($f'_{1.0}$) has a smaller crack spacing and crack width, and hence the reinforcement requirement is lower for a flat post-peak behaviour.

The following relationships for beams and slabs provide a good fit with the calculated minimum reinforcement ratios:

For beams with D > 300 mm:
$$\rho_{min} = \alpha_b \sqrt{\frac{f'_{1.0} - f'_{3.0}}{f'_{1.0} \times D}} \tag{6.5}$$

For slabs with D ≤ 300 mm:
$$\rho_{min} = \alpha_s \sqrt{\frac{f'_{1.0} - f'_{3.0}}{f'_{1.0} \times D}} \tag{6.6}$$

Plotting the values of the reinforcement ratio against $\sqrt{\frac{f'_{1.0}-f'_{3.0}}{f'_{1.0}\times D}}$ in Figure 6.7 gives the values of α_b and α_s as 0.228 and 0.132, respectively.

The empirical relationships in Equations 6.5 and 6.6 are verified using the beam and slab specimens tested in this study. Tables 6.8 and 6.9 show a comparison of the provided reinforcement ratios with the required reinforcement ratios based on Equations 6.5 and 6.6 for the beam and slab specimens, respectively. The beam specimens showed almost flat post-peak behaviour for the provided reinforcement ratios. The required reinforcement ratios based on the expression in Equation 6.5 are slightly higher than the provided reinforcement ratios at some sections. The reason is that the degree of hardening of the reinforcing bars used in the tests was more than that of assumed in the expression in Equation 6.5. Thus, the proposed relationship is conservative.

For the slab specimens, the degree of hardening of the reinforcing bars used in the tests was almost same as that of assumed in the expression in Equation 6.6, and in almost all cases other than one, the required reinforcement ratios based on expression in Equation 6.6 are higher than the provided reinforcement ratios, and the slab specimens showed a softening behaviour after a brief hardening.

Table 6.6: Calculated minimum reinforcement ratios for the beam specimens.

Sample no.	Depth (mm)	$f'_{1.0}$ (MPa)	$f'_{3.0}$ (MPa)	ρ_{min}	Sample no.	Depth (mm)	$f'_{1.0}$ (MPa)	$f'_{3.0}$ (MPa)	ρ_{min}
1	400	2.0	1.75	0.0034	26	400	1.5	1.0	0.0058
2	500			0.0031	27	500			0.0054
3	600			0.0029	28	600			0.0051
4	700			0.0027	29	700			0.0047
5	800			0.0025	30	800			0.0045
6	400	2.0	1.5	0.0054	31	400	1.5	0.75	0.0075
7	500			0.0050	32	500			0.0070
8	600			0.0047	33	600			0.0067
9	700			0.0044	34	700			0.0060
10	800			0.0041	35	800			0.0057
11	400	2.0	1.25	0.0070	36	400	1.5	0.5	0.0091
12	500			0.0064	37	500			0.0083
13	600			0.0060	38	600			0.0079
14	700			0.0056	39	700			0.0074
15	800			0.0052	40	800			0.0069
16	400	2.0	1.0	0.0083	41	400	1.0	0.75	0.0049
17	500			0.0077	42	500			0.0044
18	600			0.0071	43	600			0.0043
19	700			0.0068	44	700			0.0043
20	800			0.0064	45	800			0.0042
21	400	1.5	1.25	0.0039	46	400	1.0	0.5	0.0084
22	500			0.0034	47	500			0.0078
23	600			0.0031	48	600			0.0074
24	700			0.0029	49	700			0.0069
25	800			0.0027	50	800			0.0066

Table 6.7: Calculated minimum reinforcement ratios for the slab specimens.

Sample no.	Depth (mm)	$f'_{1.0}$ (MPa)	$f'_{3.0}$ (MPa)	ρ_{min}	Sample no.	Depth (mm)	$f'_{1.0}$ (MPa)	$f'_{3.0}$ (MPa)	ρ_{min}
1	100	2.0	1.75	0.0040	26	100	1.5	1.0	0.0074
2	150			0.0030	27	150			0.0054
3	200			0.0027	28	200			0.0045
4	250			0.0025	29	250			0.0042
5	300			0.0023	30	300			0.0039
6	100	2.0	1.5	0.0067	31	100	1.5	0.75	0.0098
7	150			0.0048	32	150			0.0070
8	200			0.0041	33	200			0.0060
9	250			0.0038	34	250			0.0055
10	300			0.0035	35	300			0.0052
11	100	2.0	1.25	0.0089	36	100	1.5	0.5	0.0122
12	150			0.0064	37	150			0.0085
13	200			0.0055	38	200			0.0073
14	250			0.0051	39	250			0.0067
15	300			0.0048	40	300			0.0063
16	100	2.0	1.0	0.0109	41	100	1.0	0.75	0.0068
17	150			0.0078	42	150			0.0050
18	200			0.0067	43	200			0.0044
19	250			0.0061	44	250			0.0041
20	300			0.0058	45	300			0.0038
21	100	1.5	1.25	0.0046	46	100	1.0	0.5	0.0110
22	150			0.0034	47	150			0.0079
23	200			0.0029	48	200			0.0068
24	250			0.0027	49	250			0.0063
25	300			0.0025	50	300			0.0059

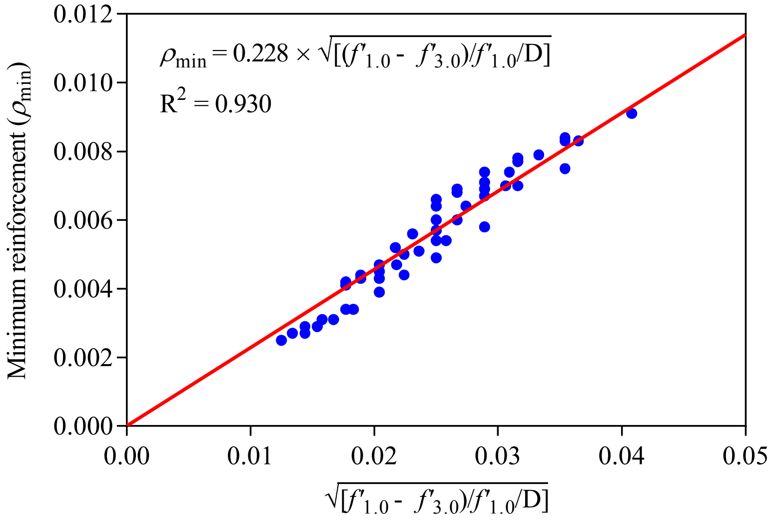

(a)

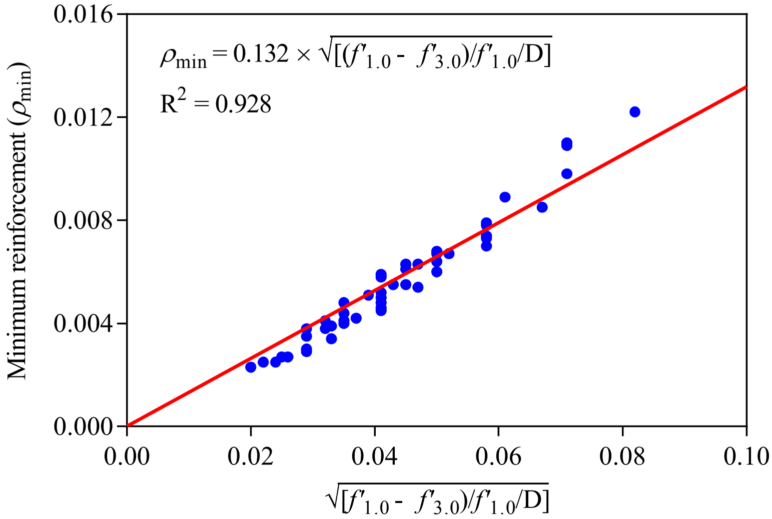

(b)

Figure 6.7: Curve fitting of minimum reinforcement ratios for (a) beam and (b) slab specimens.

Table 6.8: Comparison of provided and required reinforcement ratios for the beam specimens tested in this study.

Specimen	Reinforcement ratios (%)			
	Mid-span		Intermediate support	
	Provided	Required	Provided	Required
B30(-30)	0.69	0.80	1.38	0.80
B60(-30)	0.69	0.74	1.38	0.74
B30(+30)	1.03	0.80	0.69	0.80
B60(+30)	1.03	0.74	0.69	0.74

Table 6.9: Comparison of provided and required reinforcement ratios for the slab specimens tested in this study.

Specimen	Reinforcement ratios (%)			
	Mid-span		Intermediate support	
	Provided	Required	Provided	Required
S60(+00)	0.21	0.29	0.28	0.29
S60(+10)	0.21	0.29	0.21	0.29
S60(+20)	0.29	0.40	0.21	0.40
S60(+30)	0.42	0.40	0.21	0.40

6.5 Conclusions

In this chapter, two analytical models were used to predict the ultimate capacity of R-SFRC flexural members, one simplified based on the RSB approach of AS 3600-2018 [34] and one detailed based on the derivation of residual stress of SFRC from crack width and crack spacing. It is found that the predictions of the proposed bi-linear model are almost the same or slightly better than that of the RSB model. Since the more complex bi-linear model does not show any significantly improved accuracy over that of the simpler plasticity-based RSB mode and requires accurate determination of the crack spacings, the RSB model is recommended for design.

A parametric study was also performed in this chapter using the test data available in the literature to determine the effect of tensile reinforcement ratio and fibre dosage on the ductility of R-SFRC flexural members. For consistent evaluation of ductility of the tested specimens, a plastic deformation factor was defined. The parametric study shows that the ductility of R-SFRC flexural members increases with the increase of reinforcement ratios. However, when the reinforcement ratios are less than 0.4% and/or when the dosages of steel fibres are high, the inclusion of steel fibres decrease the ductility of the member.

Based on the parametric study, the post-peak behaviour of R-SFRC flexural members was mathematically formulated. The member shows a softening behaviour if the increase in moment due to the hardening of reinforcement cannot compensate for the decrease in moment due to the softening of steel fibres, and vice versa.

Based on the mathematical formulation, the tensile reinforcement ratio required for a flat post-peak behaviour was calculated for 100 beam and slab specimens by varying the depth of the cross-section and the slope of the softening of SFRC. The data of the parametric study was used to develop empirical relationships for minimum reinforcement ratios for R-SFRC beams and slabs. The relationships are shown to provide a good estimation of the minimum tensile reinforcement ratios required for sufficient level of ductility, as demonstrated against the tests undertaken in this study.

Chapter 7

CONCLUSIONS AND RECOMMENDATIONS

7.1 Conclusions

Researchers generally agree that the addition of steel fibres to concrete significantly improve the cracking and deformational behaviour of flexural members at service loads, as well as enhance their strength. However, as shown in Chapter 2 of this study, the ductility of R-SFRC members is questioned, particularly for members with low volumes of conventional steel reinforcement.

At high reinforcement ratios and for over-reinforced beams, the inclusion of steel fibres improves the ductility and converts dynamic concrete crushing to progressive concrete crushing, whereas at low reinforcement ratios, especially when combined with high dosages of fibres, the addition of steel fibres can lead to a reduction in ductility of RC flexural members under certain conditions. Some researchers attributed this reduction in ductility and deformational capacity by the addition of steel fibres to crack localisation. In turn, crack localisation locally increases strains in reinforcing bars crossing cracks, leading to fracture of the bars at lower member deformations (deflections). Crack localisation in R-SFRC flexural members is caused by the improved bond between the reinforcing bars and the surrounding concrete due to the influence of fibres and enhanced control of microcracking.

Although limited research has been undertaken on the flexural performance of R-SFRC simply supported members, few studies are found on the flexural performance of R-SFRC continuous members, and no prior studies have investigated the ability of

R-SFRC continuous members with low tensile reinforcement ratios to redistribute loads, or if the achievement of the maximum moment redistribution (generally ±30%) in design standards is possible. Due to the lack of research in this area, AS 3600:2018 [34] limits moment redistribution in continuous members with less than 0.4% of tensile reinforcement. Thus, this study was undertaken with the objectives of determining the moment redistribution capability of R-SFRC continuous members and formulating the post-peak behaviour of R-SFRC flexural members.

Chapter 3 presented the test results of four R-SFRC two-span continuous beams that were designed for 30% of positive and negative moment redistribution with respect to the linear-elastic condition. This experimental program was designed to determine the degree of moment redistribution that can be achieved and the levels of ductility attained. Together with the fibre-reinforced specimens, two control specimens without fibres were also tested. The specimens were 8.2 m long (4.0 m spans), 250 mm wide and 400 mm deep. The tensile reinforcement ratios varied between 0.69% and 1.38%. Dramix 5D steel fibres with nominal dosages of 30 and 60 kg/m^3 were used.

The test results showed that the inclusion of steel fibres marginally increased the load-carrying capacity of the beam specimens. It was observed that crack spacing was reduced, the number of cracks increased and the width of cracks substantially reduced with the addition of steel fibres. In all tests, two plastic hinges fully formed, one at the mid-span of the critical member and one over the intermediate support before the ultimate load was reached, indicating the achievement of full theoretical (elastic) design moment redistribution of ±30%.

The beam specimens were tested up to a displacement of 50 mm. Although for some of the R-SFRC specimens, the peak load occurred slightly before a displacement of span/100, the load did not drop to lower than 99 per cent of the peak load at the displacement of span/100 for any of the R-SFRC beams specimens, and the ductility factor values based on displacement and work done indicate good ductile behaviour displayed by the R-SFRC beam specimens for the steel reinforcement ratios tested. It is concluded that for the steel reinforcement ratios tested, steel fibres can be relied upon in plastic hinge regions for strength and the R-SFRC flexural members can maintain their load-carrying capacity during large plastic rotations and bending moment redistribution.

Chapter 4 presented the test results of four R-SFRC two-span continuous one-way slabs that were designed for 0 to 30% of positive moment redistribution with respect to the linear-elastic condition by varying the tensile reinforcement ratios between 0.21% and 0.42%. This experimental program was designed to determine if the R-SFRC flexural members with less than 0.4% of tensile reinforcement can achieve the design amount of moment redistribution, and to study the effect of low reinforcement ratios and moment redistribution on the post-peak behaviour and ductility of R-SFRC flexural members. To compare the post-peak behaviour of fibre-reinforced and non-fibre specimens, two control RC specimens with same design flexural capacity and moment redistribution of two R-SFRC specimens were also tested. The specimens were 8.2 m long (4.0 m spans), 800 mm wide and 220 mm deep. Dramix 3D steel fibres with a nominal dosage of 60 kg/m^3 were used.

The test results showed that although crack localisation happened in both RC and R-SFRC specimens, the RC specimens showed lengthy hardening regions after the formation of second plastic hinge; whereas, the R-SFRC specimens showed a shorter displacement length over which hardening occurred before the peak load was reached, followed by a period of gentle softening. A comparison of ductility based on displacement and work done indicated that all specimens had a good level of ductility; however, the deflection of the R-SFRC specimens was less than the desired span/100 at ultimate. For both the RC and R-SFRC slabs, the ductility decreased with increasing moment redistribution.

All RC and R-SFRC specimens failed after the formation of two plastic hinges, one at the mid-span of the critical member and one over the intermediate support, which indicates that the specimens achieved full theoretical (elastic) design moment redistributions. It is concluded that R-SFRC continuous members with less than 0.4% of tensile reinforcement can achieve the maximum amount of positive moment redistribution allowed by the current design standards; however, some limitations in reinforcement are appropriate to ensure sufficient ductility up to a displacement of span/100. It is to be noted that the point loads applied in the tests provide for high moment gradients, enhancing the effects of localisation. The influence of load type was further investigated through parametric studies in Chapter 5.

In Chapter 5, two-dimensional FE models of R-SFRC flexural members were developed using the FE program RECAP. The FE models were validated using the test data from this study. The validated FE models were used for parametric studies to determine the effect the slope of the tensile stress-COD of SFRC, the degree of hardening of reinforcement and the type of loading on the post-peak behaviour of R-SFRC flexural members.

The parametric studies showed that the post-peak behaviour of R-SFRC flexural members depends on the combined effect of the rate of softening of SFRC and the degree of hardening of reinforcement. When the amount of tensile reinforcement is low, the post-peak behaviour of R-SFRC flexural members is mainly dominated by the softening of SFRC. A high dosage of steel fibres usually causes a steep softening slope and increases the possibility of post-peak softening when used in flexural members with low tensile reinforcement ratios.

In Chapter 6, the ultimate strength results of the tests were compared with predictions using (1) the rectangular stress block design model of AS 3600: 2018 [34] and (2) a bi-linear model to describe the SFRC stress-COD relationship. In comparison to the RSB approach of AS 3600-2018, the more complex bi-linear model did not show significantly improved accuracy. Further, the bi-linear model requires accurate determination of crack widths and, thus, the crack spacings, which remains problematic. In the bi-linear modelling approach, the influence of errors and uncertainty in determining crack spacing and widths can far exceed any perceived increase in accuracy due to a seemingly improved mapping of the stress-COD curve by adopting a softening model, as opposed to one based on plasticity.

The test data available in the literature was used together with a parametric study to determine the effect of tensile reinforcement ratio and fibre dosage on the ductility of R-SFRC flexural members. A plastic deformation factor was defined for consistent evaluation of the ductility of tested specimens. It was found that the ductility of R-SFRC flexural members decreases with the decrease in reinforcement ratio and the increase in fibre content.

Based on the parametric studies presented in Chapters 5 and 6, the post-peak behaviour of R-SFRC flexural members was mathematically formulated. Based on the formulation, the post-peak hardening and softening of R-SFRC flexural members depends on the relative change in moment due to the hardening provided by reinforcement and softening provided by fibres. In flexural members with low reinforcement ratios and high dosages of fibres, the increase in moment due to the hardening of reinforcement may not compensate for the decrease in moment due to the softening of SFRC, which results in a softening post-peak behaviour. This conclusion depends on the tensile properties of the SFRC used; noting that in this study a relatively high dosage of lower-performing fibre was used to exacerbate the effect. Higher performing fibres in an SFRC matrix that show a higher level of ductility at the material level may not be similarly affected.

Based on the post-peak formulation of R-SFRC flexural members, the relationships for minimum tensile reinforcement for which R-SFRC flexural members will show sufficient ductility were developed and verified using the test data available in this study.

7.2 Recommendations for future study

This is the first time that the moment redistribution capability and post-peak behaviour of R-SFRC continuous members designed for moment redistribution have been studied. Further experimental investigations are recommended that consider different loading condition and fibre types and volumes. In particular, the use of better performing fibres should be studied. Recommendations for further research are as follows:

- In the beam specimens tested in this study, only a single type of fibres was used. Further research should be done by varying the types of fibres.
- For the slab specimens tested in this study, only the positive moment redistributions, and a single dose and a single type of fibres were considered. Further tests should be done on specimens with low reinforcement ratios designed for negative moment redistribution and by varying the dosages and type of fibres.
- The AS 3600:2018 [34] inverse analysis method on prism bending tests over predicted the dogbone test results in this study. Further research should be done in this area to improve the inverse models and decrease model error and uncertainty.
- The empirical relationships for minimum tensile reinforcement for which R-SFRC flexural member will show sufficient ductility are developed for concrete strength of 40 MPa and steel yield strength of 500 MPa. Further study should be undertaken by varying the strength of concrete and reinforcing steel.
- The limitations imposed on reinforcement by AS 3600:2018 [34] for SFRC moment-resisting frames forming part of the seismic-force-resisting system should be studied further.

REFERENCES

1. Bondy, K. B., *Moment redistribution: principles and practice using ACI 318-02.* PTI Journal, 2003. 1(1): 3-21.

2. Naaman, A. E., Harajli, M., and Wight, J. K., *Analysis of ductility in partially prestressed concrete flexural members.* PCI Journal, 1986. 31(3): 64-87.

3. Foster, S. J., *The application of steel-fibres as concrete reinforcement in Australia: from material to structure.* Materials and Structures, 2009. 42(9): 1209-1220.

4. Swamy, R., Al-Taan, S., and Ali, S. A., *Steel fibers for controlling cracking and deflection.* Concrete International, 1979. 1(8): 41-49.

5. Craig, R. J., Decker, J., Dombrowski Jr, L., Laurencelle, R., and Federovich, J., *Inelastic behavior of reinforced fibrous concrete.* Journal of Structural Engineering, 1987. 113(4): 802-817.

6. Kormeling, H., Reinhardt, H., and Shah, S., *Static and fatigue properties of concrete beams reinforced with continuous bars and with fibers.* ACI Journal Proceedings, 1980. 77(1): 36-43.

7. Swamy, R. and Al-Ta'an, S., *Deformation and ultimate strength in flexure of reinforced concrete beams made with steel fiber concrete.* ACI Journal Proceedings, 1981. 78(5): 395-405.

8. Bentur, A. and Mindess, S., *Concrete beams reinforced with conventional steel bars and steel fibres: properties in static loading.* International Journal of Cement Composites and Lightweight Concrete, 1983. 5(3): 199-202.

9. Lim, T.-Y., Paramasivam, P., and Lee, S.-L., *Behavior of reinforced steel-fiber-concrete beams in flexure.* Journal of Structural Engineering, 1987. 113(12): 2439-2458.

10. Dwarakanath, H. and Nagaraj, T., *Deformational behavior of reinforced fiber reinforced concrete beams in bending.* Journal of Structural Engineering, 1992. 118(10): 2691-2698.

11. Ashour, S. A. and Wafa, F. F., *Flexural behavior of high-strength fiber reinforced concrete beams.* ACI Structural Journal, 1993. 90(3): 279-287.

12. Meda, A., Minelli, F., and Plizzari, G. A., *Flexural behaviour of RC beams in fibre reinforced concrete.* Composites Part B: Engineering, 2012. 43(8): 2930-2937.

13. Pujadas, P., Blanco, A., De la Fuente, A., and Aguado, A., *Cracking behavior of FRC slabs with traditional reinforcement.* Materials and Structures, 2012. 45(5): 707-725.

14. Mertol, H. C., Baran, E., and Bello, H. J., *Flexural behavior of lightly and heavily reinforced steel fiber concrete beams.* Construction and Building Materials, 2015. 98: 185-193.

15. Yoo, D.-Y. and Moon, D.-Y., *Effect of steel fibers on the flexural behavior of RC beams with very low reinforcement ratios.* Construction and Building Materials, 2018. 188: 237-254.

16. Oh, B. H., *Flexural analysis of reinforced concrete beams containing steel fibers.* Journal of Structural Engineering, 1992. 118(10): 2821-2835.

17. Ashour, S. A., Wafa, F. F., and Kamal, M. I., *Effect of the concrete compressive strength and tensile reinforcement ratio on the flexural behavior of fibrous concrete beams.* Engineering Structures, 2000. 22(9): 1145-1158.

18. Vandewalle, L., *Cracking behaviour of concrete beams reinforced with a combination of ordinary reinforcement and steel fibers.* Materials and Structures, 2000. 33(3): 164-170.

19. Altun, F., Haktanir, T., and Ari, K., *Effects of steel fiber addition on mechanical properties of concrete and RC beams.* Construction and Building Materials, 2007. 21(3): 654-661.

20. Aoude, H., Belghiti, M., Cook, W. D., and Mitchell, D., *Response of steel fiber-reinforced concrete beams with and without stirrups.* ACI Structural Journal, 2012. 109(3): 359.

21. Alsayed, S. H., *Flexural deflection of reinforced fibrous concrete beams.* Structural Journal, 1993. 90(1): 72-76.

22. Espion, B., Devillers, J., and Halleux, P., *On the use of steel fibers as complementary reinforcement of reinforced-concrete beams in bending.* Materials and Structures, 1993. 26(162): 479-485.

23. Dancygier, A. and Savir, Z., *Flexural behavior of HSFRC with low reinforcement ratios.* Engineering Structures, 2006. 28(11): 1503-1512.

24. Dancygier, A. N. and Berkover, E., *Cracking localization and reduced ductility in fiber-reinforced concrete beams with low reinforcement ratios.* Engineering Structures, 2016. 111: 411-424.

25. Pfyl, T. and Marti, P., *Versuche an stahlfaserverstärkten Stahlbetonelementen*, in *IBK Bericht Vol. 268*. 2001, ETH Zürich: Zürich.

26. Hassoun, M. and Sahebjam, K., *Effect of steel fibers on the cracking behavior of reinforced concrete continuous beams*, in *Structural Design, Cementitious Products, and Case Histories*, 1985. pp: 26-36.

27. Iskhakov, I., Ribakov, Y., and Holschemacher, K., *Experimental investigation of continuous two-layer reinforced concrete beams.* Structural Concrete, 2017. 18(1): 205-215.

28. Küsel, F. and Kearsley, E., *Effect of steel fibres in combination with different reinforcing ratios on the performance of continuous beams.* Construction and Building Materials, 2019. 227: 116553.

29. NZS 3101:Part 1-2006, *Concrete structures standard - Part 1: The design of concrete structures*. 2006, Standards New Zealand: Wellington, New Zealand.

30. *fib* CEB-FIP, *fib model code for concrete structures 2010.* 2010, Ernst & Sohn: Berlin, Germany.

31. ACI 318-14, *Building code requirements for structural concrete and commentary*. 2014, American Concrete Institute: Farmington Hills, MI.

32. DAfStb Guideline, *Commentary on the DAfStb guideline "Steel Fibre Reinforced Concrete"*. 2015, Deutscher Ausschuss für Stahlbeton (German Committee for Structural Concrete): Beuth, Berlin.

33. AS 5100.5:2017, *Bridge design: Part 5-Concrete*. 2017, Australia Standards: Sydney, Australia.

34. AS 3600:2018, *Concrete structures*. 2018, Standards Australia: Sydney, Australia.

35. EN 1992-1-1, *Eurocode 2: Design of concrete structures - Part 1-1: General rules and rules for buildings*. 2004, Comité Européen De Normalisation (European Committee for Standardization): Brussels.

36. Smith, P. E., Bivar, A., Fehérvári, G., Burney, C., Ghirshman, R., Weiss, H., Hansman, J., Stronach, D., Tosi, M., and Sumner, W., *Survey of excavations in Iran during 1970–71.* Journal of the British Institute of Persian Studies, 1972. 10(1): 165-186.

37. Swamy, R., *Prospects of fibre reinforcement in structural applications*, in *Advances in Cement-Matrix Composites, Proceedings, Symposium L, Materials Research Society Generai Meeting, Boston, MA*, 1980. pp: 159-69.

38. Lankard, D. R. and Dickerson, R. F., *Fiber reinforced Wirand concrete.* Cem Betong, 1971. 46(5): 509-515.

39. Shah, S. P. and Rangan, B. V., *Fiber reinforced concrete properties*, in *ACI Journal Proceedings*, 1971. pp: 126-137.

40. Snyder, M. J. and Lankard, D. R., *Factors affecting the flexural strength of steel fibrous concrete strength of steel fibrous concrete*, in *ACI Journal Proceedings*, 1972. pp: 96-100.

41. Johnston, C. D., *Steel fiber reinforced mortar and concrete: A review of mechanical properties.* Special Publication, 1974. 44: 127-142.

42. Rao, C. K. and Swamy, R., *Bearing strength of steel fibre reinforced concrete.* Building Science, 1974. 9(4): 263-268.

43. Swamy, R. and Mangat, P., *Influence of fibre-aggregate interaction on some properties of steel fibre reinforced concrete.* Matériaux et Construction, 1974. 7(5): 307-314.

44. Swamy, R. and Mangat, P., *Influence of fiber geometry on the properties of steel fiber reinforced concrete.* Cement and Concrete Research, 1974. 4(3): 451-465.

45. Swamy, R. and Alnoori, K., *Flexural properties of steel fiber reinforced-concrete.* Concrete, 1975. 9(6): 30-31.

46. Swamy, R. and Mangat, P., *The onset of cracking and ductility of steel fiber concrete.* Cement and Concrete Research, 1975. 5(1): 37-53.

47. Hughes, B. and Fattuhi, N., *Load–deflection curves for fibre-reinforced concrete beams in flexure.* Magazine of Concrete Research, 1977. 29(101): 199-206.

48. Kasperkiewicz, J., *Tensile strength and ultimate strain in steel fibre reinforced concrete.* Applied and Theoretical Mechanics, 1979. 17: 19-34.

49. Johnston, C., *Properties of steel fibre reinforced mortar and concrete*, in *Proceedings of International Symposium on Fibrous Concrete*, 1980. pp: 29-47.

50. Swamy, R. and Jojagha, A., *Impact resistance of steel fibre reinforced lightweight concrete.* International Journal of Cement Composites and Lightweight Concrete, 1982. 4(4): 209-220.

51. Narayanan, R. and Kareem-Palanjian, A., *Effect of fibre addition on concrete strengths.* Indian Concrete Journal, 1984. 58(4): 100-103.

52. Otter, D. E. and Naaman, A. E., *Properties of steel fiber reinforced concrete under cyclic load.* Materials Journal, 1988. 85(4): 254-261.

53. Ramakrishnan, V., Wu, G. Y., and Hosalli, G., *Flexural behavior and toughness of fiber reinforced concretes.* Transportation Research Record, 1989. 1226: 69-77.

54. Nanni, A., *Fatigue behaviour of steel fiber reinforced concrete.* Cement and Concrete Composites, 1991. 13(4): 239-245.

55. Soroushian, P. and Bayasi, Z., *Fiber type effects on the performance of steel fiber reinforced concrete.* Materials Journal, 1991. 88(2): 129-134.

56. Taerwe, L. R., *Influence of steel fibers on strain-softening of high-strength concrete.* Materials Journal, 1993. 89(1): 54-60.

57. Gao, J., Sun, W., and Morino, K., *Mechanical properties of steel fiber-reinforced, high-strength, lightweight concrete.* Cement and Concrete Composites, 1997. 19(4): 307-313.

58. Barros, J. A. and Figueiras, J. A., *Flexural behavior of SFRC: testing and modeling.* Journal of Materials in Civil Engineering, 1999. 11(4): 331-339.

59. AO Barros, J. S. C., J, *Fracture energy of steel fiber-reinforced concrete.* Mechanics of Composite Materials and Structures, 2001. 8(1): 29-45.

60. Balendran, R., Zhou, F., Nadeem, A., and Leung, A., *Influence of steel fibres on strength and ductility of normal and lightweight high strength concrete.* Building and Environment, 2002. 37(12): 1361-1367.

61. Barros, J. A., Cunha, V. M., Ribeiro, A. F., and Antunes, J., *Post-cracking behaviour of steel fibre reinforced concrete.* Materials and Structures, 2005. 38(1): 47-56.

62. Thomas, J. and Ramaswamy, A., *Mechanical properties of steel fiber-reinforced concrete.* Journal of Materials in Civil Engineering, 2007. 19(5): 385-392.

63. Bencardino, F., Rizzuti, L., Spadea, G., and Swamy, R., *Experimental evaluation of fiber reinforced concrete fracture properties.* Composites Part B: Engineering, 2010. 41(1): 17-24.

64. Holschemacher, K., Mueller, T., and Ribakov, Y., *Effect of steel fibres on mechanical properties of high-strength concrete.* Materials & Design (1980-2015), 2010. 31(5): 2604-2615.

65. Olivito, R. and Zuccarello, F., *An experimental study on the tensile strength of steel fiber reinforced concrete.* Composites Part B: Engineering, 2010. 41(3): 246-255.

66. Buratti, N., Mazzotti, C., and Savoia, M., *Post-cracking behaviour of steel and macro-synthetic fibre-reinforced concretes.* Construction and Building Materials, 2011. 25(5): 2713-2722.

67. Tadepalli, P. R., Mo, Y., and Hsu, T. T., *Mechanical properties of steel fibre concrete.* Magazine of Concrete Research, 2013. 65(8): 462-474.

68. Hughes, B. and Fattuhi, N., *Stress-strain curves for fibre reinforced concrete in compression.* Cement and Concrete research, 1977. 7(2): 173-183.

69. Krishna Raju, N. and Basavarajaiah, B., *Compressive strength and bearing strength of steel fiber reinforced concrete.* Indian Concrete Journal, 1977(183-188).

70. Mangat, P. and Azari, M. M., *Influence of steel fibre reinforcement on the fracture behaviour of concrete in compression.* International Journal of Cement Composites and Lightweight Concrete, 1984. 6(4): 219-232.

71. Ezeldin, A. S. and Balaguru, P. N., *Normal-and high-strength fiber-reinforced concrete under compression.* Journal of Materials in Civil Engineering, 1992. 4(4): 415-429.

72. Hsu, L. S. and Hsu, C. T., *Stress-strain behavior of steel-fiber high-strength concrete under compression.* Structural Journal, 1994. 91(4): 448-457.

73. Bencardino, F., Rizzuti, L., Spadea, G., and Swamy, R. N., *Stress-strain behavior of steel fiber-reinforced concrete in compression.* Journal of Materials in Civil Engineering, 2008. 20(3): 255-263.

74. Swamy, R., *The technology of steel fibre reinforced concrete for practical applications.* Proceedings of the Institution of Civil Engineers, 1974. 56(2): 143-159.

75. Dickerson, R., *Steel fiber reinforced concrete-a new pavement material.* Roads and Streets, 1972. 115(7): 68-71.

76. Anon, *Largest fibrous concrete paving project solves clumping problem.* Engineering News Record, 1974. 192(15): 68-73.

77. Johnston, C., *Steel fibre reinforced concrete pavement—second interim performance report.* Fibre Reinforced Cement and Concrete, 1975. 1: 409.

78. Lankard, D. R. and Walker, A. J., *Pavement applications for steel fibrous concrete.* Transportation Engineering Journal of ASCE, 1975. 101(1): 137-153.

79. Williamson, G. R., *Fort Hood Fibre Concrete Overlay*, in *Fibre-reinforced Cement and Concrete, RILEM Symposium*, 1975. pp: 453-459.

80. Rice, J. L., *Fibrous concrete for airport pavements.* Airport Forum, 1977. 7(2): 39-41, 43, 46-47.

81. Carter, W., *Wire–reinforced precast concrete decking panels.* Precast Concrete (UK), 1971: 703-708.

82. Haswell, J. F. S., *BOAC demountable car park at Heathrow Airport, London.* Acier-Stahl-Steel, 1973. 38(3): 97-103.

83. Parker, H., Deere, D., Peck, R., Birkemoe, P., and Semple, R., *Testing and evaluating of prototype tunnel support systems*, in *Technical Report: FRA-ORD/D-74-11*. 1973, University of Illinois, Urbana-Champaign: United States.

84. Paul, S., Gaylord, E., Hendron, A., Kesler, C., Mohraz, B., and Peck, R., *Research to improve tunnel support systems*, in *Report Numbers: FRA-ORD/D-74-51*. 1974, Federal Railroad Administration, DOT: United States.

85. Paul, S., *Large-scale tests of tunnel supports*, in *Rapid Excavation and Tunneling Conference, 2nd Proceedings*, 1974. pp: 22.

86. Henager, C., *A new wrinkle-shotcrete containing steel fibers.* Concrete Construction, 1975. 20(8): 345-347.

87. Murphy, E. M., *Steel-fiber shotcrete in mines.* Concrete Construction - World of Concrete, 1975. 20(10): 443-445.

88. Anon, *New dimensions in bridge deck construction.* Concrete Construction, 1973. 18(7): 321-324.

89. Beckett, R., *Fibrous concrete bridge decks.* Civil Engineering, 1974(814): 32-35.

90. Batson, G., Ball, C., Bailey, L., Landers, E., and Hooks, J., *Flexural fatigue strength of steel fiber reinforced concrete beams*, in *Journal Proceedings*, 1972. pp: 673-677.

91. Hannant, D. J., *Steel fibres and lightweight beams.* Concrete (London), 1972. 6(8): 39-40.

92. Rajagopalan, K., Parameswaran, V., and Ramaswamy, G., *Strength of steel fibre reinforced concrete beams.* Indian Concrete Journal, 1974. 48(1).

93. Hafeez Khan, T. A., Sanjeeva Reddy, T., and Sadananda Murthy, P., *Experimental study of fibre-reinforced concrete beams under pure torsion.* Indian Concrete Journal, 1976. 50(10): 313-317.

94. Henager, C. H. and Doherty, T. J., *Analysis of reinforced fibrous concrete beams.* Journal of the Structural Division, 1976. 102(ST 1): 177-188.

95. Halvorsen, G. T. and Kesler, C. E., *Moment-curvature relationships for concrete beams with plain and deformed steel fibers*, in *ACI Journal Proceedings*, 1979. pp: 697-706.

96. Kormeling, H. A., *Experiments on concrete beams reinforced with conventional reinforcement and steel fibres subjected to fatigue loading.* Heron, 1979. 24(4): 48-65.

97. Narayanan, R. and Toorani-Goloosalar, Z., *Fibre reinforced concrete in pure torsion and in combined bending and torsion*, in *Institution of Civil Engineers, Proceedings*, 1979. pp: 987-1001.

98. Reinhardt, H., *A concrete beam reinforced with bars and steel fibres in pure bending*. Heron, 1979. 24(4).

99. Adepegba, D. and Regan, P. E., *Performance of steel fibre reinforced concrete in axially loaded short columns.* International Journal of Cement Composites and Lightweight Concrete, 1981. 3(4): 255-259.

100. Craig, R. J., McConnell, J., Germann, H., Dib, N., and Kashani, F., *Behavior of reinforced fibrous concrete columns.* ACI Special Publication, 1984. 81: 69-106.

101. Tanaka, Y., Kaneko, Y., Yashiro, H., and Fukushima, S., *Shear failure of steel fiber reinforced concrete (SFRC) short column.* Transaction of the Japan Construction Institute, 1985. 6: 403-408.

102. Mangat, P. and Azari, M. M., *Influence of steel fibre and stirrup reinforcement on the properties of concrete in compression members.* International Journal of Cement Composites and Lightweight Concrete, 1985. 7(3): 183-192.

103. Ganesan, N. and Murthy, J. R., *Strength and behavior of confined steel fiber reinforced concrete columns.* Materials Journal, 1990. 87(3): 221-227.

104. Craig, R. J., Mahadev, S., Patel, C., Viteri, M., and Kertesz, C., *Behavior of joints using reinforced fibrous concrete.* ACI Special Publication, 1984. 81: 125-168.

105. Jindal, R. L. and Hassan, K. A., *Behavior of steel fiber reinforced concrete beam-column connections.* ACI Special Publication, 1984. 81: 107-124.

106. Panda, A. K., Spencer, R., and Mindess, S., *Bond of deformed bars in steel fibre reinforced concrete under cyclic loading.* International Journal of Cement Composites and Lightweight Concrete, 1986. 8(4): 239-249.

107. Gefken, P. R. and Ramey, M. R., *Increased joint hoop spacing in type 2 seismic joints using fiber reinforced concrete.* ACI Structural Journal, 1989. 86(2): 168-172.

108. Jiuru, T., Chaobin, H., Kaijian, Y., and Yongcheng, Y., *Seismic behavior and shear strength of framed joint using steel-fiber reinforced concrete.* Journal of Structural Engineering, 1992. 118(2): 341-358.

109. Bayasi, Z. and Zhou, J., *Seismic resistance of steel fiber reinforced concrete beam-column joints*, in *Structural Engineering in Natural Hazards Mitigation*, 1993. pp: 1402-1408.

110. Filiatrault, A., Ladicani, K., and Massicotte, B., *Seismic performance of code-designed fiber reinforced concrete joints.* ACI Structural Journal, 1994. 91(5): 564-571.

111. Katzensteiner, B., Mindess, S., Filiatrault, A., and Banthia, N., *Dynamic tests of steel-fiber reinforced concrete frames.* Concrete International, 1994. 16(9): 57-60.

112. Filiatrault, A., Pineau, S., and Houde, J., *Seismic behavior of steel-fiber reinforced concrete interior beam-column joints.* Structural Journal, 1995. 92(5): 543-552.

113. Elvery, R. H. and Samarai, M., *Reduction of shrinkage cracking in reinforced concrete due to the inclusion of steel fibres*, in *Fibre Reinforced Cement and Concrete, Rilem Symposium*, 1975. pp: 149-159.

114. Ghalib, M. A., *Moment capacity of steel fiber reinforced small concrete slabs*, in *ACI Journal Proceedings*, 1980. pp: 247-257.

115. Knab, L. and Clifton, J., *Cumulative damage of reinforced concrete subjected to repeated impact.* Cement and Concrete Research, 1982. 12(3): 359-370.

116. Hülsewig, M., Schneider, E., and Stilp, A., *Behaviour of fiber reinforced concrete slabs under impact loading*. 1983, Fraunhofer Inst Fuer Kurzzeitdynamik-Ernst-Mach-Inst Frieburg (Germany F R).

117. Fattuhi, N., *Toughness of thin slabs under flexural or impact loading*, in *Proceedings of the Fourth International Conference*, 1983. Stockholm, Sweden, pp: 573-580.

118. Narayanan, R. and Darwish, I., *Punching shear tests on steel-fibre-reinforced micro-concrete slabs.* Magazine of Concrete Research, 1987. 39(138): 42-50.

119. Hossain, N. B. and Stewart, M. G., *Probabilistic models of damaging deflections for floor elements.* Journal of Performance of Constructed Facilities, 2001. 15(4): 135-140.

120. Sahoo, D. R., Solanki, A., and Kumar, A., *Influence of steel and polypropylene fibers on flexural behavior of RC beams.* Journal of Materials in Civil Engineering, 2015. 27(8): 04014232.

121. Schumacher, P., Walraven, J. C., Den Uijl, J. A., and Bigaj-van Vliet, A., *Rotation capacity of self-compacting steel fibre reinforced concrete beams.* Heron, 2009. 54(2/3): 127-161.

122. Deluce, J. R. and Vecchio, F. J., *Cracking behavior of steel fiber-reinforced concrete members containing conventional reinforcement.* ACI Structural Journal, 2013. 110(3): 481-490.

123. Dancygier, A., Karinski, Y., and Navon, Z., *Cracking localization in tensile conventionally reinforced fibrous concrete bars.* Construction and Building Materials, 2017. 149: 53-61.

124. Walraven, J. C., *High performance fiber reinforced concrete: progress in knowledge and design codes.* Materials and Structures, 2009. 42(9): 1247.

125. Yuguang, Y., Walraven, J. C., and den Uijl, J. A., *Combined effect of fibers and steel rebars in high performance concrete.* Heron, 2009. 54(2/3): 205-224.

126. Dancygier, A. N. and Karinski, Y. S., *Probabilistic model of the crack localization in axially loaded fibrous reinforced concrete bars.* Engineering Structures, 2014. 79: 417-426.

127. Karinski, Y. S. and Dancygier, A. N., *Effects of fibers and conventional reinforcement contents on fibers scaterring in prismatic bars.* Cement and Concrete Composites, 2018. 86: 171-177.

128. Karinsrki, Y. S., Dancygier, A. N., and Navon, Z., *Experimental verification for a probabilistic model of fibers distribution along a reinforced concrete bar.* Materials and Structures, 2017. 50(2): 119.

129. Liu, H., Xiang, T., and Zhao, R., *Research on non-linear structural behaviors of prestressed concrete beams made of high strength and steel fiber reinforced concretes.* Construction and Building Materials, 2009. 23(1): 85-95.

130. Abas, F., Gilbert, R., Foster, S., and Bradford, M., *Strength and serviceability of continuous composite slabs with deep trapezoidal steel decking and steel fibre reinforced concrete.* Engineering Structures, 2013. 49: 866-875.

131. Foster, S. and Parvez, A., *Assessment of model error for reinforced concrete beams with steel fibers in bending.* Structural Concrete, 2019. 20(3): 1010-1021.

132. AS 1391-2007, *Metallic materials—Tensile testing at ambient temperature*. 2007, Standards Australia: Sydney, Australia.

133. AS 1012.9:2014, *Methods of testing concrete - Method 9: Compressive strength tests - Concrete, mortar and grout specimens* 2014, Standards Australia: Sydney, Australia.

134. AS 1012.10:2000, *Methods of testing concrete - Method 10: Determination of indirect tensile strength of concrete cylinders ('Brazil' or splitting test).* 2000, Standards Australia: Sydney, Australia.

135. EN 14651, *Test method for metallic fibered concrete - Measuring the flexural tensile strength (limit of proportionality (LOP), residual)*. 2005, Comité Européen De Normalisation (European Committee for Standardization): Brussels.

136. Park, R., *Evaluation of ductility of structures and structural assemblages from laboratory testing.* Bulletin of the New Zealand national society for earthquake engineering, 1989. 22(3).

137. Bernardo, L. and Lopes, S., *Neutral axis depth versus flexural ductility in high-strength concrete beams.* Journal of Structural Engineering, 2004. 130(3): 452-459.

138. Yang, I. H., Joh, C., and Kim, B.-S., *Structural behavior of ultra high performance concrete beams subjected to bending.* Engineering Structures, 2010. 32(11): 3478-3487.

139. Shin, S.-W., Ghosh, S. K., and Moreno, J., *Flexural ductility of ultra-high-strength concrete members.* Structural Journal, 1989. 86(4): 394-400.

140. Hadi, M. N. and Elbasha, N., *Effects of tensile reinforcement ratio and compressive strength on the behaviour of over-reinforced helically confined HSC beams.* Construction and Building Materials, 2007. 21(2): 269-276.

141. Gilbert, R. I. and Sakka, Z. I., *Strength and ductility of reinforced concrete slabs containing welded wire fabric and subjected to support settlement.* Engineering Structures, 2010. 32(6): 1509-1521.

142. Cohn, M., *Continuity in prestressed concrete*, in *Partial Prestressing, From Theory To Practice*. 1986, Springer. 189-256.

143. Foster, S., *An application of the arc length method involving concrete cracking.* International Journal for Numerical Methods in Engineering, 1992. 33(2): 269-285.

144. Foster, S., *The structural behaviour of reinforced concrete deep beams*. PhD Dissertation, 1992. University of New South Wales, Sydney, Australia.

145. Foster, S., Budiono, B., and Gilbert, R., *Rotating crack finite element model for reinforced concrete structures.* Computers & Structures, 1996. 58(1): 43-50.

146. Foster, S. and Marti, P., *Cracked membrane model: finite element implementation.* Journal of Structural Engineering, 2003. 129(9): 1155-1163.

147. Darwin, D. and Pecknold, D. A., *Nonlinear biaxial stress-strain law for concrete.* Journal of the Engineering Mechanics Division, 1977. 103(2): 229-241.

148. Attard, M. M., Minh, N., and Foster, S. J., *Finite element analysis of out-of-plane buckling of reinforced concrete walls.* Computers & Structures, 1996. 61(6): 1037-1042.

149. Thorenfeldt, E., *Mechanical properties of high-strength concrete and applications in design*, in *International Symposium on Utilization of High-Strength Concrete*, 1987. Stavanger, Norway, pp: 149-159.

150. Petersson, P.-E., *Crack growth and development of fracture zone in plain concrete and similar materials.* Report TVBM-1006, Division of Building Materials, Lund Institute of Technology, Lund, Sweden, 1981.

151. Voo, Y. L. and Foster, S., *Reactive powder concrete: analysis and design of RPC girders*. 2009: Lambert Academic Publishing.

152. Voo, Y. L., Poon, W. K., and Foster, S., *Shear strength of steel fiber-reinforced ultrahigh-performance concrete beams without stirrups.* Journal of Structural Engineering, 2010. 136(11): 1393-1400.

153. Ngo, D. and Scordelis, A. C., *Finite element analysis of reinforced concrete beams*, in *ACI Journal Proceedings*, 1967. pp: 152-163.

154. Nilson, A. H., *Nonlinear analysis of reinforced concrete by the finite element method*, in *ACI Journal Proceedings*, 1968. pp: 757-766.

155. Mufti, A., Mirza, M., McCutcheon, J., and Houde, J., *A study of the nonlinear behavior of structural concrete elements.* in Proceeding of the Specialty Conference of Finite Element Method in Civil Engineering, Montreal, Canada, 1972.

156. Al-Mahaidi, R. S. H., *Nonlinear finite-element analysis of reinforced concrete deep members*. PhD Thesis, 1979. Cornell University,

157. Rashid, Y., *Ultimate strength analysis of prestressed concrete pressure vessels.* Nuclear Engineering and Design, 1968. 7(4): 334-344.

158. Cope, R., *Modeling of reinforced concrete behavior for finite element analysis of bridge slabs.* Numerical Method for Nonlinear Problems, 1980. 1: 457-470.

159. Okamura, H. and Maekawa, K., *Nonlinear analysis and constitutive methods of reinforced concrete*. 1991, ISBN 7655-1506-0, University of Tokyo: Tokyo.

160. Kaufmann, W. and Marti, P., *Structural concrete: cracked membrane model.* Journal of Structural Engineering, 1998. 124(12): 1467-1475.

161. Barzegar-Jamshidi, F. and Schnobrich, W. C., *Nonlinear finite element analysis of reinforced concrete under short term monotonic loading*, in *Civil Engineering Studies SRS-530*. 1986, University of Illinois, Urbana-Champaign: United States.

162. Ayoub, A. and Filippou, F. C., *Nonlinear finite-element analysis of RC shear panels and walls.* Journal of Structural Engineering, 1998. 124(3): 298-308.

163. Vecchio, F. J., *Disturbed stress field model for reinforced concrete: formulation.* Journal of structural engineering, 2000. 126(9): 1070-1077.

164. Bažant, Z. P. and Pijaudier-Cabot, G., *Nonlocal continuum damage, localization instability and convergence.* Journal of Applied Mechanics, 1988. 55(2): 287-293.

165. Bažant, Z. P. and Ožbolt, J., *Nonlocal microplane model for fracture, damage, and size effect in structures.* Journal of Engineering Mechanics, 1990. 116(11): 2485-2505.

166. De Borst, R. and Mühlhaus, H. B., *Gradient-dependent plasticity: formulation and algorithmic aspects.* International Journal for Numerical Methods in Engineering, 1992. 35(3): 521-539.

167. Borst, R. d., Muhlhaus, H., Pamin, J., and Sluys, L., *A continuum mechanics approach to concrete fracture.* Numerical Models in Fracture Mechanics of Concrete, 1993: 115-127.

168. Bažant, Z. P., Belytschko, T. B., and Chang, T.-P., *Continuum theory for strain-softening*. Journal of Engineering Mechanics, 1984. 110(12): 1666-1692.

169. Bažant, Z., *Recent advances in failure localization and non-local models.* Micromechanics of Failure of Quasi-brittle Materials, 1990: 12-32.

170. Jirásek, M. and Zimmermann, T., *Rotating crack model with transition to scalar damage.* Journal of Engineering Mechanics, 1998. 124(3): 277-284.

171. Foster, S. J., Voo, Y., and Chong, K., *FE analysis of steel fiber reinforced concrete beams failing in shear: variable engagement model.* ACI Special Publication, 2006. 237: 55-70.

172. Bažant, Z. P. and Oh, B. H., *Crack band theory for fracture of concrete.* Matériaux et Construction, 1983. 16(3): 155-177.

APPENDIX A

This appendix provides detail calculations of the design of RC and R-SFRC two-span continuous beams for moment redistribution tested in this study and presented in Chapter 3.

A1 Design data

Design Standard = AS 3600-2018

Depth of the beams, $D = 400$ mm

Width of the beams, $b = 250$ mm

Characteristic compressive strength of concrete, $f_c' = 40$ MPa

$\alpha_2 = 0.85 - 0.0015 f_c' = 0.80$; $\alpha_2 \geq 0.67$

$\gamma = 0.97 - 0.0025 f_c' = 0.89$; $\gamma \geq 0.67$

Yield strength of steel, $f_{sy} = 500$ MPa

Elastic modulus of steel, $E_s = 200 \times 10^3$ MPa

Characteristic residual tensile strength of SFRC for 30 kg/m^3 of Dramix 5D fibres, $f_{1.5}' = 0.8$ MPa

Characteristic residual tensile strength of SFRC for 60 kg/m^3 of Dramix 5D fibres, $f_{1.5}' = 1.6$ MPa

Effective depth of tensile reinforcement, $d_t = 360$ mm

Effective depth of compressive reinforcement, $d_c = 40$ mm

A2 Design of the specimens in Series A

A2.1 Specimen B00(-30)

A2.1.1 Preliminary design

Specimen B00(-30) was designed for 30% of negative moment redistribution with respect to linear elastic condition.

Design load, $P = 200$ kN

For a two-span continuous beam with a span length of 4 m,

Elastic moment at mid-span, ${M_E}^{+} = 0.625P$

Elastic moment at intermediate support, ${M_E}^{-} = 0.75P$

For 30% of negative moment redistribution with respect to linear elastic condition,

$M^{-} = 1.3{M_E}^{-} = 1.3 * 0.75P = 0.975P = 195$ kN-m

$M^{+} = 1 - 0.5M^{-} = 0.5125P = 102.5$ kN-m

Ignoring the effect of compressive reinforcement,

$M^{+} = {A_{st}}^{+} f_{sy}(0.9d_t) = 102.5$ kN-m

${A_{st}}^{+} = 633$ mm^2

Try 2-N20 bars, ${A_{st}}^{+} = 2 \times 310 = 620$ mm^2

$M^{-} = {A_{st}}^{-} f_{sy}(0.9d_t) = 195$ kN-m

${A_{st}}^{-} = 1204$ mm^2

Try 2-N20 and 1-N28 bars, ${A_{st}}^{-} = 2 \times 310 + 1 \times 620 = 1240$ mm^2

A2.1.2 Calculation of ultimate capacity and moment redistribution for the provided reinforcement

Figure A.1 shows the stress block and forces on RC section based on AS 3600-2018 model.

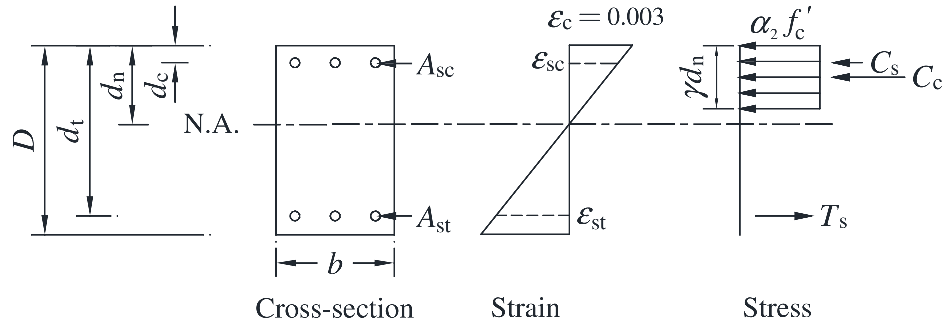

Figure A.1: Stress block and forces on RC section based on AS 3600-2018 model.

At mid-span:

Compressive force of concrete, $C_c = \alpha_2 f_c' \gamma d_n b = 6.87 d_n$ kN

Tensile reinforcement, $A_{st} = 620$ mm^2

Tensile force of steel reinforcement, $T_s = A_{st} f_{sy} = 310$ kN

Compressive reinforcement, $A_{sc} = 620$ mm^2 (2-N20 bars were continued throughout the span)

Compressive force of steel reinforcement, $C_s = A_{sc} E_s \varepsilon_{sc}$

$$= A_{sc} E_s \times 0.003 \times (d_n - d_c)/d_n$$

$$= 372(d_n - 40)/d_n \text{ kN}$$

Solving equilibrium: $C_c + C_s = T_s$

$d_n = 42.2$ mm

Forces:

$C_c = 290.3$ kN

$C_s = 19.7$ kN

$T_s = 310$ kN

Moment capacity at mid-span:

Taking moment about the neutral axis,

$M^+ = C_c(d_n - \gamma d_n/2) + C_s(d_n - d_c) + T_s(d_t - d_n)$

$= 105.5$ kN-m

At intermediate support:

Compressive force of concrete, $C_c = \alpha_2 f_c' \gamma d_n b = 6.87 d_n$ kN

Tensile reinforcement, $A_{st} = 1240$ mm^2

Tensile force of steel reinforcement, $T_s = A_{st} f_{sy} = 620$ kN

Compressive reinforcement, $A_{sc} = 620$ mm^2

Compressive force of steel reinforcement, $C_s = A_{sc} E_s \varepsilon_{sc}$

$= A_{sc} E_s \times 0.003 \times (d_n - d_c)/d_n$

$= 372(d_n - 40)/d_n$ kN

Solving equilibrium: $C_c + C_s = T_s$

$d_n = 67.9$ mm

Forces:

$C_c = 467$ kN

$C_s = 153$ kN

$T_s = 620$ kN

Moment capacity at intermediate support:

Taking moment about the neutral axis,

$M^- = C_c(d_n - \gamma d_n/2) + C_s(d_n - d_c) + T_s(d_t - d_n)$

$= 203.3$ kN-m

Ultimate capacity of the beam specimen, $P = M^+ + 0.5M^- = 207.1$ kN (OK)

Elastic moment at intermediate support, $M_E{}^- = 0.75P = 155.3$ kN-m

Moment redistribution (%) = $(M_E{}^- - M^-)/M_E{}^- \times 100\% = -30.9\%$ (OK)

A2.2 Specimen B30(-30)

Specimen B30(-30) was designed for the same reinforcement ratios as specimen B00(-30) considering the contribution of 30 kg/m^3 of steel fibres. Figure A.2 shows the stress block and forces on R-SFRC section based on AS 3600-2018 model.

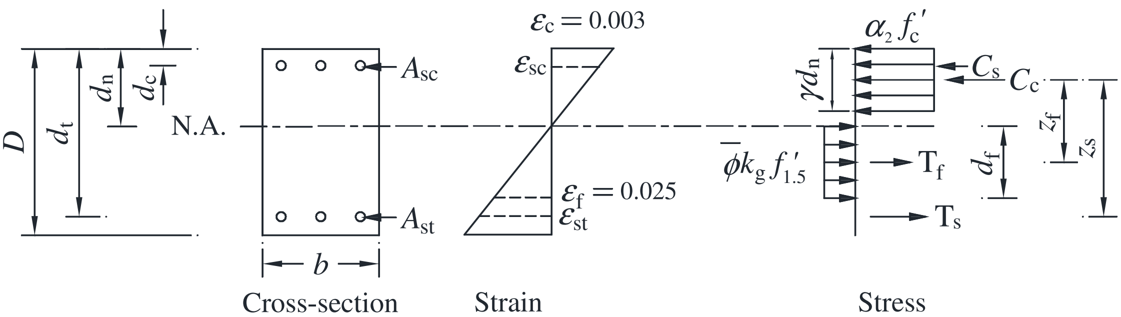

Figure A.2: Stress block and forces on R-SFRC section based on AS 3600-2018 model.

At mid-span:

Compressive force of concrete, $C_c = \alpha_2 f'_c \gamma d_n b = 6.87 d_n$ kN

Tensile reinforcement, $A_{st} = 620$ mm^2

Tensile force of steel reinforcement, $T_s = A_{st} f_{sy} = 310$ kN

Compressive reinforcement, $A_{sc} = 620$ mm^2 (2-N20 bars were continued throughout the span)

Compressive force of steel reinforcement, $C_s = A_{sc} E_s \varepsilon_{sc}$

$$= A_{sc} E_s \times 0.003 \times (d_n - d_c)/d_n$$

$$= 372(d_n - 40)/d_n \text{ kN}$$

Tensile force of fibre, $T_f = \overline{\emptyset} k_g f'_{1.5} b d_f$

Assume, $\overline{\emptyset} = 1, k_g = 1, d_f = D - d_n$

$T_f = 0.2(400 - d_n)$ kN

Solving equilibrium: $C_c + C_s = T_s + T_f$

$d_n = 47.2$ mm

Check tensile strain at the bottom face of the cross-section:

$\varepsilon_t = 0.003 \times (D - d_n)/d_n = 0.0224 < 0.025$ (OK)

$d_f = D - d_n = 352.8$ mm

Forces:

$C_c = 324.1$ kN

$C_s = 56.5$ kN

$T_s = 310$ kN

$T_f = 70.6$ kN

Moment capacity at mid-span:

Taking moment about the neutral axis,

$M^+ = C_c(d_n - \gamma d_n/2) + C_s(d_n - d_c) + T_s(d_t - d_n) + T_f \times d_f/2$

$= 118.5$ kN-m

At intermediate support:

Compressive force of concrete, $C_c = \alpha_2 f_c' \gamma d_n b = 6.87 d_n$ kN

Tensile reinforcement, $A_{st} = 1240$ mm^2

Tensile force of steel reinforcement, $T_s = A_{st} f_{sy} = 620$ kN

Compressive reinforcement, $A_{sc} = 620$ mm^2

Compressive force of steel reinforcement, $C_s = A_{sc} E_s \varepsilon_{sc}$

$= A_{sc} E_s \times 0.003 \times (d_n - d_c)/d_n$

$= 372(d_n - 40)/d_n$ kN

Tensile force of fibre, $T_f = 0.2(400 - d_n)$ kN

Solving equilibrium: $C_c + C_s = T_s + T_f$

$d_n = 74.6$ mm

Check tensile strain at the bottom face of the cross-section:

$\varepsilon_t = 0.003 \times (D - d_n)/d_n = 0.0131 < 0.025$ (OK)

$d_f = D - d_n = 325.4$ mm

Forces:

$C_c = 512.6$ kN

$C_s = 172.5$ kN

$T_s = 620$ kN

$T_f = 65.1$ kN

Moment capacity at intermediate support:

Taking moment about the neutral axis,

$M^{-} = C_c(d_n - \gamma d_n/2) + C_s(d_n - d_c) + T_s(d_t - d_n) + T_f \times d_f/2$

$= 215.1$ kN-m

Ultimate capacity of the beam specimen, $P = M^{+} + 0.5M^{-} = 226$ kN

Elastic moment at intermediate support, $M_E{}^{-} = 0.75P = 169.5$ kN-m

Moment redistribution (%) = $(M_E{}^{-} - M^{-})/M_E{}^{-} \times 100\% = -26.9\%$

A2.3 Specimen B60(-30)

Specimen B60(-30) was designed for the same reinforcement ratios as specimen B00(-30) considering the contribution of 60 kg/m^3 of steel fibres.

At mid-span:

Compressive force of concrete, $C_c = \alpha_2 f'_c \gamma d_n b = 6.87 d_n$ kN

Tensile reinforcement, $A_{st} = 620$ mm^2

Tensile force of steel reinforcement, $T_s = A_{st} f_{sy} = 310$ kN

Compressive reinforcement, $A_{sc} = 620$ mm^2 (2-N20 bars were continued throughout the span)

Compressive force of steel reinforcement, $C_s = A_{sc} E_s \varepsilon_{sc}$

$$= A_{sc} E_s \times 0.003 \times (d_n - d_c)/d_n$$

$$= 372(d_n - 40)/d_n \text{ kN}$$

Tensile force of fibre, $T_f = f'_{1.5} b d_f = 1.6 \times 250 \times (D - d_n) = 0.4(400 - d_n)$ kN

Solving equilibrium: $C_c + C_s = T_s + T_f$

$d_n = 52.5$ mm

Check tensile strain at the bottom face of the cross-section:

$\varepsilon_t = 0.003 \times (D - d_n)/d_n = 0.0199 < 0.025$ (OK)

$d_f = D - d_n = 347.5$ mm

Forces:

$C_c = 360.6$ kN

$C_s = 88.4$ kN

$T_s = 310$ kN

$T_f = 139$ kN

Moment capacity at mid-span:

Taking moment about the neutral axis,

$M^+ = C_c(d_n - \gamma d_n/2) + C_s(d_n - d_c) + T_s(d_t - d_n) + T_f \times d_f/2$

$= 131.3$ kN-m

At intermediate support:

Compressive force of concrete, $C_c = \alpha_2 f_c' \gamma d_n b = 6.87 d_n$ kN

Tensile reinforcement, $A_{st} = 1240$ mm^2

Tensile force of steel reinforcement, $T_s = A_{st} f_{sy} = 620$ kN

Compressive reinforcement, $A_{sc} = 620$ mm^2

Compressive force of steel reinforcement, $C_s = A_{sc} E_s \varepsilon_{sc}$

$= A_{sc} E_s \times 0.003 \times (d_n - d_c)/d_n$

$= 372(d_n - 40)/d_n$ kN

Tensile force of fibre, $T_f = f_{1.5}' b d_f = 1.6 \times 250 \times (D - d_n) = 0.4(400 - d_n)$ kN

Solving equilibrium: $C_c + C_s = T_s + T_f$

$d_n = 81.3$ mm

Check tensile strain at the bottom face of the cross-section:

$\varepsilon_t = 0.003 \times (D - d_n)/d_n = 0.0118 < 0.025$ (OK)

$d_f = D - d_n = 318.7$ mm

Forces:

$C_c = 558.6$ kN

$C_s = 188.9$ kN

$T_s = 620$ kN

$T_f = 127.5$ kN

Moment capacity at intermediate support:

Taking moment about the neutral axis,

$M^- = C_c(d_n - \gamma d_n/2) + C_s(d_n - d_c) + T_s(d_t - d_n) + T_f \times d_f/2$

$= 226.6$ kN-m

Ultimate capacity of the beam specimen, $P = M^+ + 0.5M^- = 244.6$ kN

Elastic moment at intermediate support, $M_E{}^- = 0.75P = 183.4$ kN-m

Moment redistribution (%) = $(M_E{}^- - M^-)/M_E{}^- \times 100\% = -23.5\%$

A3 Design of the specimens in Series B

A3.1 Specimen B00(+30)

A3.1.1 Preliminary design

Specimen B00(+30) was designed for 30% of positive moment redistribution with respect to linear elastic condition.

Design load, $P = 200$ kN

For 30% of positive moment redistribution with respect to linear elastic condition,

$M^- = 0.7 M_E{}^- = 0.7 * 0.75P = 0.525P = 105$ kN-m

$M^+ = 1 - 0.5M^- = 0.7375P = 147.5$ kN-m

Ignoring the effect of compressive reinforcement,

$M^+ = A_{st}{}^+ f_{sy}(0.9d_t) = 147.5$ kN-m

$A_{st}{}^+ = 910$ mm^2

Try 3-N20 bars, $A_{st}{}^+ = 3 \times 310 = 930$ mm^2

$M^- = A_{st}{}^- f_{sy}(0.9d_t) = 105$ kN-m

$A_{st}{}^- = 648$ mm^2

Try 2-N20 bars, $A_{st}{}^- = 2 \times 310 = 620$ mm^2

A3.1.2 Calculation of ultimate capacity and moment redistribution for the provided reinforcement

At mid-span:

Compressive force of concrete, $C_c = \alpha_2 f_c' \gamma d_n b = 6.87 d_n$ kN

Tensile reinforcement, $A_{st} = 930$ mm^2

Tensile force of steel reinforcement, $T_s = A_{st} f_{sy} = 465$ kN

Compressive reinforcement, $A_{sc} = 620$ mm^2

Compressive force of steel reinforcement, $C_s = A_{sc} E_s \varepsilon_{sc}$

$$= A_{sc} E_s \times 0.003 \times (d_n - d_c)/d_n$$

$$= 372(d_n - 40)/d_n \text{ kN}$$

Solving equilibrium: $C_c + C_s = T_s$

$d_n = 53.8$ mm

Forces:

$C_c = 369.7$ kN

$C_s = 95.3$ kN

$T_s = 465$ kN

Moment capacity at mid-span:

Taking moment about the neutral axis,

$$M^+ = C_c(d_n - \gamma d_n/2) + C_s(d_n - d_c) + T_s(d_t - d_n)$$

$$= 154.9 \text{ kN-m}$$

At intermediate support:

Compressive force of concrete, $C_c = \alpha_2 f_c' \gamma d_n b = 6.87 d_n$ kN

Tensile reinforcement, $A_{st} = 620$ mm^2

Tensile force of steel reinforcement, $T_s = A_{st} f_{sy} = 310$ kN

Compressive reinforcement, $A_{sc} = 620$ mm^2 (2-N20 bars were continued throughout the span)

Compressive force of steel reinforcement, $C_s = A_{sc} E_s \varepsilon_{sc}$

$$= A_{sc} E_s \times 0.003 \times (d_n - d_c)/d_n$$

$$= 372(d_n - 40)/d_n \text{ kN}$$

Solving equilibrium: $C_c + C_s = T_s$

$d_n = 42.2$ mm

Forces:

$C_c = 290.3$ kN

$C_s = 19.7$ kN

$T_s = 310$ kN

Moment capacity at intermediate support:

Taking moment about the neutral axis,

$$M^- = C_c(d_n - \gamma d_n/2) + C_s(d_n - d_c) + T_s(d_t - d_n)$$

$$= 105.5 \text{ kN-m}$$

Ultimate capacity of the beam specimen, $P = M^+ + 0.5M^- = 207.7$ kN (OK)

Elastic moment at intermediate support, $M_E{}^- = 0.75P = 155.8$ kN-m

Moment redistribution (%) = $(M_E{}^- - M^-)/M_E{}^- \times 100\% = +32.3\%$ (OK)

A3.2 Specimen B30(+30)

Specimen B30(+30) was designed for the same reinforcement ratios as specimen B00(+30) considering the contribution of 30 kg/m^3 of steel fibres.

At mid-span:

Compressive force of concrete, $C_c = \alpha_2 f_c' \gamma d_n b = 6.87 d_n$ kN

Tensile reinforcement, $A_{st} = 930$ mm^2

Tensile force of steel reinforcement, $T_s = A_{st} f_{sy} = 465$ kN

Compressive reinforcement, $A_{sc} = 620$ mm^2

Compressive force of steel reinforcement, $C_s = A_{sc} E_s \varepsilon_{sc}$

$$= A_{sc} E_s \times 0.003 \times (d_n - d_c)/d_n$$

$$= 372(d_n - 40)/d_n \text{ kN}$$

Tensile force of fibre, $T_f = f_{1.5}' b d_f = 0.8 \times 250 \times (D - d_n) = 0.2(400 - d_n)$ kN

Solving equilibrium: $C_c + C_s = T_s + T_f$

$d_n = 59.7$ mm

Check tensile strain at the bottom face of the cross-section:

$\varepsilon_t = 0.003 \times (D - d_n)/d_n = 0.0171 < 0.025$ (OK)

$d_f = D - d_n = 340.3$ mm

Forces:

$C_c = 410.3$ kN

$C_s = 122.7$ kN

$T_s = 465$ kN

$T_f = 68.1$ kN

Moment capacity at mid-span:

Taking moment about the neutral axis,

$M^+ = C_c(d_n - \gamma d_n/2) + C_s(d_n - d_c) + T_s(d_t - d_n) + T_f \times d_f/2$

$= 167.5$ kN-m

At intermediate support:

Compressive force of concrete, $C_c = \alpha_2 f_c' \gamma d_n b = 6.87 d_n$ kN

Tensile reinforcement, $A_{st} = 620$ mm^2

Tensile force of steel reinforcement, $T_s = A_{st} f_{sy} = 310$ kN

Compressive reinforcement, $A_{sc} = 620$ mm^2 (2-N20 bars were continued throughout the span)

Compressive force of steel reinforcement, $C_s = A_{sc} E_s \varepsilon_{sc}$

$= A_{sc} E_s \times 0.003 \times (d_n - d_c)/d_n$

$= 372(d_n - 40)/d_n$ kN

Tensile force of fibre, $T_f = f_{1.5}' b d_f = 0.8 \times 250 \times (D - d_n) = 0.2(400 - d_n)$ kN

Solving equilibrium: $C_c + C_s = T_s + T_f$

$d_n = 47.2$ mm

Check tensile strain at the bottom face of the cross-section:

$\varepsilon_t = 0.003 \times (D - d_n)/d_n = 0.0224 < 0.025$ (OK)

$d_f = D - d_n = 352.8$ mm

Forces:

$C_c = 324.1$ kN

$C_s = 56.5$ kN

$T_s = 310$ kN

$T_f = 70.6$ kN

Moment capacity at intermediate support:

Taking moment about the neutral axis,

$M^- = C_c(d_n - \gamma d_n/2) + C_s(d_n - d_c) + T_s(d_t - d_n) + T_f \times d_f/2$

$= 118.5$ kN-m

Ultimate capacity of the beam specimen, $P = M^+ + 0.5M^- = 226.7$ kN

Elastic moment at intermediate support, $M_E{}^- = 0.75P = 170$ kN-m

Moment redistribution (%) = $(M_E{}^- - M^-)/M_E{}^- \times 100\% = +30.3\%$

A3.3 Specimen B60(+30):

Specimen B60(+30) was designed for the same reinforcement ratios as specimen B00(+30) considering the contribution of 60 kg/m^3 of steel fibres.

At mid-span:

Compressive force of concrete, $C_c = \alpha_2 f_c' \gamma d_n b = 6.87 d_n$ kN

Tensile reinforcement, $A_{st} = 930$ mm^2

Tensile force of steel reinforcement, $T_s = A_{st} f_{sy} = 465$ kN

Compressive reinforcement, $A_{sc} = 620$ mm^2

Compressive force of steel reinforcement, $C_s = A_{sc} E_s \varepsilon_{sc}$

$$= A_{sc} E_s \times 0.003 \times (d_n - d_c)/d_n$$

$$= 372(d_n - 40)/d_n \text{ kN}$$

Tensile force of fibre, $T_f = f_{1.5}' b d_f = 1.6 \times 250 \times (D - d_n) = 0.4(400 - d_n)$ kN

Solving equilibrium: $C_c + C_s = T_s + T_f$

$d_n = 65.9$ mm

Check tensile strain at the bottom face of the cross-section:

$\varepsilon_t = 0.003 \times (D - d_n)/d_n = 0.0152 < 0.025$ (OK)

$d_f = D - d_n = 334.1$ mm

Forces:

$C_c = 452.6$ kN

$C_s = 146$ kN

$T_s = 465$ kN

$T_f = 133.7$ kN

Moment capacity at mid-span:

Taking moment about the neutral axis,

$M^+ = C_c(d_n - \gamma d_n/2) + C_s(d_n - d_c) + T_s(d_t - d_n) + T_f \times d_f/2$

$= 179.7$ kN-m

At intermediate support:

Compressive force of concrete, $C_c = \alpha_2 f_c' \gamma d_n b = 6.87 d_n$ kN

Tensile reinforcement, $A_{st} = 620$ mm^2

Tensile force of steel reinforcement, $T_s = A_{st} f_{sy} = 310$ kN

Compressive reinforcement, $A_{sc} = 620$ mm^2 (2-N20 bars were continued throughout the span)

Compressive force of steel reinforcement, $C_s = A_{sc} E_s \varepsilon_{sc}$

$= A_{sc} E_s \times 0.003 \times (d_n - d_c)/d_n$

$= 372(d_n - 40)/d_n$ kN

Tensile force of fibre, $T_f = f_{1.5}' b d_f = 1.6 \times 250 \times (D - d_n) = 0.4(400 - d_n)$ kN

Solving equilibrium: $C_c + C_s = T_s + T_f$

$d_n = 52.5$ mm

Check tensile strain at the bottom face of the cross-section:

$\varepsilon_t = 0.003 \times (D - d_n)/d_n = 0.0199 < 0.025$ (OK)

$d_f = D - d_n = 347.5$ mm

Forces:

$C_c = 360.6$ kN

$C_s = 88.4$ kN

$T_s = 310$ kN

$T_f = 139$ kN

Moment capacity at intermediate support:

Taking moment about the neutral axis,

$M^- = C_c(d_n - \gamma d_n/2) + C_s(d_n - d_c) + T_s(d_t - d_n) + T_f \times d_f/2$

$= 131.3$ kN-m

Ultimate capacity of the beam specimen, $P = M^+ + 0.5M^- = 245.4$ kN

Elastic moment at intermediate support, $M_E{}^- = 0.75P = 184$ kN-m

Moment redistribution (%) = $(M_E{}^- - M^-)/M_E{}^- \times 100\% = +28.7\%$

APPENDIX B

This appendix contains the crack patterns and strains of the concrete measured at critical sections (mid-spans and intermediate support) of the beam specimens tested in this study and presented in Chapter 3.

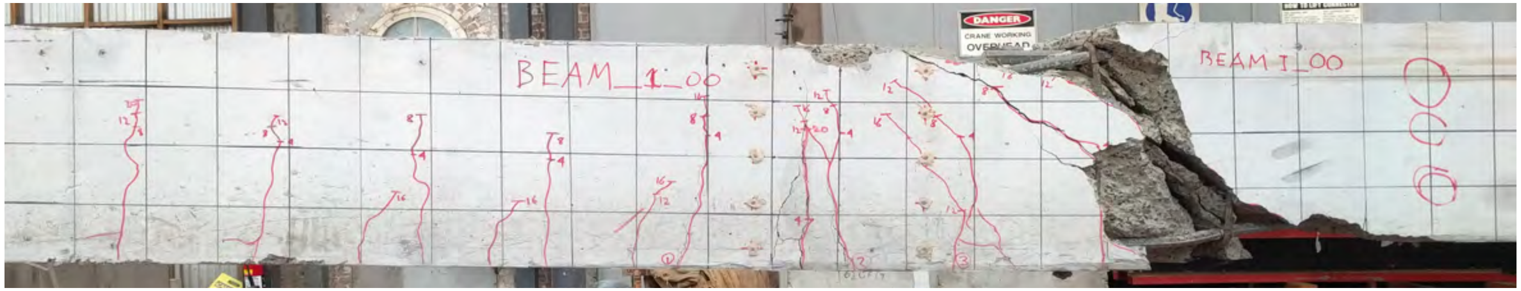

(a) West mid-span

(b) Intermediate support

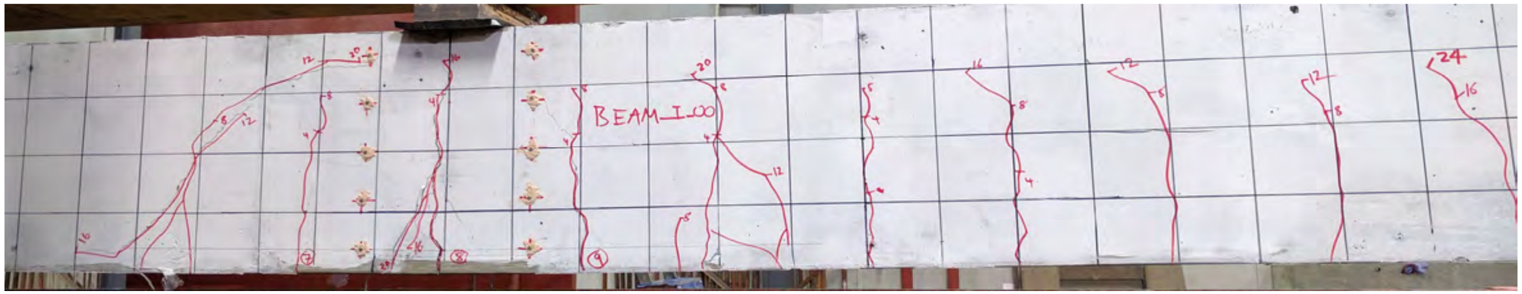

(c) East mid-span

Figure B.1: Crack patterns for Specimen B00(−30).

(a) West mid-span

(b) Intermediate support

(c) East mid-span

Figure B.2: Crack patterns for Specimen B30(−30).

(a) West mid-span

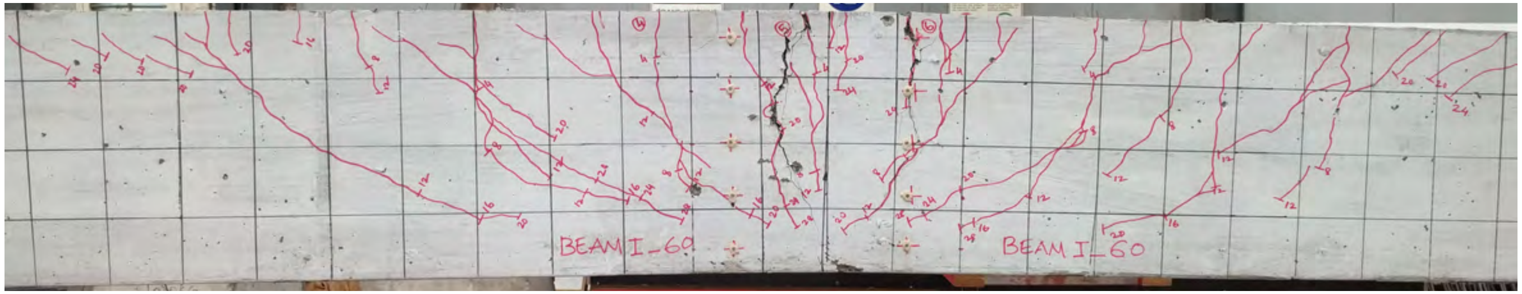

(b) Intermediate support

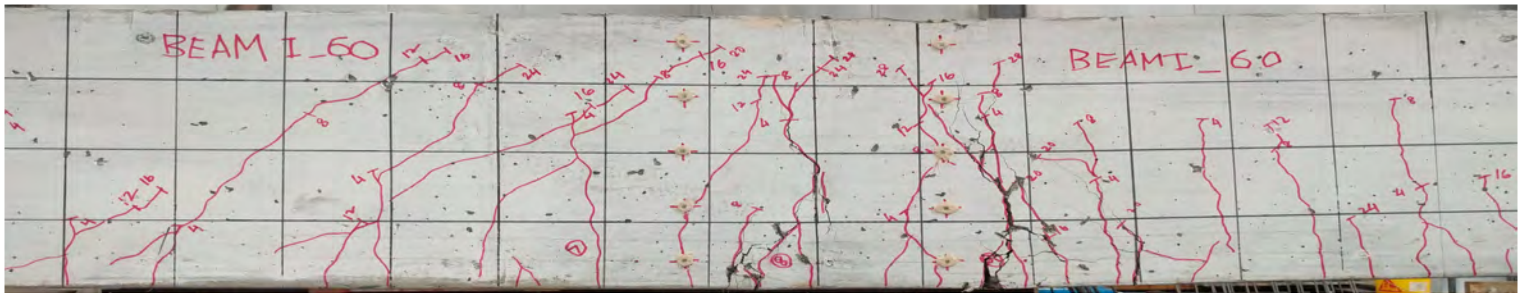

(c) East mid-span

Figure B.3: Crack patterns for Specimen B60(−30).

(a) West mid-span

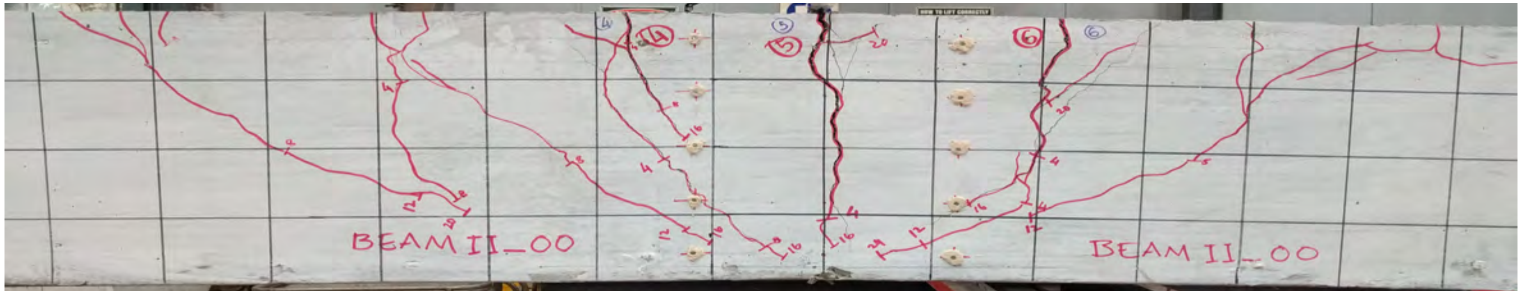

(b) Intermediate support

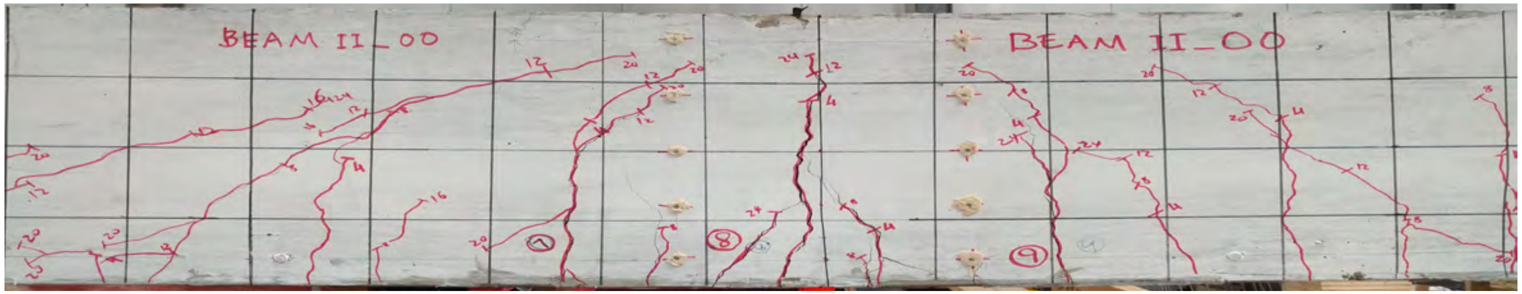

(c) East mid-span

Figure B.4: Crack patterns for Specimen B00(+30).

(a) West mid-span

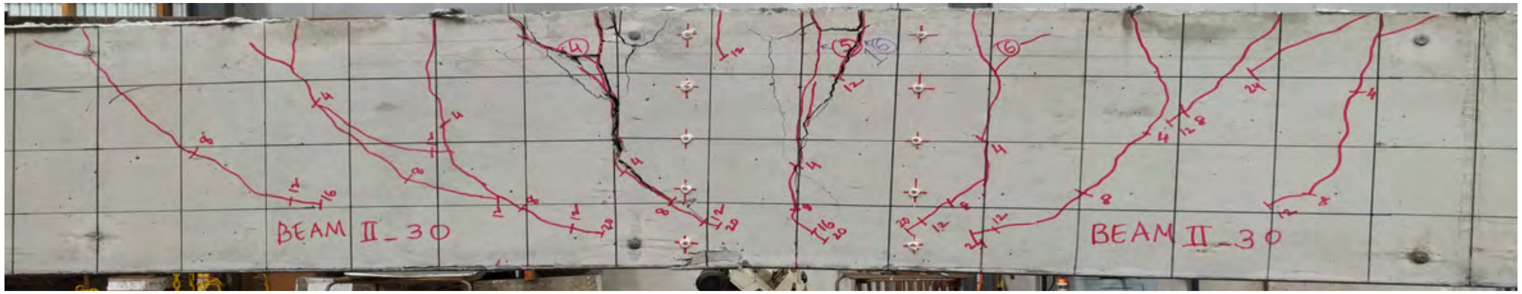

(b) Intermediate support

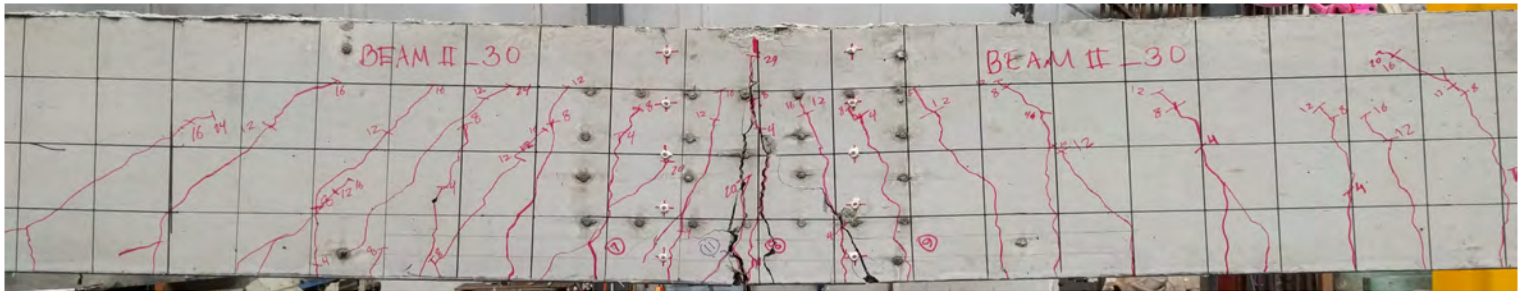

(c) East mid-span

Figure B.5: Crack patterns for Specimen B30(+30).

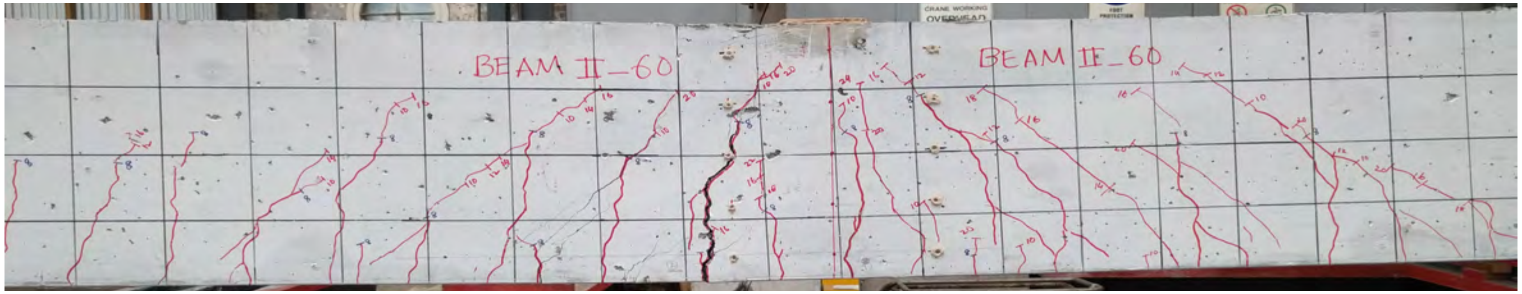

(a) West mid-span

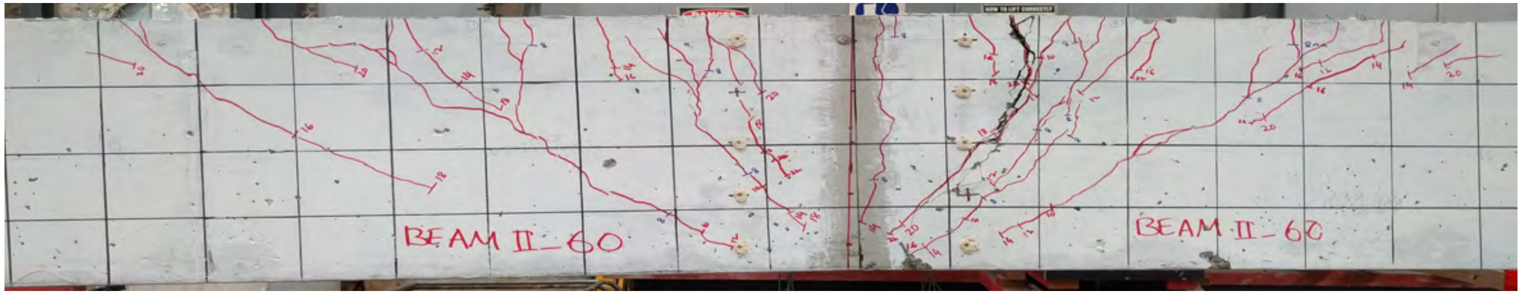

(b) Intermediate support

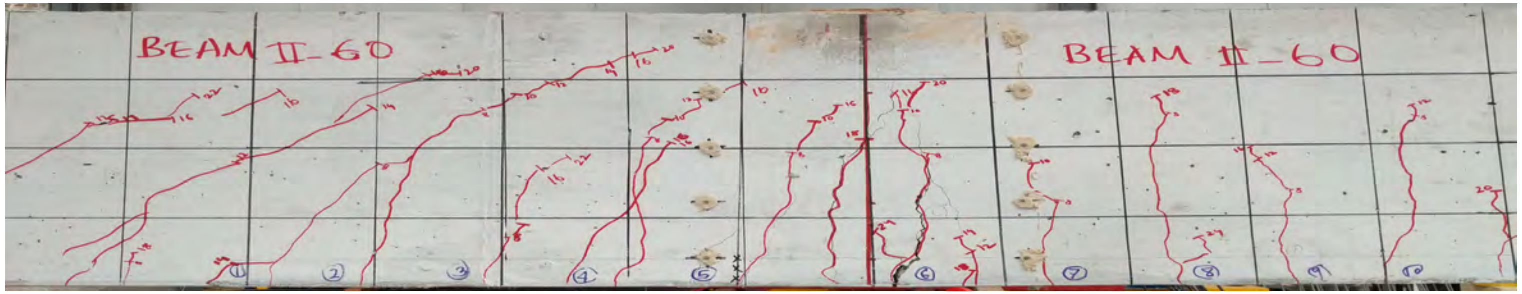

(c) East mid-span

Figure B.6: Crack patterns for Specimen B60(+30).

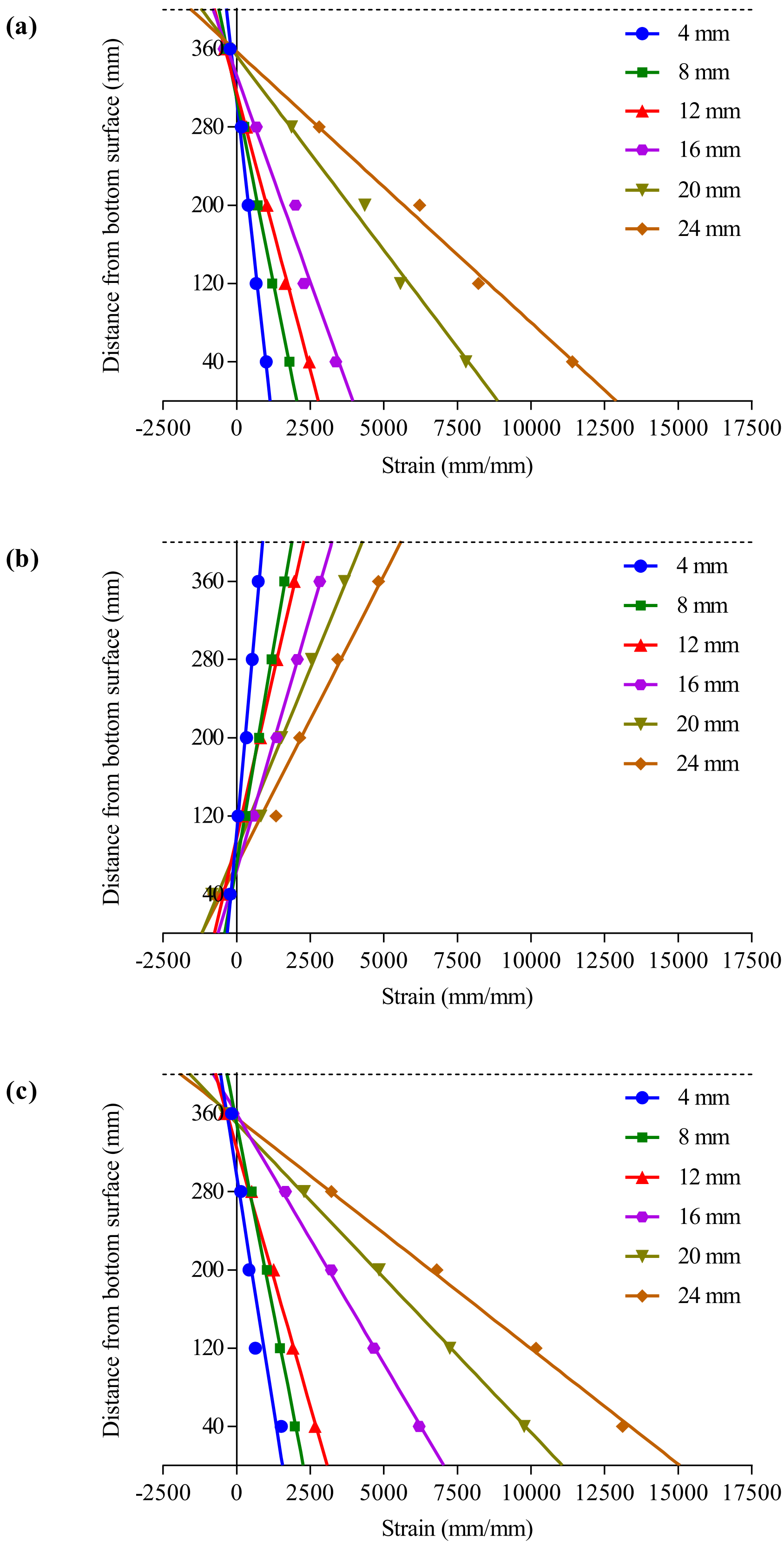

Figure B.7: Strains of concrete for specimen B00(−30) at (a) west mid-span, (b) intermediate support, and (c) east mid-span.

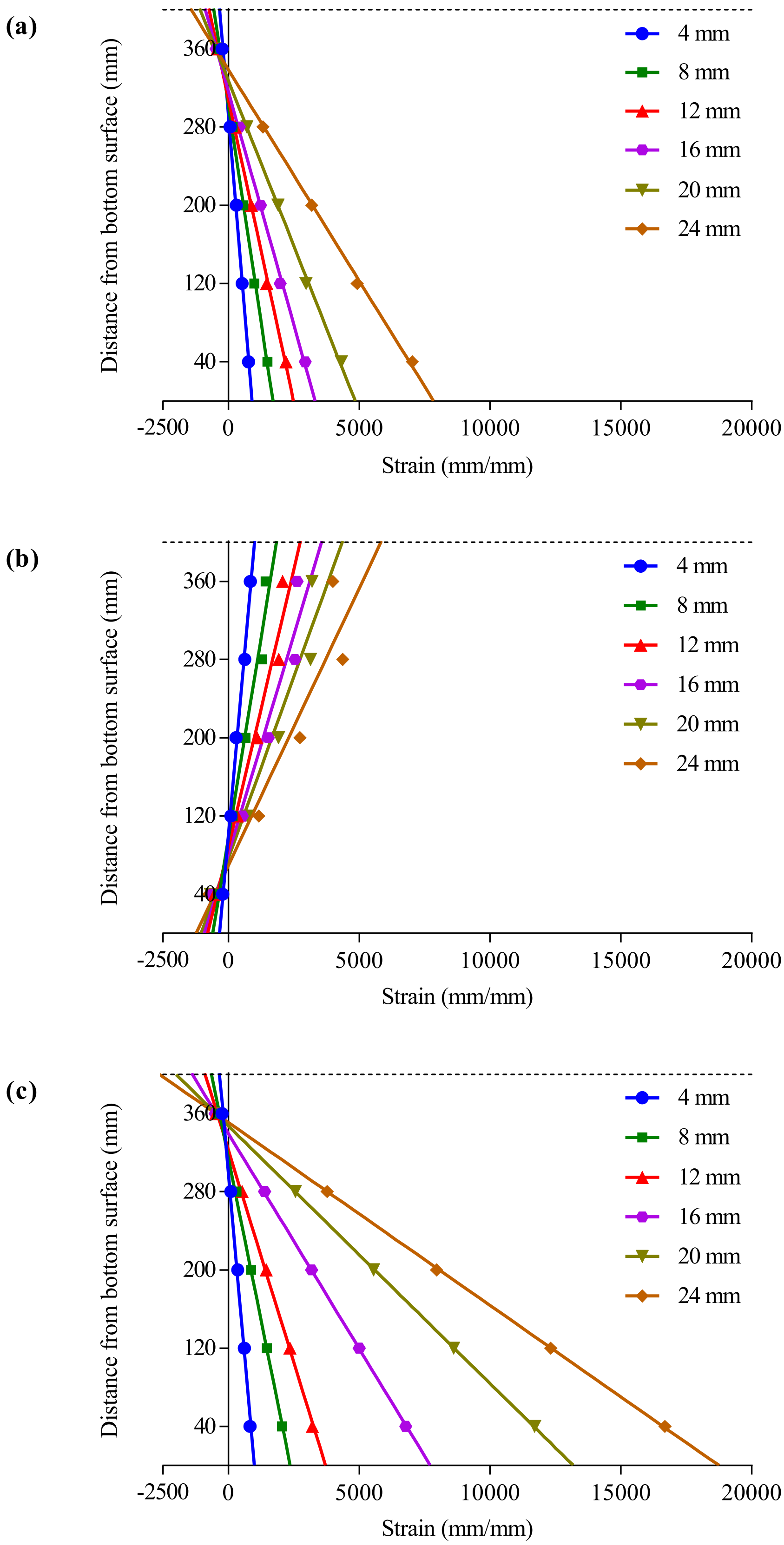

Figure B.8: Strains of concrete for specimen B30(−30) at (a) west mid-span, (b) intermediate support, and (c) east mid-span.

(a)

(b)

(c)

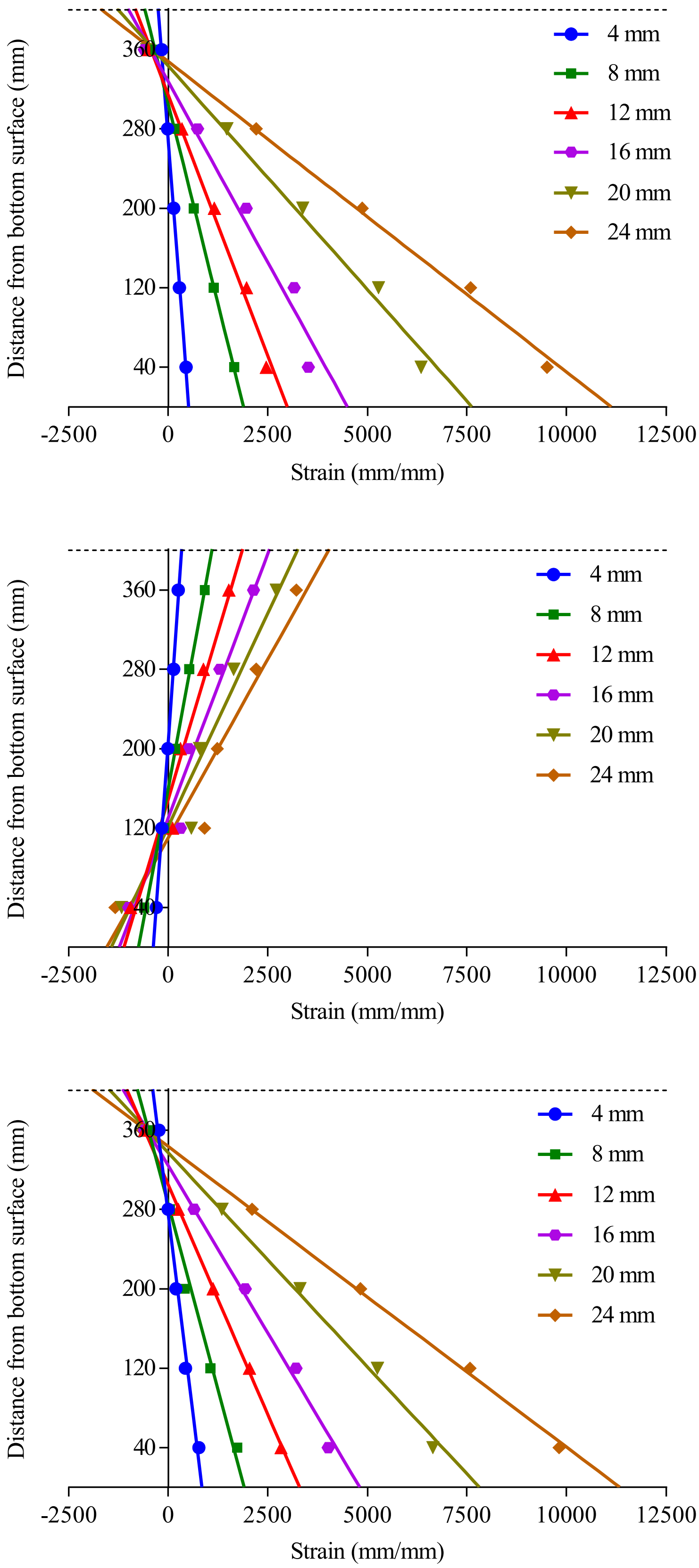

Figure B.9: Strains of concrete for specimen B60(−30) at (a) west mid-span, (b) intermediate support, and (c) east mid-span.

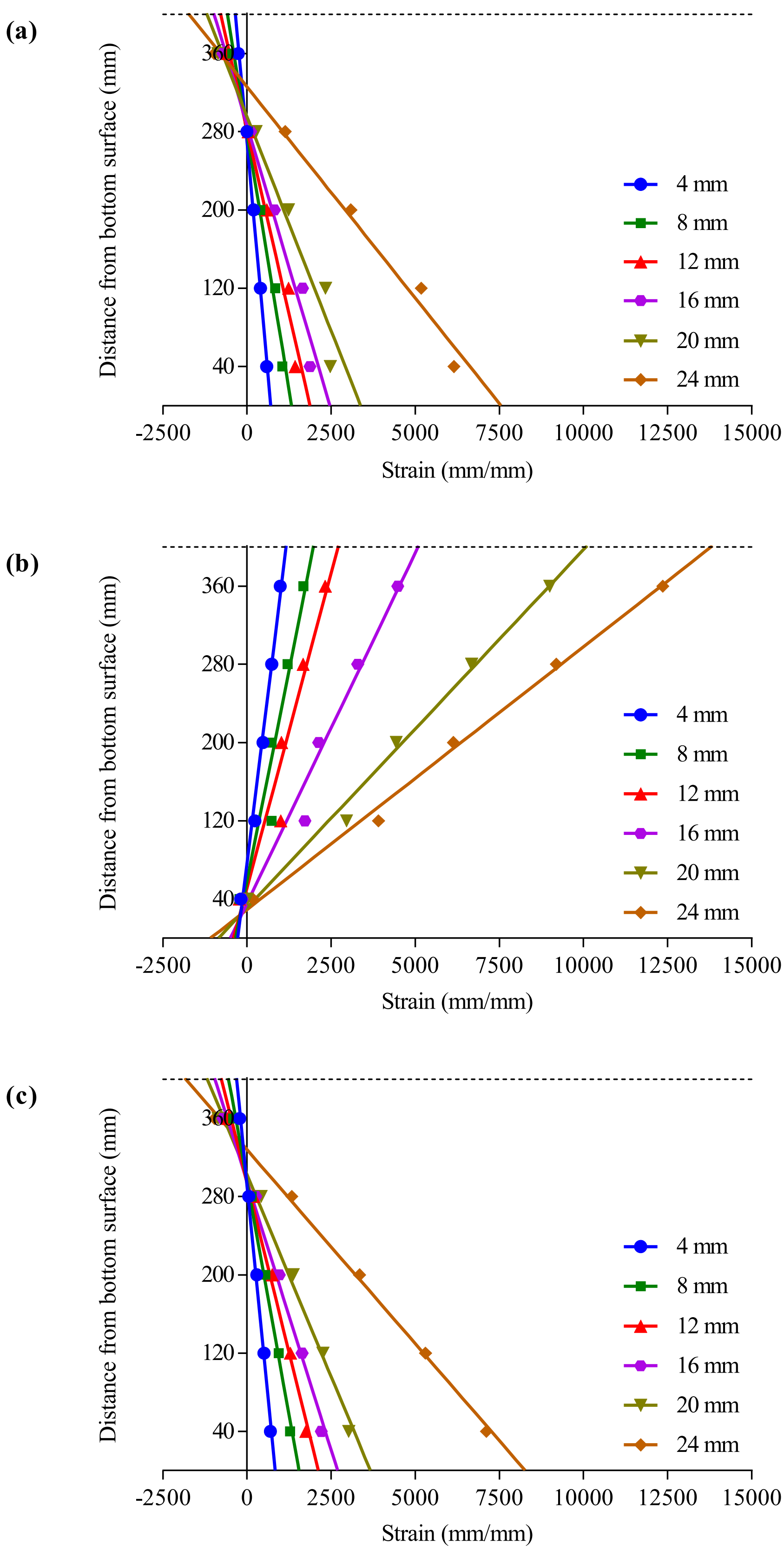

Figure B.10: Strains of concrete for specimen B00(+30) at (a) west mid-span, (b) intermediate support, and (c) east mid-span.

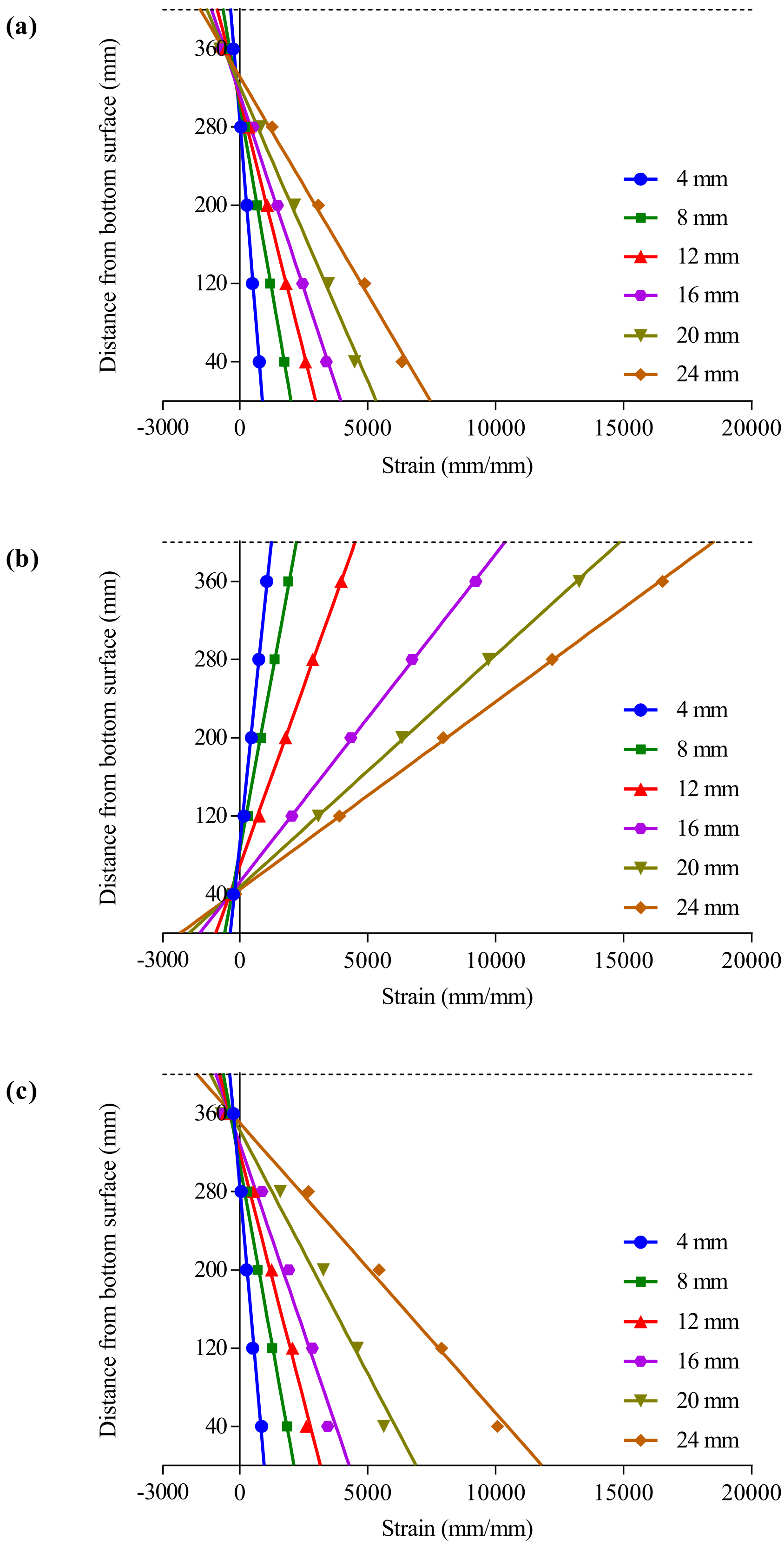

Figure B.11: Strains of concrete for specimen B30(+30) at (a) west mid-span, (b) intermediate support, and (c) east mid-span.

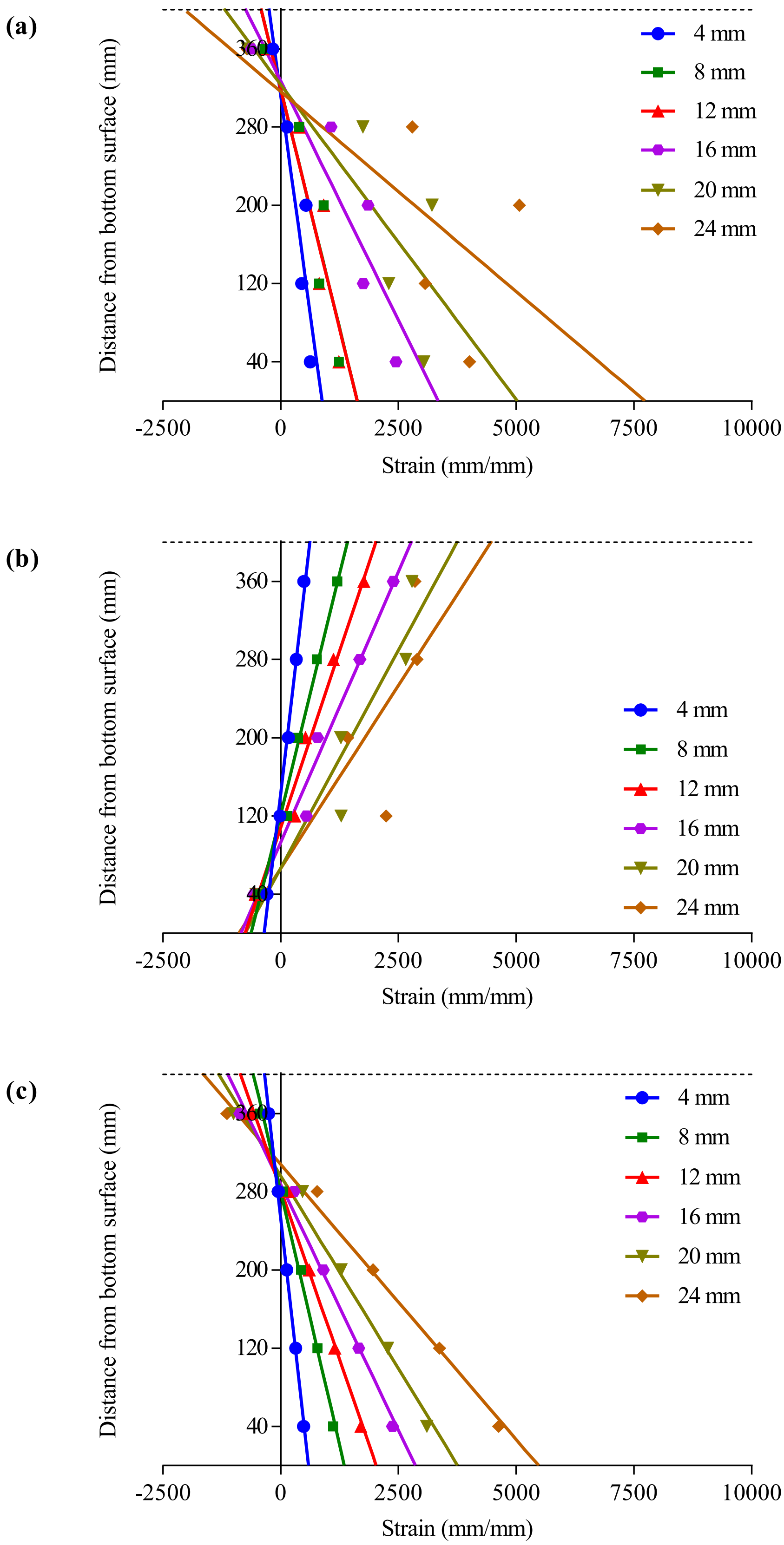

Figure B.12: Strains of concrete for specimen B60(+30) at (a) west mid-span, (b) intermediate support, and (c) east mid-span.

APPENDIX C

This appendix provides detail calculations of the design of RC and R-SFRC two-span continuous slabs for moment redistribution tested in this study and presented in Chapter 4.

C1 Design data

Design standard = AS 3600-2018

Depth of the slabs, $D = 220$ mm

Width of the slabs, $b = 800$ mm

Characteristic compressive strength of concrete, $f_c' = 32$ MPa

$\alpha_2 = 0.85 - 0.0015 f_c' = 0.80$; $\alpha_2 \geq 0.67$

$\gamma = 0.97 - 0.0025 f_c' = 0.89$; $\gamma \geq 0.67$

Yield strength of steel, $f_{sy} = 500$ MPa

Elastic modulus of steel, $E_s = 200 \times 10^3$ MPa

Characteristic residual tensile strength of SFRC for 60 kg/m^3 of Dramix 3D fibres, $f_{1.5}' = 1.6$ MPa

Effective depth of tensile reinforcement, $d_t = 190$ mm

Effective depth of compressive reinforcement, $d_c = 30$ mm

C2 Design of the specimens in Series A

C2.1 Specimen S60(+00)

C2.1.1 Preliminary design

Specimen S60(+00) was designed for linear elastic condition (0% moment redistribution). Figure C.1 shows the stress block and forces on R-SFRC section based on AS 3600-2018 model.

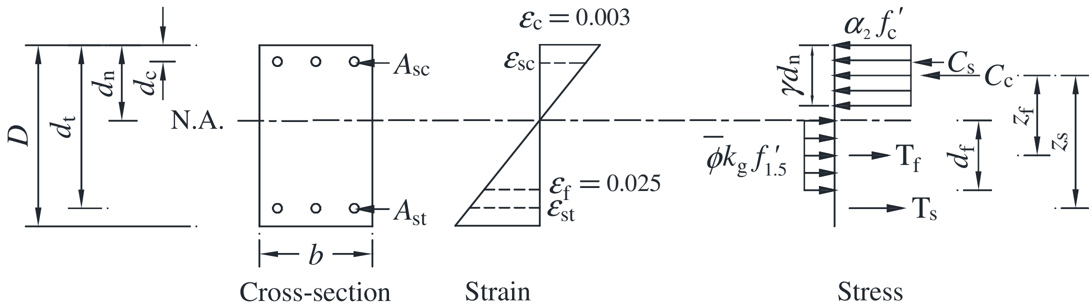

Figure C.1: Stress block and forces on R-SFRC section based on AS 3600-2018 model.

Reinforcement ratio at mid-span, $\rho_{st}^{+} = 0.002$

$A_{st}{}^{+} = \rho_{st}^{+} b d_t = 0.002 \times 800 \times 190 = 304$ mm^2

Try 4-N10 bars, $A_{st}{}^{+} = 4 \times 80 = 320$ mm^2

Positive moment capacity at mid-span (ignoring the effect of compressive reinforcement)

$$M^{+} = T_s z_s + T_f z_f$$

$$= A_{st}{}^{+} f_{sy}(d_t - \gamma d_n/2) + \overline{\emptyset} k_g f_{1.5}' b d_f \left(d_n - \gamma d_n/2 + d_f/2\right)$$

Assume, $d_n = 0.1D = 22$ mm, $\overline{\emptyset} = 1, k_g = 1, d_f = D - d_n$

$M^{+} = 57.0$ kN-m

For a two-span continuous slab of with a span length of 4 m,

Elastic moment at mid-span, ${M_E}^+ = 0.625P$

Elastic moment at intermediate support, ${M_E}^- = 0.75P$

where P is the applied load on each span.

For 0% moment redistribution,

$M^+ = {M_E}^+ = 0.625P = 57.0$ kN-m

$P = 91.2$ kN

$M^- = {M_E}^- = 0.75P = 68.4$ kN-m

${A_{st}}^- = (M^- - T_f z_f)/f_{sy} z_s = 447$ mm^2

Try 4-N12 bars, ${A_{st}}^- = 4 \times 110 = 440$ mm^2

C2.1.2 Calculation of ultimate capacity and moment redistribution for the provided reinforcement

At mid-span:

Compressive force of concrete, $C_c = \alpha_2 f_c' \gamma d_n b = 18.3 d_n$ kN

Tensile reinforcement, $A_{st} = 320$ mm^2

Tensile force of steel reinforcement, $T_s = A_{st} f_{sy} = 160$ kN

Compressive reinforcement, $A_{sc} = 440$ mm^2

Compressive force of steel reinforcement, $C_s = A_{sc} E_s \varepsilon_{sc}$

$$= A_{sc} E_s \times 0.003 \times (d_n - d_c)/d_n$$

$$= 264(d_n - 30)/d_n \text{ kN}$$

Tensile force of fibre, $T_f = \overline{\emptyset} k_g f'_{1.5} b d_f$

$$= 1 \times 1 \times 1.6 \times 800 \times (D - d_n) = 1.28(220 - d_n) \text{ kN}$$

Solving equilibrium: $C_c + C_s = T_s + T_f$

$d_n = 25.2$ mm

Check tensile strain at the bottom face of the cross-section:

$\varepsilon_t = 0.003 \times (D - d_n)/d_n = 0.0232 < 0.025$ (OK)

$d_f = D - d_n = 194.8$ mm

Forces:

$C_c = 460$ kN

$C_s = -50.6$ kN (in tension)

$T_s = 160$ kN

$T_f = 249.4$ kN

Moment capacity at mid-span:

Taking moment about the neutral axis,

$M^+ = C_c(d_n - \gamma d_n/2) + C_s(d_n - d_c) + T_s(d_t - d_n) + T_f \times d_f/2$

$= 57.3$ kN-m

At intermediate support:

Compressive force of concrete, $C_c = \alpha_2 f_c' \gamma d_n b = 18.3 d_n$ kN

Tensile reinforcement, $A_{st} = 440$ mm^2

Tensile force of steel reinforcement, $T_s = A_{st} f_{sy} = 220$ kN

Compressive reinforcement, $A_{sc} = 320$ mm^2

Compressive force of steel reinforcement, $C_s = A_{sc} E_s \varepsilon_{sc}$

$$= A_{sc} E_s \times 0.003 \times (d_n - d_c)/d_n$$

$$= 192(d_n - 30)/d_n \text{ kN}$$

Tensile force of fibre, $T_f = \overline{\emptyset} k_g f_{1.5}' b d_f = 1.28(220 - d_n)$ kN

Solving equilibrium: $C_c + C_s = T_s + T_f$

$d_n = 26.8$ mm

Check tensile strain at the bottom face of the cross-section:

$\varepsilon_t = 0.003 \times (D - d_n)/d_n = 0.0216 < 0.025$ (OK)

$d_f = D - d_n = 193.2$ mm

Forces:

$C_c = 490$ kN

$C_s = -22.8$ kN (in tension)

$T_s = 220$ kN

$T_f = 247.3$ kN

Moment capacity at intermediate support:

Taking moment about the neutral axis,

$M^{-} = C_c(d_n - \gamma d_n/2) + C_s(d_n - d_c) + T_s(d_t - d_n) + T_f \times d_f/2$

$= 67.2$ kN-m

Ultimate capacity of the slab, $P = M^{+} + 0.5M^{-} = 90.9$ kN

Elastic moment at intermediate support, $M_E{}^{-} = 0.75P = 68.2$ kN-m

Moment redistribution (%) = $(M_E{}^{-} - M^{-})/M_E{}^{-} \times 100\% = 1.5\%$

C2.2 Specimen S60(+10)

C2.2.1 Preliminary design

Specimen S60(+10) was designed for 10% of positive moment redistribution with respect to linear elastic condition.

Reinforcement ratio at intermediate support, $\rho_{st}^{-} = 0.002$

$A_{st}{}^{-} = 0.002 \times 800 \times 190 = 304$ mm^2

Try 4-N10 bars, $A_{st}{}^{-} = 4 \times 80 = 320$ mm^2

Negative moment capacity at intermediate support (ignoring the effect of compressive reinforcement)

$$M^{-} = T_s z_s + T_f z_f$$

$$= A_{st}{}^{-} f_{sy}(d_t - \gamma d_n/2) + \bar{\emptyset} k_g f'_{1.5} b d_f \left(d_n - \gamma d_n/2 + d_f/2\right)$$

Assume, $d_n = 0.1D = 22$ mm, $\bar{\emptyset} = 1, k_g = 1$, $d_f = D - d_n$

$M^{-} = 57.0$ kN-m

For 10% of positive moment redistribution with respect to linear elastic condition,

$M^{-} = 0.9 M_E{}^{-} = 0.9 * 0.75P = 0.675P = 57.0$ kN-m

$P = 84.5$ kN

$M^{+} = 1 - 0.5M^{-} = 0.6625P = 56.0$ kN-m

$A_{st}{}^{+} = (M^{+} - T_f z_f)/f_{sy} z_s = 308$ mm^2

Try 4-N10 bars, $A_{st}{}^{+} = 4 \times 80 = 320$ mm^2

C2.2.2 Calculation of ultimate capacity and moment redistribution for the provided reinforcement

At mid-span:

Compressive force of concrete, $C_c = \alpha_2 f_c' \gamma d_n b = 18.3 d_n$ kN

Tensile reinforcement, $A_{st} = 320$ mm^2

Tensile force of steel reinforcement, $T_s = A_{st} f_{sy} = 160$ kN

Compressive reinforcement, $A_{sc} = 320$ mm^2

Compressive force of steel reinforcement, $C_s = A_{sc} E_s \varepsilon_{sc}$

$$= A_{sc} E_s \times 0.003 \times (d_n - d_c)/d_n$$

$$= 192(d_n - 30)/d_n \text{ kN}$$

Tensile force of fibre, $T_f = \overline{\emptyset} k_g f'_{1.5} b d_f = 1.28(220 - d_n)$ kN

Solving equilibrium: $C_c + C_s = T_s + T_f$

$d_n = 24.7$ mm

Check tensile strain at the bottom face of the cross-section:

$\varepsilon_t = 0.003 \times (D - d_n)/d_n = 0.0237 < 0.025$ (OK)

$d_f = D - d_n = 195.3$ mm

Forces:

$C_c = 451.2$ kN

$C_s = -41.2$ kN (in tension)

$T_s = 160$ kN

$T_f = 250.0$ kN

Moment capacity at mid-span:

Taking moment about the neutral axis,

$$M^+ = C_c(d_n - \gamma d_n/2) + C_s(d_n - d_c) + T_s(d_t - d_n) + T_f \times d_f/2$$

$$= 57.3 \text{ kN-m}$$

At intermediate support:

Same amount of reinforcement like mid-span.

$M^- = 57.3$ kN-m

Ultimate capacity of the slab, $P = M^+ + 0.5M^- = 85.9$ kN

Elastic moment at intermediate support, $M_E{}^- = 0.75P = 64.4$ kN-m

Moment redistribution (%) = $(M_E{}^- - M^-)/M_E{}^- \times 100\% = 11.1\%$

C2.3 Specimen S60(+20)

C2.3.1 Preliminary design

Specimen S60(+20) was designed for 20% of positive moment redistribution with respect to linear elastic condition.

Reinforcement ratio at intermediate support, $\rho_{st}^{-} = 0.002$

Try 4-N10 bars, $A_{st}{}^{-} = 4 \times 80 = 320$ mm^2

$M^{-} = 57.0$ kN-m

For 20% of positive moment redistribution with respect to linear elastic condition,

$M^{-} = 0.8 M_E{}^{-} = 0.8 * 0.75P = 0.6P = 57.0$ kN-m

$P = 95.0$ kN

$M^{+} = 1 - 0.5M^{-} = 0.7P = 66.5$ kN-m

$A_{st}{}^{+} = (M^{+} - T_f z_f)/f_{sy} z_s = 425$ mm^2

Try 4-N12 bars, $A_{st}{}^{+} = 4 \times 110 = 440$ mm^2

C2.3.2 Calculation of ultimate capacity and moment redistribution for the provided reinforcement

At mid-span:

Compressive force of concrete, $C_c = \alpha_2 f_c' \gamma d_n b = 18.3 d_n$ kN

Tensile reinforcement, $A_{st} = 440$ mm^2

Tensile force of steel reinforcement, $T_s = A_{st} f_{sy} = 220$ kN

Compressive reinforcement, $A_{sc} = 320$ mm^2

Compressive force of steel reinforcement, $C_s = A_{sc}E_s\varepsilon_{sc}$

$= A_{sc}E_s \times 0.003 \times (d_n - d_c)/d_n$

$= 192(d_n - 30)/d_n$ kN

Tensile force of fibre, $T_f = \overline{\emptyset}k_g f'_{1.5}bd_f = 1.28(220 - d_n)$ kN

Solving equilibrium: $C_c + C_s = T_s + T_f$

$d_n = 26.8$ mm

Check tensile strain at the bottom face of the cross-section:

$\varepsilon_t = 0.003 \times (D - d_n)/d_n = 0.0216 < 0.025$ (OK)

$d_f = D - d_n = 193.2$ mm

Forces:

$C_c = 490.0$ kN

$C_s = -22.8$ kN (in tension)

$T_s = 220$ kN

$T_f = 247.3$ kN

Moment capacity at mid-span:

Taking moment about the neutral axis,

$M^+ = C_c(d_n - \gamma d_n/2) + C_s(d_n - d_c) + T_s(d_t - d_n) + T_f \times d_f/2$

$= 67.2$ kN-m

At intermediate support:

Compressive force of concrete, $C_c = \alpha_2 f_c' \gamma d_n b = 18.3 d_n$ kN

Tensile reinforcement, $A_{st} = 320$ mm^2

Tensile force of steel reinforcement, $T_s = A_{st} f_{sy} = 160$ kN

Compressive reinforcement, $A_{sc} = 440$ mm^2

Compressive force of steel reinforcement, $C_s = A_{sc} E_s \varepsilon_{sc}$

$$= A_{sc} E_s \times 0.003 \times (d_n - d_c)/d_n$$

$$= 264(d_n - 30)/d_n \text{ kN}$$

Tensile force of fibre, $T_f = \overline{\emptyset} k_g f_{1.5}' b d_f = 1.28(220 - d_n)$ kN

Solving equilibrium: $C_c + C_s = T_s + T_f$

$d_n = 25.2$ mm

Check tensile strain at the bottom face of the cross-section:

$\varepsilon_t = 0.003 \times (D - d_n)/d_n = 0.0232 < 0.025$ (OK)

$d_f = D - d_n = 194.8$ mm

Forces:

$C_c = 460.0$ kN

$C_s = -50.6$ kN (in tension)

$T_s = 160$ kN

$T_f = 249.4$ kN

Moment capacity at intermediate support:

Taking moment about the neutral axis,

$M^- = C_c(d_n - \gamma d_n/2) + C_s(d_n - d_c) + T_s(d_t - d_n) + T_f \times d_f/2$

$= 57.3$ kN-m

Ultimate capacity of the slab, $P = M^+ + 0.5M^- = 95.8$ kN

Elastic moment at intermediate support, $M_E{}^- = 0.75P = 71.9$ kN-m

Moment redistribution (%) = $(M_E{}^- - M^-)/M_E{}^- \times 100\% = 20.2\%$

C2.4 Specimen S60(+30)

C2.4.1 Preliminary design

Specimen S60(+30) was designed for 30% of positive moment redistribution with respect to linear elastic condition.

Reinforcement ratio at intermediate support, $\rho_{st}^{-} = 0.002$

Try 4-N10 bars, $A_{st}{}^{-} = 4 \times 80 = 320$ mm^2

$M^{-} = 57.0$ kN-m

For 30% of positive moment redistribution with respect to linear elastic condition,

$M^{-} = 0.7M_E{}^{-} = 0.7 * 0.75P = 0.525P = 57.0$ kN-m

$P = 108.6$ kN

$M^{+} = 1 - 0.5M^{-} = 0.7375P = 80.1$ kN-m

$A_{st}{}^{+} = (M^{+} - T_f z_f)/f_{sy} z_s = 576$ mm^2

Try 2-N16 and 2-N12 bars, $A_{st}{}^{+} = 2 \times 200 + 2 \times 110 = 620$ mm^2

C2.4.2 Calculation of ultimate capacity and moment redistribution for the provided reinforcement

At mid-span:

Compressive force of concrete, $C_c = \alpha_2 f_c' \gamma d_n b = 18.3 d_n$ kN

Tensile reinforcement, $A_{st} = 620$ mm^2

Tensile force of steel reinforcement, $T_s = A_{st} f_{sy} = 310$ kN

Compressive reinforcement, $A_{sc} = 320$ mm^2

Compressive force of steel reinforcement, $C_s = A_{sc}E_s\varepsilon_{sc}$

$= A_{sc}E_s \times 0.003 \times (d_n - d_c)/d_n$

$= 192(d_n - 30)/d_n$ kN

Tensile force of fibre, $T_f = \overline{\emptyset}k_g f'_{1.5} b d_f = 1.28(220 - d_n)$ kN

Solving equilibrium: $C_c + C_s = T_s + T_f$

$d_n = 30.2$ mm

Check tensile strain at the bottom face of the cross-section:

$\varepsilon_t = 0.003 \times (D - d_n)/d_n = 0.0189 < 0.025$ (OK)

$d_f = D - d_n = 189.8$ mm

Forces:

$C_c = 551.7$ kN

$C_s = 1.2$ kN

$T_s = 310$ kN

$T_f = 243.0$ kN

Moment capacity at mid-span:

Taking moment about the neutral axis,

$M^+ = C_c(d_n - \gamma d_n/2) + C_s(d_n - d_c) + T_s(d_t - d_n) + T_f \times d_f/2$

$= 81.8$ kN-m

At intermediate support:

Compressive force of concrete, $C_c = \alpha_2 f_c' \gamma d_n b = 18.3 d_n$ kN

Tensile reinforcement, $A_{st} = 320$ mm^2

Tensile force of steel reinforcement, $T_s = A_{st} f_{sy} = 160$ kN

Compressive reinforcement, $A_{sc} = 620$ mm^2

Compressive force of steel reinforcement, $C_s = A_{sc} E_s \varepsilon_{sc}$

$$= A_{sc} E_s \times 0.003 \times (d_n - d_c)/d_n$$

$$= 372(d_n - 30)/d_n \text{ kN}$$

Tensile force of fibre, $T_f = \overline{\emptyset} k_g f_{1.5}' b d_f = 1.28(220 - d_n)$ kN

Solving equilibrium: $C_c + C_s = T_s + T_f$

$d_n = 25.7$ mm

Check tensile strain at the bottom face of the cross-section:

$\varepsilon_t = 0.003 \times (D - d_n)/d_n = 0.0226 < 0.025$ (OK)

$d_f = D - d_n = 194.3$ mm

Forces:

$C_c = 470.3$ kN

$C_s = -61.6$ kN (in tension)

$T_s = 160$ kN

$T_f = 248.7$ kN

Moment capacity at intermediate support:

Taking moment about the neutral axis,

$$M^{-} = C_c(d_n - \gamma d_n/2) + C_s(d_n - d_c) + T_s(d_t - d_n) + T_f \times d_f/2$$

$$= 57.4 \text{ kN-m}$$

Ultimate capacity of the slab, $P = M^{+} + 0.5M^{-} = 110.5$ kN

Elastic moment at intermediate support, ${M_E}^{-} = 0.75P = 82.9$ kN-m

Moment redistribution (%) = $({M_E}^{-} - M^{-})/{M_E}^{-} \times 100\% = 30.8\%$

C3 Design of the specimens in Series B

C3.1 Specimen S00(+00)

C3.1.1 Preliminary design

Specimen S00(+00) was designed as equivalent to specimen S60(+00).

$M^{+} = A_{st}{}^{+} f_{sy}(0.9d_t) = 57.3$ kN-m (ignoring the effect of compressive reinforcement)

$A_{st}{}^{+} = 670$ mm^2

Try 2-N16 and 2-N12 bars, $A_{st}{}^{+} = 2\times 200 + 2 \times 110 = 620$ mm^2

$M^{-} = A_{st}{}^{-} f_{sy}(0.9d_t) = 67.2$ kN-m (ignoring the effect of compressive reinforcement)

$A_{st}{}^{-} = 786$ mm^2

Try 3-N16 and 2-N10 bars, $A_{st}{}^{-} = 3\times 200 + 2 \times 80 = 760$ mm^2

C3.1.2 Calculation of ultimate capacity and moment redistribution for the provided reinforcement

Figure C.2 shows the stress block and forces on RC section based on AS 3600-2018 model.

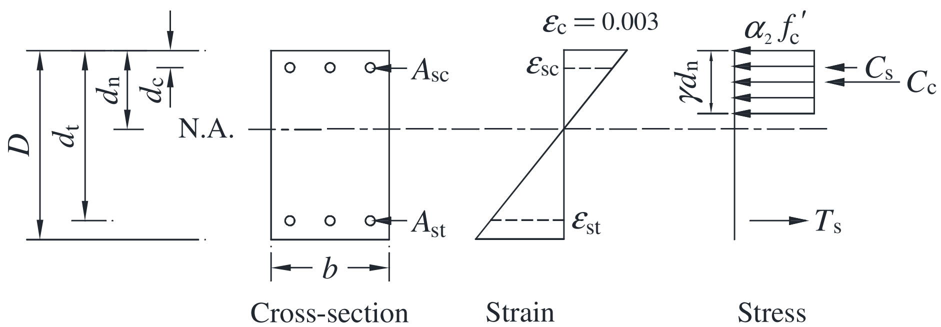

Figure C.2: Stress block and forces on RC section based on AS 3600-2018 model.

At mid-span:

Compressive force of concrete, $C_c = \alpha_2 f_c' \gamma d_n b = 18.3 d_n$ kN

Tensile reinforcement, $A_{st} = 620$ mm^2

Tensile force of steel reinforcement, $T_s = A_{st} f_{sy} = 310$ kN

Compressive reinforcement, $A_{sc} = 760$ mm^2

Compressive force of steel reinforcement, $C_s = A_{sc} E_s \varepsilon_{sc}$

$= A_{sc} E_s \times 0.003 \times (d_n - d_c)/d_n$

$= 456(d_n - 30)/d_n$ kN

Solving equilibrium: $C_c + C_s = T_s$

$d_n = 23.7$ mm

Forces:

$C_c = 432.3$ kN

$C_s = -122.3$ kN (in tension)

$T_s = 310$ kN

Moment capacity at mid-span:

Taking moment about the neutral axis,

$M^+ = C_c(d_n - \gamma d_n/2) + C_s(d_n - d_c) + T_s(d_t - d_n)$

$= 58.0$ kN-m ≈ 57.3 kN-m (OK)

At intermediate support:

Compressive force of concrete, $C_c = \alpha_2 f_c' \gamma d_n b = 18.3 d_n$ kN

Tensile reinforcement, $A_{st} = 760$ mm^2

Tensile force of steel reinforcement, $T_s = A_{st} f_{sy} = 380$ kN

Compressive reinforcement, $A_{sc} = 620$ mm^2

Compressive force of steel reinforcement, $C_s = A_{sc} E_s \varepsilon_{sc}$

$= A_{sc} E_s \times 0.003 \times (d_n - d_c)/d_n$

$= 372(d_n - 30)/d_n$ kN

Solving equilibrium: $C_c + C_s = T_s$

$d_n = 24.9$ mm

Forces:

$C_c = 455.6$ kN

$C_s = -75.6$ kN (in tension)

$T_s = 380$ kN

Moment capacity at intermediate support:

Taking moment about the neutral axis,

$M^- = C_c(d_n - \gamma d_n/2) + C_s(d_n - d_c) + T_s(d_t - d_n)$

$= 69.4$ kN-m ≈ 67.2 kN-m (OK)

Ultimate capacity of the slab, $P = M^{+} + 0.5M^{-} = 92.7$ kN ≈ 90.9 kN (OK)

Elastic moment at intermediate support, ${M_E}^{-} = 0.75P = 69.5$ kN-m

Moment redistribution (%) = $({M_E}^{-} - M^{-})/{M_E}^{-} \times 100\% = 0.2\%$ (OK)

C3.2 Specimen S00(+30)

C3.2.1 Preliminary design

Specimen S00(+30) was designed as equivalent to specimen S60(+30).

$M^{+} = {A_{st}}^{+} f_{sy}(0.9d_t) = 81.8$ kN-m (ignoring the effect of compressive reinforcement)

${A_{st}}^{+} = 957$ mm^2

Try 4-N16 and 1-N12 bars, ${A_{st}}^{+} = 4\times 200 + 1 \times 110 = 910$ mm^2

$M^{-} = {A_{st}}^{-} f_{sy}(0.9d_t) = 57.4$ kN-m (ignoring the effect of compressive reinforcement)

${A_{st}}^{-} = 671$ mm^2

Try 2-N16 and 2-N12 bars, ${A_{st}}^{-} = 2\times 200 + 2 \times 110 = 620$ mm^2

C3.2.2 Calculation of ultimate capacity and moment redistribution for the provided reinforcement

At mid-span:

Compressive force of concrete, $C_c = \alpha_2 f_c' \gamma d_n b = 18.3 d_n$ kN

Tensile reinforcement, $A_{st} = 910$ mm^2

Tensile force of steel reinforcement, $T_s = A_{st} f_{sy} = 455$ kN

Compressive reinforcement, $A_{sc} = 620$ mm^2

Compressive force of steel reinforcement, $C_s = A_{sc} E_s \varepsilon_{sc}$

$= A_{sc} E_s \times 0.003 \times (d_n - d_c)/d_n$

$= 372(d_n - 30)/d_n$ kN

Solving equilibrium: $C_c + C_s = T_s$

$d_n = 27.1$ mm

Forces:

$C_c = 495.0$ kN

$C_s = -40.0$ kN (in tension)

$T_s = 455.0$ kN

Moment capacity at mid-span:

Taking moment about the neutral axis,

$M^+ = C_c(d_n - \gamma d_n/2) + C_s(d_n - d_c) + T_s(d_t - d_n)$

$= 81.7$ kN-m ≈ 81.8 kN-m (OK)

At intermediate support:

Compressive force of concrete, $C_c = \alpha_2 f_c' \gamma d_n b = 18.3 d_n$ kN

Tensile reinforcement, $A_{st} = 620$ mm^2

Tensile force of steel reinforcement, $T_s = A_{st} f_{sy} = 310$ kN

Compressive reinforcement, $A_{sc} = 910$ mm^2

Compressive force of steel reinforcement, $C_s = A_{sc} E_s \varepsilon_{sc}$

$= A_{sc} E_s \times 0.003 \times (d_n - d_c)/d_n$

$= 546(d_n - 30)/d_n$ kN

Solving equilibrium: $C_c + C_s = T_s$

$d_n = 24.2$ mm

Forces:

$C_c = 441.7$ kN

$C_s = -131.7$ kN (in tension)

$T_s = 310.0$ kN

Moment capacity at intermediate support:

Taking moment about the neutral axis,

$M^- = C_c(d_n - \gamma d_n/2) + C_s(d_n - d_c) + T_s(d_t - d_n)$

$= 58.1$ kN-m ≈ 57.4 kN-m (OK)

Ultimate capacity of the slab, $P = M^+ + 0.5M^- = 110.7$ kN ≈ 110.5 kN (OK)

Elastic moment at intermediate support, $M_E{}^- = 0.75P = 83.0$ kN-m

Moment redistribution (%) = $(M_E{}^- - M^-)/M_E{}^- \times 100\% = 30.0\%$ (OK)

APPENDIX D

This appendix contains the crack patterns and strains of the concrete measured at critical sections (mid-spans and intermediate support) of the slab specimens tested in this study and presented in Chapter 4.

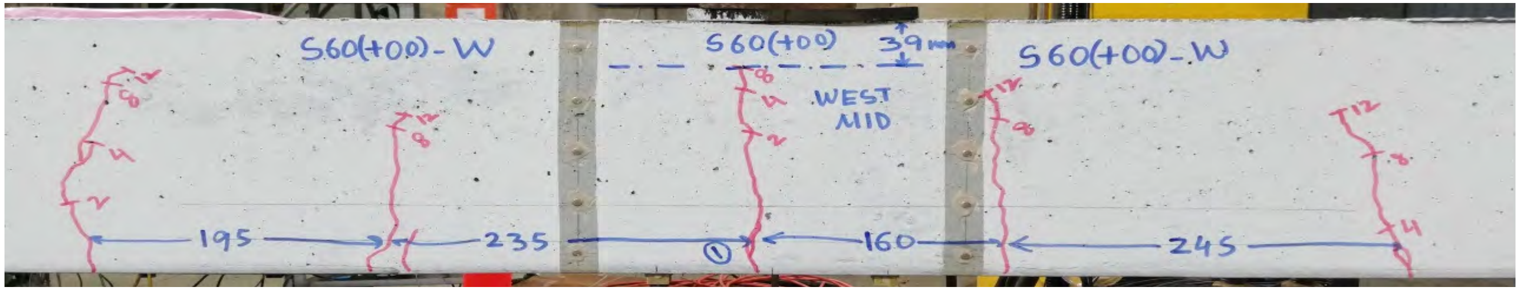

(a) West mid-span

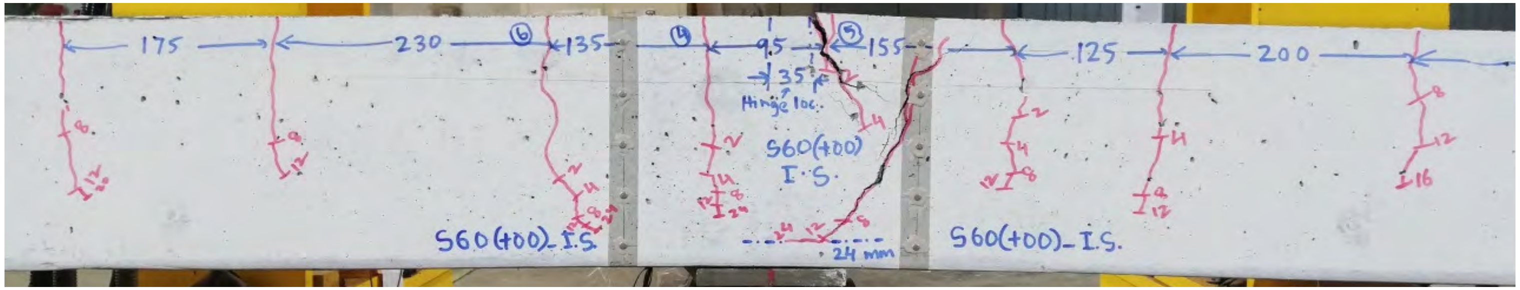

(b) Intermediate support

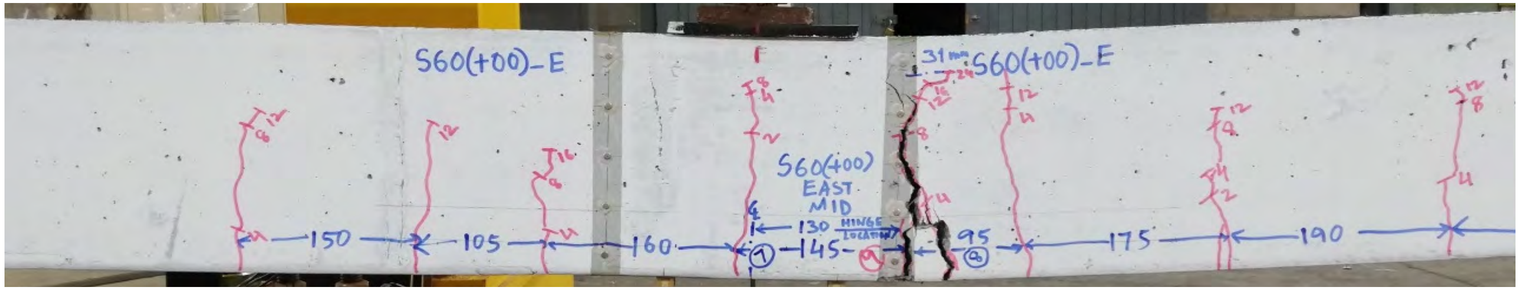

(c) East mid-span

Figure D.1: Crack patterns for Specimen S60(+00).

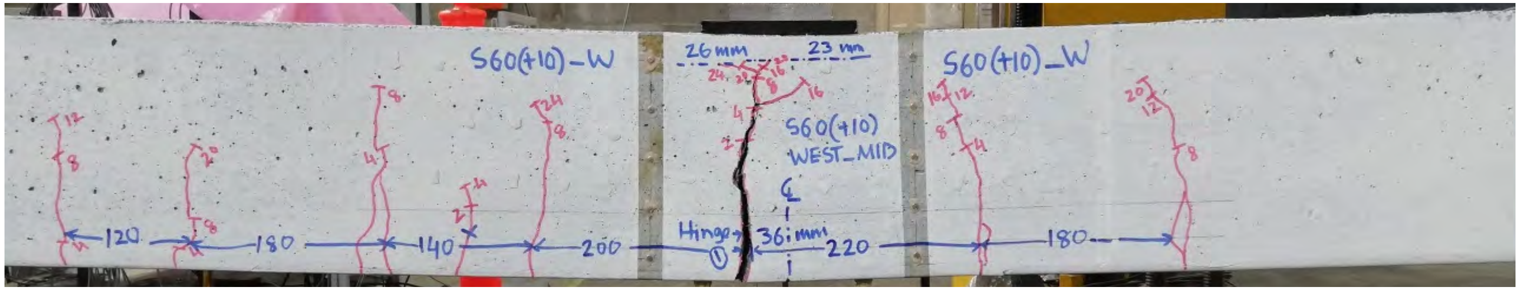

(a) West mid-span

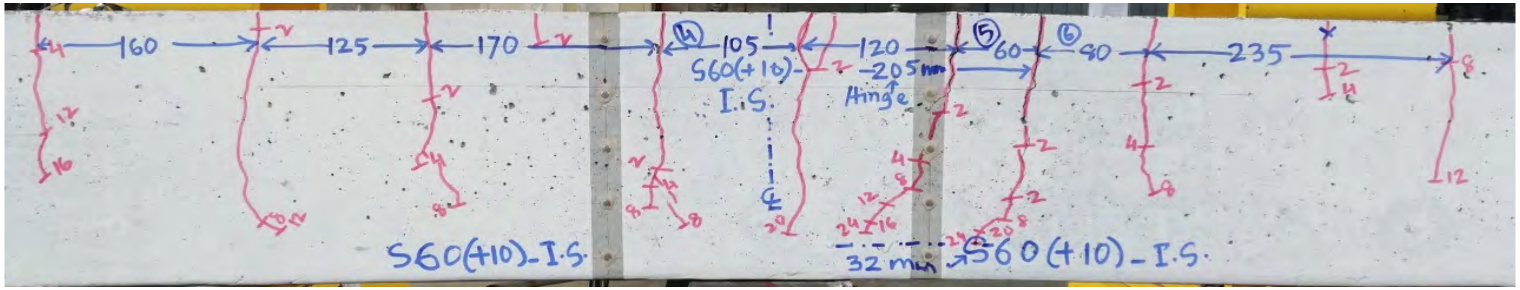

(b) Intermediate support

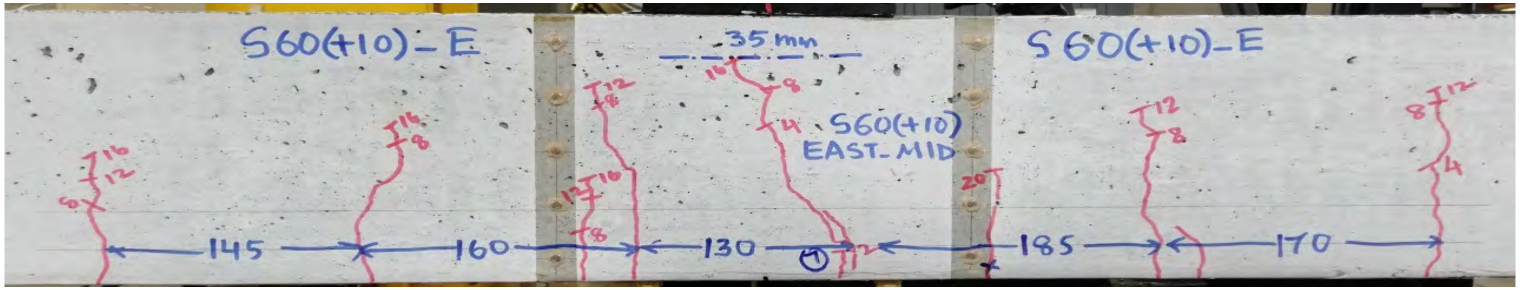

(c) East mid-span

Figure D.2: Crack patterns for Specimen S60(+10).

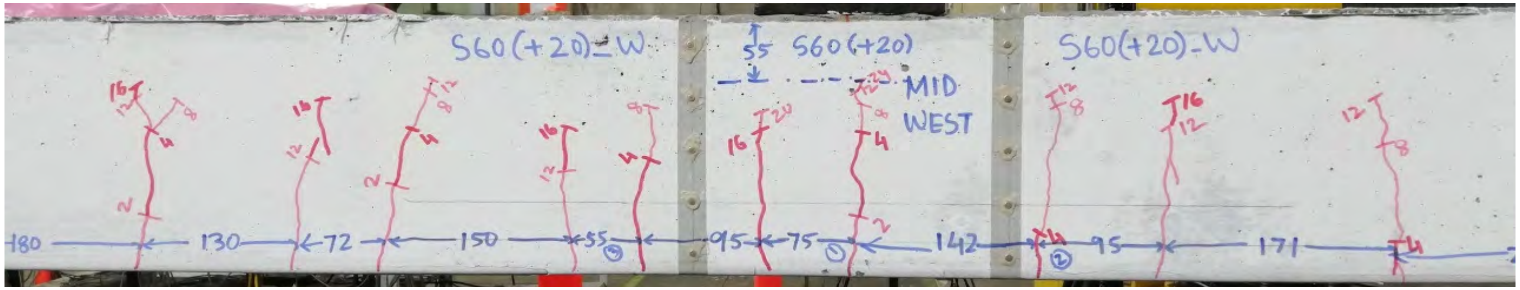

(a) West mid-span

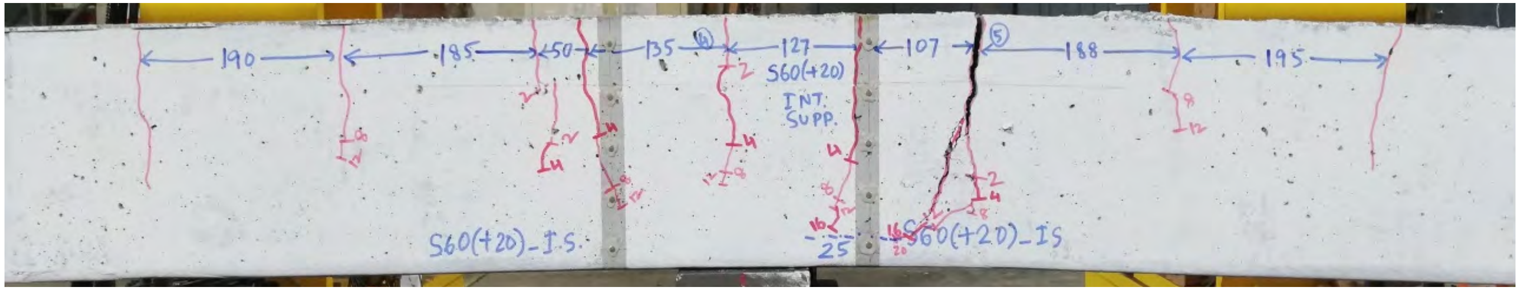

(b) Intermediate support

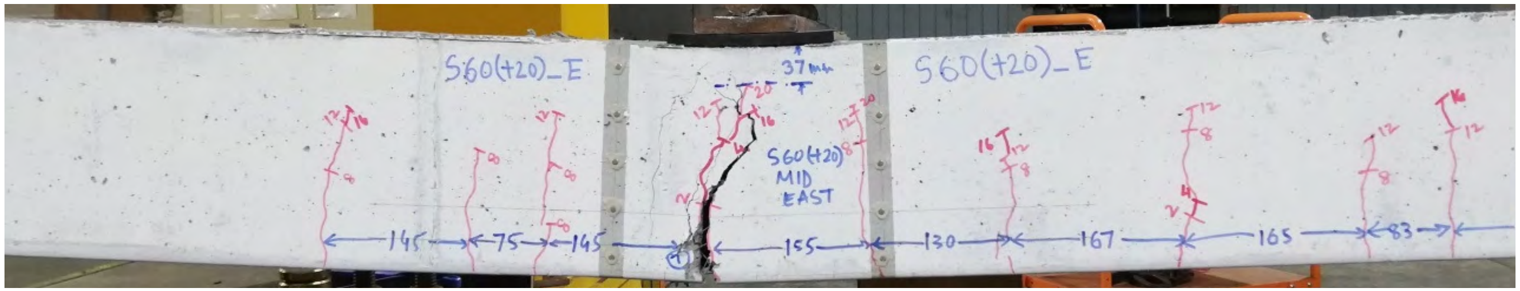

(c) East mid-span

Figure D.3: Crack patterns for Specimen S60(+20).

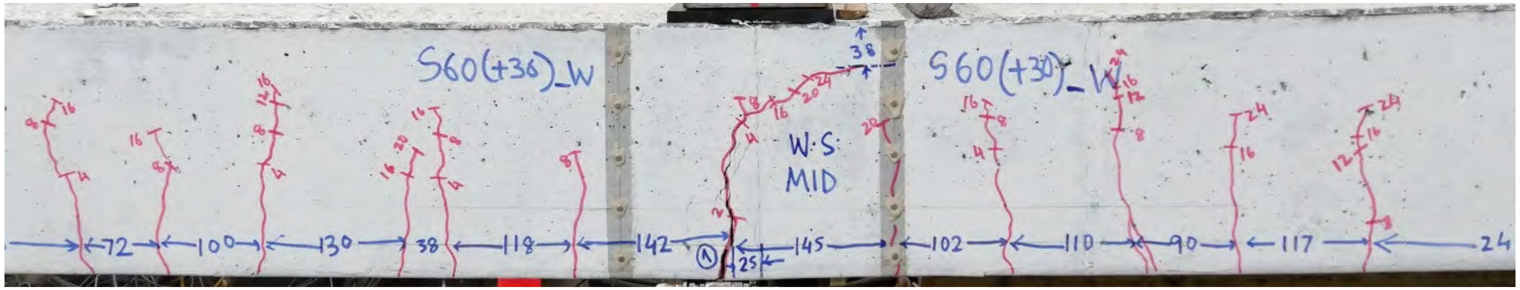

(a) West mid-span

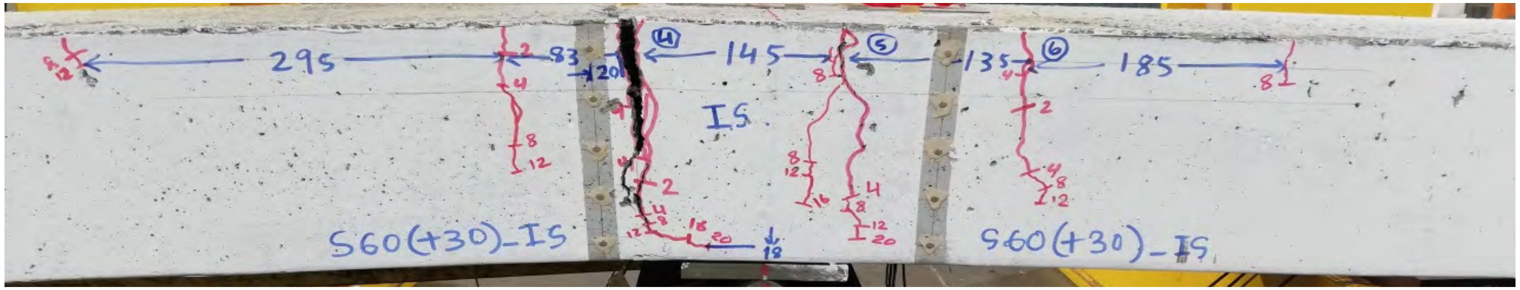

(b) Intermediate support

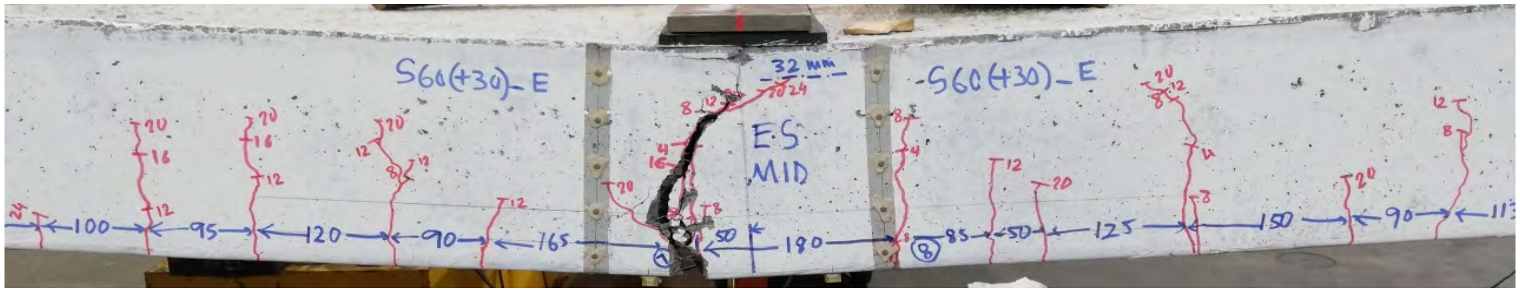

(c) East mid-span

Figure D.4: Crack patterns for Specimen S60(+30).

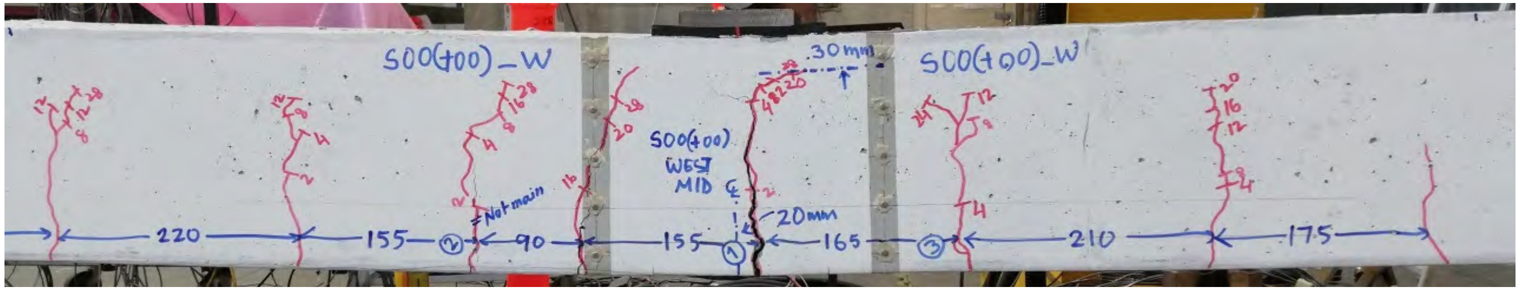

(a) West mid-span

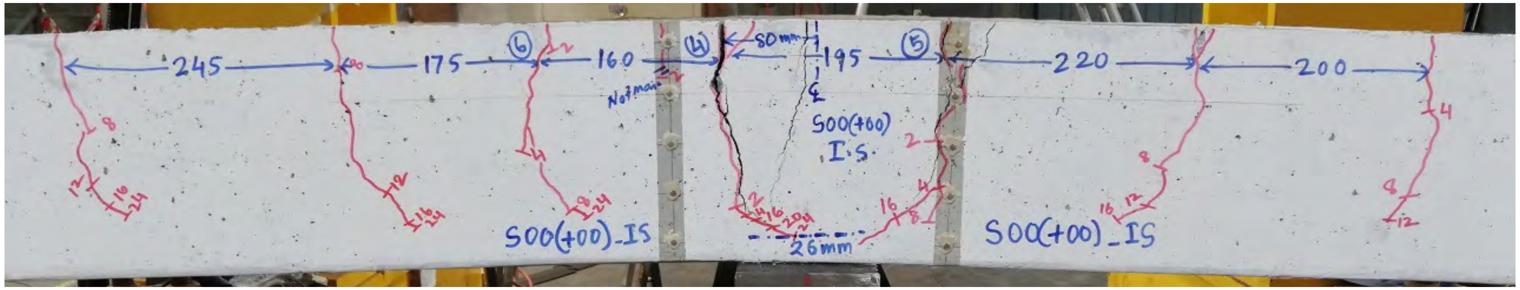

(b) Intermediate support

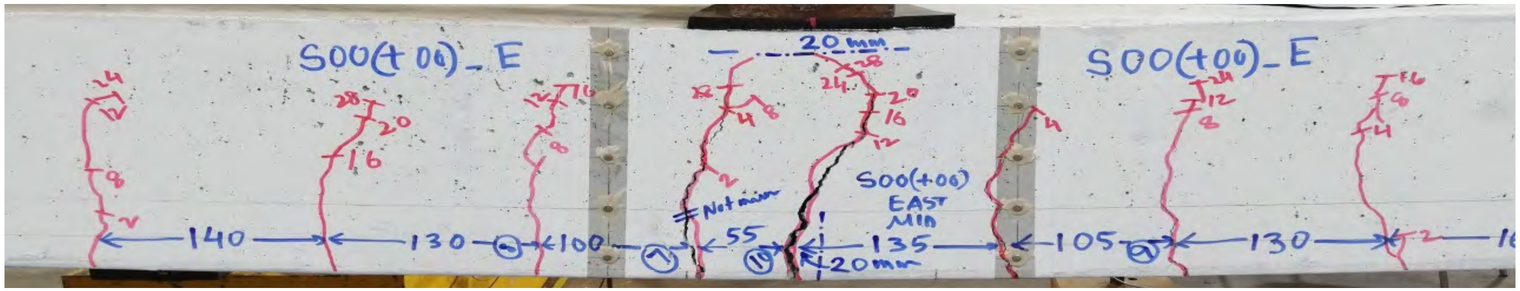

(c) East mid-span

Figure D.5: Crack patterns for Specimen S00(+00).

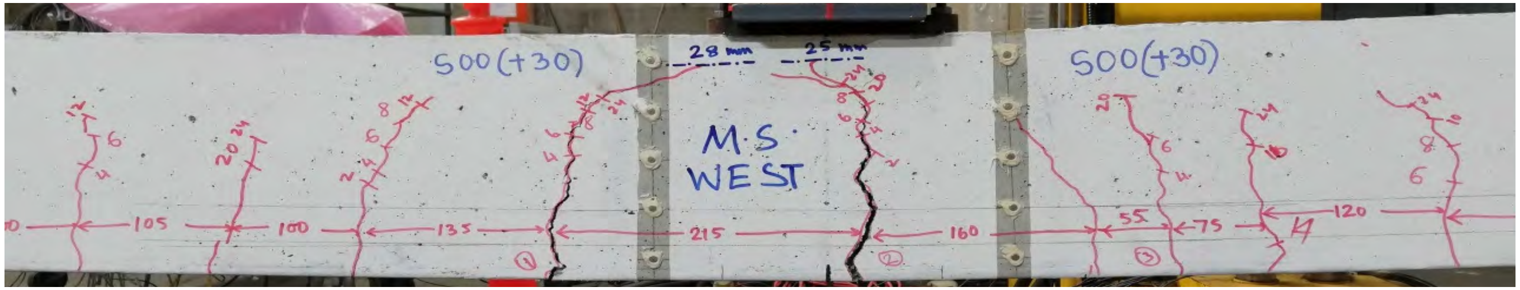

(a) West mid-span

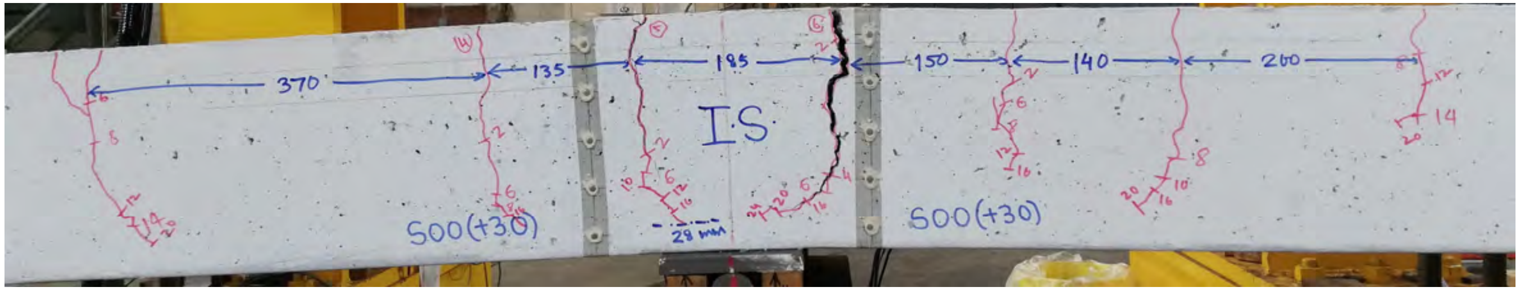

(b) Intermediate support

(c) East mid-span

Figure D.6: Crack patterns for Specimen S00(+30).

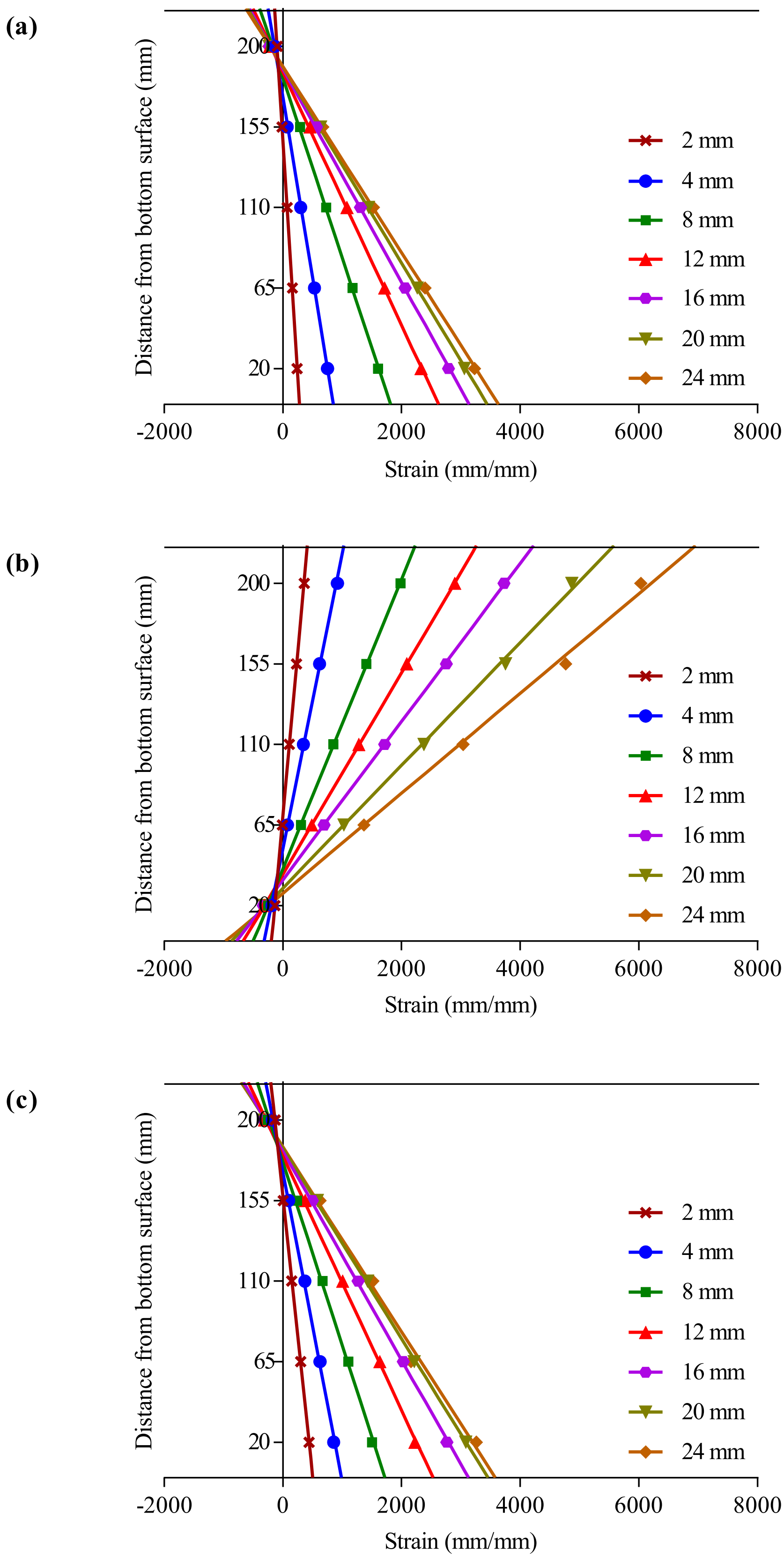

Figure D.7: Strains of concrete for specimen S60(+00) at (a) west mid-span, (b) intermediate support, and (c) east mid-span.

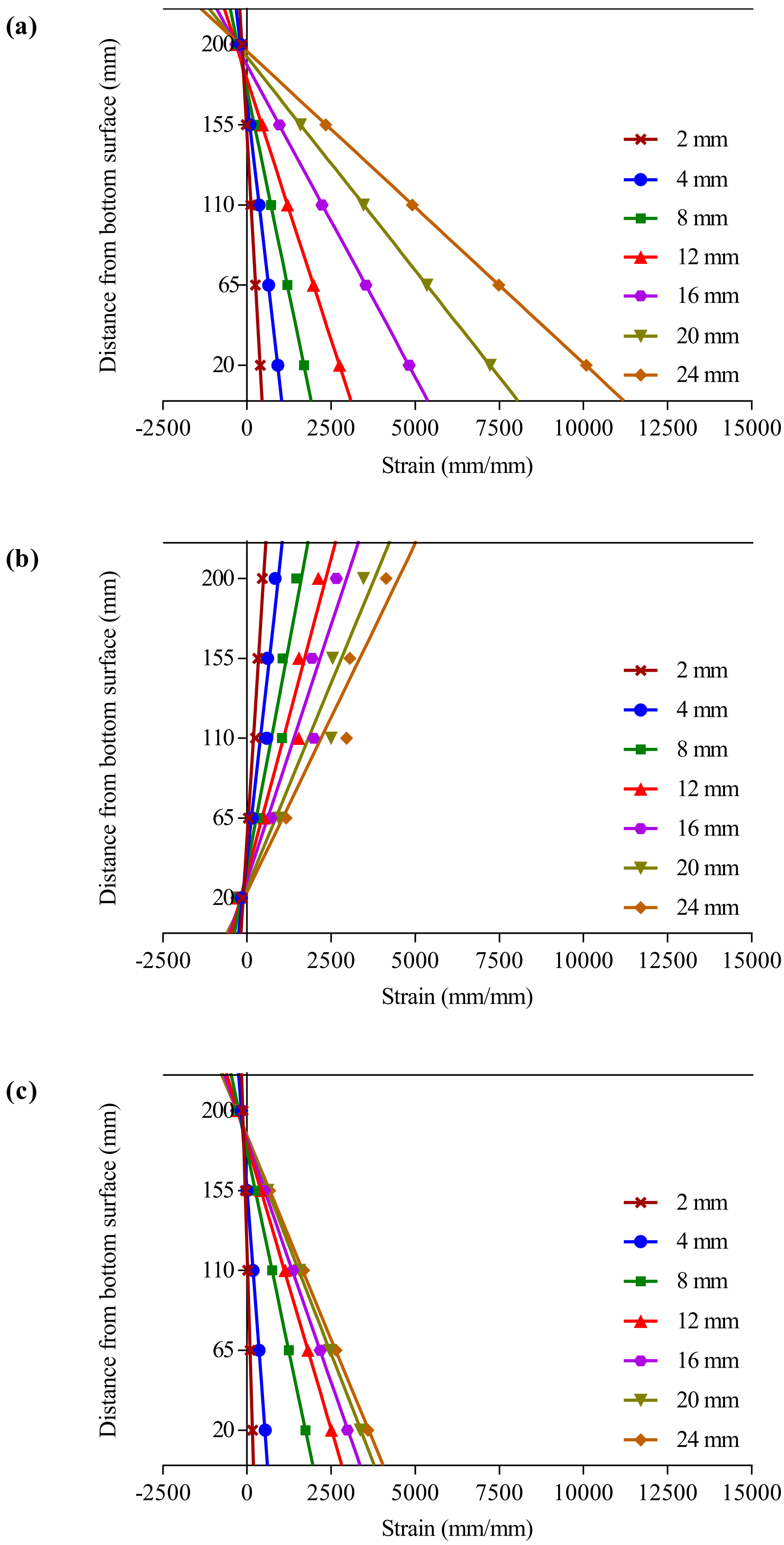

Figure D.8: Strains of concrete for specimen S60(+10) at (a) west mid-span, (b) intermediate support, and (c) east mid-span.

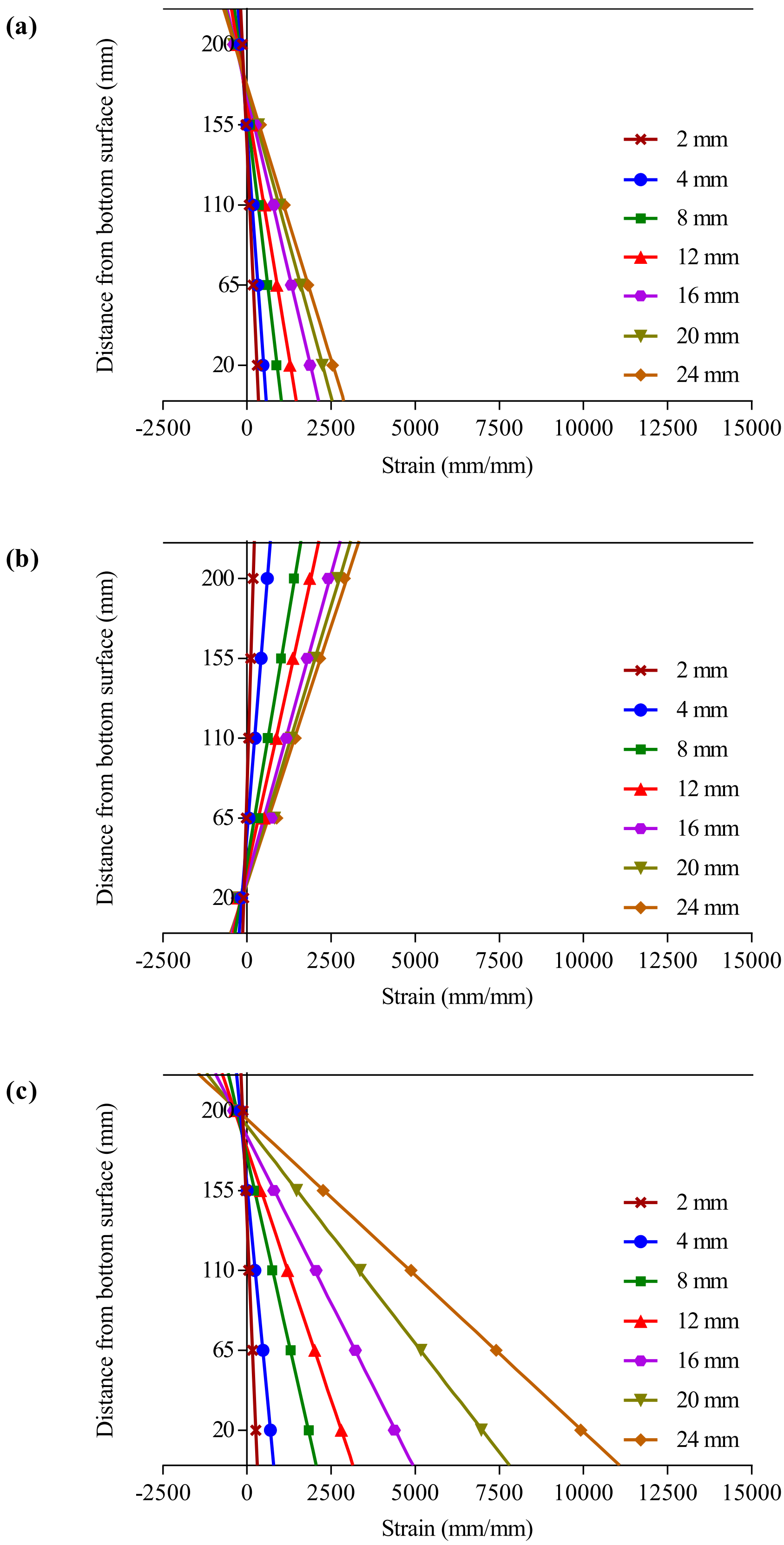

Figure D.9: Strains of concrete for specimen S60(+20) at (a) west mid-span, (b) intermediate support, and (c) east mid-span.

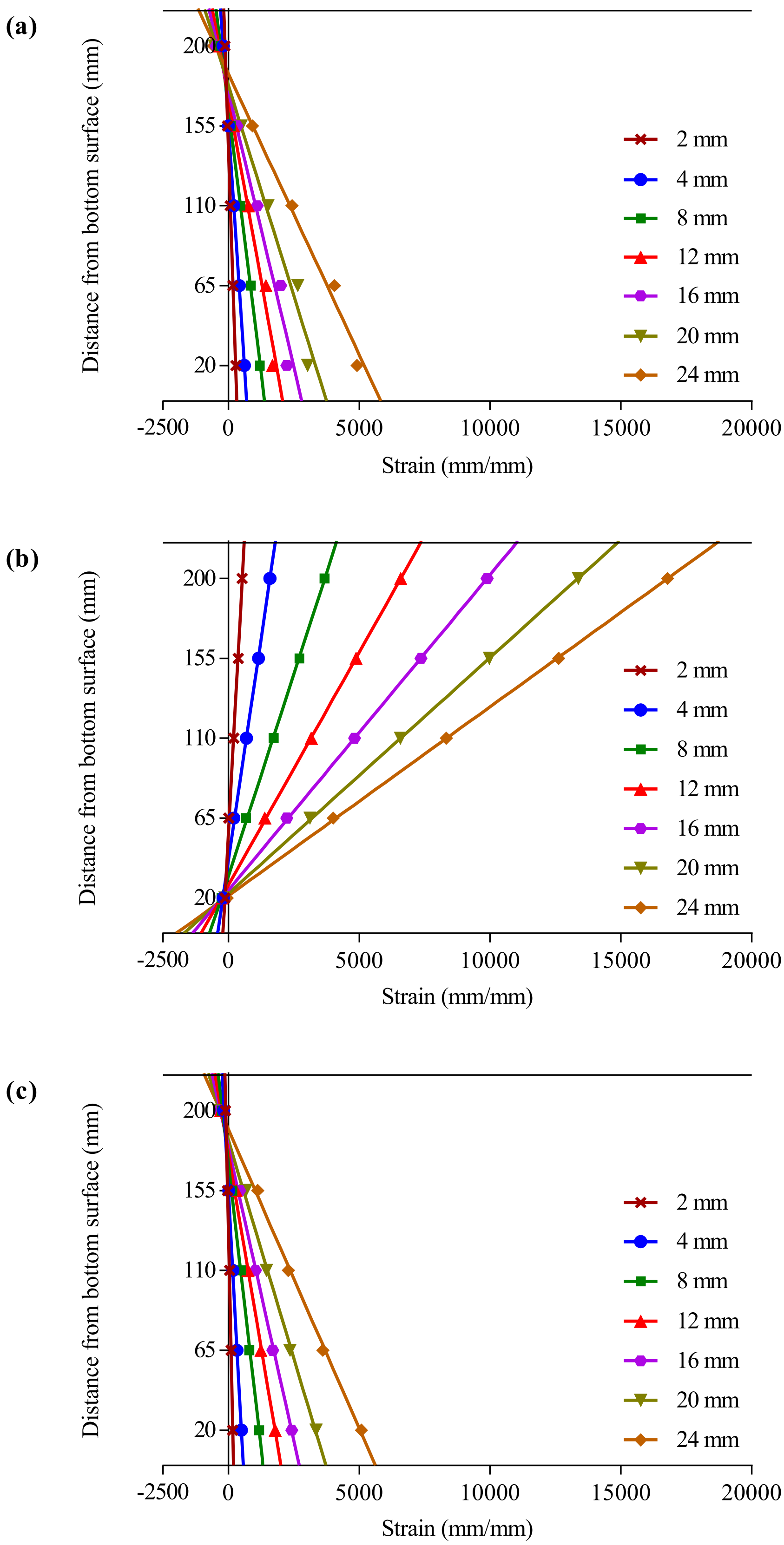

Figure D.10: Strains of concrete for specimen S60(+30) at (a) west mid-span, (b) intermediate support, and (c) east mid-span.

(a)

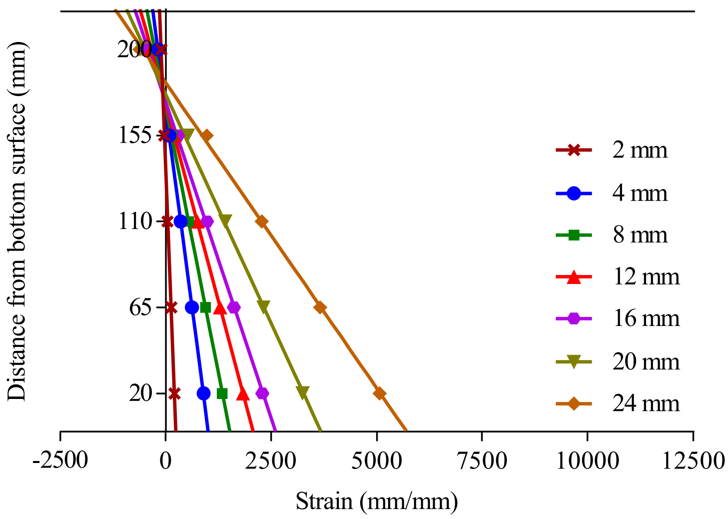

(b)

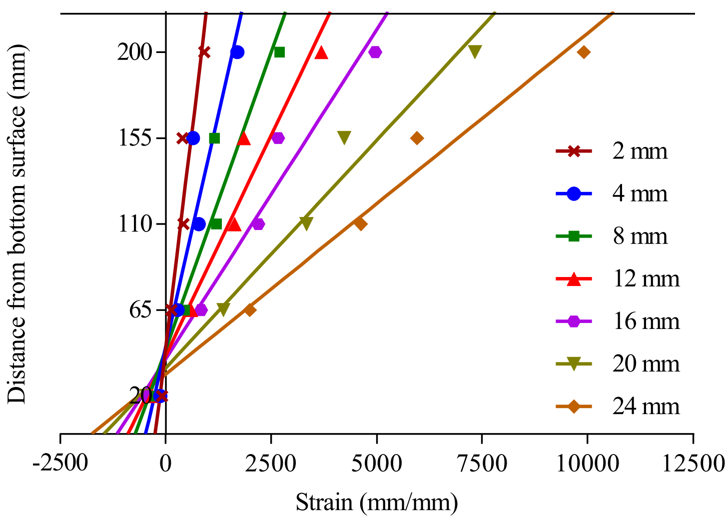

(c)

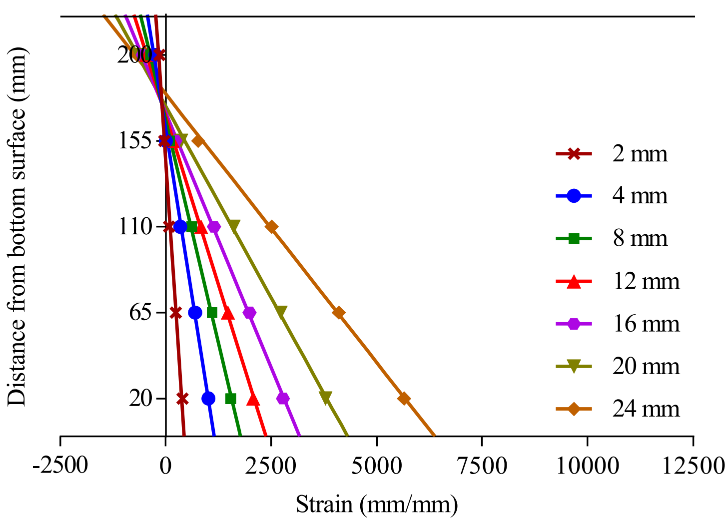

Figure D.11: Strains of concrete for specimen S00(+00) at (a) west mid-span, (b) intermediate support, and (c) east mid-span.

(a)

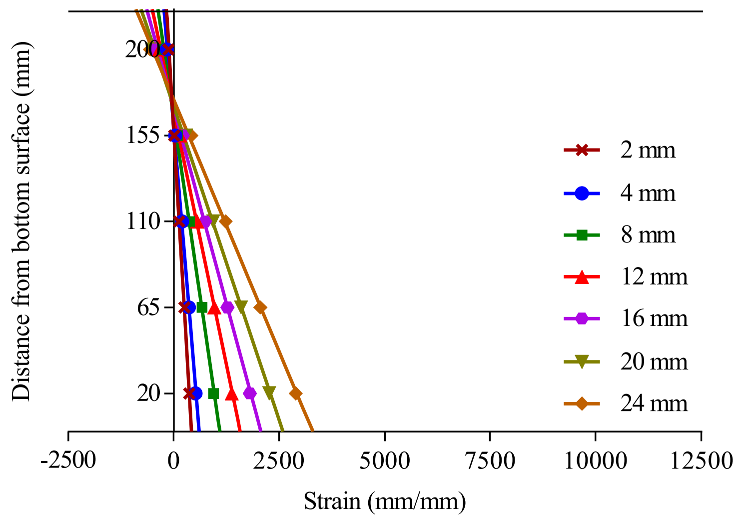

(b)

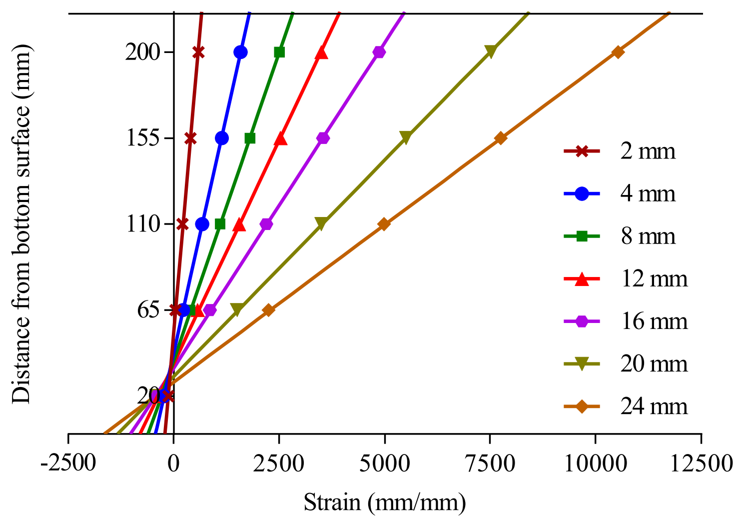

(c)

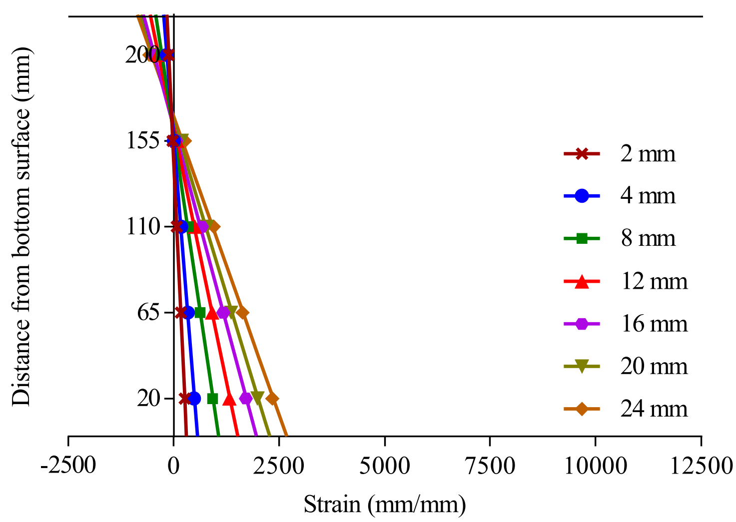

Figure D.12: Strains of concrete for specimen S00(+30) at (a) west mid-span, (b) intermediate support, and (c) east mid-span.

THE END